

Solution to the Broadside Problem and Symmetry Properties of Periodic Leaky-Wave Antennas



Simon Otto

Solution to the Broadside Problem and Symmetry Properties of Periodic Leaky-Wave Antennas

Von der Fakultät für Ingenieurwissenschaften der
Abteilung Elektrotechnik und Informationstechnik
der Universität Duisburg-Essen

zur Erlangung des akademischen Grades

Doktor der Ingenieurwissenschaft

genehmigte Dissertation

von

Simon Otto

aus

Oberhausen

Erster Gutachter: Professor Dr.-Ing. Klaus Solbach
Zweiter Gutachter: Professor Christophe Caloz, Eng., Ph.D.

Tag der mündlichen Prüfung:

18. April 2016



Solution to the Broadside Problem and Symmetry Properties of Periodic Leaky-Wave Antennas

Von der Fakultät für Ingenieurwissenschaften der
Abteilung Elektrotechnik und Informationstechnik
der Universität Duisburg-Essen

zur Erlangung des akademischen Grades
Doktor der Ingenieurwissenschaft
genehmigte Dissertation von

Dipl.-Ing. Simon Otto, geboren am 13. Mai 1978 in Oberhausen

Erster Gutachter: Professor Dr.-Ing. Klaus Solbach
Fachgebiet Hochfrequenztechnik (HFT)
Universität Duisburg-Essen, Deutschland

Zweiter Gutachter: Professor Christophe Caloz, Eng., Ph.D.
Department of Electrical Engineering
Polytechnique Montréal, Canada

Einreichung vorgelegte Dissertation am: 16. Oktober 2015

Mündliche Prüfung am: 18. April 2016

Veröffentlichung genehmigte Dissertation am: 18. Juli 2016

Vorgelegte Version:

Kompiliert am 15.10.2015 - 20:56:11, GIT Commit vom: 2015-10-15 20:55:57 +0200, GIT Hash: f2fd2a6

Genehmigte Version:

Kompiliert am 7.7.2016 - 14:14:21, GIT Commit vom: 2016-07-07 14:14:07 +0200, GIT Hash: 5298fe2

Genehmigte Version (Web):

Kompiliert am 16.7.2016 - 17:13:08, GIT Commit vom: 2016-07-16 17:12:54 +0200, GIT Hash: 679048a

For My Loved Ones

Rina

Sophie & Joshua

Acknowledgments

The road to completing this dissertation and making my dream come true has been a long one. Many people have supported me with their individual skills and abilities, helping me to reach the end of this arduous but rewarding project. Pursuing the Ph.D. part-time while working half-time as a researcher at the University of Duisburg-Essen and the other half as a project manager at IMST GmbH, I can only call myself lucky to have had such wonderful colleagues from both institutions.

This doctoral thesis is the culmination of a long research collaboration between Professor Christophe Caloz at Polytechnique Montréal in Canada and me during my doctoral studies at the University of Duisburg-Essen in Germany. My sincere thanks to Professor Caloz for keeping up our long-distance research collaboration all these years. This collaboration has called for countless video chat sessions about papers or to debate the latest research results. Christophe, your fantastic interest in this work motivated me tremendously.

My thanks also to Professor Klaus Solbach, University of Duisburg-Essen, for employing me as a researcher in his department and giving me his full support. Professor Solbach gave me the freedom to find my own research path even as he kept his office door open whenever I needed his guidance. This freedom is something for which I will be forever grateful.

I am truly appreciative of my friends and colleagues at the Hochfrequenztechnik department (HFT) at the University of Duisburg-Essen. For so many years, the positive influence of Rolf Küppers and Paul Lehmann ensured that we had a warm, companionable work environment characterized by a perfect team spirit. Each, with his individually great character and personality, showed wonderful kindness toward my colleagues and me, even in our lives beyond the university. Rolf, we were all devastated when you suddenly left this world—and us. We miss you very much! Let me deeply thank you for all you have done for me.

Let me also express my gratitude to my long-time research friend Andreas Rennings. Andreas, you made the combination of research and fun perfectly logical—a rare feat. Thank you so much for all we have accomplished together.

I would like to thank my former bachelor's and master's students for choosing me as their supervisor. Many of you have contributed a lot to this work. In particular, I mention

Zhichao Chen and Amar Al-Bassam. When we first knew each other, you both were still doing your undergraduate studies, and now you are finalizing your own Ph.Ds. It was a real pleasure to work with you and to see you progress in academia. During my own Ph.D. studies our relationship moved from supervision to friendship, a transformation that has been rewarding and enjoyable. Thank you so much.

To my friends and colleagues in the Antenna & EM Modeling Department at IMST GmbH, I say thank you, because working with you has always been pleasant and respectful. During my challenging part-time pursuit of the Ph.D., you always made me feel like an integral part of the team, even though my presence was naturally limited. I think this inclusion should not be taken for granted. It is rather the result of many kind coworkers organized in a good team which I am thankful to be a part of.

A very special person on this team is Andreas Lauer, to whom I express my particular gratitude. You have an extremely bright mind and you are always up for lively scientific discussions, though I must admit I had some difficulties keeping up with you here and there. Thank you very much for coaching me in hard times, when the end of the road was still far from sight.

Ismael Nistal, my former officemate at IMST, thank you for putting up with sharing an office with me for so many years before you returned to Spain, your home country. I really appreciate our great office atmosphere and admire your discipline. Flying in from Spain to attend my dissertation defense was the perfect surprise and an honor for me, my friend!

Finalizing a manuscript can be a demanding and sometimes even painful task, and it's always helpful to have a second pair of eyes. Here, I got additional support from my IMST colleagues Jordi Balcells-Ventura, Tassilo Gernandt, and Jürgen Kunisch—my second, third, and fourth pairs of eyes—who helped me to eliminate errors in various parts of the manuscript, thus improving its final form. Thank you all for giving me your time.

My reaching the end of this Ph.D. road would not have been possible without my family and friends backing me up. On countless occasions, I took a pass on social gatherings with friends to focus on my work. Yet they were always understanding and never gave up on me socially. Thanks, guys—I am back now!

What's more, my brother-in-law, Kyle Hollingsworth, a native English speaker and a lawyer, offered the ideal combination of knowledge and precision to help me to shape up my English wording. Thanks so much, Kyle, for your feedback.

At this point, I must thank my best friend Robin Aly, who truly knows me better than I do myself. Knowing me for so many years, and going through your own Ph.D. studies, you helped me to overcome those inevitably frustrating moments in my dissertation writing period. Your mentoring skills are amazing, and I really appreciate our close friendship.

Last but not least, I want to thank the most important persons in my life, my wife Rina and our kids, for their encouragement, patience, and belief in my ability to finalize this project. Without you, there would be no meaning to any of this.

Statement of Originality

I hereby declare that all of the work described within this dissertation is my own original work. Any published or unpublished ideas and/or techniques from the work of others are fully acknowledged in accordance with standard referencing practices.

The present dissertation proposes a consistent theoretical framework embedding my published work from four journal contributions and 13 conference papers. These works were produced solely by me, with the co-authors participating as scientific advisors. For the sake of readability, I chose not to cite text paragraphs and figures taken from my own original publications.

Furthermore, I certify that neither this research thesis nor any part of it has been previously submitted for a degree or any other qualification at any other institution in Germany or abroad.

July 7, 2016

Simon Otto

Contents

1	Introduction	1
1.1	Periodic Leaky-Wave Antennas	1
1.2	Propagation and Radiation Characteristics	3
1.3	Broadside Radiation Problem	5
1.4	Research Gap	6
1.5	Research Approach	7
1.6	Scientific and Engineering Impact	8
1.7	Thesis Organization	9
2	Leaky-Wave Antenna Theory and Classifications	11
2.1	Theory of Periodic Structures	11
2.1.1	Floquet Theorem and Space Harmonics	11
2.1.2	Dispersion Diagram: $\omega - \beta$	14
2.2	Radiation Properties of Leaky-Wave Antennas	15
2.2.1	Main Beam Scanning with Frequency	17
2.2.2	Scanning Range	18
2.3	Network Modeling of Unit Cells	20
2.3.1	Propagation Constant	21
2.3.2	Bloch Impedance	22
2.4	Class of Periodic LWAs Considered	23
2.5	Symmetry Classification - Transversal and Longitudinal Unit Cell Axes	24
3	Fully Symmetric LWAs and their Limitations	25
3.1	Generic Two-Port Network Model	25
3.1.1	Lattice Circuit Model for Transversally Symmetric Unit Cells	26
3.1.2	Series and Shunt Resonators and Immittance Linearization	28
3.1.3	Propagation Constant and Broadside Frequency	32
3.1.4	Bloch Impedance	34
3.1.5	Radiation Efficiency	36
3.1.6	At-Broadside Radiation Efficiency	37
3.1.7	Off-Broadside Radiation Efficiency	38

3.2	Frequency-Balancing and Q-Balancing Conditions	39
3.2.1	Equalization for Scanning Through Broadside	40
3.2.2	Comparison of the Four Balanced/Imbalanced Conditions	41
3.2.3	Discussion on Balancing Conditions and Stopband Closure	44
3.2.4	Relationship between Q-Balancing and the Heaviside Condition in homogeneous Transmission Lines	45
3.3	Asymptotic Study on At- and Off-Broadside Properties	46
3.3.1	At-Broadside Frequency Regime	47
3.3.2	Asymptotic Off-Broadside Frequency Regime	48
3.3.3	Comparison of At- and Off-Broadside Properties	49
3.4	Extraction of Circuit Model Parameters using Fullwave Simulation	50
3.4.1	Drivenmode Simulation of a Single Unit Cell	51
3.4.2	Drivenmode Simulation Considering Mutual Coupling between Multiple Unit Cells	54
3.4.3	Eigenmode Simulation of an Infinite Cascade using Periodic Boundaries	57
3.5	Fundamental Broadside Radiation and Efficiency Limitations	63
3.5.1	Series and Shunt Radiation Direction and Polarization	63
3.5.2	Limitation of the Radiation Efficiency to 50% Maximum	65
3.6	Case Study LWAs for Model Validation	66
3.6.1	Series-Fed Patch LWAs	67
3.6.2	Composite Right/Left-Handed LWAs	73
3.7	Summary of Symmetry Properties	75
4	Transversally Asymmetric LWAs for Solving the Broadside Problem	77
4.1	Two-Port Model for Transversally Asymmetric UCs	77
4.1.1	Transformer-Lattice Circuit Model	78
4.1.2	Two-Port Parameters of the Transformer-Lattice Circuit	80
4.1.3	Propagation Constant	82
4.1.4	Bloch Impedance	83
4.1.5	Radiation Efficiency	85
4.1.6	Comparison At-/Off-BS of Symmetrical/Asymmetrical UCs	86
4.2	Optimal Asymmetry Condition for Equalization	86
4.2.1	Bloch Impedance and Efficiency Equalization	86
4.2.2	Illustration of Asymmetry Controlling Broadside	88
4.3	Complex Frequency Approach and Q-Balancing	91
4.3.1	Complex Propagation Constant versus Complex Frequency	91
4.3.2	Equality of the Two Analyses under Optimal Asymmetry	98
4.3.3	Q-Balancing and Mode Degeneration	99
4.3.4	The “Complex-Frequency-Balancing” Condition – Unification of Frequency and Q-Balancing Conditions	104
4.4	Fullwave Optimization based on Eigenmode Solutions in the Complex Frequency Domain	104
4.4.1	Isolation of the Series Mode with PEC Boundaries	105
4.4.2	Isolation of the Shunt Mode with PMC Boundaries	107
4.4.3	Optimization Procedure	109
4.5	Case Study LWAs for Model Validation	110
4.5.1	Composite Right/Left-Handed LWA	110
4.5.2	A Novel Series-Fed Coupled Patch (SFCP) LWA Design	116

4.6 Summary of Symmetry Properties	118
5 Longitudinally Asymmetric LWAs for Achieving Circular Polarization	119
5.1 Modeling of Series/Shunt Radiation Contributions	119
5.1.1 Edge Radiation from Equivalent Voltage Sources	120
5.1.2 Fully Symmetric Unit Cell	122
5.1.3 Asymmetric Unit Cell with Respect to the Longitudinal Axis	123
5.2 Quadrature Phase Relation in Periodic LWA	124
5.2.1 Simplified Illustration using the SFP LWA	127
5.3 CRLH and SFP Case Study LWAs	128
5.3.1 CRLH and SFP LWA Structures	129
5.3.2 Circuit Modeling	130
5.3.3 Experimental Validation of the Quadrature Phase	131
5.3.4 Measurement of Circularly Polarized LWA Prototypes	133
5.4 Axial Ratio Optimization	135
5.5 Summary of Symmetry Properties	140
6 Summary, Conclusion and Outlook	143
6.1 Summary and Conclusion	143
6.2 Outlook	144
List of Figures	147
List of Tables	155
List of Acronyms and Symbols	157
Bibliography	165

The broadside radiation problem has plagued periodic leaky-wave antennas (LWAs) for more than four decades. A severe loss in performance, particularly in gain and efficiency, occurs when LWAs radiate in the broadside direction, which is the direction normal to the antenna plane. This broadside degradation has just recently been resolved in *metamaterial* LWAs, a special class of LWAs, as demonstrated by several research groups. This suggests that metamaterial LWAs exhibit *extraordinary* properties when compared with *conventional* LWAs. Intrigued by this finding, the author revisits conventional and metamaterial LWAs to answer the following research questions: why does the broadside problem exist, and how can the broadside problem be rigorously solved in periodic LWAs?

These research questions are approached by studying symmetry and asymmetry in the LWA unit cells. The work unveils fundamental broadside radiation limitations and proposes a systematic resolution procedure. Beyond providing physical insight into the wave propagation mechanism of periodic LWAs, this thesis provides a practical framework for the design of periodic LWAs.

1.1 Periodic Leaky-Wave Antennas

Periodic leaky-wave antennas (LWAs) belong to the class of electrically large antennas. Electrically large antennas [1, 2] form an essential part of many of today's electronic systems, including for example:

1. communication systems, such as satellite links, point-to-point links and the new emerging 5G mobile communication generation [3–6],
2. sensor systems, such as automotive radars [7, 8], and
3. medical devices for imaging [9] and for hyperthermia treatment [10, 11].

Electrically large antennas, as any other antenna, may be used for reception and transmission of electromagnetic waves. A major advantage of using an electrically large antenna for reception is an increase in the received power level, as there exists a proportional relationship between antenna size (area) and received power. Similarly, an electrically large transmitting antenna focuses or *directs* the radiated power in the particular direction of the receiver and hence provides a higher power level at the receiver side. Due to reciprocity [2], the same relation holds between antenna size and radiated power as it does between antenna size and received power.

Generally, an increase in the power level is strongly beneficial in a wireless system, since it increases the signal to noise ratio (SNR) [12]. A better SNR yields, for example, a higher data rate in a communication system [13, 14] or a higher probability in the detection of radar targets [15]. Alternatively, the output power of the RF frontend could be reduced with a more directive antenna, while still maintaining the same link performance. Moreover, employing directive antennas also reduces interference and systems can co-exist working at the same frequency without disturbing each other.

Compared to other classes of electrically large antennas, periodic LWAs provide the two following beneficial properties. First, they have high directivity without requiring a complex feed network and are therefore simple to realize. Second, their radiation direction and hence their main beam angle may be steered by varying the excitation frequency or by using electronically tunable circuit elements. The latter is a particularly beneficial property, since the antenna can be pointed into arbitrary directions continuously without mechanical movement. Normally, such a feature is only provided in phased array systems [2, 16, 17], where a complex and expensive phase shifting network is required to scan the beam, yet at a fixed operation frequency.

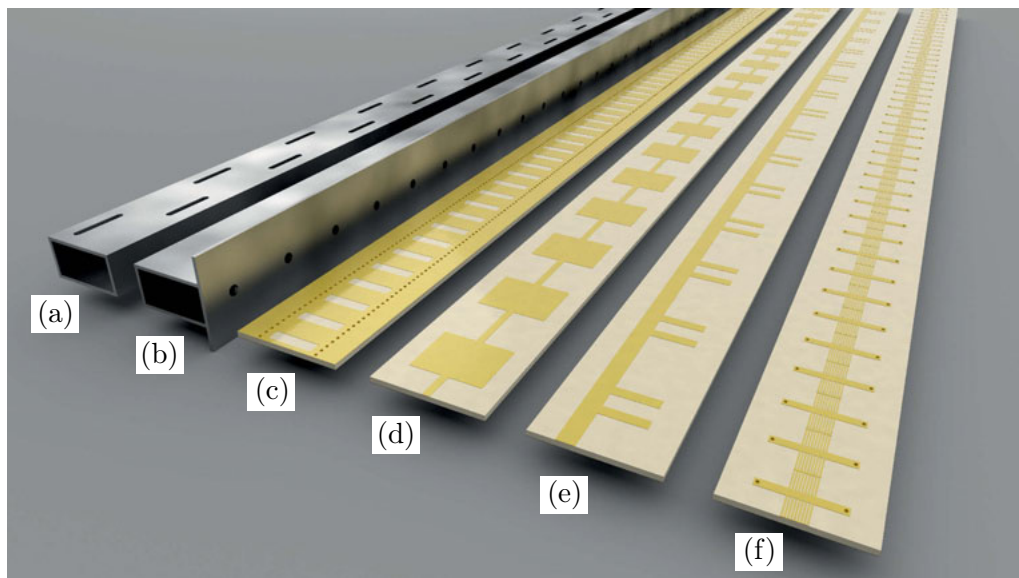


Figure 1.1: Examples of different periodic LWA types. (a) and (b) rectangular waveguide LWAs. (c) Substrate integrated waveguide LWA. (d) to (f) Planar microstrip LWAs.

Research on periodic LWAs dates back to the late 1950's, when Hines and Upson developed the first antenna of this type, consisting of a dielectric filled waveguide periodically

loaded with radiating holes along its side wall [18] as shown in Figure 1.1(b). Approximately ten years later, Hessel provided an extensive synthesis on theoretical advances in the book “Antenna Theory” edited by Collin and Zucker [19]. Since then, a myriad of LWA implementations have been reported based on various technologies including waveguide, dielectric image line, substrate integrated waveguide and planar technologies [20, 21]. Figure 1.1 shows some typical periodic LWA implementations:

- (a) a slotted waveguide LWA [20],
- (b) the “holey waveguide” LWA [18],
- (c) a substrate integrated waveguide (SIW) LWA [22],
- (d) a series-fed patch (SFP) LWA [23],
- (e) a double-stub microstrip LWA [24, 25] and
- (f) a composite right/left-handed (CRLH) LWA [26, 27].

Commonly, periodic¹ LWAs are formed by the repetition of identical cells, *unit cells* (UCs), along a one-dimensional² (1D) line, as shown in Figure 1.1. This thesis focuses on that case and the abbreviation “LWAs” henceforth refers to 1D periodic leaky-wave antennas.

1.2 Propagation and Radiation Characteristics

Figure 1.2 shows an LWA example along with the definitions of the excitation side³, the termination side and the radiation directions. The LWA is fed from the excitation side. A matched load at the termination side absorbs the power and prevents reflections from this side. Under such a configuration, a traveling wave is propagating along the LWA structure, where the periodic modulation of the structure causes power leakage in the form of radiation. This results in an exponential decay of the electromagnetic field and hence an exponential power decay profile along the LWA aperture.

The electromagnetic field of LWAs can be mathematically decomposed into an infinite number of spatial harmonics [19], where the superposition of all spatial harmonics reconstructs the total field distribution. The analysis of the space harmonics provides insight into the radiation mechanism. In this thesis, the distinction between conventional and metamaterial LWAs is made based on the dominant radiating space harmonic.

Usually, in conventional LWAs, only the $\mathbf{n} = -1$ space harmonic is of fast-wave nature and therefore contributes to far-field radiation, where \mathbf{n} is the order of a given space harmonic [19, 32]. Typical examples are the SFP LWA and the double-stub microstrip LWA given in Figure 1.1(d) and 1.1(e), respectively. These LWAs are essentially composed of transmission line (TL) or waveguide sections with a unit cell period p of one guided wavelength, where a single or multiple radiator elements are placed within the unit cell.

¹In this thesis, the term *periodic* refers to *identical* LWA cells, namely unit cells (UCs). Here, *periodic* does not necessarily imply an infinite extent of the LWA structure.

²Two-dimensional (2D) *periodic* structures excited by a cylindrical wave do not usually operate as periodic LWAs [28, 29]. Exceptions are 2D periodic LWAs that are *quasi-uniform* for example 2D metamaterial LWA. They provide either a pencil beam at broadside or a scanned conical beam [30, 31].

³For simplicity, all LWAs in this thesis are considered as transmitting antennas, which, due to reciprocity, covers the receive LWA properties as well.

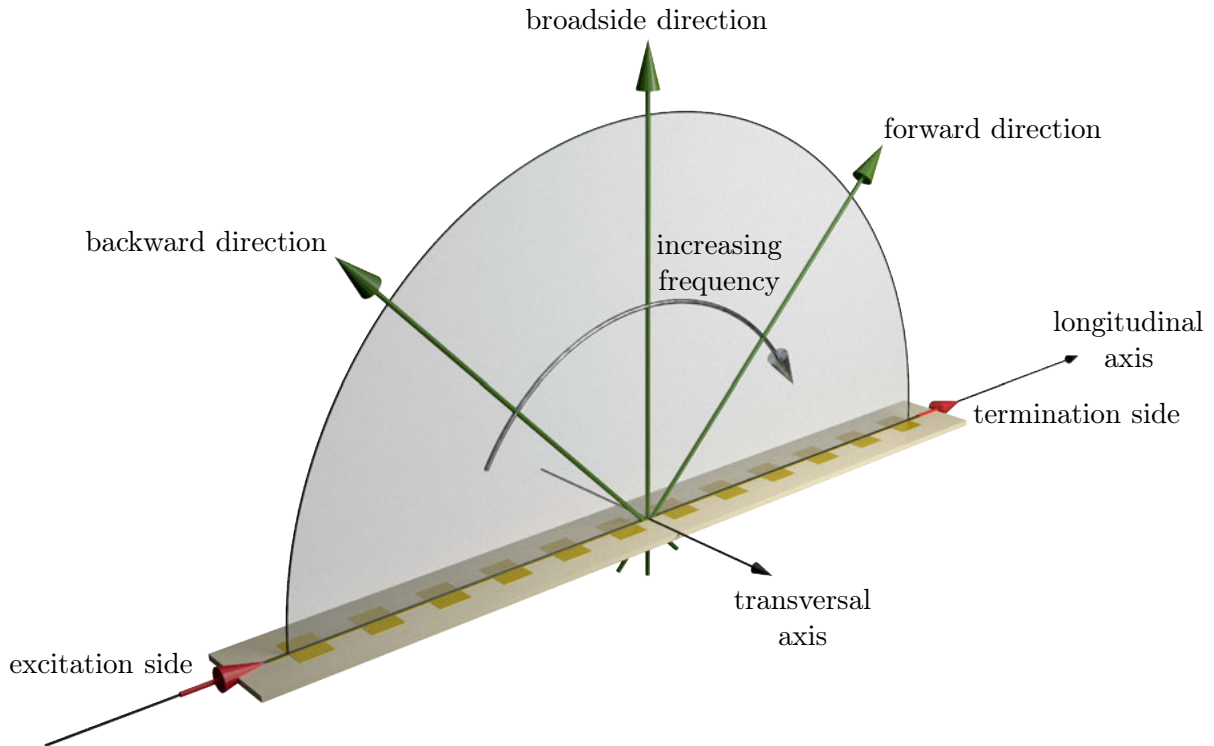


Figure 1.2: Illustration of a typical operation of an LWA, where the radiation main beam scans with frequency from the backward quadrant through broadside to the forward quadrant. The shaded half circle indicates the scanning plane.

If this is the case, the fundamental space harmonic, $\mathbf{n} = 0$, is a slow-wave and hence a purely guided wave.

However, LWA implementations with metamaterial-type transmission lines, in particular composite right/left-handed (CRLH) LWAs, have been recently shown to radiate in their fundamental space harmonic [26, 30]. A typical example is the CRLH LWA given in Figure 1.1(f). This LWA is composed of quasi-lumped element resonators and therefore has a unit cell period p much smaller than one wavelength. Radiation in higher space harmonics could also be possible, although radiating higher space harmonics generally show limitations of the single-beam scanning range and are therefore avoided [33].

Beam scanning with frequency is a beneficial property of LWAs as aforementioned. Metamaterial and conventional LWAs share a qualitatively similar scanning behavior with frequency. Quantitatively, the two classes exhibit different scanning sensitivities with frequency. Usually, metamaterial LWAs are more sensitive [34] resulting from their smaller period p . Figure 1.2 illustrates the concept of *beam scanning with frequency* in LWAs, where the LWA is excited with a sinusoidal signal of frequency f at its excitation side. With increasing frequency the main radiation direction and hence the main beam is steered from backward direction through broadside to forward direction. The frequency point, where the LWA radiates into the broadside direction is defined as the broadside radiation frequency f_{bs} . At frequencies lower than the broadside radiation frequency, the traveling wave excites successive radiator elements with a phase progression. This phase progression produces a radiation beam into the backward direction. At the broadside radiation frequency all elements are excited in-phase and the main beam is directed to broadside, which is the direction normal to the antenna plane. Frequencies higher than

the broadside radiation frequency excite successive radiator elements with a phase lag and hence a beam in forward direction is produced.

This beam steering functionality and the exponential power decay along the LWA are characterized by the complex propagation constant, $\gamma = \alpha + j\beta$, [20, 28, 31]. The phase constant, β , accounts for the phase shift between successive unit cells and therefore carries the relevant information on the main beam direction as described above. The phase constant monotonically increases with frequency yielding a beam scan from backward through broadside to forward. The leakage constant α models the exponential decay of the power along the LWA structure. A large leakage constant results in a short length of the radiating aperture, hence a broad beamwidth with less directivity. A small leakage constant, on the other hand, produces a high directive beam having a small beamwidth.

The complex propagation constant is therefore an important quantity that dominantly controls the radiation characteristics in the scanning plane. For this reason, the frequency behavior of the leakage constant and the phase constant must be carefully considered in the analysis and the design of LWAs. In particular, the broadside radiation frequency and hence radiation in the broadside direction are critical and lead to a general problem in LWAs.

1.3 Broadside Radiation Problem

Radiation in the broadside direction has been a fundamental problem in LWAs, as already pointed out over forty years ago [19]. This degradation has severely restricted practical applications of these types of antennas over such time. If no specific precautions are taken, an *open-stopband*⁴ occurs at broadside [21, 28]. This open-stopband is associated with strong variations over frequency of the leakage constant and the input impedance. As a consequence of these variations, LWAs suffer from efficiency and gain degradations around broadside.

Figure 1.3 qualitatively shows these parameters. The phase constant and the leakage constant are plotted in Figure 1.3(a). The broadside frequency is indicated by the dashed line. Here, at the broadside frequency, the phase constant is zero and the leakage constant exhibits a pronounced minimum together with a strong variation.

Figure 1.3(b) shows the magnitude of the input impedance⁵ for an infinite LWA. Around broadside a well-pronounced peak is observed with a strong frequency dependency. This peak prevents the LWA from being matched over the entire frequency and scanning range. As a result of the mismatch at broadside, the incident power is reflected, since the LWA is not able to accept the provided source power. Typical radiation patterns are given in Figure 1.3(c), where the beam scanning with frequency is illustrated. The gain in the broadside direction is degraded as compared to the backward and forward radiation directions. A degradation of, for example, 3 dB would lower the range of a communication

⁴A proper stopband definition in terms of a well-defined frequency range to delimit a stopband is strictly not possible in an LWA. Therefore, the term *open-stopband* only qualitatively describes the characteristic of the propagation constant around broadside, which is discussed in the forthcoming Section 3.2.3.

⁵The input impedance for an *infinite* LWA, where the termination side is placed at infinity, is the *Bloch impedance*, which is defined later in Section 2.3.2.

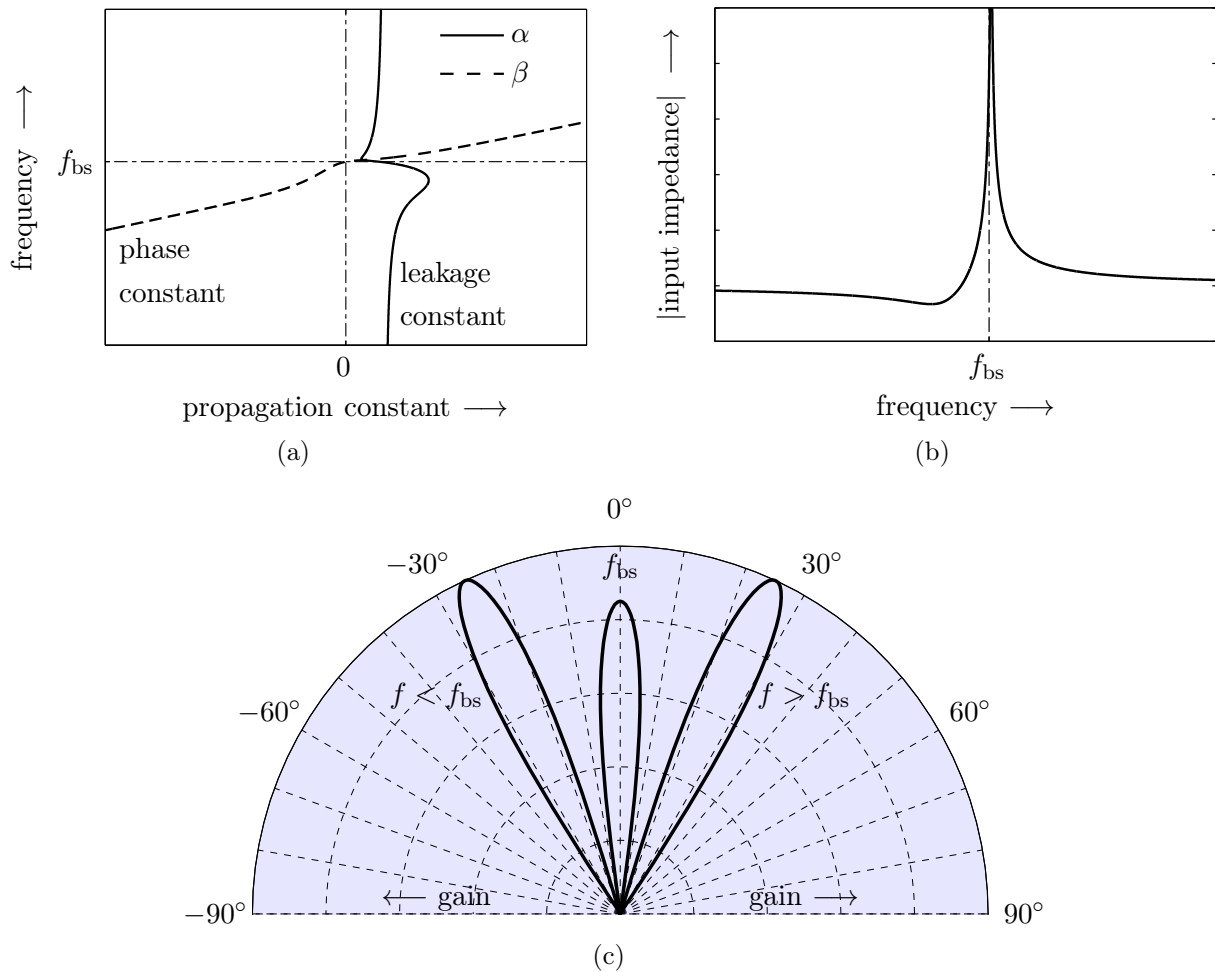


Figure 1.3: Qualitative illustration of the broadside radiation problem, where a strong variation in the parameters are observed generally at broadside. (a) Phase constant and leakage constant. (b) Magnitude of the input impedance. (c) Gain patterns showing a beam scan with frequency in the scanning plane. The broadside radiation is degraded compared to the radiation in the backward and forward directions.

system by a factor of 2 if both receiving and transmitting antenna are impaired by the broadside radiation problem.

1.4 Research Gap

The strong variations of the leakage constant and the gain degradation have been reduced in conventional LWAs in [24, 35]. In these works, the radiation elements (stubs in [24] and strip grating in [35]) are placed a quarter wavelength apart along the longitudinal axis of the waveguide structure. Starting with CRLH LWAs, a similar improvement has been achieved in [26, 27] by fulfilling the *frequency-balancing* condition. In all these designs [24, 26, 27, 35], the broadside radiation has been improved by minimizing the aforementioned variations around broadside, yet the problem has not been fully resolved.

A CRLH LWA has been reported in [36], where the broadside problem has been *empirically* resolved. In this work, a frequency independent leakage constant and impedance for beam scanning through broadside have been reported, where the at- and off-broadside regimes

have been equalized. An *analytical* condition for the equalization has been presented for CRLH LWAs in [37]. More recently, the broadside problem in a conventional LWA (stub-loaded microstrip transmission line) has been empirically solved in [38, 39].

Despite the fact, that the optimized LWAs in [37, 40] and in [38, 39] are different in terms of their electrical unit cell lengths and the radiating space harmonics, they share a common feature, namely *–asymmetry–*. While the CRLH LWAs are asymmetric with respect to their longitudinal axes, the stub-load LWAs are asymmetric with respect to both axes. Symmetries and their implications on the broadside radiation have already been theoretically investigated on the basis of the generalized Floquet’s theorem more than forty years ago in [41, 42]. In these works, only closed waveguide structures, having neither radiation nor dissipation loss, have been considered. It has been concluded that the coupling of space harmonics must be suppressed by enforcing certain symmetries within the unit cell, as otherwise a stopband persists which strongly impairs the broadside radiation.⁶

So far, the resolution of the broadside problem has been achieved only for some specific LWAs, where no link between these solutions exists. No first-principle and general study has been presented to explain how *transversal* and *longitudinal* asymmetry affect the broadside characteristics of *radiating* LWAs and how this may be exploited for an optimal design. The possibility that the degree of coupling needs to be specifically adjusted to the radiation loss to close the stopband and equalize the at- and off-broadside regimes has not been considered thus far. No general approach has been reported to systematically solve the broadside problem and to equalize the at- and off-broadside regimes in arbitrary LWAs. This dissertation fills this gap by answering the following research questions:

1. Why does the broadside problem exist and how is this related to transversal and longitudinal asymmetry?
2. How to rigorously solve the broadside problem in periodic LWAs?

1.5 Research Approach

These research questions are addressed by first classifying periodic LWAs with respect to their transversal and longitudinal axes into symmetric and asymmetric. Second, for transversally *symmetric* LWAs, a generic circuit modeling approach is pursued that is inspired by metamaterial theory, in particular composite right/left-handed (CRLH) transmission line theory [26, 43]. Conceptually, this thesis models *all* transversally symmetric periodic LWAs, metamaterial *and* conventional LWAs, through an adapted CRLH circuit model. Specifically, a lattice circuit topology [44–47] with a series and shunt resonator is chosen as a generic equivalent circuit model.

Next, this *symmetric* lattice model is extended to also model transversally *asymmetric* periodic LWAs. An ideal transformer is introduced in the lattice to model the degree of transversal asymmetry by a single parameter, namely the transformation ratio. Based on this transformer-lattice circuit model, meaningful formulas for the propagation constant,

⁶In [41], the theoretical derivations, including the mode coupling, are restricted to *lossless* closed waveguide structures. In contradiction to this restriction, [41] also discusses the open-stopband problem of *radiating* LWAs.

the Bloch impedance and the radiation efficiency are derived. These formulas provide the explanation and the resolution of the broadside problem.

An investigation of the electromagnetic field is done under infinite periodicity in order to account for all mutual coupling effects. The use here is twofold. First, this allows the derivation of specific field conditions on the unit cell boundaries, providing physical insight into radiation direction and polarization features. These conditions together with the results from the circuit modeling approach reveal fundamental broadside radiation limitations. Second, it allows the development of a fullwave parameter extraction method to extract the circuit model parameters, offering a quantitative LWA analysis and design tool.

Based on the aforementioned methodology, transversal and longitudinal symmetries and asymmetries are studied in periodic LWAs. All theory is confirmed through experimental results, using metamaterial and conventional LWAs as case study examples.

1.6 Scientific and Engineering Impact

Broadside radiation degradation is of scientific interest and of practical relevance. Its general solution resolves this long term problem persisting for more than forty years. Furthermore, a general solution unifies the few existing broadside optimized LWAs [36–39] under the umbrella of a consistent theory that is applicable to all. Scientifically, it is particularly interesting to bridge the gap between metamaterial CRLH LWAs [26, 27, 36, 37] and conventional LWAs [24, 35, 38, 39] and prove that for *both* LWA classes, the broadside remedy lies in unit cell asymmetry. The impact here is twofold. First, a long-term misconception is resolved, as the *extraordinary* broadside properties of CRLH LWAs, in particular the seamless scanning through broadside without degradation, are explained through asymmetries in the unit cell. Second, an *inevitable* broadside limitation in conventional LWAs does *not* exist and current LWA structures can be revised and systematically optimized for efficient broadside radiation [48]. Moreover, novel LWA concepts may be devised based on unit cell asymmetries [48, 49]. This thesis, together with its underlying publications [34, 48–66], systematically builds and organizes knowledge to explain and resolve the broadside degradation in 1D periodic LWAs.

From an engineering viewpoint, the resolution of the broadside radiation problem reaches far beyond the classical periodic LWA design, since it is inherent to all electrically large series-fed antennas [23, 67–74]. In particular, beam steering with frequency is undesired in some applications and most often communication or radar systems operate within a fixed and narrow frequency bandwidth. Nevertheless, many of these systems, particularly high volume and low cost RF-modules, e.g. 24 GHz or 77 GHz automotive radar sensors [7, 72], use planar series-fed antennas, so to avoid a complex feeding and yet realize reasonably high gain at broadside. These antennas will ultimately operate as periodic LWAs, if they are sufficiently long. In other words, a standing wave along the series aperture is no longer present and a traveling wave is dominating, due to the negligible reflection from the antenna’s termination side. Therefore, the rigorous resolution of the broadside radiation problem has a strong engineering impact on the design of series-fed array antennas in high-volume sensor and communication systems.

1.7 Thesis Organization

The thesis is divided into six chapters including the introduction and the conclusion. Chapter 2 provides the required theoretical background of LWAs and the LWA symmetry/asymmetry classifications as a basis for understanding later developments. Chapters 3 to 5 form the main contribution chapters, with each chapter investigating a specific LWA symmetry class.

Chapter 3 investigates *fully symmetric* LWAs and analyzes their limitations. First, a symmetric lattice circuit is proposed as a generic circuit model and derives analytical formulas for the propagation constant, the Bloch impedance and the radiation efficiency. Next, the at-broadside radiation efficiency is proven to be degraded as compared to off-broadside. Fundamental broadside radiation and polarization limitations are then discussed based on the evaluation of the periodic field distribution in the fully symmetric unit cell. Two case study LWAs, a conventional series-fed patch array and a metamaterial CRLH LWA are examined and compared against the circuit model. Finally, the properties of fully symmetric LWAs are briefly summarized at the end of this third chapter.

Chapter 4 analyzes *transversally asymmetric* LWAs and explains how transversal asymmetry resolves the broadside degradation. First, the symmetric lattice circuit model is extended by ideal transformers to generically take into account transversal asymmetry by the transformation ratio. Next, the propagation constant, the Bloch impedance and the radiation efficiency are analytically derived and compared to the former fully symmetric case. A closed-form expression for optimal asymmetry is then derived, which equalizes the at-broadside and off-broadside radiation efficiency and hence rigorously resolves the broadside degradation. The optimal asymmetry case is subsequently analyzed in the complex frequency domain to establish the concept of *complex frequency-balancing*. Finally, two case study LWAs are used for validation, and the properties of transversally asymmetric LWAs are summarized.

Chapter 5 investigates LWA asymmetry with respect to the *longitudinal* axis. It is demonstrated that the broadside degradation may also be resolved by introducing only longitudinal asymmetry, which can result in circular broadside polarization. First, series and shunt radiation contributions are examined, which are polarized in the longitudinal and transversal direction, respectively. Next, the relationship between longitudinal asymmetry and the shunt radiation in broadside direction is established. A quadrature phase relationship between the series and shunt radiation contributions is then theoretically derived. Finally, experimental confirmation that longitudinal asymmetry controls the axial ratio is provided and the properties of longitudinally asymmetric LWAs are summarized at the end of this fifth chapter.

Chapter 6 summarizes the relevant research results, concludes and presents an outlook of this thesis.

Leaky-Wave Antenna Theory and Classifications

This chapter provides the theoretical background for the analysis of periodic LWAs. First, the theory of periodic structures is addressed in preparation of modeling periodic LWAs. Floquet's theorem is used to decompose the electric field distribution along the propagation direction into spatial harmonics. Next, the radiation properties of LWAs are derived from the complex propagation constant taking into account the radiating spatial harmonics. A network modeling approach, based on cascaded two-port networks, is outlined and the Bloch impedance as an important LWA property is defined. A broad class of periodic LWAs is then introduced, for which the theoretical developments in Chapters 3 to 5 hold. Finally, transversal and longitudinal LWA asymmetries are defined.

2.1 Theory of Periodic Structures

The general theory of periodic structures is reviewed. Periodic LWAs form a sub class of periodic structures that are non-shielded and provide specific radiation characteristics. The French mathematician Gaston Floquet worked on the solution of periodic linear differential equations [75] and he established a theorem useful for the analysis of wave propagation in periodic structures [19, 76, 77].

2.1.1 Floquet Theorem and Space Harmonics

Figure 2.1 shows the SFP LWA as an example for a 1D periodic structure. The direction of wave propagation on this structure is along the y -axis. The unit cell, indicated by the two dashed lines in Figure 2.1, is an elementary building block of the infinite cascade. The unit cell has a length, which is referred to as period p . The infinite repetition of unit cells along the y -axis, with multiple integer periods of p , forms the periodic structure.

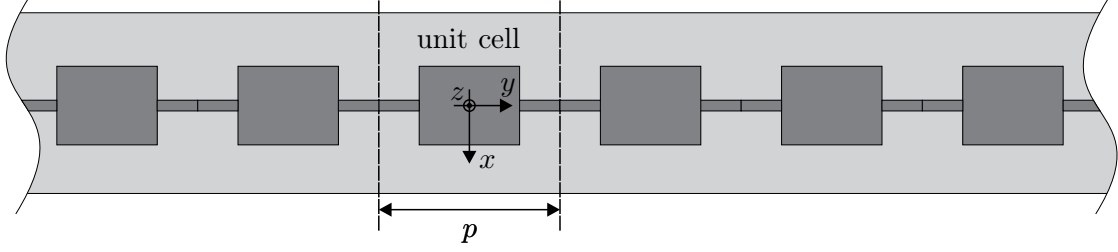


Figure 2.1: SFP LWA as an example for a general periodic structure. The unit cell period is p and the wave propagates along the y -axis.

By means of Floquet's theorem, one can express the electric field of a wave propagating along the infinite periodic structure in positive y -direction as

$$\bar{E}(x, y + mp, z) = \bar{E}(x, y, z)e^{-\gamma mp}, \quad (2.1)$$

where \bar{E} is the electric field¹ vector, m is an integer number and γ is the complex propagation constant. In other words, the electric field at the location y and $y + p$ are only distinguishable by a scalar complex factor, the propagation term $e^{-\gamma p}$. This essentially defines the complex propagation constant γ , which is a quantity of major importance throughout this thesis. The propagation constant is a complex number with

$$\gamma = \alpha + j\beta, \quad (2.2)$$

where α is the leakage constant and β is the phase constant.

In order to better represent and understand the periodic nature of the fields, a periodic vector function \bar{F} with period p along the propagation direction is introduced with

$$\bar{F}(x, y + mp, z) = \bar{F}(x, y, z). \quad (2.3)$$

Next, the electric field is expressed as a product of this periodic function in Equation (2.3) and the complex propagation term,

$$\bar{E}(x, y, z) = \bar{F}(x, y, z)e^{-\gamma y}. \quad (2.4)$$

To confirm that the electric field representation in Equation (2.4) fulfills Equation (2.1), one may write

$$\bar{E}(x, y + mp, z) = \bar{F}(x, y + mp, z)e^{-\gamma(y+mp)}. \quad (2.5)$$

Making use of the periodicity in Equation (2.3) of \bar{F} , Equation (2.5) simplifies to

$$\bar{E}(x, y + mp, z) = \bar{F}(x, y, z)e^{-\gamma y} e^{-\gamma mp} \quad (2.6)$$

By finally back-substituting Equation (2.4) in Equation (2.6), one obtains

$$\bar{E}(x, y + mp, z) = \bar{E}(x, y, z)e^{-\gamma mp}, \quad (2.7)$$

which confirms Equation (2.1).

The most relevant result is given in Equation (2.4), which is now discussed in further detail. The electric field along the periodic structure can be expressed as a periodic

¹For the magnetic field, the derivation is the same.

function multiplied by the propagation term. Any periodic function can be represented by a Fourier series. The Fourier series for the periodic function in Equation (2.3) is

$$\bar{F}(x, y, z) = \sum_{n=-\infty}^{\infty} \bar{E}_n(x, z) \exp\left(-jn\frac{2\pi}{p}y\right), \quad (2.8)$$

where \mathbf{n} is an integer number referring to the order of the space harmonic, $\bar{E}_n(x, z)$ is the cross-sectional field distribution of the \mathbf{n}^{th} space harmonic and corresponds to the Fourier coefficient. By inserting Equation (2.8) into (2.4) one finds an expression for the electric field

$$\bar{E}(x, y, z) = \left[\sum_{n=-\infty}^{\infty} \bar{E}_n(x, z) \exp\left(-jn\frac{2\pi}{p}y\right) \right] \exp(-\gamma y). \quad (2.9)$$

Bringing the propagation term under the sum, the electric field along the periodic structure finally reads

$$\bar{E}(x, y, z) = \sum_{n=-\infty}^{\infty} \bar{E}_n(x, z) \exp\left[-\left(\gamma + jn\frac{2\pi}{p}\right)y\right]. \quad (2.10)$$

If now, the propagation constant of the \mathbf{n}^{th} space harmonic is introduced as follows

$$\gamma_n = \gamma + jn\frac{2\pi}{p} = \alpha + j\left(\beta_0 + \mathbf{n}\frac{2\pi}{p}\right), \quad (2.11)$$

one may write the field along the periodic structure as

$$\bar{E}(x, y, z) = \sum_{n=-\infty}^{\infty} \bar{E}_n(x, z) e^{-\gamma_n y}. \quad (2.12)$$

This final result in Equation (2.12) needs appreciation. It is important to note that the cross sectional field distribution $\bar{E}_n(x, z)$ is independent of y . The only y -dependency is found in the propagation term, so that the total field is decomposed into sinusoidal waves, of different phase constants (or wavenumbers), traveling along an effective homogeneous transmission line. These waves are referred to as space harmonics. All space harmonic experience the same leakage α and the phase constant differs by integer multiples of $2\pi/p$. Moreover, it is worth mentioning that each individual space harmonic \mathbf{n} does not fulfill the boundary condition imposed by the periodicity. Only the sum of all space harmonics reconstructs the total field mode that propagates along the periodic structure and fulfills the boundary conditions.

Before introducing the dispersion diagram as a graphical representation of the complex propagation constant γ_n in the following section, the calculation of the Fourier coefficients,

$$\bar{E}_n(x, y) = \frac{1}{p} \int_{-p/2}^{p/2} \bar{E}(x, y, z) e^{\gamma_n y} dy \quad (2.13)$$

is provided for the sake of completeness.

2.1.2 Dispersion Diagram: $\omega - \beta$

The dispersion diagram or $\omega - \beta$ diagram is a graphical representation of the complex propagation constant. Since the leakage constant is equal to all space harmonics, the focus here lies first on the phase constant. Recalling the phase constant from Equation (2.11), one obtains

$$\beta_n(\omega) = \beta_0(\omega) + n\frac{2\pi}{p}, \quad (2.14)$$

where $\beta_0 = \beta$. Once the phase constant is known, the dispersion diagram is constructed by shifting β_0 with $n2\pi/p$ along the horizontal axes as shown in the dispersion diagram in Figure 2.2. The horizontal axis reads the normalized phase constant $\beta_n p$ and the vertical axis reads the angular frequency ω . The blue solid lines represent an overall wave propagation in positive y -direction. *Overall* here means that the associated power flow is in positive y -direction, as if the structure were excited at $y \rightarrow -\infty$. The green dashed lines show the opposite case, where power flows in negative y -direction with a virtual excitation at $y \rightarrow \infty$.

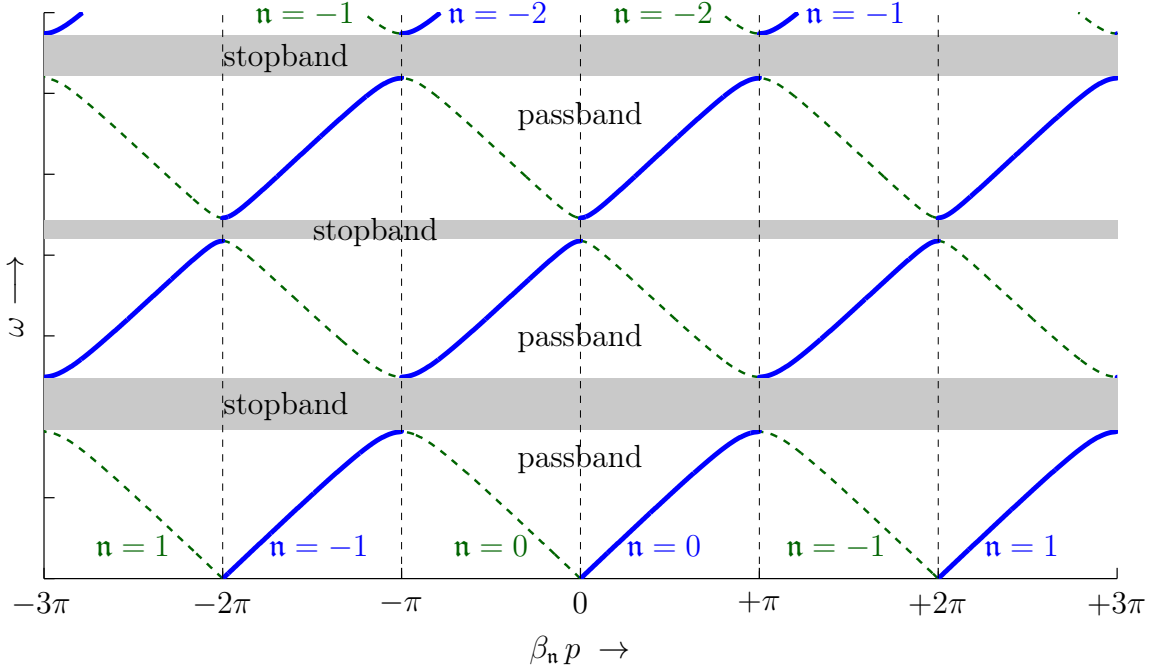


Figure 2.2: Dispersion diagram as a graphical representation of the complex propagation constant. Periodic structures generally show passband (white regions) and stopband (grey shaded regions) behaviors over frequency. The spatial harmonics are separated by multiple of $2\pi/p$. The blue solid lines represent the case of power propagation in *positive* y -direction. The green dashed line represent the case of power propagation in *negative* y -direction.

Moreover, the dispersion diagram visualizes the alternating pass- and stopbands of the periodic structure. Generally, periodic structures exhibit such a behavior [19, 76, 78, 79]. The periodic structure used as example in Figure 2.2 is a lossless and non-radiating structure of alternating low and high impedance transmission lines. This corresponds to a shielded version of the periodic structure in Figure 2.1, which is composed of low and high impedance microstrip TLs. Only if the structure is lossless and non-radiative, clear stopbands are delimited as shown in Figure 2.2. A detailed investigation and modeling of

such a behavior, particularly of the stopband around the critical broadside frequency, is one major focus of this thesis.

Two important quantities related to the propagation of the space harmonics are the phase and group velocities. Both are directly derived from the dispersion relation. The phase velocity of the \mathbf{n}^{th} space harmonic is

$$v_{\text{pn}} = \frac{\omega}{\beta_{\mathbf{n}}} = \frac{\omega}{\beta_0 + \mathbf{n} 2\pi/p} = \frac{1}{1/v_{\text{p0}} + \mathbf{n} 2\pi/(\omega p)}, \quad (2.15)$$

where v_{p0} is the phase velocity of the fundamental harmonic with $\mathbf{n} = 0$. The phase velocities differ for all space harmonics and they can take on positive and negative values depending on the sign of $\beta_{\mathbf{n}}$. The group velocity, on the other hand,

$$v_{\text{gn}} = \frac{d\omega}{d\beta_{\mathbf{n}}} = \frac{d\omega}{d(\beta_0 + \mathbf{n} 2\pi/p)} = \frac{d\omega}{d\beta_0} = v_{\text{g0}}, \quad (2.16)$$

is equal for all space harmonics. It is equal to the group velocity of the fundamental harmonic v_{g0} . This can be easily confirmed in Figure 2.2, where the slopes of all blue lines at a fixed frequency are equal. The case of opposite phase and group velocity, e.g. negative phase and positive group velocity, is referred to as *backward wave* propagation. If the phase and group velocity are in the same direction, e.g. positive phase and positive group velocity, the propagation mechanism is called *forward wave* propagation.

2.2 Radiation Properties of Leaky-Wave Antennas

This section applies the theory established in Section 2.1 to analyze the radiation properties of periodic LWAs. Specifically, the main beam scanning property and the scanning range are addressed with the help of the dispersion analysis and the dispersion diagram.

The dispersion diagram in Figure 2.2 carries strongly redundant information, since the $\beta_{\mathbf{n}}$ are just shifted curves sharing the same frequency behavior as $\beta_0(\omega)$. Therefore, it is sufficient for the forthcoming analysis to restrict the dispersion diagram to a normalized range of $-\pi < \beta p < \pi$. It is furthermore assumed that the power flow along the LWA is in positive y -direction. In this case only the space harmonics with positive group velocity [Equation (2.16)] are present and must be considered (blue curves in Figure 2.2). In addition, any LWA has radiation and dissipation loss, which must be taken into account. These losses strongly impact the dispersion behavior, particularly around the stopbands.

A typical dispersion diagram for an LWA is provided in Figure 2.3. This dispersion diagram is based on the one in Figure 2.2 under the aforementioned constraints. In order to clearly distinguish guided wave propagation and radiated wave propagation it is convenient to plot the *light line*, $k_0 = \pm\omega/c_0$ in the diagram. The light line represents the non-dispersive free-space wave propagation, which divides the dispersion diagram into two fundamentally different regimes, *guided wave regime* and *radiated wave regime*. The radiated wave regime is indicated by the shaded areas in Figure 2.3, which is also called the *radiation cone*.²

²In 2D periodic structures, the dispersion relation is a function of two coordinates and the radiation regime is therefore a volumetric object, namely the radiation cone.

If a specific space harmonic falls into this cone, it fulfills the condition $|v_{pn}| > c_0$ and the propagation is referred to as to *fast-wave* propagation. This fast-wave propagation on the periodic structure allows free-space radiation. In the particular case of broadside radiation, as indicated in Figure 2.3, the phase velocity $|v_{p,n=-1}|$ approaches infinity. This means all unit cells are excited simultaneously without delay, which from a *phased array* antenna perspective (uniform phase taper) [2], intuitively confirms the broadside radiation direction.

If a space harmonic is not within the radiation cone, its phase velocity is slower than the speed of light, $|v_{pn}| < c_0$, hence the propagation is referred to as to *slow-wave* propagation. This is the case for the fundamental space harmonic with $\mathbf{n} = 0$ in Figure 2.3, which is located only in the *guided waves* regime. This wave is purely guided and cannot radiate into free-space. From an phased array antenna viewpoint [20], the radiation is not in the *visible region* and hence trapped in the structure.

Figure 2.3 also shows the leakage constant α . Around the stopbands a large attenuation is observed. This high attenuation is associated with reactive field storage, so called *evanescent waves*, similar to the operation of a standard waveguide below cutoff [76]. Within the passbands, α is comparatively small and it is associated with power decay of the propagating wave along the LWA. Moreover, the LWA beamwidth depend on the power decay profile along the structure. A small α results in a long exponential aperture illumination and hence a narrow beam, whereas a large α results in a short exponential aperture illumination and hence in a wide beam.

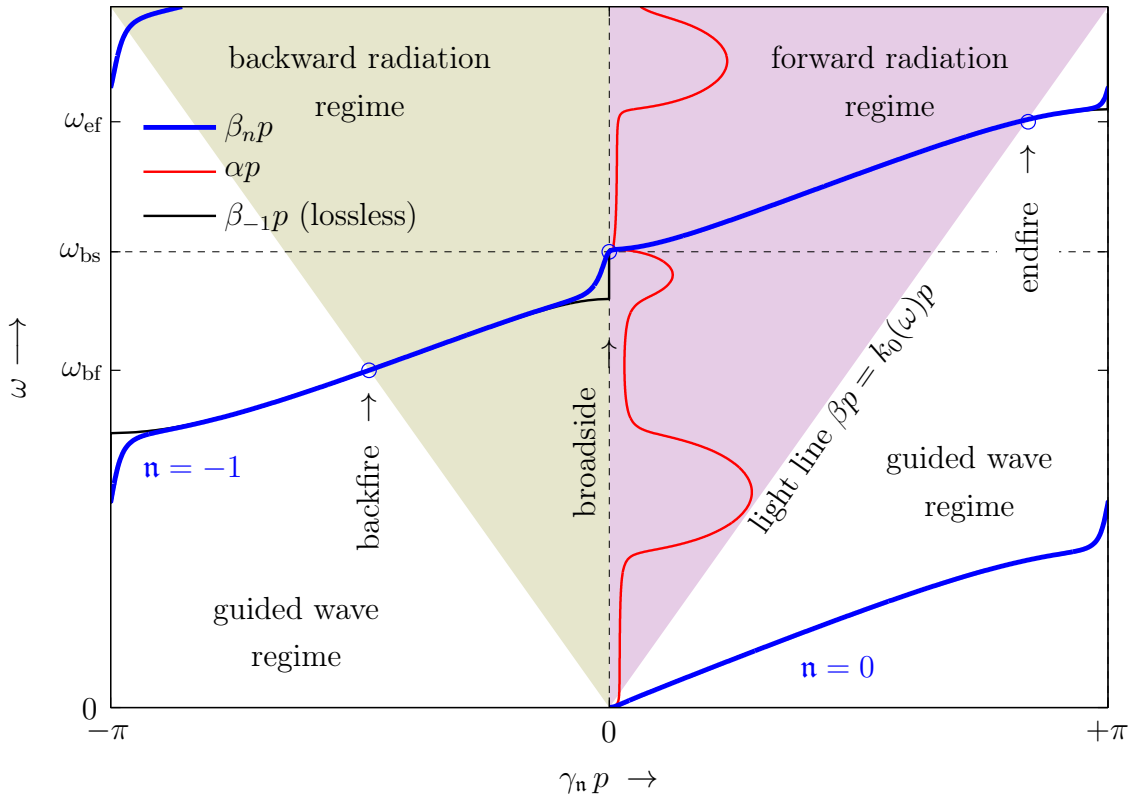


Figure 2.3: Dispersion diagram for an SFP LWA as shown in Figure 2.1 (non-shielded periodic structure). Beam scanning is achieved with the $\mathbf{n} = -1$ space harmonic, which is of fast-wave nature and therefore lies in the radiation regime. The light line with $k_0 = \pm\omega/c_0$ divides the dispersion diagram into the radiation regime and the guided wave regime.

By comparing the phase constants of the shielded lossless structure (Figure 2.2) with the radiating structure (Figure 2.3), a different behavior around the stopbands is observed. The black solid line, $\beta_{-1}p$ (lossless), in Figure 2.3 shows the propagation constant for the shielded lossless structure taken from Figure 2.2. Due to radiation, dissipation or both mechanisms, a well-delimited stopband does not exist anymore and β is significantly influenced (compare solid blue with black line) by the loss mechanisms. In the passband, on the other hand, the loss mechanisms only have a negligible effect on β , where the two lines are perfectly superimposed.

This is an important observation of major theoretical and practical relevance. The propagation characteristics in stopbands, in particular around broadside, is dominated by “loss” (radiation and/or dissipation). Therefore, a common *perturbational modeling approach*,³ which assumes that losses do not affect the field distribution and the propagation mode distribution, is not possible, since this assumption does not hold. A detailed investigation of this phenomenon and a suitable modeling approach is provided in the forthcoming chapters.

2.2.1 Main Beam Scanning with Frequency

The main beam direction in a periodic LWA is steered with frequency. At lower frequencies ($\omega < \omega_{\text{bs}}$) the LWA radiates into the backward direction, as $\beta_{\mathbf{n}}$ is negative. At the broadside frequency ω_{bs} , the LWA radiates into the broadside direction (z -direction), as $\beta_{\mathbf{n}}=0$. At frequencies higher than the broadside frequency ($\omega > \omega_{\text{bs}}$), the LWA radiates into the forward direction, as $\beta_{\mathbf{n}}$ is positive. This beam steering property is described by the main beam scanning law of periodic LWAs [20, 28],

$$\vartheta_{\text{mb}}(\omega) = \arcsin \left[\frac{\beta_{\mathbf{n}}(\omega)}{k_0} \right] = \arcsin \left[\frac{c_0 \beta_{\mathbf{n}}(\omega)}{\omega} \right], \quad (2.17)$$

where ϑ is the angle measured in the y - z -plane from the z -axis and $k_0 = \omega/c_0$ is the free-space wavenumber with c_0 being the speed of light.⁴

Equation (2.17) depends on $\beta_{\mathbf{n}}$, so that the main beam angle θ_{mb} depends on a specific space harmonic. This results in multiple main beams, if more than one space harmonic radiate. Therefore, it is important to ensure that, within in the frequency or scanning range of interest, only a single space harmonic (e.g. $\mathbf{n} = -1$) is of *fast-wave* nature and hence contributes to farfield radiation. This is, for example, the case in the dispersion diagram in Figure 2.3, which shows the dispersion characteristic for the SFP example. Only the $\mathbf{n} = -1$ space harmonic lies in the radiation regime (fast-wave propagation), whereas the other space harmonics, e.g. $\mathbf{n} = 0$, are in the guided wave regime (slow-wave propagation) as aforementioned.

³A perturbational modeling approach assumes that losses do not change the electromagnetic field distribution as compared to the lossless case. The loss contribution is then calculated based on the unperturbed field. A typical example is a transmission line with weak losses or a high-Q cavity resonator.

⁴The derivation of Equation (2.17) is based on the assumption that α is small and can be neglected for the calculation of the main beam direction [28]. This is usually a sufficiently good approximation for medium and high gain LWA of more than 10 dBi gain.

2.2.2 Scanning Range

Periodic LWAs provide *partial* or *full range* beam scanning. Full range means from *backfire* to *endfire*. Backfire is the direction in negative y -direction, where the excitation side is located and endfire is the direction in positive y -direction, where the termination side is located (Figure 1.2). *Partial range* beam scanning refers to a sub-range of this with an angular range of less than 180° .

There are two limitations in LWAs, which prevent them from full range scanning. One limitation is the single beam condition, which ensures that only a single space harmonic in the entire scanning range is of fast-wave nature and lies in the radiation cone [28]. If this condition is violated, the LWA scans with two main beams, which is undesired in almost all practical cases. The second limitation are stopbands, in which the propagation along the LWA structure and hence the radiation leakage are suppressed. In many LWAs, the single beam condition is the more conservative criterion that limits LWAs in their scanning range and is therefore addressed next.

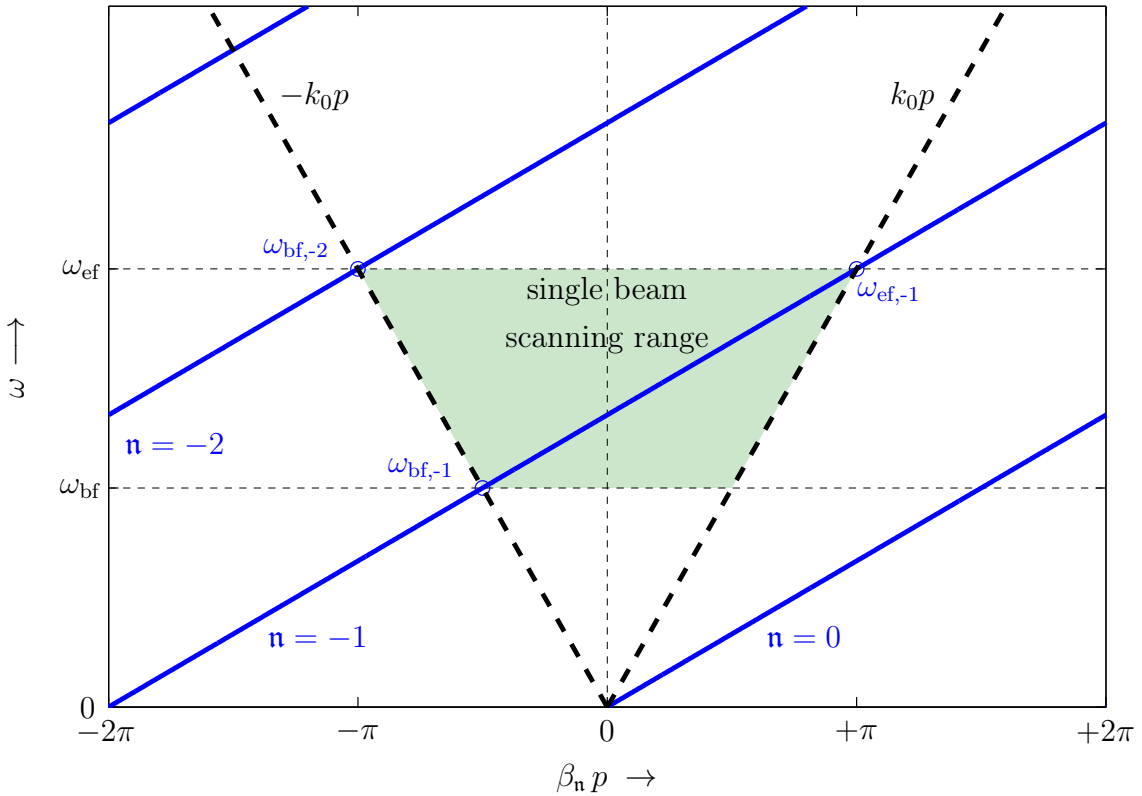


Figure 2.4: Simplified illustration of full range scanning with a single main beam. The dispersion relation of a homogeneous (non-periodic) transmission line structure without stopbands is shown. The case of an effective permittivity of $\epsilon_{r,\text{eff}} = 9$ is plotted, following that $\omega_{\text{bf},-2} = \omega_{\text{ef},-1}$.

Generally, one has to ensure that the higher order space harmonic (in case of the SFP LWA, $\mathbf{n} = -2$), does not start to radiate into the backfire direction, before the radiating space harmonic ($\mathbf{n} = -1$) reaches the endfire direction. This condition ensures a single beam in the entire scanning range, which is illustrated in Figure 2.4. For simpler illustration, the dispersion of a homogeneous (non-periodic) transmission line is used, which

results in straight β -lines without stopbands. This condition is expressed in terms of frequencies as

$$\omega_{\text{bf},-2} > \omega_{\text{ef},-1}, \quad (2.18)$$

where $\omega_{\text{bf},-2}$ is the frequency with backfire radiation generated by $\mathbf{n} = -2$ and $\omega_{\text{ef},-1}$ is the frequency of endfire radiation by $\mathbf{n} = -1$, the desired radiating harmonic. For an effective permittivity $\epsilon_{\text{r,eff}}$, the intersection points of the respective space harmonic with the light lines are given by

$$\beta_{-1} = \frac{\omega_{\text{ef},-1}}{c_0} \sqrt{\epsilon_{\text{r,eff}}} - \frac{2\pi}{p} \stackrel{!}{=} \frac{\omega_{\text{ef},-1}}{c_0} = k_0. \quad (2.19a)$$

and

$$\beta_{-2} = \frac{\omega_{\text{bf},-2}}{c_0} \sqrt{\epsilon_{\text{r,eff}}} - \frac{4\pi}{p} \stackrel{!}{=} -\frac{\omega_{\text{bf},-2}}{c_0} = -k_0 \quad (2.19b)$$

With the condition $\omega_{\text{bf},-2} > \omega_{\text{ef},-1}$, Equations (2.19) simplifies to

$$\frac{\sqrt{\epsilon_{\text{r,eff}}} + 1}{\sqrt{\epsilon_{\text{r,eff}}} - 1} < 2. \quad (2.20)$$

Furthermore, solving Equation (2.20) for the effective permittivity, one obtains [28]

$$\epsilon_{\text{r,eff}} > 9, \quad (2.21)$$

which is the required minimum effective permittivity in a (non-periodic) transmission line structure to achieve full range scanning with a single main beam. Figure 2.4 shows the limiting case, where $\epsilon_{\text{r,eff}} = 9$ yields $\omega_{\text{bf},-2} = \omega_{\text{ef},-1}$.

The constraint in (2.21) on the effective permittivity, is derived from a homogeneous transmission line, which lacks the actual periodicity. Nevertheless, it serves as a first good approximation to estimate, whether or not, an LWA is capable of full range scanning. For example the SFP LWA in Figure 2.1 is formed by microstrip transmission lines of alternating high (connection lines) and low impedance (patches) transmission line sections. Usually, the permittivity ϵ_{r} of the microwave laminates, used as substrate materials, is less than 6, so that the effective permittivity is even less. Therefore, most SFP LWA types provide just partial range beam scanning with a single main beam.

Other LWA types, for example, LWAs with no TEM⁵ or quasi-TEM⁶ propagation, exhibit different dispersion characteristics, yielding different constraints for achieving full range scanning. For example, the rectangular waveguide LWA in Figure 1.1(a) has the following constraint [80]

$$\epsilon_{\text{r}} > 9 + \left(\frac{p}{a}\right)^2, \quad (2.22)$$

on the dielectric filling to achieve full range scanning, where a is the width of a rectangular waveguide operated in the TE₁₀ mode.

In the special case of a phase reversal LWA [33], the minimum effective permittivity to ensure the single-beam condition is $\epsilon_{\text{r,eff}} > 4$. Here, due to the *phase reversing*, the unit cell period is effectively reduced by a factor of 2 as compared to the SFP LWA.

⁵Transverse electromagnetic (TEM) mode, where the electric *and* magnetic field are both in transverse direction (x - z plane).

⁶Longitudinal field components exist, but they are small compared to the dominate transverse components. A typical example is a microstrip transmission line.

The forthcoming analysis focuses primarily on a small angular scanning range of about $\pm 30^\circ$ around broadside. Within this relatively small range, the class of LWAs considered in this thesis radiate with a single space harmonic and hence produce a single main beam.

2.3 Network Modeling of Unit Cells

This section introduces the network modeling of LWA unit cells using two-port networks⁷ as shown in Figure 2.5. The radiation properties of periodic LWAs are dominantly controlled through the complex propagation constant as discussed in Section 2.2. Using the network modeling approach, the complex propagation constant can be analyzed based on two-port parameters, as for example, the transmission matrix [78], which allows to predict the LWA radiation behavior. In addition, the Bloch impedance is calculated and can be analyzed based on these two-port parameters. In this section, the modeling and the calculation of the propagation constant and the Bloch impedance is provided on a *general two-port network* basis, whereas a *specific circuit topology* together with an in-depth analysis is given in the next chapter, which analyzes fully symmetric LWAs.

Figure 2.5 shows the SFP LWA example together with a cascade of corresponding two-port networks. The unit cell interfaces are located at $y = \pm p/2$. If the field distribution at these interfaces is a TEM, quasi-TEM or a single modal field distribution,⁸ voltage and current quantities can be defined.

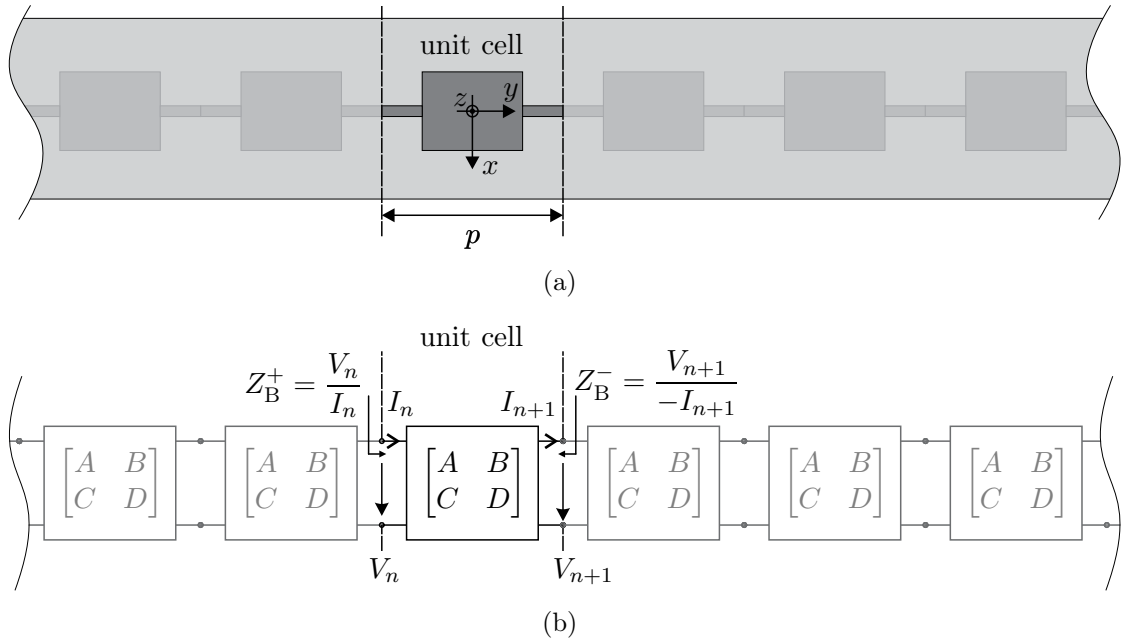


Figure 2.5: Equivalent two-port network representation of LWAs. (a) SFP LWA example formed by a cascade of an infinite number of unit cells. (b) Infinite cascade of equivalent two-port networks represented by the transmission matrix (ABCD-matrix).

⁷ A two-port network is a four-terminal network with the restriction that two terminals form one port, where the two terminal currents flowing in and out of the network must be equal. This is always the case for the considered LWAs, since no independent sources exist in the unit cells.

⁸For example a TE_{10} waveguide mode.

Once voltage and current are properly defined, the unit cell is fully characterized by e.g. the transmission matrix (ABCD-matrix). Particularly, the ABCD-matrix representation is convenient here. The overall ABCD-matrix of a cascade of two-port networks is calculated by a multiplication of the individual ABCD-matrices [78]. Eventually, for the infinite cascade as assumed here, the ABCD-matrix can be conveniently used to calculate the propagation constant and the Bloch impedance.

2.3.1 Propagation Constant

The Floquet theorem in Section 2.1.1 states that the transversal field distribution [e.g. $\bar{E}(x, z)$] at $-p/2$ and $+p/2$ is unaltered, except for a complex propagation term $e^{-\gamma p}$ as given in Equation (2.1). Since, the integral quantities, terminal voltage and current, are based on these field quantities, the Floquet theorem directly applies to the terminal voltages and currents.

Therefore, one can relate the terminal voltage and the current in Figure 2.5(b) by

$$V_{n+1} = V_n e^{-\gamma p} \quad (2.23a)$$

and

$$I_{n+1} = I_n e^{-\gamma p}, \quad (2.23b)$$

where n is an integer number referring to the n^{th} unit cell terminal.

By using the definition of the ABCD-matrix [78, 79] and inserting Equation (2.23), one obtains

$$\begin{bmatrix} V_n \\ I_n \end{bmatrix} = \begin{bmatrix} A & B \\ C & D \end{bmatrix} \begin{bmatrix} V_{n+1} \\ I_{n+1} \end{bmatrix} = \begin{bmatrix} V_{n+1} \\ I_{n+1} \end{bmatrix} e^{\gamma p}, \quad (2.24)$$

which, after simplifications reads

$$\begin{bmatrix} A - e^{\gamma p} & B \\ C & D - e^{\gamma p} \end{bmatrix} \begin{bmatrix} V_{n+1} \\ I_{n+1} \end{bmatrix} = 0. \quad (2.25)$$

Equation (2.24) is a classical eigenvalue equation with the propagation term $e^{\gamma p}$ as eigenvalue. For a non-trivial solution with non-zero voltage and current in Equation (2.25), the determinate must be zero,

$$AD + e^{2\gamma p} - (A + D)e^{\gamma p} - BC = 0. \quad (2.26)$$

Equation (2.26) is the characteristic polynomial of the 2x2 ABCD-matrix and its two solutions correspond to the propagation terms in positive and negative y -direction [Figure 2.5]. Assuming the LWA is a reciprocal device, it follows $AD - BC = 1$ [78]. Finally, Equation (2.26) is solved for the complex propagation constant by

$$\gamma = \frac{1}{p} \operatorname{arccosh} \frac{A + D}{2}, \quad (2.27)$$

where the solution for wave propagation in positive y -direction is chosen among the two possible ones.

It is worth mentioning that one can arbitrarily chose or shift the terminal planes (as long as the unit cell period p is fixed), since the complex propagation constant is invariant to any translation along the propagation axis [Section 2.1.1].

2.3.2 Bloch Impedance

In addition to the propagation constant, the Bloch impedance is an important LWA quantity. The Bloch impedance corresponds to the input impedance of an infinite cascade of unit cells and hence approximates the input impedance of an electrically long⁹ LWA. The Bloch impedance for a wave traveling in *positive* y -direction (direction of increasing n in Figure 2.5) at the n^{th} terminal plane is defined by

$$Z_{\text{B}}^+ = \frac{V_n}{I_n} = \frac{V_{n+1}}{I_{n+1}}. \quad (2.28)$$

Similarly, the Bloch impedance for a wave traveling in *negative* y -direction (direction of decreasing n in Figure 2.5) at the $(n^{\text{th}} + 1)$ terminal plane is defined by

$$Z_{\text{B}}^- = \frac{V_{n+1}}{-I_{n+1}} = \frac{V_n}{-I_n}. \quad (2.29)$$

By first multiplying the first row in Equation (2.25) with the voltage/current vector, one obtains

$$(A - e^{\gamma p})V_{n+1} + BI_{n+1} = 0. \quad (2.30)$$

Solving Equation (2.30) for the Bloch impedance reads

$$Z_{\text{B}}^{\pm} = \frac{\mp B}{A - e^{\gamma p}}. \quad (2.31)$$

Next, Equation (2.27) is solved for

$$e^{\gamma p} = \frac{(A + D) \pm \sqrt{(A + D)^2 - 4}}{2}, \quad (2.32)$$

which is inserted into Equation (2.31) by considering the respective propagation directions. The Bloch impedance then reads

$$Z_{\text{B}}^{\pm} = \frac{\pm 2B}{(D - A) \pm \sqrt{(A + D)^2 - 4}}. \quad (2.33)$$

The two solutions¹⁰ with Z_{B}^{\pm} correspond to the wave impedances in positive and negative y -direction as defined in Figure 2.5.

While the propagation constant in Section 2.3.1 is directly defined through the fields [Equation 2.1], the Bloch impedance, as any other impedance quantity, relies on the definition of voltages and currents [76]. Moreover, the Bloch impedance depends on the terminal location and is, unlike the propagation constant, non-invariant to translational changes of the terminals planes. This is obvious by observing, for example, the SFP LWA unit cell in Figure 2.5(b). By slightly shifting the n^{th} terminal plane in positive y -direction, the Bloch impedance undergoes an impedance transformation according to the length of the high impedance feed line of the patch element.

⁹An LWA is considered electrically long, if the power ratio, power at the termination side over power at excitation side $\log(e^{-\alpha p N})$, of a finite length LWA with N cells, is about -20 dB or less. Depending on the leakage constant and hence on the LWA type, this can be achieved for approximately $N \gtrsim 20$.

¹⁰Note that in most text books, for example, [78, 79] the Bloch impedance in negative direction Z_{B}^- is defined without changing the reference direction for the current.

2.4 Class of Periodic LWAs Considered

This section describes the class of periodic LWAs, for which the forthcoming theory holds. Technically, the class could only be *properly* defined, once the theory of the next chapters is established. At this stage, the class is mainly described based on the properties that are discussed so far.

Generally, the class considered restricts to one-dimensional periodic LWAs that are passive, linear, time-invariant and reciprocal. At microwave frequencies, this is usually the case for all LWAs composed of metal and dielectric materials as shown in Figure 1.1. Moreover, the LWAs considered are electrically long, so that the power level at the termination side is negligible as compared to the power level at the excitation side. This ensures the propagation of a traveling wave in positive y -direction without a reflection from the termination side. Under such a condition, LWAs can be modeled through an infinite cascade of unit cells.

LWAs belonging to the considered class, scan from backward to forward through the broadside direction, according to the beam scanning law in Equation (2.17). The radiating space harmonic can be either $\mathbf{n} = -1$ or the fundamental harmonic with $\mathbf{n} = 0$, where in most LWAs the single main beam condition around broadside safely holds. LWAs of the considered class are furthermore characterized by full range or partial range beam scanning with frequency as described in Section 2.2.2. The unit cell interfaces are restricted to TEM, quasi-TEM or a single modal field distribution, which allows the definition of voltage and current quantities and prepares for the network modeling approach.

This covers a large class of metamaterial and conventional periodic LWAs, including the microstrip LWAs in Figure 1.1. The individual LWAs may show major differences in the unit cell period, radiating space harmonic, scanning range, scanning sensitivity and polarization. However, around the broadside frequency they may exhibit a qualitative similar two-port network response. If this two-port response can be dominantly represented by exactly *two independent resonances*, which are defined in the forthcoming Section 3.1, the theoretical analyzes of the following Chapters 3, 4 and 5 applies. For example, the LWAs in [27, 34, 36–40, 49, 58, 62, 81–85] belong to this class.

The theoretical analysis in the following chapters is limited to the modeling of *two independent resonances* as aforementioned. If a third resonance, closely around the broadside frequency is involved, the modeling is strictly not applicable anymore. An additional resonance is possible, if for example, the radiating slots of the waveguide LWA of Figure 1.1(a) are in resonance, or the patch width of the SFP in Figure 1.1(d) supports a λ -mode in transverse direction around broadside. In the double-stub microstrip LWA in Figure 1.1(e), an additional resonance occurs for specific stub lengths, where the stubs are in resonance. Most often, one can avoid such additional resonances, particularly in microstrip LWAs¹¹ [Figures 1.1(d) to (f)], by modifying the dimensions and shift this resonance away from the broadside frequency.

¹¹In the slotted waveguide LWA [Figures 1.1(a)], the slot needs to be resonant to radiate efficiently.

2.5 Symmetry Classification - Transversal and Longitudinal Unit Cell Axes

Figure 2.6 defines the four possible unit cell symmetries and asymmetries. While, in Figure 2.6, these definitions are illustrated for the SFP unit cell, they can be generally applied to arbitrary LWA unit cells. The forthcoming Chapters 3, 4 and 5 investigate LWA symmetry classes as defined in Figures 2.6(a), 2.6(b) and 2.6(c), respectively, where each chapter is dealing with a particular symmetry class. The results for the double asymmetry class in Figure 2.6(d) are not reported with the scope of this thesis. This class essentially combines the features and properties of transversal and longitudinal asymmetry classes in Figure 2.6(b) and 2.6(c), respectively, which is demonstrated in [65].

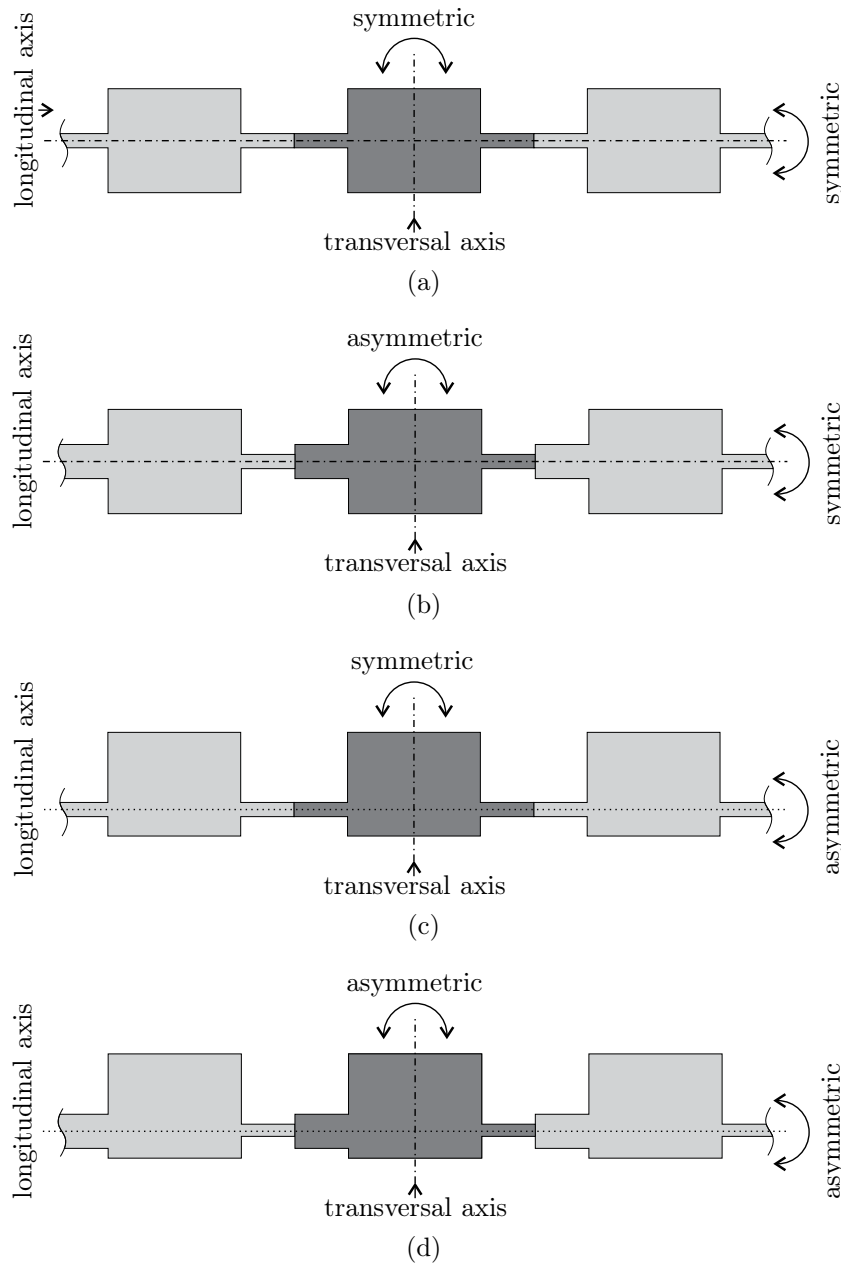


Figure 2.6: Definition of LWA symmetry classes. (a) Fully symmetric unit cell. (b) Transversally asymmetric unit cell. (c) Longitudinally asymmetric unit cell. (d) Transversally and longitudinally asymmetric unit cell.

Fully Symmetric LWAs and their Limitations

This chapter analyzes *fully symmetric* LWAs and proves the existence of a fundamental radiation efficiency limitation in these antennas. Figure 3.1 recalls the LWA symmetry class that is referred to as *fully symmetric*. The SFP LWA [Figure 1.1(d)] is used as a simple illustration example throughout this chapter. However, the analysis is not restricted to the SFP case and applies to a broad class of LWAs as discussed in Section 2.4. Finally, several LWA configurations are examined to validate the modeling and to confirm the efficiency limitation. This chapter is based on the author’s journal publications in [34, 62].

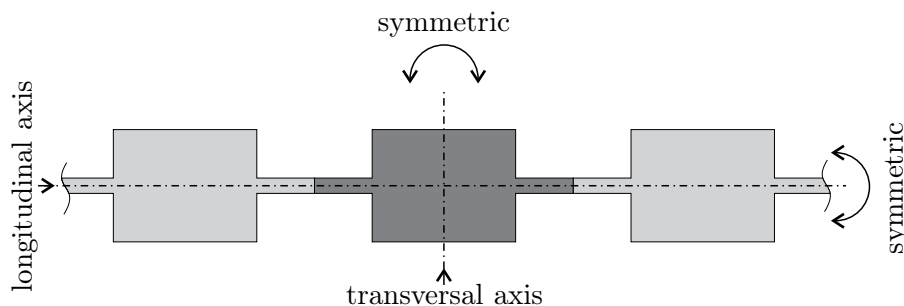


Figure 3.1: Class of *fully symmetric* LWAs that is considered in this chapter.

3.1 Generic Two-Port Network Model

The unit cell of an LWA is modeled as a two-port network as already discussed in Section 2.3 and can therefore be described by two-port parameters. These two-port parameters are 2×2 matrices and they mathematically describe the voltage/current relationship between the two ports. The definition of a corresponding circuit model topology is generally arbitrary, since there is an infinite number of possibilities. The challenge is to

determine an equivalent circuit model topology with ideal circuit elements that shows equivalent behavior, is simple and yet powerful enough to extract the dominant effects, so to provide understanding and insight. One may think of two different approaches to develop this equivalent circuit model.

The first approach consists in finding circuit elements that are directly derived from structural features within the two-port and can be referred to as microscopic modeling. Here, the advantage is that inner physical effects are mapped onto a corresponding circuit element. Such a circuit topology gives insight, but is always very specific to a particular two-port and therefore has a lack of generality.

In the second approach, the two-port is seen as a “black box”. A circuit topology is predefined and not derived from the knowledge of the interior of the two-port. This is referred to as macroscopic modeling. The parameters of the circuit elements are determined by matching the circuit model response to the response of the two-port. This approach provides more generality, but it does not necessarily provide physical insight. Here, the second approach is pursued to develop a simple circuit topology along with idealized circuit elements that is capable of modeling LWAs around broadside.

The two most simple and common circuit topologies in microwave engineering are T- and Π -circuits, [78, 79, 86]. The question arises which one to prefer as a generic model for the unit cell, T or Π ? In principle, both topologies work, but they have different element parameters leading to different sets of formulas; more importantly, both circuits have a distinct disadvantage, as they do not have *isolated* series and shunt elements under odd and even port excitation. This *isolation* feature is particularly interesting for three reasons. First, it provides simpler formulas for the propagation constant and the Bloch impedance. Second, a fullwave simulation method, that is developed later in this chapter, is based on the isolation of series and shunt element parameters. Third, radiation originated under odd and even excitation is modeled by the isolated series and shunt elements, respectively. These radiation contributions, series and shunt, have an orthogonal farfield polarization. A more detailed discussion of these reasons is provided in the forthcoming sections, when the model and the analysis are developed.

The series element can only be isolated in the T-circuit under odd excitation, whereas the shunt element can be isolated only in the Π -circuit under even excitation. Unfortunately, neither the T- nor the Π -circuit provides a simultaneous isolation of both elements, series *and* shunt. This suggests *topology-wise* a combination of T and Π so to form a circuit that simultaneously provides both. Such a circuit topology exists and is known under the name lattice, bridge or x-circuit topology.

3.1.1 Lattice Circuit Model for Transversally Symmetric Unit Cells

Figure 3.2 shows the lattice circuit with the series impedance Z_{se} and the shunt admittance Y_{sh} . This circuit was already used back in 1930 as an all-pass filter in the context of artificial transmission lines [44]. It was found that it is particularly suited for symmetric networks. Moreover, it was mentioned that the lattice implementation leads to simpler formulas as compared to the T or Π [44]. Roughly at the same time, Otto Zobel invented a phase shifter based on this topology, which was used in telecommunication as an equalizer in these days [45]. More recently, the lattice was used to analyze space-discretizing numerical simulation schemes [46]. The first time the lattice circuit was presented in the

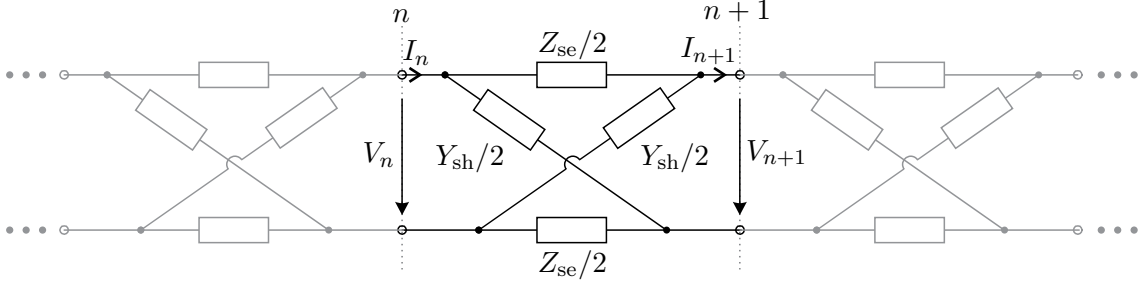


Figure 3.2: Lattice circuit model for the unit cell of fully symmetric periodic LWAs.

context of an LWA was in 2009 [47], where a CRLH unit cell was implemented featuring the lattice topology and exploiting the all-pass characteristic. In this thesis, the lattice is used as a generic unit cell model for fully symmetric LWAs that are described in Section 2.4.

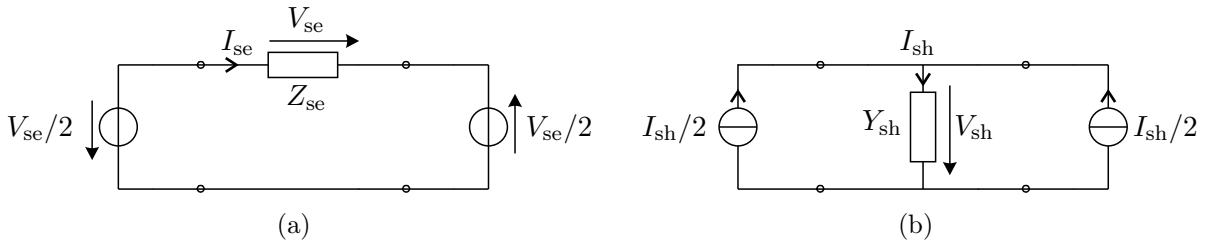


Figure 3.3: Equivalent circuits under odd/even excitation. (a) Odd excitation, where the series element Z_{se} is isolated. (b) Even excitation, where the shunt element Y_{sh} is isolated.

Using Bartlett's bi-section theorem¹ [87] and applying odd and even excitations to the lattice given in Figure 3.2, one decomposes the lattice and isolates the series and the shunt elements, respectively [88]. Figure 3.3(a) shows the lattice circuit under odd excitation, where only the series impedance Z_{se} persists. Figure 3.3(b) shows the lattice circuit under even excitation, where only the shunt admittance Y_{sh} persists. It is clearly confirmed that the lattice combines the features of the T and the Π by providing the required isolation.

Based on the impedance matrix \mathbf{Z} and the admittance matrix \mathbf{Y} , the series and shunt immittances are calculated next. The impedance matrix parameters Z_{ij} of the lattice circuit in Figure 3.2 are given by [88, 89],

$$Z_{11} = Z_{22} = \frac{1}{2} \left(\frac{Z_{se}}{2} + \frac{2}{Y_{sh}} \right), \quad (3.1a)$$

$$Z_{21} = Z_{12} = \frac{1}{2} \left(\frac{-Z_{se}}{2} + \frac{2}{Y_{sh}} \right). \quad (3.1b)$$

The difference of these two expressions yields

$$Z_{se} = 2(Z_{11} - Z_{21}), \quad (3.2a)$$

whereas the sum yields $Y_{sh} = 2/(Z_{11} + Z_{12})$, which leads, using two-port network transformation formulas [78], to

$$Y_{sh} = 2(Y_{11} + Y_{21}), \quad (3.2b)$$

¹Any symmetric two-port network, bisected with respect to the transversal symmetry axis into two identical halves and applying odd/even excitation to the terminals, results in short-/open-circuit condition, respectively, in the bi-section plane. The corresponding input impedances of the short circuit half Z_{short} and the open circuit Z_{open} fully characterize the two-port and they are identical to the series and shunt elements in the lattice, here Z_{se} and Y_{sh} , respectively.

where Y_{ij} are the admittance matrix parameters. The series impedance Z_{se} and the shunt admittance Y_{sh} in Equation (3.2), are calculated from the impedance and admittance matrices, respectively. They can now be obtained from any calculated, simulated or measured two-port parameters, e.g. scattering parameters, using two-port conversion formulas.

3.1.2 Series and Shunt Resonators and Immittance Linearization

Now, the circuit topology is determined. The circuit parameters of the series impedance and the shunt admittance are analyzed next. A common feature of the LWAs in Section 2.4 is that the series impedance exhibits the characteristic of a series resonance circuit, whereas the shunt admittance has the characteristic of a parallel resonance circuit. For CRLH LWAs series and shunt resonators can be identified in the topology of the unit cells, since CRLH LWAs are composed of quasi-lumped elements. LWAs radiating in their first order space harmonic, $\mathbf{n} = -1$, are composed of transmission lines, where the period p is one guided wavelength at broadside. Here, no direct topological mapping is possible. Yet, it is required that the equivalent circuit must provide an *all-pass* response having a series resonator in the series path and a parallel resonator in the shunt path².

If these two resonance frequencies are equal, they will correspond to the broadside radiation frequency of the LWA, which is derived later in this chapter. By keeping the main focus on the critical broadside direction and therefore on a relatively small frequency range around the series and shunt resonances, one can introduce a narrow band approximation. The series impedance and the shunt admittance are linearized by using reactance and susceptance slope parameters, respectively, a concept that is widely used in filter theory [86].

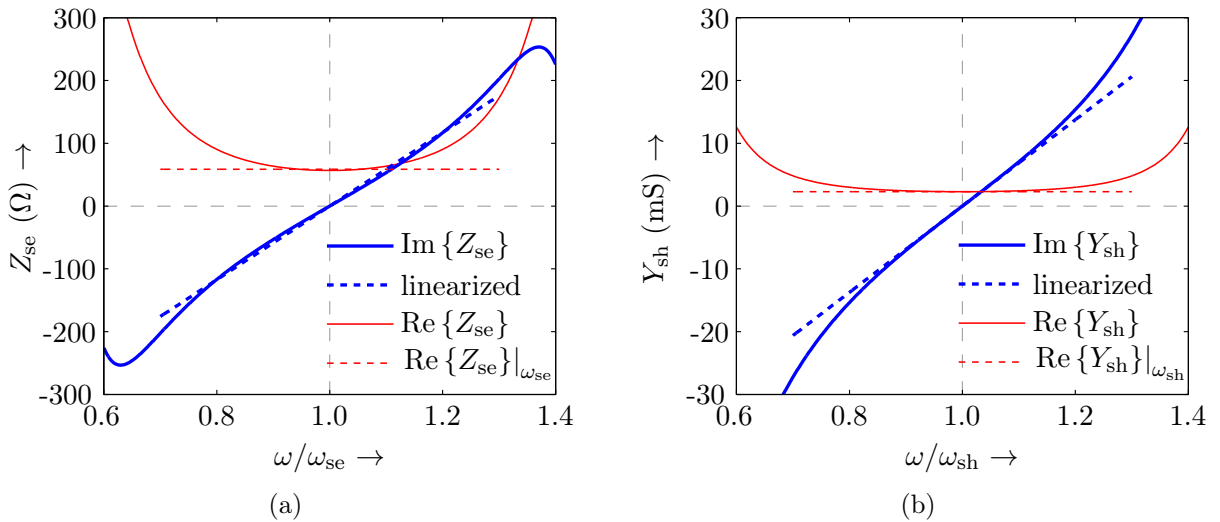


Figure 3.4: Immittances, Z_{se} and Y_{sh} , and linearization procedure using the SFP example. (a) Linearization of the reactance $\text{Im}\{Z_{se}\}$ at the resonance frequency ω_{se} . (b) Linearization of the susceptance $\text{Im}\{Y_{sh}\}$ at the resonance frequency ω_{sh} .

²Exchanging the resonator types, i.e. a parallel resonator in the series path and a series resonator in the shunt path, yields a band-stop filter or a Dual-CRLH circuit [90], where β is always different from zero and hence no broadside radiation can be achieved.

3.1.2.1 Series Resonator

First, the series resonance frequency ω_{se} is determined by the zero crossing of the reactance

$$\text{Im} \{Z_{se}\}|_{\omega_{se}} = 0. \quad (3.3)$$

Figure 3.4(a) shows a typical frequency behavior of Z_{se} for the SFP example. For a relative bandwidth of around 40% (ω/ω_{se} from 0.8 to 1.2) an almost linear reactance and a nearly constant resistance is observed. This supports the idea of simplifying the resonator model by introducing the reactance slope parameter³ L and the resistance R are subsequently defined by

$$L = \frac{1}{2} \frac{d}{d\omega} \text{Im} \{Z_{se}\}|_{\omega_{se}}, \quad R = \text{Re} \{Z_{se}\}|_{\omega_{se}}. \quad (3.4)$$

The resonator parameters, ω_{se} , L and R , fully characterize the series element Z_{se} of the model. Both radiation and dissipation is lumped in R . By formally discriminating radiation and dissipation one may express the overall resistance as $R = R_{rad} + R_{diss}$, where R_{rad} is accounting for radiation and R_{diss} for dissipation. Finally, the series radiation efficiency is defined as

$$\eta_{se} = \frac{R_{rad}}{R_{rad} + R_{diss}} = \frac{R_{rad}}{R}. \quad (3.5)$$

Furthermore, the series quality factor Q_{se} is introduced. Following the general definition of the quality factor in [78],

$$Q = \omega \frac{(\text{average energy stored})}{(\text{energy loss/second})} = \omega \frac{(\text{average energy stored})}{(\text{power loss})}, \quad (3.6)$$

one obtains

$$Q_{se} = \frac{\omega_{se} L}{R}. \quad (3.7)$$

Finally the linearized impedance reads

$$Z_{se} = R + j2L(\omega - \omega_{se}) = R \left(1 + j2Q_{se} \frac{\omega - \omega_{se}}{\omega_{se}} \right). \quad (3.8)$$

3.1.2.2 Shunt Resonator

Similar to the previous case, ω_{sh} is the resonance frequency of the shunt resonator and it is defined by

$$\text{Im} \{Y_{sh}\}|_{\omega_{sh}} = 0. \quad (3.9)$$

Figure 3.4(b) shows a typical frequency behavior of Y_{sh} for the SFP example, exhibiting similar bandwidth characteristics as the series resonator. Following the same line as in the

³The reactance slope parameter definition in [86] is an impedance quantity ($\omega_{se}L$) that differs from the definition in this thesis. Here, the reactance slope parameter corresponds to an inductor and is measured in Henry.

previous case, the shunt resonator is approximated by the susceptance slope parameter⁴ C and the conductance G . They are defined by

$$C = \frac{1}{2} \frac{\partial}{\partial \omega} \text{Im} \{Y_{\text{sh}}\} |_{\omega_{\text{sh}}}, \quad G = \text{Re} \{Y_{\text{sh}}\} |_{\omega_{\text{sh}}}, \quad (3.10)$$

and they fully characterize the admittance element Y_{sh} of the model. By discriminating radiation and dissipation one obtains $G = G_{\text{rad}} + G_{\text{diss}}$, where G_{rad} and G_{diss} account for radiation and dissipation, respectively. The radiation efficiency of the shunt resonator is then given by

$$\eta_{\text{sh}} = \frac{G_{\text{rad}}}{G_{\text{rad}} + G_{\text{diss}}} = \frac{G_{\text{rad}}}{G}. \quad (3.11)$$

The shunt quality factor is

$$Q_{\text{sh}} = \frac{\omega_{\text{sh}} C}{G}. \quad (3.12)$$

Finally, the linearized admittance reads as follows

$$Y_{\text{sh}} = G + j2C(\omega - \omega_{\text{sh}}) = G \left(1 + j2Q_{\text{sh}} \frac{\omega - \omega_{\text{sh}}}{\omega_{\text{sh}}} \right). \quad (3.13)$$

3.1.2.3 Summary LCRG Model Parameters and Resonator Radiation Efficiencies

The modeling so far is summarized in the following manner. A lattice topology is used, where the series and the shunt elements are approximated around their resonance frequencies by linearizing the reactance and the susceptance, respectively. The resistance and conductance are extracted at the respective resonance frequency and they are assumed to be constant.

The model is based on eight independent parameters: L , C , R and G , which are referred to as the LCRG parameters, two resonance frequencies ω_{se} and ω_{sh} and two resonator radiation efficiencies η_{se} and η_{sh} . To give a clear overview, Table 3.1 lists these parameters, as they are defined with their symbols and physical units.

Table 3.1: Summary of lattice circuit model parameters for transversally symmetric unit cells

definition:	series resonator		shunt resonator	
	symbol	unit	symbol	unit
series/shunt resonance frequency	ω_{se}	Hz	ω_{sh}	Hz
series/shunt slope parameters	L	H	C	F
series/shunt radiation resistance/cond.	R_{rad}	Ω	G_{rad}	S
series/shunt dissipation resistance/cond.	R_{diss}	Ω	G_{diss}	S
series/shunt resistance/cond.	$R = R_{\text{rad}} + R_{\text{diss}}$	Ω	$G = G_{\text{rad}} + G_{\text{diss}}$	S
series/shunt radiation efficiency	$\eta_{\text{se}} = R_{\text{rad}}/R$	-	$\eta_{\text{sh}} = G_{\text{rad}}/G$	-
series/shunt quality factor	$Q_{\text{se}} = \omega_{\text{se}} L/R$	-	$Q_{\text{sh}} = \omega_{\text{sh}} C/G$	-

⁴The susceptance slope parameter definition in [86] is an admittance quantity ($\omega_{\text{se}} C$), here the susceptance slope parameter corresponds to a capacitor and is measured in Farad.

3.1.2.4 Series and Shunt Radiation

Associated with the two resonances are the radiated fields of the unit cell. Series radiation is defined as the radiated farfield at the resonance frequency ω_{se} under odd excitation of the unit cell. On the other hand, shunt radiation is defined as the radiated farfield at the resonance frequency ω_{sh} under even excitation of the unit cell.

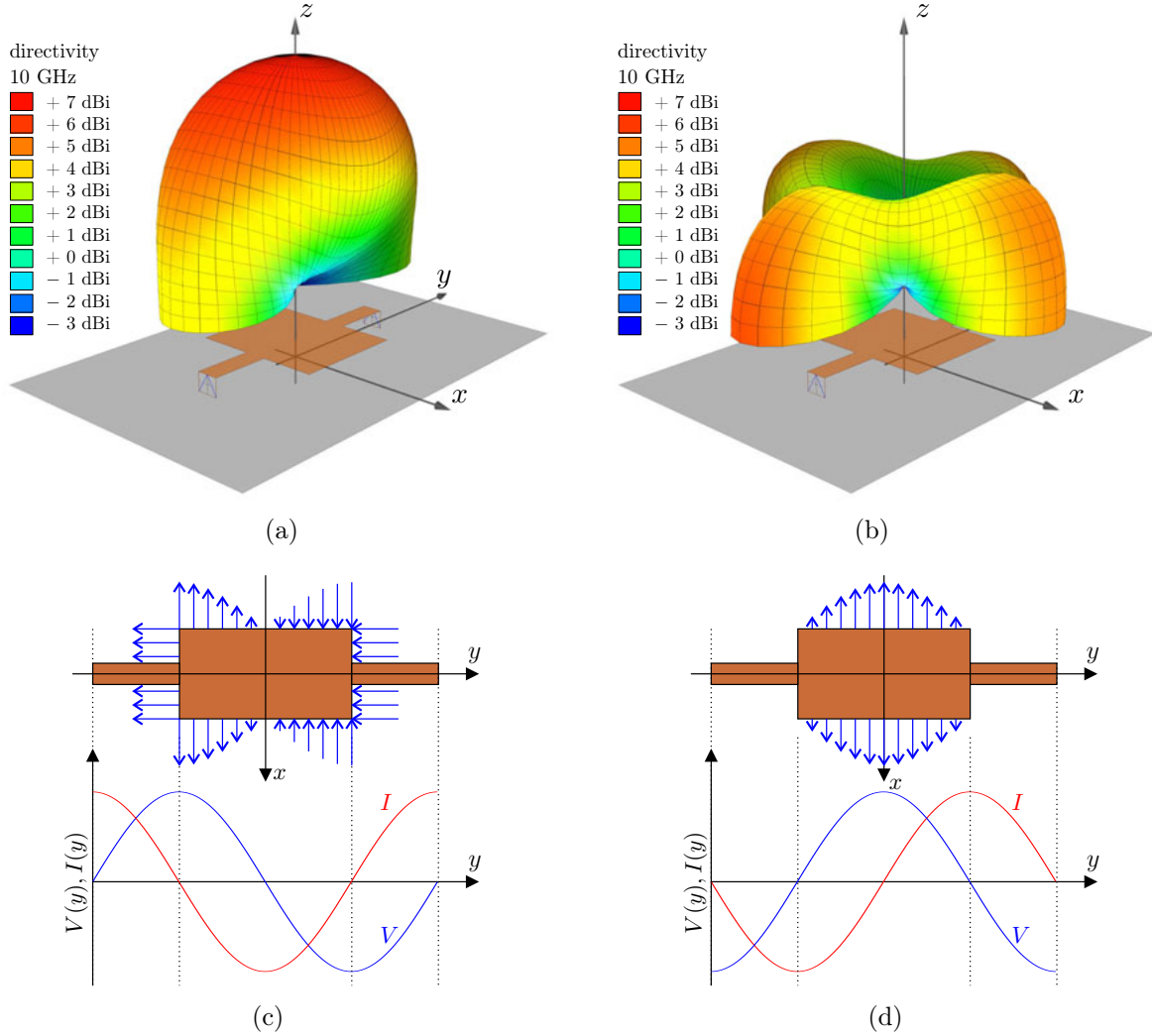


Figure 3.5: Series-fed patch example under odd and even excitation: Directivity patterns (vector sum of both far-field polarizations) for the SFP example. (a) Odd excitation generating series radiation, where the patch is operated in the conventional $\lambda/2$ -patch mode and radiates broadside. (b) Even excitation generating shunt radiation, where the radiation null in broadside direction is confirmed and the main radiation is directed to the $\pm x$ - and $\pm y$ -directions. (c) Qualitative sketch of the electric field in the x - y -plane and simplified voltage/current distributions⁴ along the patch under odd excitation. (d) Simplified distributions⁴ under even excitation.

Figure 3.5 illustrates the situation for the SFP example. The series radiation along with a sketch of the voltage/current distribution⁵ are shown in Figures 3.5(a) and 3.5(c), respectively. Here, it can be observed that the conventional $\lambda/2$ -mode of the patch is excited

⁵ Voltage and current quantities are *only* properly defined at the ports and *not* within the unit cell.

and the main radiation is directed to broadside. Figures 3.5(b) and 3.5(d) show the shunt radiation and the voltage/current distribution⁴ for the even excitation scenario. While for the previous series radiation case a maximum in broadside direction exists, a null in broadside direction is observed for the case of shunt radiation under even excitation. The main radiation is directed to the sides in $\pm x$ -direction and to the longitudinal direction ($\pm y$ -direction).

The SFP unit cell is used as a simple and well-known example to introduce the concept of series and shunt radiation in a very intuitive manner. Nevertheless, the following general statements can be made regarding the radiation characteristics of arbitrary fully symmetric unit cells. Series radiation can have a pronounced maximum, whereas shunt radiation always has a null in broadside direction.

For the sake of simplicity and convenience, mutual coupling of the unit cells, as well as the polarization of the series and the shunt radiation contributions are not considered so far. With the forthcoming development of the analysis, the thesis elaborates on this in Sections 3.4 and 3.5 by taking into account the periodicity of the electromagnetic field.

3.1.3 Propagation Constant and Broadside Frequency

The generic unit cell model is now analyzed in terms of its propagation characteristics for an infinite cascade of unit cells. The propagation constant $\gamma = \alpha + j\beta$, where β and α are the phase and leakage constant, respectively, carries important information about the radiation characteristics of the LWA. The term βp , phase constant multiplied with the period of the unit cell p , is the *phase difference* in radian from one cell at terminal pair n to the following one at $n + 1$. The main beam direction ϑ_{mb} of the LWA [Equation (2.17)] depends on this *phase difference*, where a phase progression results in backward radiation, a zero phase⁶ in broadside radiation and a phase lag results in forward radiation, as already discussed in Chapters 1 and 2.

3.1.3.1 Propagation Constant

The propagation constant, in terms of the transmission matrix \mathbf{ABCD} , is recalled from Equation (2.27). By making use of two-port conversion formulas [78], the transmission matrix of the lattice circuit is derived from the impedance matrix (3.1) and reads

$$\mathbf{ABCD} = \begin{pmatrix} A & B \\ C & D \end{pmatrix} = \frac{1}{4 - Z_{\text{se}}Y_{\text{sh}}} \begin{pmatrix} 4 + Z_{\text{se}}Y_{\text{sh}} & 4Z_{\text{se}} \\ 4Y_{\text{sh}} & 4 + Z_{\text{se}}Y_{\text{sh}} \end{pmatrix}. \quad (3.14)$$

From the transversal symmetry follows that $A = D$, as can be confirmed in (3.14). Inserting A from (3.14) into the following equation for the propagation constant [78]

$$\cosh(\gamma p) = \frac{A + D}{2} = A = \frac{4 + Z_{\text{se}}Y_{\text{sh}}}{4 - Z_{\text{se}}Y_{\text{sh}}}, \quad (3.15)$$

Therefore, the plot of the voltage/current distribution shown in Figures 3.5(c) and 3.5(d) is a simplified illustration, in which the distributions correspond to an *ideal homogeneous transmission line* without any periodic discontinuities.

⁶Or integer multiples of 360° .

and isolating the propagation constant⁷ yields

$$\gamma = \frac{1}{p} \operatorname{arccosh} \frac{4 + Z_{\text{se}} Y_{\text{sh}}}{4 - Z_{\text{se}} Y_{\text{sh}}}. \quad (3.16)$$

Considering the main focus on the direction around the broadside, where $|\gamma| \approx 0$, one can further simplify (3.16) by means of a Taylor series expanded around broadside. First, p is brought to the left in (3.16) and both sides are squared to get

$$(\gamma p)^2 = \operatorname{arccosh}^2 \left(\frac{4 + Z_{\text{se}} Y_{\text{sh}}}{4 - Z_{\text{se}} Y_{\text{sh}}} \right). \quad (3.17)$$

Next, knowing from Section 3.1.2 that the series and shunt resonators are operated reasonably close to their resonances, the product of the two is essentially $|Z_{\text{se}} Y_{\text{sh}}| \ll 1$, following that $|\gamma p| \ll \pi/4$. This suggests a first order Taylor approximation around the expansion point $Z_{\text{se}} Y_{\text{sh}} = 0$ to approximate the propagation constant around broadside by

$$(\gamma p)^2 \approx (\gamma p)^2|_{Z_{\text{se}} Y_{\text{sh}}=0} + Z_{\text{se}} Y_{\text{sh}} \left[\frac{d}{d(Z_{\text{se}} Y_{\text{sh}})} (\gamma p)^2 \right]_{Z_{\text{se}} Y_{\text{sh}}=0} = Z_{\text{se}} Y_{\text{sh}}, \quad (3.18)$$

where the term $(\gamma p)^2|_{Z_{\text{se}} Y_{\text{sh}}=0}$ is zero and the linear term $\frac{d}{d(Z_{\text{se}} Y_{\text{sh}})} (\gamma p)^2|_{Z_{\text{se}} Y_{\text{sh}}=0}$ in (3.18) is found to be equal to one, after a somewhat lengthy calculation. Finally, the approximated propagation constant reads

$$\gamma \approx \frac{1}{p} \sqrt{Z_{\text{se}} Y_{\text{sh}}}, \quad (3.19)$$

which establishes a simple result that formally corresponds to the propagation constant of a conventional homogeneous transmission line [78]. The result in (3.19) is also well-known in the context of CRLH transmission lines [26] to describe the propagation in an effective homogeneous medium where $p \rightarrow 0$.

By furthermore inserting the linearized immittance of (3.8) and (3.13) into (3.19) the following expression is obtained

$$\gamma p \approx \sqrt{Z_{\text{se}} Y_{\text{sh}}} = \sqrt{[R + j2L(\omega - \omega_{\text{se}})] [G + j2C(\omega - \omega_{\text{sh}})]}. \quad (3.20)$$

Equation (3.20) is a very useful approximation of the propagation constant around broadside, which is based on the simple set of intuitive resonator parameters, namely the LCRG parameters.

3.1.3.2 Broadside Frequency

Broadside radiation with $\vartheta_{\text{mb}} = 0$ occurs, according to the scanning law in Equation (2.17), for a zero phase shift across the unit cells. In order to determine the broadside radiation frequency ω_{bs} , one has to equate $\operatorname{Im} \{ \gamma(\omega_{\text{bs}}) \} p = \beta(\omega_{\text{bs}}) p = 0$. In other words, γ has to be real, so that the product of $Z_{\text{se}} Y_{\text{sh}}$ in Equation (3.16) must be real as well, following that the imaginary part $\operatorname{Im} \{ Z_{\text{se}} Y_{\text{sh}} \}$ is zero,

$$j2LG(\omega_{\text{bs}} - \omega_{\text{se}}) + j2CR(\omega_{\text{bs}} - \omega_{\text{sh}}) = 0. \quad (3.21)$$

⁷Two solutions of opposite sign exist for γ , corresponding to wave propagation in positive and negative y -direction [Figure 2.5]. In the following, wave propagation in positive y -direction is assumed.

Using the quality factor definition in (3.7) and (3.12), and solving (3.21) for ω_{bs} , leads to

$$\omega_{bs} = \frac{Q_{se} + Q_{sh}}{Q_{se}/\omega_{se} + Q_{sh}/\omega_{sh}}, \quad (3.22)$$

which defines the broadside radiation frequency in terms of quality factors of the two resonances. Equation (3.22) reveals that under the condition, where the two resonator frequencies are equal, the broadside frequency is exactly the resonance frequency of the series and the shunt resonator $\omega_{se} = \omega_{sh} = \omega_{bs}$.

It is worth mentioning that the formula for the broadside frequency in Equation (3.22) is mathematically *exact*, since it is directly derived from propagation constant in Equation (3.16).

3.1.4 Bloch Impedance

Besides the propagation constant, the Bloch impedance is another important quantity to examine. The Bloch impedance is the ratio of the terminal voltage over the terminal current for an infinite cascade of unit cells at a given frequency. For a large number of unit cells the input impedance of the LWA converges to the Bloch impedance. Therefore, it is important to understand and control the Bloch impedance, especially when it comes to matching the LWA to a system or reference impedance. Moreover, the Bloch impedance is the critical parameter that affects the radiation efficiency, as shown later in this chapter.

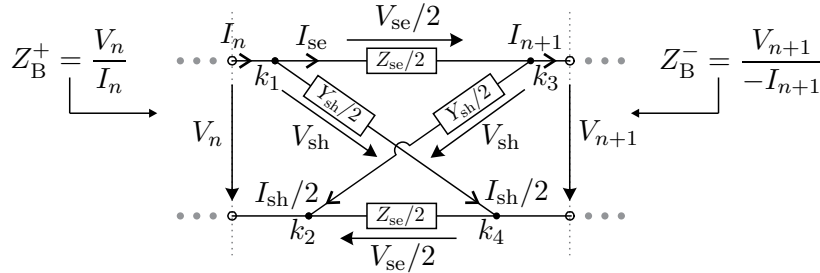


Figure 3.6: Equivalent lattice circuit with the definition of the inner series current and shunt voltage quantities.⁸

Figure 3.6 shows the lattice circuit with the definition of the Bloch impedances Z_B^+ and Z_B^- for waves propagating in positive and negative y -direction, respectively. The series current I_{se} flows through the two series elements $Z_{se}/2$ and the shunt voltage⁷ V_{sh} applies across the two shunt elements $Y_{sh}/2$. The lattice in Figure 3.6 is next analyzed by using Kirchhoff's voltage and current laws to determine the Bloch impedance in terms of the LCRG model parameter.

First, from the loop along the nodes k_1, k_4, k_3 and k_2 one obtains the following relationship for the voltages, $V_{sh} - V_{n+1} + V_{sh} - V_n = 0$, which solved for the shunt voltage reads

$$V_{sh} = \frac{1}{2}(V_n + V_{n+1}) = \frac{1}{2}V_n(1 + e^{-\gamma p}), \quad (3.23)$$

⁸ The voltages across the upper and lower series elements in the lattice are always equal. Moreover, the voltages across the left and right shunt elements in the lattice are always equal. This property of the symmetric lattice can be proven based on the fact that the lattice is a *two-port*, where equal currents flowing in and out on the two terminals forming the port.

where $V_{n+1} = V_n e^{-\gamma p}$ is substituted to obtain the last equation.

From the evaluation of the currents at node k_1 and k_3 , one gets the following set of equations

$$I_n - I_{se} - I_{sh}/2 = 0 \quad (3.24a)$$

$$-I_{n+1} + I_{se} - I_{sh}/2 = 0. \quad (3.24b)$$

The difference, (3.24a) - (3.24b), yields the expression for the series current,

$$I_{se} = \frac{1}{2}(I_n + I_{n+1}) = \frac{1}{2}I_n(1 + e^{-\gamma p}), \quad (3.25)$$

where, the term I_{n+1} is substituted by $I_n e^{-\gamma p}$ to get the second equation in (3.25). Finally, by relating (3.23) and (3.25) the Bloch impedance is given as

$$Z_B^+ = \frac{V_n}{I_n} = \frac{V_{sh}}{I_{se}}. \quad (3.26)$$

This is an interesting result which may require a small break and some appreciation. The Bloch impedance is identical to the ratio of the terminal voltage over the terminal current, which basically “is” the definition of the Bloch impedance $Z_B^+ = V_n/I_n$. More surprisingly, this ratio is identical to the shunt voltage over the series current, V_{sh}/I_{se} . Physically, the lattice exhibits very similar behavior to a homogeneous transmission line section of infinitely small length as shown in [34].

The sum, (3.24a) + (3.24b), leads to $I_n - I_{n+1} - I_{sh} = 0$, which after further inserting $I_{sh} = Y_{sh} V_{sh}$, allows to write the shunt voltage as

$$V_{sh} = \frac{1}{Y_{sh}}(I_n - I_{n+1}) = \frac{1}{Y_{sh}}I_n(1 - e^{-\gamma p}). \quad (3.27)$$

Similarly, the voltage loop: k_1, k_2, k_4 and k_3 results in $V_n - V_{se}/2 - V_{n+1} - V_{se}/2 = 0$, which after substitution of $V_{se} = Z_{se} I_{se}$ is

$$I_{se} = \frac{1}{Z_{se}}(V_n - V_{n+1}) = \frac{1}{Z_{se}}V_n(1 - e^{-\gamma p}). \quad (3.28)$$

If now, the equations for the shunt voltage and series current, (3.27) and (3.28), respectively, are finally inserted into (3.26), an expression for the Bloch impedance is found

$$Z_B^+ = \frac{V_{sh}}{I_{se}} = \frac{Z_{se}}{Y_{sh}} \frac{I_n(1 - e^{-\gamma p})}{V_n(1 - e^{-\gamma p})} = \frac{Z_{se}}{Y_{sh}} \frac{1}{Z_B^+}, \quad (3.29)$$

where again V_n/I_n is substituted by Z_B^+ to get the last equation in (3.29). Solving for the Bloch impedance⁹ (3.29) yields

$$Z_B^+ = \sqrt{\frac{Z_{se}}{Y_{sh}}}, \quad (3.30)$$

which is consistent with the results reported back in 1930 [44, 45]. By finally inserting the linearized impedance and admittance of (3.8) and (3.13), respectively, into (3.30) gives the Bloch impedance,

$$Z_B^+ = \sqrt{\frac{R + j2L(\omega - \omega_{se})}{G + j2C(\omega - \omega_{sh})}}. \quad (3.31)$$

⁹The definitions of the Bloch impedances Z_B^+ and Z_B^- , for wave propagation in positive and negative y -direction, respectively [Figure 3.6], results in $Z_B^+ = Z_B^-$, which follows from transversal symmetry.

The Bloch impedance has an analogy to the characteristic impedance of homogeneous transmission lines, $Z_0 = \sqrt{(R' + j\omega L')/(G' + j\omega C')}$, where the dashes refer to the *per unit length* parameters of the homogeneous transmission line [78].

One can summarize that the Bloch impedance formula for the lattice is a very simple and intuitive expression –analogy to homogeneous transmission lines–, which follows directly from the lattice topology. Neither a T nor a Π -topology provides this simplicity. Unlike the simplified formula for the propagation constant in (3.20), the Bloch impedance formula in (3.31) is mathematically exact without approximation.

3.1.5 Radiation Efficiency

The analysis of the radiation efficiency forms a central contribution of this chapter. In the previous section the broadside radiation frequency and the Bloch impedance are derived paving the way for the forthcoming derivation of the radiation efficiency of fully symmetric LWAs. For the determination of the efficiency, it is assumed that the antenna structure is electrically sufficiently long so that the power reflected at its termination side is considered negligible. In this case, the radiation efficiency for a single unit cell corresponds to the efficiency of the overall structure, which allows to restrict the investigation of radiation efficiency of the LWA to that of the single unit cell [62]. The overall radiation efficiency of an LWA, as any other antenna, is general given by

$$\eta = \frac{P_{\text{rad}}}{P} = \frac{P_{\text{rad}}}{P_{\text{rad}} + P_{\text{diss}}}, \quad (3.32)$$

where P_{rad} is the radiated power and P the total power, sum of radiated and dissipated power P_{diss} . The radiated power can be expressed as the sum of the series and the shunt radiated powers $P_{\text{rad}} = P_{\text{se,rad}} + P_{\text{sh,rad}}$ and the total power is the sum of the series and shunt total powers $P = P_{\text{se}} + P_{\text{sh}}$. For the efficiency in terms of the series and shunt power quantities one may write¹⁰

$$\eta = \frac{P_{\text{rad}}}{P} = \frac{P_{\text{se,rad}} + P_{\text{sh,rad}}}{P_{\text{se}} + P_{\text{sh}}}. \quad (3.33)$$

The radiated series and shunt powers in terms of the inner lattice shunt voltage and series current in Figure 3.6 read

$$P_{\text{se,rad}} = \frac{1}{2}|I_{\text{se}}|^2 R_{\text{rad}}, \quad \text{and} \quad P_{\text{sh,rad}} = \frac{1}{2}|V_{\text{sh}}|^2 G_{\text{rad}}, \quad (3.34)$$

respectively. Similarly, the total powers read

$$P_{\text{se}} = \frac{1}{2}|I_{\text{se}}|^2 R, \quad \text{and} \quad P_{\text{sh}} = \frac{1}{2}|V_{\text{sh}}|^2 G. \quad (3.35)$$

¹⁰ In case of a lossless LWA, obviously the radiation efficiency is 100%. If then only one radiation mechanism, series or shunt, radiates (e.g. $P_{\text{se,rad}} \neq 0$), whereas the other one is non-radiating (e.g. $P_{\text{sh,rad}} = 0$), the LWA input reflection coefficient becomes one, $|S_{11}| = 1$, and hence no power is accepted by the LWA. In such a case, the *radiation efficiency* is strictly not defined. A scenario, in which the shunt radiation is fully suppressed with $P_{\text{sh,rad}} = 0$, is discussed later in Section 3.5.2.

By inserting (3.34) and (3.35) into (3.33) the following expression for the LWA radiation efficiency is obtained,

$$\eta = \frac{P_{\text{se,rad}} + P_{\text{sh,rad}}}{P_{\text{se}} + P_{\text{sh}}} = \frac{|I_{\text{se}}|^2 R_{\text{rad}} + |V_{\text{sh}}|^2 G_{\text{rad}}}{|I_{\text{se}}|^2 R + |V_{\text{sh}}|^2 G} = \frac{R_{\text{rad}} + G_{\text{rad}} |V_{\text{sh}}/I_{\text{se}}|^2}{R + G |V_{\text{sh}}/I_{\text{se}}|^2}, \quad (3.36)$$

where for the last equation the fraction is divided by $|I_{\text{se}}|^2$. The ratio $V_{\text{sh}}/I_{\text{se}}$ is equivalent to the Bloch impedance Z_{B}^+ according to (3.26). Furthermore, recalling that $R_{\text{rad}} = \eta_{\text{se}}R$ in (3.5) and $G_{\text{rad}} = \eta_{\text{sh}}G$ in (3.11), the LWA efficiency formula is given by

$$\eta = \frac{\eta_{\text{se}}R + \eta_{\text{sh}}G|Z_{\text{B}}^+|^2}{R + G|Z_{\text{B}}^+|^2}. \quad (3.37)$$

By finally inserting the Bloch impedance of (3.31) into the efficiency formula (3.37) and substituting the LCRG quantities with the quality factors (3.7) and (3.12), the LWA efficiency reads

$$\eta = \frac{\eta_{\text{se}} |1 + j2Q_{\text{sh}}(\omega - \omega_{\text{sh}})/\omega_{\text{sh}}| + \eta_{\text{sh}} |1 + j2Q_{\text{se}}(\omega - \omega_{\text{se}})/\omega_{\text{se}}|}{|1 + j2Q_{\text{sh}}(\omega - \omega_{\text{sh}})/\omega_{\text{sh}}| + |1 + j2Q_{\text{se}}(\omega - \omega_{\text{se}})/\omega_{\text{se}}|} \quad (3.38)$$

Equation (3.38) is based on six parameters, series and shunt efficiencies, resonance frequencies and quality factors. All those quantities are frequency independent within a reasonable frequency range around broadside. The frequency dependence in (3.38) is only introduced by the terms $(\omega - \omega_{\text{se}})$ and $(\omega - \omega_{\text{sh}})$. In other words, the efficiency variation over frequency can be explained by a variation in the Bloch impedance. This can be directly confirmed in Equation (3.37) assuming frequency independent LCRG parameters and resonator efficiencies. The actual extraction of the series and shunt efficiencies using fullwave simulation is provided later in this chapter along with a discussion on fundamental limitations.

3.1.6 At-Broadside Radiation Efficiency

Now, the broadside radiation degradation is addressed via the theoretical framework that is established so far. The Bloch impedance in Equation (3.31) is evaluated at the broadside frequency by inserting the broadside condition in (3.21) into (3.31) to express the denominator in (3.31) in terms of series resonator parameters,

$$Z_{\text{B}}^+(\omega_{\text{bs}}) = \sqrt{\frac{1/G[RG + j2LG(\omega_{\text{bs}} - \omega_{\text{se}})]}{1/R[RG + j2CR(\omega_{\text{bs}} - \omega_{\text{sh}})]}} = \sqrt{\frac{R}{G}} \sqrt{\frac{RG + j2LG(\omega_{\text{bs}} - \omega_{\text{se}})}{RG - j2LG(\omega_{\text{bs}} - \omega_{\text{se}})}}. \quad (3.39)$$

By calculating the magnitude of $Z_{\text{B}}^+(\omega_{\text{bs}})$, since only this is required in (3.37), one simplifies (3.39) to

$$|Z_{\text{B}}^+(\omega_{\text{bs}})| = \sqrt{\frac{R}{G}} \sqrt{\left| \frac{RG + j2LG(\omega_{\text{bs}} - \omega_{\text{se}})}{RG - j2LG(\omega_{\text{bs}} - \omega_{\text{se}})} \right|} = \sqrt{\frac{R}{G}} \quad (3.40)$$

Finally, inserting (3.40) into (3.37), yields the broadside radiation efficiency of fully symmetric LWAs,

$$\eta_{\text{bs}} = \frac{\eta_{\text{se}} + \eta_{\text{sh}}}{2}, \quad (3.41)$$

which forms the central contribution of this chapter. At the first glance, it might not be so surprising that the overall efficiency is simply the average of the series and the

shunt efficiency. It could be easily accepted that they have an equal share on the overall efficiency, but there is a strong practical impact. The general problem one faces in most LWAs is that only one resonator is radiating efficiently, with the other being mainly dissipative. In the extreme case, where only one resonator is radiating (e.g. $\eta_{se} = 1$) and the other resonator is purely dissipative¹¹ (e.g. $\eta_{sh} = 0$), a maximum overall efficiency limitation of 50% persists.

The SFP example helps to illustrate the aforementioned efficiency limitation. Figure 3.5 shows the radiation characteristics of the series resonator and the shunt resonator. The series resonance mode corresponds to the conventional $\lambda/2$ -patch mode and is a good radiator having a series efficiency of around 90%. On the other hand, the shunt mode comprises mainly unwanted or parasitic radiation, which is not directed to broadside and has therefore a poor shunt efficiency around 20%. The efficiency values of around 90% and 20% for the series and shunt efficiencies, respectively, are reasonable estimates, as can be confirmed in the forthcoming Section 3.6, where Table 3.8 provides numerically extracted data for the series and shunt efficiencies.

The understanding of the efficiency limitation in (3.41) becomes even clearer by also investigating the radiation efficiency for off-broadside frequencies. Here, it is shown next that much higher overall efficiencies can be realized, even if one resonator is strongly dissipative.

3.1.7 Off-Broadside Radiation Efficiency

The off-broadside radiation efficiency is examined by considering frequency ranges below and above the broadside frequency. This is an asymptotic study to investigate the efficiency trends of the LWA model scanning backward and forward. The model with linearized immittance is a narrow band model of approximately 40% relative bandwidth (depending on the LWA type) as discussed in Section 3.1.2, where the series and shunt parameters are assumed to be frequency independent. It is therefore obvious that for either $\omega \gg \omega_{bs}$ or $\omega \ll \omega_{bs}$ the model does not capture all physical effects. Nevertheless, this asymptotic study helps to define the complementary regime to *at-broadside*, namely the *off-broadside* regime, which includes the backward and forward regime except broadside.

3.1.7.1 Asymptotic Backward Radiation Efficiency

For the backward radiation case, where $\omega < \omega_{bs}$, the asymptotic behavior of the efficiency in (3.38) is evaluated for $\omega \rightarrow 0$. The backward radiation efficiency is

$$\eta_{bw} = \frac{\eta_{se} |1 - j2Q_{sh}| + \eta_{sh} |1 - j2Q_{se}|}{|1 - j2Q_{sh}| + |1 - j2Q_{se}|} \approx \frac{\eta_{se} Q_{sh} + \eta_{sh} Q_{se}}{Q_{sh} + Q_{se}}. \quad (3.42)$$

The last approximation is made assuming that both quality factors, the series and the shunt quality factor, are much larger than unity, $Q_{se} \gg 1$ and $Q_{sh} \gg 1$, which generally holds.

¹¹This is, for example, the case in a uniformly excited array of 1D LWAs that is discussed later in Section 3.5.2.

3.1.7.2 Asymptotic Forward Radiation Efficiency

For the forward radiation case, where $\omega > \omega_{bs}$, the asymptotic behavior of the efficiency in (3.38) is evaluated for $\omega \rightarrow \infty$. The forward radiation efficiency is

$$\eta_{fw} = \frac{\eta_{se}Q_{sh}/\omega_{sh} + \eta_{sh}Q_{se}/\omega_{se}}{Q_{sh}/\omega_{sh} + Q_{se}/\omega_{se}}, \quad (3.43)$$

where no further approximations are made.

3.1.7.3 Off-Broadside Radiation Efficiency

Backward and forward radiation efficiencies can be unified under the condition that the two resonance frequencies are similar $\omega_{se} \approx \omega_{sh}$ or even identical $\omega_{se} = \omega_{sh}$, which defines the frequency-balancing condition. Equations (3.42) and (3.43) become identical with

$$\eta_{off-bs} = \frac{\eta_{se}Q_{sh} + \eta_{sh}Q_{se}}{Q_{sh} + Q_{se}}, \quad (3.44)$$

where η_{off-bs} is the off-broadside radiation efficiency. From a practical view point, Equation (3.44) is more relevant as compared to (3.42) and (3.43), since most unit cells are designed to be frequency-balanced.

It is interesting to compare the off-broadside efficiency in (3.44) with the at-broadside efficiency in (3.41). Much higher overall efficiencies can be realized for off-broadside scanning angles, even for a vanishing shunt efficiency $\eta_{sh} = 0$. The reason is that the series efficiency is weighted with the shunt quality factor in (3.44), so that the overall efficiency can approach η_{se} if $Q_{sh} \gg Q_{se}$.

While for the *physical* LWA the efficiencies and the quality factors are strongly related, they represent independent quantities in the *model*. Usually, a good and efficient radiator has a low quality factor, whereas a resonator of a high quality factor, is usually a poor radiator with a poor efficiency. The quality factors and efficiencies are not linked in the model and therefore treated independently. This offers the flexibility to investigate LWAs on a more general and abstract level.

Before starting a more detailed investigation and illustration of the frequency scanning behavior and the radiation efficiencies, the classification into four canonical unit cell conditions is made.

3.2 Frequency-Balancing and Q-Balancing Conditions

This section classifies unit cells into four different balanced and imbalanced conditions and discusses their properties. More specifically, the propagation constant, the Bloch impedance and the overall radiation efficiency are plotted over frequency for the sake of comparing these four conditions.

3.2.1 Equalization for Scanning Through Broadside

The Bloch impedance is recalled from (3.31) and the series resonator in the nominator and the shunt resonator in the denominator are expressed in terms of their quality factors, (3.8) and (3.13), respectively,

$$Z_B^+ = \sqrt{\frac{R + j2L(\omega - \omega_{se})}{G + j2C(\omega - \omega_{sh})}} = \sqrt{\frac{R}{G}} \sqrt{\frac{1 + j2Q_{se}(\omega - \omega_{se})/\omega_{se}}{1 + j2Q_{sh}(\omega - \omega_{sh})/\omega_{sh}}}. \quad (3.45)$$

Under the specific condition that $\omega_{se} = \omega_{sh}$ and $Q_{se} = Q_{sh}$, the Bloch impedance in (3.45) becomes frequency independent and reads

$$Z_B^+ = \sqrt{\frac{R}{G}} = \sqrt{\frac{L}{C}}. \quad (3.46)$$

The condition

$$\omega_{se} = \omega_{sh} = \omega_{bal} \quad (3.47)$$

is defined as the *frequency-balancing condition*, which is well-known in CRLH theory [26]. This condition was reported to improve the broadside characteristic of CRLH LWA in [27]. In this thesis the frequency-balancing condition is so far generalized to arbitrary LWAs falling under the class described in Section 2.4.

The condition

$$Q_{se} = Q_{sh} = Q_{bal} \quad (3.48)$$

is defined as the *Q-balancing condition*. This condition along with the terminology “Q-balancing” was first reported in the underlying publications of this thesis [51, 63].

The simultaneous satisfaction of both conditions, *frequency-balancing* and *Q-balancing*, is necessary and sufficient for a frequency independent Bloch impedance, which is confirmed in (3.45). This is referred to as *equalization*, since the at- and off-broadside impedances and radiation efficiencies are equalized. The radiation efficiency then reads

$$\eta_{bs} = \eta_{off-bs} = \frac{\eta_{se} + \eta_{sh}}{2}. \quad (3.49)$$

Following the same logics of balanced and imbalanced conditions for the resonant frequencies and the quality factors, one can systematically distinguish four canonical cases,

1. Frequency-imbalanced and Q-imbalanced
2. Frequency-balanced and Q-imbalanced
3. Frequency-imbalanced and Q-balanced
4. Frequency-balanced and Q-balanced

which are subsequently addressed and illustrated.

3.2.2 Comparison of the Four Balanced/Imbalanced Conditions

An artificial set of LCRG parameters, series and shunt resonance frequencies and efficiencies is chosen to compare the four balanced/imbalanced conditions for two reasons. First, by doing so the focus can be kept solely on the model properties without the need of elaborating on the details of a physical unit cell structure and parameter extraction, which is dealt with later in Section 3.4. Second, the illustration based on artificial parameters is much simpler and more significant, since they can be arbitrarily and independently adjusted to put the emphasis on the relevant effects. A validation linking the model to physical LWA structures is given at a later stage in Section 3.6.

For later convenience the harmonic mean resonance frequency is defined as

$$\omega_0 = \frac{2}{1/\omega_{se} + 1/\omega_{sh}} \quad (3.50)$$

to normalize the resonance frequencies ω_{se} and ω_{sh} .

The following set of fixed parameters is introduced, $L = 40$ nH, $C = 16$ pF, a series efficiency of $\eta_{se} = 0.9$ and a shunt efficiency of $\eta_{sh} = 0.2$. Despite the fact that these efficiencies are artificial, they are based on realistic quantities taken from [61, 62]. In addition, a qualitative discussion on the series and shunt efficiency and the reason for their difference is given in Section 3.1.6.

Figure 3.7 shows the propagation constant, the Bloch impedance and the radiation efficiency to overview and compare the four different balancing conditions. The resonance frequencies and the quality factors are adjusted to meet the four conditions.

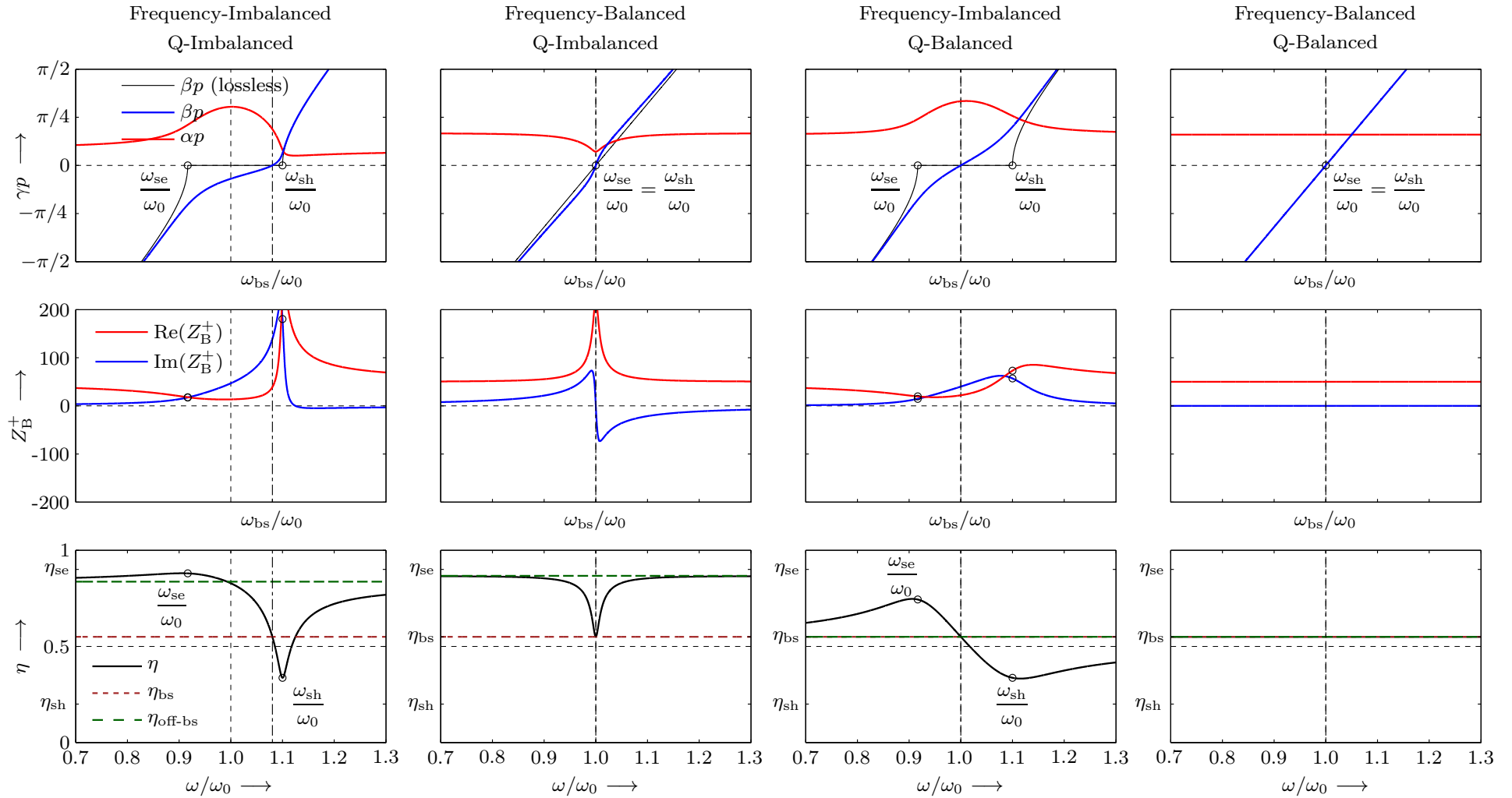


Figure 3.7: Overview *frequency-balancing* and *Q-balancing* conditions. The series and shunt efficiencies are chosen to be $\eta_{se} = 0.9$ and $\eta_{sh} = 0.2$, respectively. The broadside radiation efficiency is $\eta_{bs} = (\eta_{se} + \eta_{sh})/2$ in all four cases. (The thin solid black lines in the dispersion diagrams show the corresponding *lossless* cases, with $R = G = 0$, to clearly indicate that only in a *lossless* periodic structure a well-defined stopband is delimited by ω_{se} and ω_{sh} .)

3.2.2.1 Frequency-Imbalanced and Q-Imbalanced

The first column in Figure 3.7 shows the most general case, where no specific design considerations are made. The unit cell is frequency-imbalanced¹² with $\omega_{se} = 0.917 \cdot \omega_0$ and $\omega_{sh} = 1.1 \cdot \omega_0$ and Q-imbalanced with $Q_{se} = 10$ and $Q_{sh} = 100$. The broadside frequency is calculated from (3.22) and the dispersion diagram¹³ (top row) clearly confirms the zero crossing of the phase constant at broadside. It is observed that the broadside frequency ω_{bs} is shifted to the resonator frequency with the higher quality factor, here ω_{sh} , as predicted from (3.22). Generally, the propagation constant, the Bloch impedance and the radiation efficiency show a strong variation around broadside. Furthermore, the backward and forward radiation regimes, below and above the broadside frequency, are different and they cannot be unified to a common off-broadside regime as already discussed in Section 3.1.7. In other words, there is no symmetry in all the plots with respect to the broadside frequency. The radiation efficiency at broadside (bottom row) is $\eta = 0.55$ as predicted by (3.41). By moving to slightly higher frequencies, one can observe a well-pronounced notch with a minimum efficiency of 0.34 at the frequency corresponding to the shunt resonance ω_{sh} . On the other hand, considering the frequency range below broadside, much higher efficiencies can be realized with values almost approaching η_{se} around the series resonance frequency.

3.2.2.2 Frequency-Balanced and Q-Imbalanced

The second column in Figure 3.7 illustrates the scenario, where $\omega_{se} = \omega_{sh} = \omega_0$ and the quality factors are $Q_{se} = 5$ and $Q_{sh} = 100$, representing the frequency-balanced and Q-imbalanced case. The frequency-balancing condition was first introduced in CRLH LWAs as a condition to improve the broadside radiation [27, 28, 30, 43]. Therefore, the plots in this column represent the typical behavior of CRLH LWAs that are designed for frequency balancing. Here, the broadside frequency is equal to the resonator frequencies $\omega_{bs} = \omega_{se} = \omega_{sh}$ according to (3.22). On a qualitative basis, one can observe less variation in all plots around broadside as compared to the first column. This is maybe seen as improvement compared to the case without special design precautions. Especially, the backward and forward regimes are matched and they converge to the same values for below and above broadside frequencies. At ω_{bs} one virtually has a vertical symmetry line through the plots unifying the backward and forward regimes. The radiation efficiency at broadside (3.41) is $\eta = 0.55$ with a well-defined minimum. For off-broadside frequencies the efficiency rapidly approaches the asymptotic off-broadside efficiency in (3.44) with $\eta_{off-bs} = 0.87$.

3.2.2.3 Frequency-Imbalanced and Q-Balanced

The third column in Figure 3.7 shows that case where the unit cell is frequency-imbalanced and Q-balanced with $\omega_{se} = 0.917 \cdot \omega_0$, $\omega_{sh} = 1.1 \cdot \omega_0$ and $Q_{se} = Q_{sh} = 10$, respectively. This is a rather artificial case, which was not reported in the literature so far, since the concept of Q-balancing is new and most designs are aiming at frequency-balancing. The

¹²The series and shunt resonance frequencies are normalized to the harmonic mean frequency [Equation (3.50)]

¹³The axes of the dispersion diagram are exchanged, where now the horizontal axis shows the frequency and the vertical axis shows the propagation constant.

practical LWA relevance of this case is considered low, yet to present a complete overview of all balanced/imbalanced condition it is also addressed here. The broadside frequency is equal to the harmonic mean resonance frequency, $\omega_{bs} = \omega_0$, which results from the definition of ω_0 in (3.50). The broadside efficiency is $\eta = 0.55$ as predicted by (3.41). The efficiency maximum is shifted to ω_{se} , whereas the minimum is shifted to ω_{sh} , which is qualitative comparable to column 1, but without a pronounced notch of the minimum.

3.2.2.4 Frequency-Balanced and Q-Balanced

The fourth column in Figure 3.7 shows the case when frequency and Q-balancing conditions are simultaneously fulfilled with $\omega_{se} = \omega_{sh} = \omega_0$ and $Q_{se} = Q_{sh} = 10$. Under these conditions one obtains a frequency independent behavior for the leakage constant, the Bloch impedance and the radiation efficiency. This case was derived in Section 3.2.1 by equalizing the at- and off-broadside regime so to obtain a frequency invariant scanning through broadside. Practically, this scenario is of strong interest, since it partly solves the broadside degradation allowing a seamless scan through broadside without Bloch impedance or efficiency variation. A highly linear β is observed following a dispersionless wave propagation along the LWA. The broadside frequency is $\omega_{bs} = \omega_{se} = \omega_{sh}$, same as in column two. The at- and off-broadside efficiencies for this equalized case is $\eta = \eta_{bs} = \eta_{off-bs} = 0.55$, calculated from (3.49). The price of the equalization is the lowered efficiency in the off-broadside frequency regime.

3.2.2.5 Summary of Balancing Conditions

The four combinations of balanced and imbalanced conditions are given in Figure 3.7 showing propagation constant, Bloch impedance and efficiency in a very compact fashion for an optimal overview of all quantities. The formulas for the at- and off-broadside radiation efficiencies in (3.41) and (3.44) are confirmed. It is clearly demonstrated that in *all* cases, a poor broadside efficiency of $\eta = (\eta_{se} + \eta_{sh})/2$ is realized, whereas off-broadside much higher efficiencies are realizable. Frequency-balancing is practically most relevant, since it is a first measure to minimize the variation in the propagation constant and it matches the backward and forward radiation regimes. For this reason, in all the forthcoming analyses frequency-balancing is assumed, which allows to define the two complementary frequency regimes, at- and off-broadside (second column in Figure 3.7). To gain a better physical understanding of the mechanisms behind the two regimes, they are investigated later in detail in Section 3.3.

3.2.3 Discussion on Balancing Conditions and Stopband Closure

A term that is associated with the *broadside radiation problem* of periodic LWAs throughout the literature is the term “open-stopband” [19, 21, 28, 31, 38, 39, 81, 82, 91]. The first part, “open” refers to a *non-shielded* periodic wave guiding structure, which is capable of radiating into free-space. The second part, “stopband” *strictly* refers to a *shielded* periodic structure, where the fields in a certain frequency band are highly attenuated and do not propagate (evanescent waves), same as the operation below cut-off in a conventional rectangular waveguide.

The contradiction here is that a *stopband* or a *band gap* is only properly defined in a lossless periodic structure. To illustrate this, Figure 3.7 shows in addition the propagation constant also for the corresponding *lossless* unit cells (thin solid black lines). In the first and third column a well-defined stopband is delimited by the two resonance frequencies ω_{se} and ω_{sh} , whereas for the case with radiation and dissipation a well-defined stopband does not exist. One might understand the procedure of “closing” the open-stopband [38, 39, 81, 82] as the simultaneous satisfaction of two independent conditions, frequency-balancing *and* Q-balancing, to equalize the at- and off-broadside radiation regimes.

Based on the author’s opinion, the term open-stopband is synonymously used to absorb all the broadside related problems in periodic LWAs without specifically classifying them. The terminology can therefore be misleading and the concept of “open-stopband closure” does not provide a measurable quantity. This thesis proposes the concept of *equalization*, as the result from the simultaneous satisfaction of the frequency-balancing condition and the quality-factor-balancing condition, to classify and quantify the broadside degradation.

3.2.4 Relationship between Q-Balancing and the Heaviside Condition in homogeneous Transmission Lines

In the derivation of the Bloch impedance formula in (3.31) its correspondence to a homogeneous transmission line was discussed. On the same basis, the concept of Q-balancing is investigated and related to a condition in homogeneous transmission lines, which is known as the Heaviside condition [92]. Recalling the propagation constant from (3.20), which reads $\gamma = 1/p\sqrt{[R + j2L(\omega - \omega_{se})][(G + j2C(\omega - \omega_{sh}))]}$ and expressing the series L, R and the shunt C, G in terms of the series and shunt quality factors, (3.8) and (3.13), one obtains

$$\gamma = \frac{\sqrt{RG}}{p} \sqrt{\left[1 + j2Q_{se} \frac{\omega - \omega_{se}}{\omega_{se}}\right] \left[1 + j2Q_{sh} \frac{\omega - \omega_{sh}}{\omega_{sh}}\right]}. \quad (3.51)$$

If next, the condition of Q-balancing, $Q_{se} = Q_{sh}$, is inserted into (3.51) and the radiant is squared, the square root can be taken, following that

$$\gamma = \alpha + j\beta = \frac{\sqrt{RG}}{p} \left[1 + j2Q_{bal} \frac{\omega - \omega_{bal}}{\omega_{bal}}\right]. \quad (3.52)$$

From a physical wave propagation point of view, equation (3.52) is an interesting result. The imaginary part of the propagation constant, namely the phase constant β is not affected by the losses and is purely linear,¹⁴ which becomes more obvious by rewriting (3.52) as

$$\gamma = \alpha + j\beta = \frac{\sqrt{RG}}{p} + j2 \frac{\sqrt{LC}}{p} (\omega - \omega_{bal}). \quad (3.53)$$

Practically, this implies wave propagation along the periodic structure that does not undergo *dispersion* or *distortion*, following that the wave propagation under Q-balancing is distortionless. Back in 1887, Oliver Heaviside reported a condition for achieving distortionless propagation in telegraph lines [92]. This condition is $L'/R' = C'/G'$ and it simplifies the propagation constant $\gamma = \sqrt{(R' + j\omega L')(G' + j\omega C')}$ to $\gamma = \sqrt{R'G'} + j\omega\sqrt{L'C'}$,

¹⁴Linear refers to a *linear equation*.

where the dashed values are per unit length parameters of a homogeneous transmission line. The Q-balancing condition is essentially equivalent to the Heaviside condition as can be easily verified by

$$Q_{se} = Q_{sh} = \frac{\omega_{se}L}{R} = \frac{\omega_{sh}C}{G} \rightarrow \frac{L}{R} = \frac{C}{G} \rightarrow \frac{L'}{R'} = \frac{C'}{G'}. \quad (3.54)$$

3.3 Asymptotic Study on At- and Off-Broadside Properties

In the following, the at- and off-broadside properties are studied in detail to understand the wave propagation mechanisms in these two fundamentally different frequency regimes. It is assumed that the unit cell is frequency-balanced, which is the case given in the second and fourth column in Figure 3.7. This assumption is required in the forthcoming asymptotic analysis, but this does not imply a severe restriction. Frequency-balancing, as aforementioned, is a first necessary condition to improve the situation at broadside, which can be easily realized in fully symmetric LWAs.

For convenience, a frequency deviation from the broadside frequency ω_{bs} is introduced and defined as

$$\Delta\omega = (\omega - \omega_{bs}), \quad (3.55)$$

where $\omega_{bs} = \omega_{se} = \omega_{sh}$.

Using the definition in (3.55), the propagation constant in (3.20) is expressed as follows

$$\begin{aligned} \gamma p &= \sqrt{RG - 4LC\Delta\omega^2 + j2(CR + LG)\Delta\omega} \\ &= \omega_{bs}\sqrt{LC}\sqrt{\frac{1}{Q_{se} + Q_{sh}} - 4\frac{\Delta\omega^2}{\omega_{bs}^2} + j2\left(\frac{1}{Q_{se}} + \frac{1}{Q_{sh}}\right)\frac{\Delta\omega}{\omega_{bs}}}, \end{aligned} \quad (3.56)$$

where R and G are replaced by $\omega_{bs}L/Q_{se}$ and $\omega_{bs}C/Q_{sh}$, respectively, so to obtain the last equality.

Similarly, the Bloch impedance reads

$$Z_B^+ = \sqrt{\frac{R + j2\Delta\omega L}{G + j2\Delta\omega C}} = \sqrt{\frac{L}{C}}\sqrt{\frac{\frac{1}{Q_{se}Q_{sh}} + j2\frac{\Delta\omega}{\omega_{bs}}\left(\frac{1}{Q_{sh}} - \frac{1}{Q_{se}}\right) + 4\frac{\Delta\omega^2}{\omega_{bs}^2}}{\frac{1}{Q_{sh}^2} + 4\frac{\Delta\omega^2}{\omega_{bs}^2}}}, \quad (3.57)$$

which is obtained from (3.45) following the same procedure as before.

In addition, the transmission quality factor, Q , for a dispersive periodic structure is

$$Q = \omega \frac{\text{energy per unit length}}{\text{power loss per unit length}} = \omega \frac{W}{P} = \omega \frac{\partial[\text{Im}(\gamma p)]/\partial\omega}{2\text{Re}(\gamma p)} = \omega \frac{\partial\beta/\partial\omega}{2\alpha}, \quad (3.58)$$

where P and W are the power loss and stored energy per unit cell, respectively, [76]. This transmission quality factor is a useful measure to relate energy and power of the leaky wave. It is subsequently examined together with the propagation constant and the Bloch impedance for the two aforementioned regimes, at- and off-broadside.

3.3.1 At-Broadside Frequency Regime

Consider the frequency range $RG \gg 4\Delta\omega^2 LC$ (still assuming $\Delta\omega \ll \omega_{\text{bs}}$), which corresponds to an extremely narrow frequency region centered at ω_{bs} , where $\Delta\omega \approx 0$ according to Equation (3.55). In this range, the general propagation constant of Equation (3.20) becomes

$$\begin{aligned}\gamma p &\approx \sqrt{RG + j2(CR + LG)\Delta\omega} \\ &= \sqrt{RG} \sqrt{1 + j2(Q_{\text{se}} + Q_{\text{sh}}) \frac{\Delta\omega}{\omega_{\text{bs}}}} \\ &= \alpha_{\text{bs}} p \sqrt{1 + 2j \frac{\beta_{\text{bs}}}{\alpha_{\text{bs}}}} \approx \gamma_{\text{bs}} p = (\alpha_{\text{bs}} + j\beta_{\text{bs}}) p\end{aligned}\quad (3.59a)$$

where the term in $\Delta\omega^2$ in (3.56) is set to zero. The leakage constant is

$$\alpha_{\text{bs}} p = \sqrt{RG}, \quad (3.59b)$$

and the phase constant is

$$\beta_{\text{bs}} p = \frac{\Delta\omega}{\omega_{\text{bs}}} \sqrt{RG} (Q_{\text{se}} + Q_{\text{sh}}), \quad (3.59c)$$

where the subscript “bs” refers to the at-broadside regime. The last approximation in Equation (3.59a) is obtained using the Taylor approximation $\sqrt{1 \pm x} \approx 1 \pm x/2$ for $|x| \ll 1$, with $x = 2j\beta_{\text{bs}}/\alpha_{\text{bs}}$. The condition $|2j\beta_{\text{bs}}/\alpha_{\text{bs}}| \ll 1$ safely holds here, since $\beta \approx 0$ around broadside.

An explicit expression for the at-broadside transmission quality factor is then obtained by inserting (3.59b) and (3.59c) into Equation (3.58), which yields

$$Q_{\text{bs}} = \omega \frac{\partial \beta_{\text{bs}} / \partial \omega}{2\alpha_{\text{bs}}} = \frac{\omega}{\omega_{\text{bs}}} \frac{Q_{\text{se}} + Q_{\text{sh}}}{2}. \quad (3.60)$$

Finally, the at-broadside characteristic impedance is obtained by neglecting the term $4\Delta\omega^2/\omega_0^2$ in the nominator and denominator of Eq. (3.57), and by reusing the aforementioned Taylor approximation, which yields

$$Z_{\text{B,bs}}^+ = \sqrt{\frac{R}{G}} \left[1 + j \frac{\Delta\omega}{\omega_{\text{bs}}} (Q_{\text{se}} - Q_{\text{sh}}) \right]. \quad (3.61)$$

For $\Delta\omega = 0$, which is the exact broadside frequency point, the characteristic impedance of (3.61) may be further simplified to

$$Z_{\text{B,bs}}^+ = \frac{V_n}{I_n} = \frac{V_{\text{sh}}}{I_{\text{se}}} = \sqrt{\frac{R}{G}}, \quad (3.62)$$

where the series current I_{se} and the shunt voltage V_{sh} are recalled from (3.26). Equation (3.62) becomes a strong and meaningful result by using the definitions of series and shunt powers in (3.35) to rewrite (3.62) as

$$\frac{1}{2} |I_{\text{se}}|^2 R = \frac{1}{2} |V_{\text{sh}}|^2 G = P_{\text{se}} = P_{\text{sh}} = \frac{1}{2} P, \quad (3.63)$$

revealing that the total powers, dissipation plus radiation, in the series and shunt resonators are always equal, if the unit cell is loaded with $Z_{B,bs}^+$, e.g. in an infinite LWA. This result clearly confirms the broadside radiation efficiency, $\eta = (\eta_{se} + \eta_{sh})/2$ in (3.41), from another perspective. Since the power P is equally split between the series and shunt resonator, it is obvious that they have an equal power share and that each resonator can only contribute to the overall efficiency with maximal 50%.

An alternative approach to the transmission quality factor, that physically provides more insight, is an agreement with (3.60) and is presented next. Using the definition of the *transmission quality factor* in (3.58) along with the definition of the general *resonator quality factor* in (3.6), one again obtains the at-broadside quality factor

$$\begin{aligned} Q_{bs} &= \omega \frac{W_{se} + W_{sh}}{P_{se} + P_{sh}} = \frac{\omega}{\omega_{bs}} \frac{1}{2} \left(\frac{\omega_{bs} W_{se}}{P/2} + \frac{\omega_{bs} W_{sh}}{P/2} \right) \\ &= \frac{\omega}{\omega_{bs}} \frac{Q_{se} + Q_{sh}}{2}, \end{aligned} \quad (3.64)$$

which is identical to (3.60). The quantities W_{se} and W_{sh} are the series and shunt energies, respectively.

The transmission quality factor formula in (3.64) is a most unusual result that is calculated from the *sum* of two quality factors. Normally, the general procedure to compute the overall quality factor from individual loss mechanisms in a resonance system comprises the calculation of the reciprocal sum, $1/Q = 1/Q_{loss1} + 1/Q_{loss2}$, [78, 79]. In this normal and well-understood case, the resonator has one common energy storage and two different power loss mechanisms. For the at-broadside frequency, the energy and power relations are effectively exchanged. The power loss (radiation and dissipation) in the two resonators are equal, following that the stored energies in the individual series and shunt resonators must be different according to (3.64).

3.3.2 Asymptotic Off-Broadside Frequency Regime

Now, one considers the complementary frequency range $RG \ll 4\Delta\omega^2 LC$ (still assuming $\Delta\omega \ll \omega_{bs}$), which extends on both sides of ω_{bs} , excluding a small region around ω_{bs} . Note that the condition $RG \ll 4\Delta\omega^2 LC$ may be satisfied even very close to ω_{bs} , because the RG product represents a very small quantity, essentially modeling the radiation loss per unit cell of the leaky-wave antenna. In this range, the general propagation constant in Equation (3.56) reduces to

$$\begin{aligned} \gamma p &\approx \sqrt{j2(CR + LG)\Delta\omega - 4LC\Delta\omega^2} \\ &= \omega_{bs} \sqrt{LC} \sqrt{-4\frac{\Delta\omega^2}{\omega_{bs}^2} + j2\left(\frac{1}{Q_{se}} + \frac{1}{Q_{sh}}\right)\frac{\Delta\omega}{\omega_{bs}}} \\ &= j\beta_{off-bs} p \sqrt{1 - j\frac{2\alpha_{off-bs}}{\beta_{off-bs}}} \approx \gamma_{off-bs} p = (\alpha_{off-bs} + j\beta_{off-bs})p, \end{aligned} \quad (3.65a)$$

with

$$\alpha_{off-bs} p = \frac{1}{2}\omega_{bs} \sqrt{LC} \left(\frac{1}{Q_{se}} + \frac{1}{Q_{sh}} \right) \quad (3.65b)$$

and

$$\beta_{off-bs} p = 2\Delta\omega \sqrt{LC}, \quad (3.65c)$$

where the subscript “off-bs” has been introduced to indicate the off-broadside regime. The last result in Equation (3.65a) is obtained using Taylor approximation as done before by having $\sqrt{1 \pm x} \approx 1 \pm x/2$ for $|x| \ll 1$, with $x = j2\alpha_{\text{off-bs}}/\beta_{\text{off-bs}}$. The condition $|2\alpha_{\text{off-bs}}/\beta_{\text{off-bs}}| \ll 1$ safely holds here due to the low per-unit-cell leaky-wave radiation loss.

An explicit expression for the off-broadside transmission quality factor is then obtained by inserting (3.65b) and (3.65c) into Equation (3.58), which yields

$$Q_{\text{off-bs}} = \omega \frac{\partial \beta_{\text{off-bs}} / \partial \omega}{2\alpha_{\text{off-bs}}} = \frac{\omega}{\omega_{\text{bs}}} \frac{2}{1/Q_{\text{se}} + 1/Q_{\text{sh}}}. \quad (3.66)$$

Finally, the off-broadside characteristic impedance is obtained by neglecting the terms $1/Q_{\text{se}}Q_{\text{sh}}$ and $1/Q_{\text{sh}}^2$ in Equation (3.57), and by reusing the aforementioned Taylor approximation, which yields

$$Z_{\text{B,off-bs}}^+ = \sqrt{\frac{L}{C}} \left[1 + \frac{j \omega_{\text{bs}}}{4 \Delta \omega} \left(\frac{1}{Q_{\text{sh}}} - \frac{1}{Q_{\text{se}}} \right) \right]. \quad (3.67)$$

Assume $R \ll j2\Delta\omega L$ and $G \ll j2\Delta\omega C$, so to fully neglect the loss contributions R and G , (3.67) further simplifies to

$$Z_{\text{B,off-bs}}^+ \approx \frac{V_n}{I_n} = \frac{V_{\text{sh}}}{I_{\text{se}}} = \sqrt{\frac{L}{C}}, \quad (3.68)$$

where I_{se} is the series current and V_{sh} is the shunt voltage in the lattice model. Rearranging (3.68), one obtains the relation

$$\frac{1}{4} |I_{\text{se}}|^2 L = \frac{1}{4} |V_{\text{sh}}|^2 C = W_{\text{se}} = W_{\text{sh}} = \frac{1}{2} W, \quad (3.69)$$

showing that the time-average stored energies $W_{\text{se}} = \frac{1}{4} |I_{\text{se}}|^2 L$ and $W_{\text{sh}} = \frac{1}{4} |V_{\text{sh}}|^2 C$ are equal. Alternatively, the transmission quality factor is again calculated based on powers and energies to confirm the result in Equation (3.66) by

$$\begin{aligned} Q_{\text{off-bs}} &= \omega \frac{W_{\text{se}} + W_{\text{sh}}}{P_{\text{se}} + P_{\text{sh}}} = \frac{\omega}{\omega_{\text{bs}}} \frac{\omega_{\text{bs}} W}{P_{\text{se}} + P_{\text{sh}}} = \frac{\omega}{\omega_{\text{bs}}} \frac{2}{\frac{P_{\text{se}}}{\omega_{\text{bs}} W/2} + \frac{P_{\text{sh}}}{\omega_{\text{bs}} W/2}} \\ &= \frac{\omega}{\omega_{\text{bs}}} \frac{2}{1/Q_{\text{se}} + 1/Q_{\text{sh}}}. \end{aligned} \quad (3.70)$$

The transmission quality factor in Equation (3.70) shows the “normal” behavior of the reciprocal sum. Here, for the off-broadside propagation, the energy stored in the two resonators are equal, whereas the powers differ.

3.3.3 Comparison of At- and Off-Broadside Properties

Table 3.2 summaries the asymptotic formulas for the two fundamentally different propagation regimes, at- and off-broadside. The at-broadside propagation is characterized by equal powers, whereas the off-broadside propagation is characterized by equal energies in series and shunt resonator. Therefore, these propagation mechanisms might be referred

to as *resistive* (broadside) and *reactive* wave propagation (off-broadside) mechanisms, a concept, which to the author's best knowledge, has not been reported in the context of periodic LWA so far.

Table 3.2: Summary of the asymptotic at- and off-broadside formulas of this section including the asymptotic radiation efficiency results from Sections 3.3.2 and 3.1.7.

	at-broadside (bs)	off-broadside (off-bs)
αp	$\sqrt{RG} = \omega_{bs} \sqrt{LC} \frac{1}{\sqrt{Q_{se} Q_{sh}}}$	$\frac{1}{2} \omega_{bs} \sqrt{LC} \left(\frac{1}{Q_{se}} + \frac{1}{Q_{sh}} \right) = \frac{1}{2} \sqrt{RG} \frac{Q_{se} + Q_{sh}}{\sqrt{Q_{se} Q_{sh}}}$
βp	$\frac{\Delta\omega}{\omega_{bs}} \sqrt{RG} (Q_{se} + Q_{sh}) =$ $2\Delta\omega \sqrt{LC} \frac{Q_{se} + Q_{sh}}{\sqrt{Q_{se} Q_{sh}}}$	$2\Delta\omega \sqrt{LC} =$ $2 \frac{\Delta\omega}{\omega_{bs}} \sqrt{RG} \sqrt{Q_{se} Q_{sh}}$
W	$W_{se} \neq W_{sh}$ (for $Q_{se} \neq Q_{sh}$)	$W_{se} = W_{sh} = W/2$
P	$P_{se} = P_{sh} = P/2$	$P_{se} \neq P_{sh}$ (for $Q_{se} \neq Q_{sh}$)
Q	$\omega \frac{W_{sh} + W_{se}}{P} = \frac{\omega}{\omega_{bs}} \frac{Q_{se} + Q_{sh}}{2}$	$\omega \frac{W}{P_{sh} + P_{se}} = \frac{\omega}{\omega_{bs}} \frac{2}{1/Q_{se} + 1/Q_{sh}}$
Z_B^+	$\sqrt{\frac{R}{G}} \left[1 + j \frac{\Delta\omega}{\omega_{bs}} (Q_{se} - Q_{sh}) \right]$	$\sqrt{\frac{L}{C}} \left[1 + \frac{j}{4} \frac{\omega_{bs}}{\Delta\omega} \left(\frac{1}{Q_{sh}} - \frac{1}{Q_{se}} \right) \right]$
η	$\frac{\eta_{se} + \eta_{sh}}{2}$	$\frac{Q_{sh} \eta_{se} + Q_{se} \eta_{sh}}{Q_{se} + Q_{sh}}$

3.4 Extraction of Circuit Model Parameters using Fullwave Simulation

This section develops three methods, of increasing accuracy, to extract the LCRG parameters and the radiation efficiencies η_{se} and η_{sh} from fullwave simulation.¹⁵ First, a *single* unit cell is investigated. Next, *multiple* cascaded unit cells are considered to take into account the effects of mutual coupling. Finally, a truly *infinite* periodic structure is investigated by using periodic boundaries to effectively study the infinite cascade by taken into account all coupling effects.

The simulation method dealing with the truly *infinite* periodic case is of major relevance for the following reasons. This method provides an accurate scheme for the extraction

¹⁵ The thesis employs commercially available simulation tools for parameter extraction, rather than developing new simulation schemes particularly suited for the analysis of periodic structures. The reason is twofold. First, the focus of this thesis is the analysis and the resolution of the broadside problem. The development or even only the application of specialized simulation schemes, e.g. in [93,94] is complex and it would diverge from the main path of this thesis. Second, extraction methods which are based on commercial simulation tools, have the distinct advantage that generally, they can be used by a large community having access to these tools.

of the LCRG parameters and the radiation efficiencies; and more importantly, the development of this method reveals fundamental broadside radiation and polarization limitations.

Sections 3.4.1 and 3.4.2 develop parameter extraction methods for a truncated finite cascade of unit cells and discuss extraction artifacts due to the finiteness. Both sections are not *directly* within the theoretical main thread of this chapter. At this point, the reader has therefore the possibility to directly continue with Section 3.4.3, *the truly infinite periodic case*, without a lack of consistency.

3.4.1 Drivenmode Simulation of a Single Unit Cell

The simplest way to extract the LCRG parameters is shown in Figure 3.8, where a single SFP unit cell is sketched as example with two excitation ports to fully characterize the two-port using a fullwave simulator. The unit cell is *driven* by these two-ports, so to obtain the required two-port matrix data and hence the terminology *drivenmode* simulation. Here, only a single isolated unit cell is considered, thus the coupling to the neighboring cells is neglected. For the exact geometry of the patch, the reader is referred to Figure 3.19 in the later Section 3.6.1, where the case study LWAs are examined.

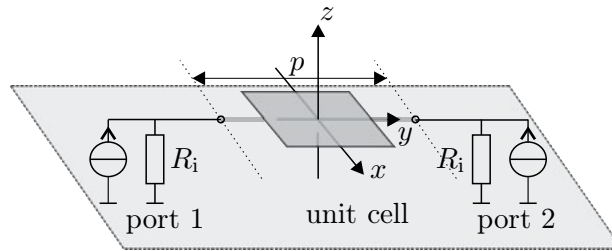


Figure 3.8: Single unit cell simulation model. The two-port parameters are obtained from a drivenmode simulation and the immittance Z_{se} , Y_{sh} and the LCRG parameters are calculated using the procedure described in Sections 3.1.1 and 3.1.2, respectively.

3.4.1.1 LCRG Parameter Extraction

The LCRG parameters are simply extracted going through the procedure that is already described in Sections 3.1.1 and 3.1.2. First, the S-parameter data is converted to the impedance and admittance matrix, so to apply Equations (3.2a) and (3.2b) to calculate Z_{se} and Y_{sh} , respectively. Next, the series and the shunt resonance frequencies are determined from the zero crossing of the reactance and susceptance given in (3.3) and (3.9). Finally, these immittances are linearized as described in Section 3.1.2, where the slopes of the immittances at resonance are evaluated to find L and C by (3.4) and (3.10) together with R and G .

Table 3.3: LCRG parameters and resonance frequencies extracted from a single SFP unit cell. The results of two commercial fullwave simulators, EMPIRE XPU and HFSS, are compared. (The value $G < 0$ is obviously non-physical, which is carefully addressed in the text.)

	L/nH	C/pF	R/Ω	G/mS	$\omega_{\text{se}}/\text{GHz}$	$\omega_{\text{sh}}/\text{GHz}$
EMPIRE	5.12	0.14	20.56	-0.047	10.0	10.0
HFSS	5.15	0.14	23.15	0.391	10.0	10.0

In Table 3.3 the LCRG parameters and the resonance frequencies are listed to compare two different simulators, EMPIRE XPU¹⁶ and HFSS¹⁷. A very good agreement is observed for the reactive parameters L and C and the resonance frequencies, whereas the resistive parameters R and G show some discrepancy. Particularly, the shunt conductance G shows a non-physical behavior with values less than zero. In the forthcoming analysis this effect is addressed and explained.

To extract the series and shunt radiation efficiencies from fullwave simulation, two different methods are proposed and discussed.

3.4.1.2 Series and Shunt Efficiencies from Antenna Gain Integration

In preparation for this method, the common gain definition in [1] needs to be adapted to antennas, and here specifically to unit cells having two-ports. This is achieved by defining the *total accepted power* by the unit cell two-port, as the *sum* of the powers accepted on each port. It is important to point out, that the antenna unit cell gain and efficiency are no longer intrinsic properties of the structure, but becomes depended on the respective port excitation [97]. In other words, with an odd excitation of the unit cell according to Figure 3.3(a), one usually obtains a different gain and efficiency as compared to an even excitation scenario in Figure 3.3(b). In fact, under odd excitation the unit cell exhibits the series radiation efficiency η_{se} , and under even excitation the unit cell exhibits the shunt radiation efficiency η_{sh} . Both efficiencies are obtained numerically from gain integration. A rigorous simulation scheme for the farfield parameters of multi-port antennas was presented in [57]. This scheme is applied to compute the radiation efficiency of unit cell under odd/even excitation. This procedure is named the *antenna gain integration* (gain integr.) method. It is not necessarily restricted to simulation, but can also be used with measured antenna gain.

3.4.1.3 Series and Shunt Efficiencies from Loss Discrimination

The second method to determine the radiation efficiency is the *loss discrimination* (loss discr.). This method purely relies on simulation results in a sense, that the antenna unit cell is simulated without loss, which is not possible in a measurement setup. The method requires two simulations, one without loss and the other with loss. Under the assumption that the field distribution in these two simulations is identical, it is possible to discriminate

¹⁶EMPIRE XPU is a 3D electromagnetic field simulator that is based on the finite difference time domain method (FDTD) [95].

¹⁷HFSSTM is a field simulator based on the finite element method (FEM) [96].

the radiation contribution and the loss. In the first simulation, where the loss is turned on, one extracts the resistance as

$$R_{\text{lossy}} = R_{\text{rad}} + R_{\text{diss}}, \quad (3.71)$$

and the conductance as

$$G_{\text{lossy}} = G_{\text{rad}} + G_{\text{diss}}. \quad (3.72)$$

In the second simulation, the loss is turned off, implying that R_{diss} and G_{diss} are zero. The parameter extraction of the resistance and conductance for the lossless simulation then reads

$$R_{\text{lossless}} = R_{\text{rad}}, \quad (3.73)$$

and

$$G_{\text{lossless}} = G_{\text{rad}}. \quad (3.74)$$

Finally, by recalling the series and shunt radiation efficiencies in (3.5) and (3.11), respectively, one obtains for the series efficiency

$$\eta_{\text{se}} = \frac{R_{\text{rad}}}{R_{\text{rad}} + R_{\text{diss}}} = \frac{R_{\text{lossless}}}{R_{\text{lossy}}} \quad (3.75)$$

and for the shunt efficiency

$$\eta_{\text{sh}} = \frac{G_{\text{rad}}}{G_{\text{rad}} + G_{\text{diss}}} = \frac{G_{\text{lossless}}}{G_{\text{lossy}}}. \quad (3.76)$$

The loss discrimination is similar to the perturbation method, [78], for determining the loss contribution, in a sense, that one assumes the reactive fields (here L and C , specifically discussed in [34, 63]) are not impacted by the losses. This is a very reasonable approximation, which is confirmed in the forthcoming Section 3.4.2.

3.4.1.4 Comparison of Efficiency Extraction Methods

Table 3.4: Series and shunt efficiencies obtained from the loss discrimination method using EMPIRE XPU and HFSS. (The values $\eta_{\text{sh}} < 0$ and $\eta_{\text{sh}} > 1$ are non-physical, which is carefully addressed in the text.)

method	η_{se}		η_{sh}	
	gain integr.	loss discr.	gain integr.	loss discr.
EMPIRE	0.69	0.82	-0.25	3.24
HFSS	0.42	0.85	0.18	0.73

Table 3.4 lists the efficiency of the SFP example that are determined following the two aforementioned procedures. The efficiencies strongly vary with the method and as well with the simulator, where non-physical efficiency values are observed for the shunt efficiency in the EMPIRE simulation. The series efficiency shows some discrepancy, yet the results obtained from the loss discrimination method are in a good agreement comparing EMPIRE and HFSS. On the other hand, the shunt efficiencies cannot be assessed at all, due to fact that all values totally differ; and more importantly they physically do not make

sense. Generally, the series and shunt efficiencies in Table 3.4 are not trustworthy and one has to understand why the two methods and the two simulators are not in agreement.

Two major problems are identified in the following. First, by recalling the radiated fields of the series and the shunt resonance in Figure 3.5(c) and Figure 3.5(d), it is observed that a large amount of shunt radiation is directed to the unit cell port planes in $\pm y$ -direction. The radiation into the ports planes is critical in EMPIRE and it makes the proper evaluation of the shunt parameters G and η_{sh} impossible, since these values are comparatively small and therefore sensitive. Moreover, the boundary condition of the unit cell in $\pm y$ -direction is critical in the simulator, since it strongly affects the shunt mode. To solve this issue, a cascade of multiple unit cells is considered in the next section so to effectively reduce the effect of outer boundaries and to take into account mutual unit cell coupling.

3.4.2 Drivenmode Simulation Considering Mutual Coupling between Multiple Unit Cells

To overcome the aforementioned problems in the simulation of a single and isolated unit cell, a cascade of N unit cells is evaluated next. From two-port theory it is known that the transmission matrix of a cascade of two-port networks is found by the matrix multiplication of the individual transmission matrices [78]. For a cascade of N unit cells, one obtains the 2×2 overall transmission matrix as $\mathbf{ABCD}^N = \mathbf{ABCD}_{N\text{-cells}}$. The N^{th} -root of $\mathbf{ABCD}_{N\text{-cells}}$ is identical to the transmission matrix of the single unit cell and is calculated as

$$\mathbf{ABCD} = \sqrt[N]{\mathbf{ABCD}_{N\text{-cells}}} = \mathbf{M} \text{diag}(\sqrt[N]{\lambda_1}, \sqrt[N]{\lambda_2}) \mathbf{M}^{-1}, \quad (3.77)$$

where \mathbf{M} is the modal matrix that takes $\mathbf{ABCD}_{N\text{-cells}}$ to its Jordan form as

$$\mathbf{ABCD}_{N\text{-cells}} = \mathbf{M} \text{diag}(\lambda_1, \lambda_2) \mathbf{M}^{-1}, \quad (3.78)$$

and $\lambda_{1,2}$ are the eigenvalues of $\mathbf{ABCD}_{N\text{-cells}}$. The physically correct solution, among the N mathematical ones, can be identified following the schemes proposed in [98–100]. Figure 3.9 shows N cascaded SFP unit cells to visualize the simulation setup.

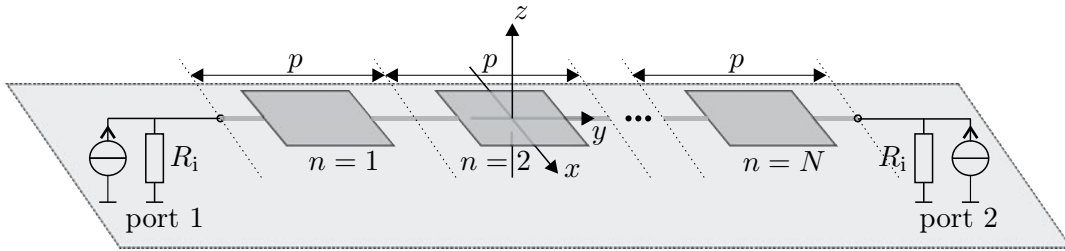


Figure 3.9: Multiple unit cell simulation model to consider the effect of mutual coupling. The overall transmission matrix \mathbf{ABCD}^N of the cascade of N unit cells is obtained from driven mode simulation. The two-port data, following the immittances and the LCRG parameters, for the de-embedded unit cell are calculated by taking the N^{th} -root of \mathbf{ABCD}^N to find \mathbf{ABCD} .

The same SFP example as before is now analyzed and the parameters are plotted for $N = 1$ to $N = 20$. The results for $N = 1$ obviously correspond to the parameters of the single unit cell, which are already listed in Table 3.3 and Table 3.4.

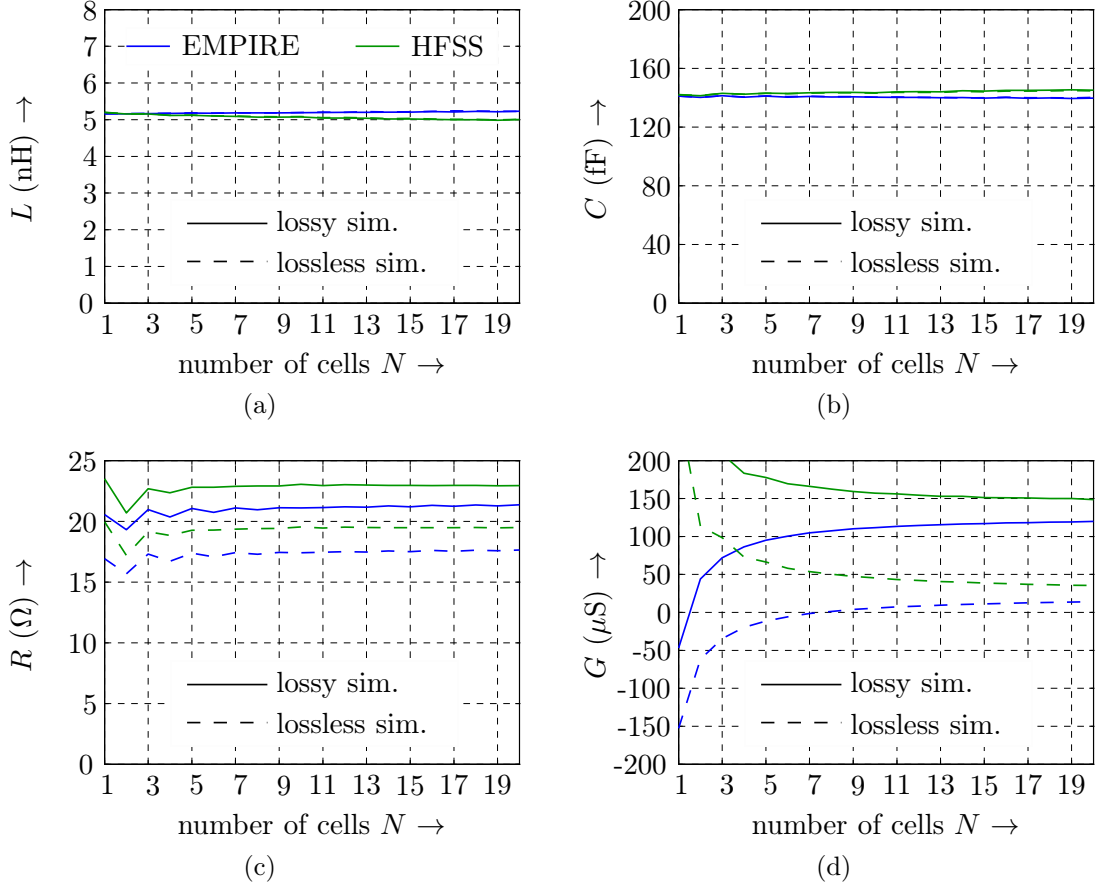


Figure 3.10: Extracted LCRG parameters from a cascade of N unit cells. The N^{th} -root is taken of the overall transmission matrix, $\mathbf{ABCD}_{N\text{-cells}}$, to obtain the transmission matrix of the unit cell, \mathbf{ABCD} and to extract the LCRG parameters. (a) Series reactance slope L . (b) Shunt susceptance slope C . (c) Series resistance R . (d) Shunt conductance G .

Figure 3.10 shows the LCRG parameters for the variation of N . There is only a minor effect on the reactive parameters, L and C , observable in Figure 3.10(a) and Figure 3.10(b).¹⁸ The solid and the dashed lines in Figure 3.10(a) and (b) are superimposed, showing that the lossy and lossless simulations yield identical reactive parameters L and C , which validates the loss discrimination. Both simulations, EMPIRE and HFSS, show a good agreement on the reactive parameters, L and C , where only a negligible discrepancy is observed.

The resistance R is plotted in Figure 3.10(c) showing a good convergence for $N > 7$. The solid and the dashed lines are expected to be different, where the difference is the loss resistance R_{diss} . Both simulation tools show a reasonable agreement in all cases, despite the fact that the HFSS resistances are about 10% higher.

The results of the conductivity G , plotted in Figure 3.10(d), show a strong dependency of the cascade length in both simulators, particularly for $N < 5$. Similarly to the previous case, the difference in the solid and the dashed lines is the loss conductance G_{diss} . For the

¹⁸This observation can not be generalized to other LWA unit cells. The SFP unit cell is electrically large as compared to a CRLH unit cell for example, which is much smaller than a guided wavelength. The smaller the unit cell is, the stronger is the interaction with the neighboring cells and therefore the parameters L and C vary if N is increased.

single unit cell with $N = 1$ the discrepancy of the two simulators is largest, whereas they seem to slowly converge, if N approaches 20. There is even an opposite trend observed in the convergence behavior, in a sense that the HFSS conductance is decreasing, whereas the EMPIRE result is increasing with N . In conclusion of this paragraph, the conductance G in Figure 3.10(d) is more sensitive as compared to the resistance R in Figure 3.10(c) and therefore the extraction of the shunt loss and the shunt efficiency requires special considerations.

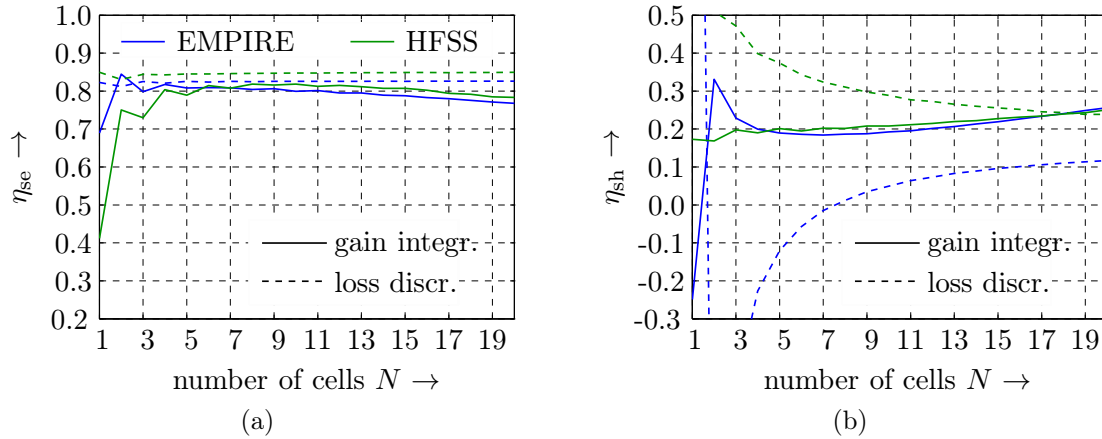


Figure 3.11: Resonator efficiencies, η_{se} and η_{sh} , comparing the two efficiency extraction methods: gain integration and loss discrimination. (a) Series efficiency with little deviation in the two methods and a good convergence for the loss discrimination method. (b) Shunt efficiency showing a larger discrepancy as in (a) and some non-physical behavior ($\eta_{sh} < 0$) for $N < 7$.

Figure 3.11 plots the series and shunt efficiencies comparing the gain integration and the loss discrimination method using EMPIRE and HFSS. For the series efficiency in Figure 3.11(a), a good agreement is observed for a cascade of $N \geq 7$ unit cells. Both extraction methods as well as both simulation tools agree on a series efficiency of around 80%. A cascade of $N = 7$ is empirically found to be a good compromise in order to apply the gain integration method [61].

Figure 3.11(b) shows the critical shunt radiation efficiency. Unfortunately, a clear convergence of the loss discrimination method (dashed lines) is not evident within the plotted range of N . Moreover, the two simulators produce different efficiency results. All in all, these results are highly questionable due to their mismatch. In contrast, the gain integration results (solid lines) fairly agree comparing EMPIRE and HFSS. Yet, there is a slight increase in the efficiencies from around 20% to 25% for N being varied from 7 to 20. This is a systematic problem, which is inherent to the gain integration method,¹⁹ where both, the extracted series and shunt efficiency, converge to the broadside efficiency η_{bs} for $N \rightarrow \infty$. Nevertheless, $\eta_{sh} \approx 20\%$ is a good approximation of the shunt efficiency, which is obtained around $N = 7$ before the values start to increase.

¹⁹ If the cascade is *too* long, two traveling waves are launched from either side under odd and even excitation. They do not form a standing wave distribution due to the leakage and the spatial separation. In other words, these traveling waves do not “see” each other and hence they individually exhibit the leaky wave broadside efficiency of $\eta = (\eta_{se} + \eta_{sh})/2$ derived in Section 3.1.6. Theoretically, if $N \rightarrow \infty$, the series and the shunt efficiencies determined by the gain integration method, approach the broadside efficiency with $\eta_{se}|_{\text{gain integr.}} \rightarrow (\eta_{se} + \eta_{sh})/2$ and $\eta_{sh}|_{\text{gain integr.}} \rightarrow (\eta_{se} + \eta_{sh})/2$, respectively. Since $\eta_{se} > \eta_{sh}$, a decreasing trend is observed for η_{se} in Figure 3.11(a), whereas an increase for η_{sh} is seen in Figure 3.11(b).

Using a cascade of multiple unit cells offers more accuracy for the parameter extraction than the evaluation of a single unit cell. Nevertheless, the results for the shunt efficiency are still unsatisfactory and a better physical understanding is required. Both are addressed next by evaluating an *infinite* cascade of unit cells using periodic boundaries.

3.4.3 Eigenmode Simulation of an Infinite Cascade using Periodic Boundaries

This method computes the LCRG parameters and the radiation efficiencies in terms of the stored energy and power loss obtained by fullwave eigenmode analysis [34, 53]. The unit cell is accurately characterized for the infinite periodic case including all electromagnetic effects. This method inherently accounts for mutual coupling between the periodic cells, and accurately determines the resistance and conductance, where particularly the accurate extraction of shunt conductance is the challenging task, as discussed before. More importantly, it provides physical insight into the radiation limitations of symmetric LWAs.

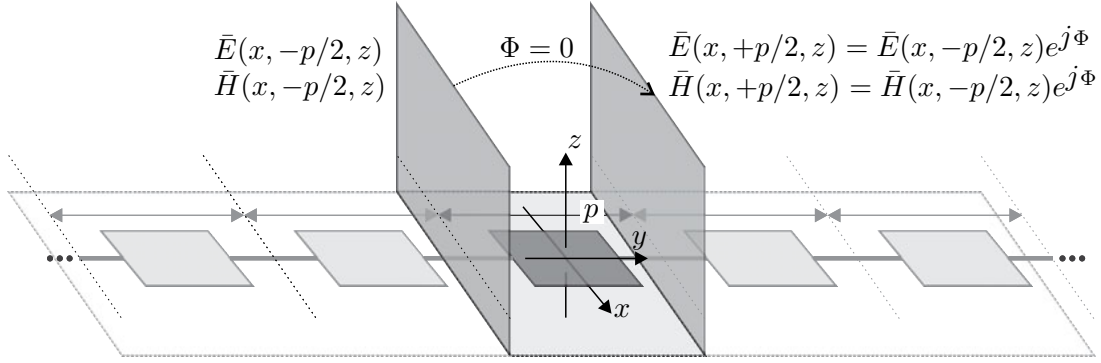


Figure 3.12: Simulation model with periodic boundaries to model the infinite cascade by accurately taking into account all mutual coupling effects. The eigenmode simulation with phase shift $\Phi = 0$ across the cell boundaries in propagation direction (y -axis) results in two modes, the series and the shunt resonance mode.

The simulation setup is illustrated in Figure 3.12, where a single unit cell is characterized using periodic boundaries at $y_{\min} = -p/2$ and $y_{\max} = +p/2$. A phase shift Φ is introduced, which links the electric and the magnetic fields on these boundaries as follows

$$\bar{E}(x, -p/2, z) = \bar{E}(x, +p/2, z)e^{j\Phi}, \quad (3.79a)$$

$$\bar{H}(x, -p/2, z) = \bar{H}(x, +p/2, z)e^{j\Phi}. \quad (3.79b)$$

For the specific case of interest, broadside radiation, the phase shift across the unit cell is zero, following that $\Phi = 0$. Equation (3.79b) simplifies to

$$\bar{E}(x, -p/2, z) = \bar{E}(x, +p/2, z), \quad (3.80a)$$

$$\bar{H}(x, -p/2, z) = \bar{H}(x, +p/2, z), \quad (3.80b)$$

showing that the electric and magnetic field distribution on either boundary side of the unit cell must be identical.

In addition, the transversal symmetry in the unit cell implies further conditions on the electric and magnetic fields on the boundaries, which are examined next. First, the two

resonance modes of interest, the anti-symmetric (odd) mode and the symmetric (even) mode are evaluated at the boundaries *without* considering the result of the periodicity in (3.80).

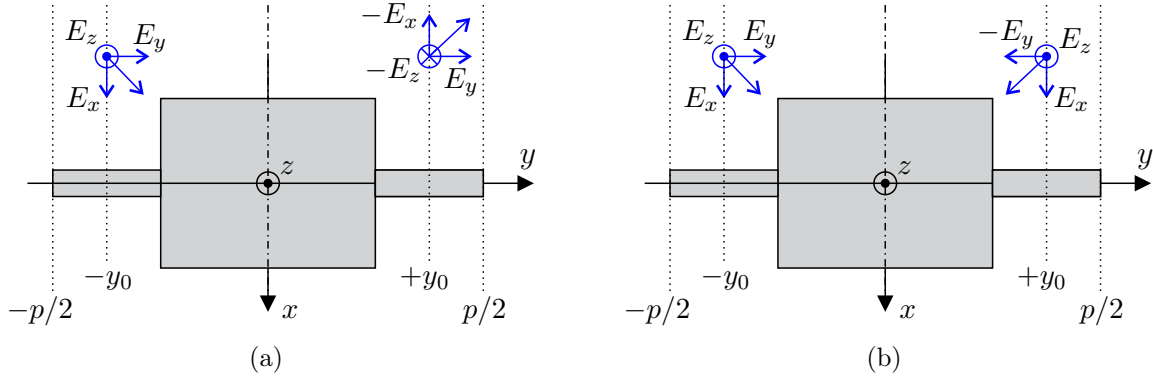


Figure 3.13: Illustration of the electric field components taking into account the structural and the vectorial field symmetry of the odd and even mode. (a) Odd mode with an anti-symmetric field distribution. (b) Even mode with a symmetric field distribution.

Figure 3.13 illustrates the electric fields, located at $\pm y_0$ as an arbitrary x - z -plane, in an exemplary manner. The three field components for the anti-symmetric mode are indicated in Figure 3.13(a) and the field components for the symmetric mode are given in Figure 3.13(b). Since these planes at $\pm y_0$ are arbitrary, they obviously include the unit cell boundaries located at $y_0 = \pm p/2$. Similar conditions can be straightforwardly derived for the magnetic field components, which is not explicitly shown in the figure. With the simple illustration of the field components in Figure 3.13, one obtains a set of general results for the conditions of the electric and the magnetic field components on the unit cell boundaries. The modal field distribution in a transversally symmetric unit cells is either symmetric or anti-symmetric with respect to the transversal axis, if the boundary condition at $y = \pm p/2$ are identical. The conditions for the Cartesian field components in Table 3.5 are purely based on symmetry and anti-symmetry considerations. Table 3.5 summaries these conditions for the electric and magnetic field components.

Table 3.5: Evaluation of the electric and magnetic fields on the cell boundaries located at $y = \pm p/2$ for the anti-symmetric mode and the symmetric mode.

anti-symmetric (odd mode)		symmetric (even mode)	
$y = -p/2$	$y = +p/2$	$y = -p/2$	$y = +p/2$
E_x	$-E_x$	E_x	E_x
E_y	E_y	E_y	$-E_y$
E_z	$-E_z$	E_z	E_z
H_x	H_x	H_x	$-H_x$
H_y	$-H_y$	H_y	H_y
H_z	H_z	H_z	$-H_z$

The periodicity with $\Phi = 0$ in Equation (3.80) and the transversal symmetry in Table 3.5 are evaluated separately so far. Both conditions must be satisfied simultaneously, which

suggests to re-evaluate Table 3.5 under the condition $\Phi = 0$. Each field component on the $y = -p/2$ boundary must be *equal* the corresponding component on the $y = +p/2$ boundary according to Equation (3.80). For this to be satisfied, all components of opposite sign in Table 3.5 must be zero.

Table 3.6 shows the final result of the electric and magnetic field components on the boundaries. For the odd mode (left column) it follows that the electric x - and z -field components are zero, $E_x = E_z = 0$, and the magnetic y -field component is zero $H_y = 0$. The tangential electric field is zero and the normal magnetic field is zero on the boundaries, corresponding to the condition of a perfect electric conductor (PEC) for the odd mode. In case of the even mode (right column), $E_y = 0$ and $H_x = H_z = 0$, implying the conditions of a perfect magnetic conductor (PMC).

Table 3.6: Evaluation of the field components in Table 3.5 under the periodic boundary condition in (3.80) with $\Phi = 0$. The x - and z -field components are tangential in the boundary plane, whereas the y -field component is normal, so that the conditions simply translate to PEC and PMC boundaries for the odd and even mode, respectively.

anti-symmetric (odd)		symmetric (even)	
$y = -p/2$	$y = +p/2$	$y = -p/2$	$y = +p/2$
PEC	PEC	PMC	PMC
$E_x = 0$	$-E_x = 0$	E_x	E_x
E_y	E_y	$E_y = 0$	$-E_y = 0$
$E_z = 0$	$-E_z = 0$	E_z	E_z
H_x	H_x	$H_x = 0$	$-H_x = 0$
$H_y = 0$	$-H_y = 0$	H_y	H_y
H_z	H_z	$H_z = 0$	$-H_z = 0$

The fact, that the series mode exhibits a PEC boundary condition and the shunt mode a PMC boundary condition, is a significant result that is impacting the radiation direction and polarization and is therefore discussed later in Section 3.5 in terms of fundamental LWA limitations.

The simulation can be simplified in a sense that *periodic boundaries* are not required and an accurate characterization is done by running two simulations, one with PEC boundaries and another one with PMC boundaries to extract the series and shunt resonator parameters, respectively. In this work, the simulation tool HFSS is employed for eigenmode analysis. As opposed to the previous drivenmode simulation, the *eigenmode* simulation does not require an excitation. It calculates the eigenmode field distribution along with the associated complex eigenfrequency²⁰

$$\Omega = \Omega_{\text{re}} + j\Omega_{\text{im}}, \quad (3.81)$$

where the real part accounts for the actual oscillation frequency and the imaginary part for the damping due to radiation and loss.

²⁰A comparison of complex propagation constant modeling versus complex frequency modeling is given later in Section 4.3.1.

Figure 3.14 shows the eigenmode simulation setup with PEC and PMC boundaries together with their corresponding equivalent resonance circuits. In the following, it is described how the series and shunt parameters and the corresponding radiation efficiencies are calculated based on stored energies and radiated/dissipated powers in the two eigenmodes.

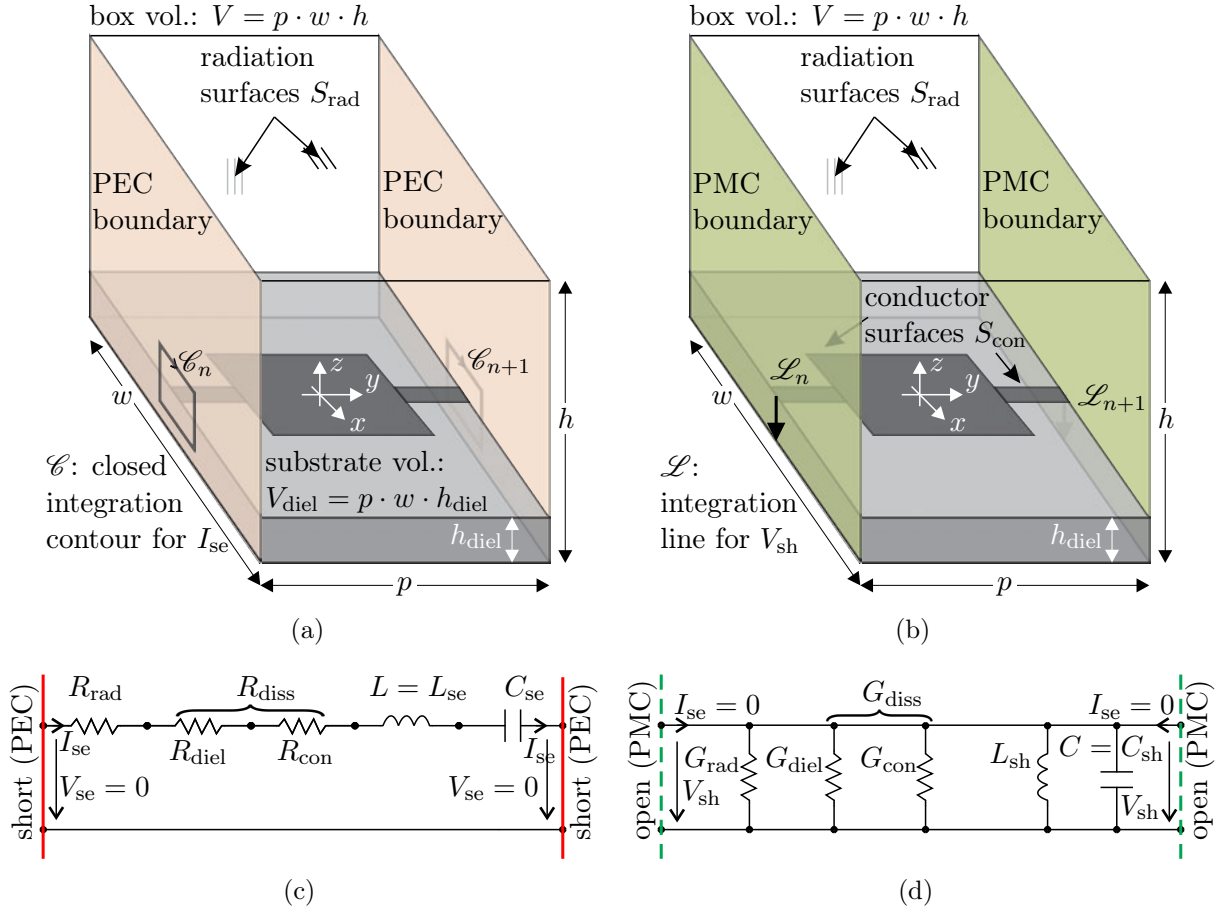


Figure 3.14: Eigenmode simulation setup for the unit cell parameter extraction using stored energy and power. (a) Simulation setup with PEC boundaries to extract the series mode parameters. (b) Setup with PMC boundaries to extract the shunt mode parameters. (c) and (d) Equivalent lattice under short circuit and open circuit condition, respectively, where the linear reactance and susceptance slopes are approximated by a LC resonator.

3.4.3.1 Extraction of L , R , ω_{se} and η_{se} with PEC Boundaries

The PEC boundary condition in Figure 3.14(a) imposes $V_n = V_{n+1} = 0$, which leads to $V_{sh} = 0$ from Equation (3.23), and hence isolates the series resonator with Z_{se} in the lattice circuit. Figure 3.14(c) shows the series resonance circuit, where an LC resonator with L_{se} and C_{sh} is introduced. The inductance L_{se} is identical to the reactance slope parameter L and the capacitance C_{sh} is calculated through the real resonance frequency. The reason to replace the linear reactance slope parameter [Section 3.1.2] by a series LC circuit is to provide a simple circuit representation with realizable elements, rather than the slightly more abstract immittance slopes. For the actual parameter extraction at the

resonance frequency, both circuit models, LC resonator and immittance slopes, deliver the same set of LCRG parameters.

The series currents I_n and I_{n+1} are computed from the electromagnetic eigenmode fields as

$$I_{se} = \oint_{\mathcal{C}_n} \bar{H} \cdot d\bar{l} = \oint_{\mathcal{C}_{n+1}} \bar{H} \cdot d\bar{l} \quad (3.82)$$

where \bar{H} is the tangential magnetic field existing on the boundaries and $\mathcal{C}_n, \mathcal{C}_{n+1}$ are the closed integration lines indicated in Figure 3.14(a). The time-average stored energies and dissipated powers for the series mode, at resonance, are subsequently determined by the following relations

$$W = W_e + W_m = 2W_m = 2W_e, \quad (3.83a)$$

$$W = 2\frac{1}{4}\mu_0 \int_V \bar{H} \cdot \bar{H}^* dv, \quad (3.83b)$$

$$P_{rad} = \frac{1}{2} \int_{S_{rad}} \text{Re} \{ \bar{E} \times \bar{H}^* \} \cdot d\bar{s}, \quad (3.83c)$$

$$P_{die} = \frac{1}{2} \int_{V_{die}} \bar{E} \cdot \bar{J}^* dv, \quad (3.83d)$$

$$P_{con} = \frac{R_s}{2} \int_{S_{con}} \bar{H}_{tan} \cdot \bar{H}_{tan}^* ds, \quad (3.83e)$$

where W and P are the energies and powers, respectively. The subscripts “e” and “m” refer to electric and magnetic quantities, respectively, while the subscripts “rad”, “die” and “con” refer to radiation, dielectric and conductor losses. Moreover, the vector quantities \bar{E} , \bar{H} and \bar{J} represent the electric field, magnetic field and current density, respectively, which are obtained by electromagnetic analysis. These vector quantities are integrated according to (3.83) over the surfaces and volume indicated in Figure 3.14(a). The overall volume is V , which includes the dielectric substrate material and the air region in between the substrate and the top radiation surface of the simulation region. The stored energy is computed in this overall volume by Equation (3.83b). The radiation surface, S_{rad} , includes the simulation boundaries at $z_{min, max}$ and $x_{min, max}$, excluding the PEC, PMC boundaries located at $y_{min, max}$. The integration of the Poynting vector (real part) on this surface allows to determine the radiated power of the respective mode according to (3.83c). By applying the calculus in Equation (3.83d), Joule’s law, one can compute the dissipation due to the losses in the dielectric substrate material, where V_{die} is the substrate volume. The metalization is modeled by an infinitely thin resistive sheet, where the tangential magnetic field and the surface resistance is sufficient to determine the conductor loss as given in Equation (3.83e). For further details of these integral equations in (3.83), the reader is referred to the text books [78, 79].

Finally, the L and R parameters are calculated from

$$\begin{aligned} L = L_{se} &= \frac{4W_m}{|I_{se}|^2}, & C_{se} &= \frac{1}{\omega_{se}^2 L_{se}}, \\ R_{rad} &= \frac{2P_{rad}}{|I_{se}|^2}, & R_{die} &= \frac{2P_{die}}{|I_{se}|^2}, & R_{con} &= \frac{2P_{con}}{|I_{se}|^2}, \\ R &= R_{rad} + R_{die} + R_{con}, \end{aligned} \quad (3.84)$$

where

$$\omega_{se} = 2\pi f_{se} = \text{Re}(\Omega_{se}) \quad (3.85)$$

is the series resonance frequency. By recalling Equation (3.5), the series radiation efficiency is then $\eta_{se} = R_{\text{rad}}/R$. Eventually, the series quality factor is given by

$$Q_{se} = \frac{\text{Re}(\Omega_{se})}{2\text{Im}(\Omega_{se})} = \frac{\text{Re}(\Omega_{se})L_{se}}{R}, \quad (3.86)$$

and can be computed, either directly through the complex eigenfrequency or through the energies and powers in (3.83).

3.4.3.2 Extraction of C , G , ω_{sh} and η_{sh} with PMC Boundaries

Similarly to the previous case, PMC boundary conditions are applied to isolate and characterize the shunt resonator. The PMC boundary condition imposes $I_n = I_{n+1} = 0$, which leads to $I_{se} = 0$ from (3.25) and hence isolates the shunt resonator, Figure 3.14(d). This corresponds to the even or shunt resonant mode, where the shunt voltages V_n and V_{n+1} are computed from the electromagnetic eigenmode as

$$V_{sh} = \int_{\mathcal{L}_n} \bar{\mathbf{E}} \cdot d\bar{\mathbf{l}} = \int_{\mathcal{L}_{n+1}} \bar{\mathbf{E}} \cdot d\bar{\mathbf{l}}, \quad (3.87)$$

where $\bar{\mathbf{E}}$ is the electric field existing on the PMC boundaries and \mathcal{L}_n , \mathcal{L}_{n+1} are the integration lines as indicated in Figure 3.14(c).

Using the energy and power relations in Equation (3.83), one then determines the shunt parameters as follows

$$\begin{aligned} C = C_{sh} &= \frac{4W_e}{|V_{sh}|^2}, & L_{sh} &= \frac{1}{\omega_{sh}^2 C_{sh}}, \\ G_{\text{rad}} &= \frac{2P_{\text{rad}}}{|V_{sh}|^2}, & G_{\text{die}} &= \frac{2P_{\text{die}}}{|V_{sh}|^2}, & G_{\text{con}} &= \frac{2P_{\text{con}}}{|V_{sh}|^2} \\ G &= G_{\text{rad}} + G_{\text{die}} + G_{\text{con}}, \end{aligned} \quad (3.88)$$

where

$$\omega_{sh} = 2\pi f_{sh} = \text{Re}(\Omega_{sh}) \quad (3.89)$$

is the shunt resonance frequency. The shunt radiation efficiency, $\eta_{sh} = G_{\text{rad}}/G$, is then obtained by (3.11), and the shunt quality factor is given by

$$Q_{sh} = \frac{\text{Re}(\Omega_{sh})}{2\text{Im}(\Omega_{sh})} = \frac{\text{Re}(\Omega_{sh})C_{sh}}{G}. \quad (3.90)$$

The numerical evaluation of the integral equations in (3.82), (3.83) and (3.87) is conveniently accomplished using the *field calculator*²¹ in HFSS, which provides a simple interface to specify them. Nevertheless, the general parameter extraction method is not

²¹The field calculator in HFSS provides an simple interface to perform complex linear algebraic computations on the simulated vector field data [101].

restricted to a particular eigenmode solver and can therefore be adapted to other simulation tools if required.

The derivation of the simulation scheme in this section provides important insight into the series and shunt radiation mechanisms, since it sheds light on the mutual coupling and the resulting boundary conditions. Both are not provided by the drivenmode simulation procedures in Section 3.4.1 and 3.4.2, where even a cascade of multiple cells is investigated. The impact of the PEC and PMC boundary condition on the overall LWA radiation is studied next, pointing out fundamental limitations.

3.5 Fundamental Broadside Radiation and Efficiency Limitations

From the previous Section 3.4.3 it is found that the series resonance mode sees PEC boundaries, whereas the shunt mode sees PMC boundaries at $y = \pm p/2$. Figure 3.15 is given to provide an alternative point of view and to illustrate the boundary condition from a different odd/even excitation perspective. First, an artificial spacing, $\Delta d > 0$, is introduced, so that in all unit cells the odd and even resonance modes can be simultaneously ($\Phi = 0$) excited as shown in Figure 3.15(a) and Figure 3.15(b), respectively. Under this excitation, the resulting fields on the planes between the unit cells exhibit PEC and PMC boundary conditions. If next, the spacing Δd is reduced to zero, one obtains the eigenoscillation of the original structure by forcing the excitation to zero, which corresponds to the previous eigenmode case. It might be worth mentioning, that the ideal voltage and current sources *circuit-wise* correspond to the PEC and PMC boundaries, with the ideal voltage source providing an internal short and the current source an internal open.

3.5.1 Series and Shunt Radiation Direction and Polarization

Before starting the evaluation and the discussion of the series and shunt radiation properties, it is important to point out that the excitation in Figure 3.15 is not the operational mode of the LWA. The setup in Figure 3.15 mainly serves to decompose radiation contributions into series and shunt. For the overall LWA radiation, they must be re-combined through the lattice equivalent circuit model.

The farfield characteristic is evaluated next, where only the x - z -plane is of interest. The radiation in y - z -plane is a perfect plane wave due to the infiniteness, which results in a dirac radiation pattern.²² Figure 3.16 shows the normalized gain pattern for the SFP example in the x - z -plane using an infinite ground. While the series mode radiates into broadside direction in Figure 3.16(a), the shunt mode exhibits a null in broadside direction as shown in Figure 3.16(b). Despite the fact, that the results are given only for the SFP example, the following *general* statements regarding the evaluation of series and shunt radiation using the infinite array in Figure 3.15 are made.

²²This is a theoretical case, since all practical LWAs have a certain beamwidth due to a non-zero leakage constant. However, the series and shunt radiation patterns in transversal direction [Figure 3.16] are, based on their definition, independent of the leakage constant and the pattern shape in the scanning plane.

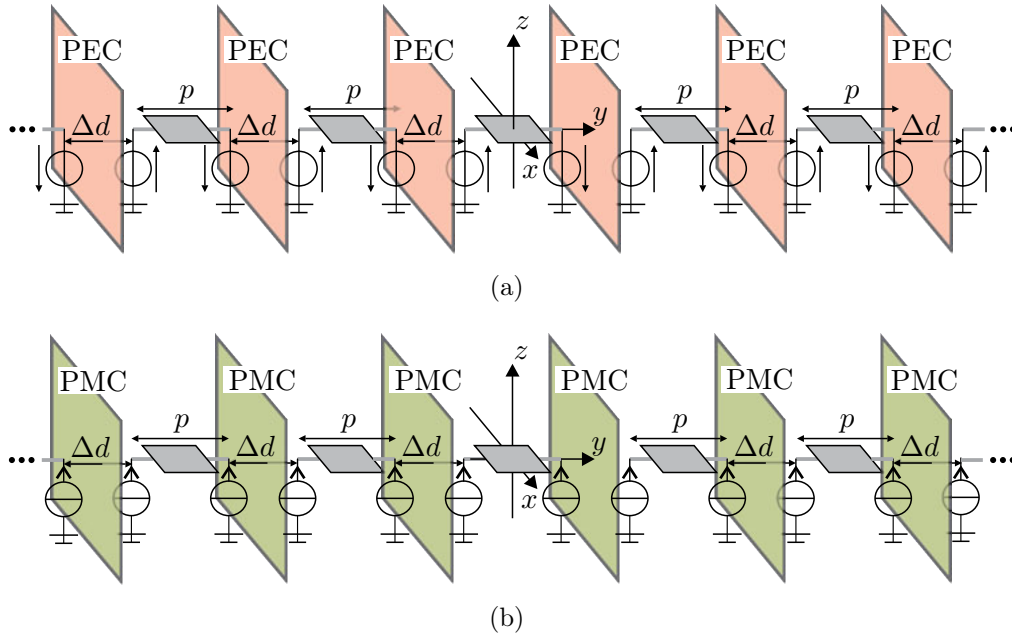


Figure 3.15: Infinite cascade of unit cells with excitation sources for the evaluation of series and shunt radiation. Artificial introduction of spacing Δd , which in the limit, $\Delta d \rightarrow 0$, forms the LWA with period p . All unit cells are uniformly excited with zero phase progression (broadside condition $\beta = 0$). (a) Odd excitation (series radiation) of the array, where the electric field on the planes between two cells (red faces) exhibits the condition of a PEC wall. (b) Even excitation (shunt radiation) of the array, where the magnetic field on the planes between two cells (green faces) exhibits the condition of a PMC wall.

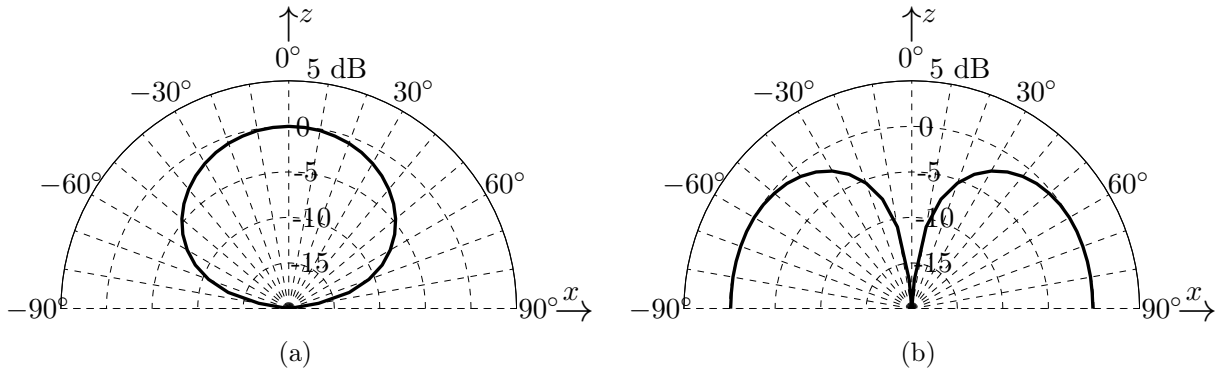


Figure 3.16: Normalized gain patterns over the angle ϑ in the $x-z$ plane (transverse to the propagation direction) for the SFP example. (a) Series radiation with maximum at broadside, cancellation in the $\pm x$ -direction and electric field polarization in φ -direction (y -direction). (b) Shunt radiation with radiation null at broadside, radiation in the $\pm x$ -direction and electric field polarization in ϑ -direction.

The farfield polarizations in the $x-z$ -plane are derived from Figure 3.15. For the series radiation setup in Figure 3.15(a), the *electric farfield* is solely polarized in y -direction to satisfy the PEC boundary condition, which, in terms of spherical coordinates, corresponds to E_φ . For the shunt radiation in Figure 3.15(b), on the other hand, the *magnetic farfield* is polarized solely in y -direction to satisfy the PMC boundary condition. As a result, the electric farfield for the shunt mode is polarized in the $x-z$ -plane, which translates to a E_ϑ farfield component in spherical coordinates.

The radiation directions for the series and shunt resonators are summarized as follows. Both modes only radiate into the x - z -plane, due to the PEC and PMC boundaries at $y = \pm p/2$, which prevent radiation in the $\pm y$ -direction. The series mode has a maximum in broadside and a null in $\pm x$ -direction, which is due to the polarization of the electric field E_φ , that is not supported by the infinite ground plane. The shunt mode has a null in broadside direction and, moreover, the infinite ground plane supports the E_θ farfield component being radiated to $\pm x$ -direction.

3.5.2 Limitation of the Radiation Efficiency to 50% Maximum

The shunt radiation in the LWA is more of a parasitic effect that does not contribute to broadside radiation. The efficiency of the shunt resonator is therefore poor, as already discussed in Section 3.4.2. Now, an aspect of major practical relevance is addressed by particularly investigating the shunt radiation of an array of uniformly driven LWA antenna lines as shown in Figure 3.17(a). A single LWA line is infinitely repeated with spacing w so to form a 2D-array antenna. Assuming that each LWA line is excited with same amplitude and phase, namely uniformly, one can simplify the model and introduce PMC boundaries in the middle between the LWA lines, located at $x = \pm w/2$, as indicated in Figure 3.17(b).

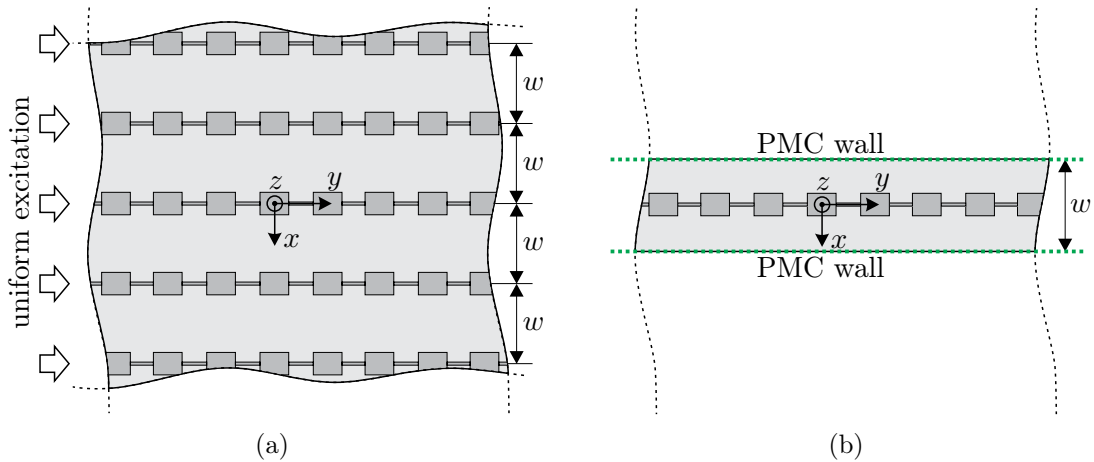


Figure 3.17: Array configuration in transverse direction of uniformly excited LWAs with spacing w . (a) Infinite model in transverse direction. (b) Equivalent single LWA simulation model with PMC side walls.

Figure 3.18 shows the boundary conditions to evaluate the series and shunt radiation in the 2D array. Radiation into the $\pm x$ -direction is fully suppressed by the PMC boundaries from the array configuration, so that radiation is only possible in positive z -direction, which is broadside. The boundary conditions for the series mode in Figure 3.18(a) allow broadside radiation, whereas for the shunt mode in Figure 3.18(b) radiation is totally prohibited, due to the four surrounding PMC walls. Since the shunt mode does not radiate at all, the shunt efficiency is zero, $\eta_{\text{sh}} = 0$. By recalling the broadside efficiency in Equation (3.41), $\eta = (\eta_{\text{se}} + \eta_{\text{sh}})/2 = \eta_{\text{se}}/2$, it is obvious that a fundamental efficiency limitation of 50% exists, independent of the series and shunt losses.

In the theoretical case of a lossless LWA array, where $G_{\text{diss}} = 0$, an efficiency of 100% is correctly expected. In this scenario, the shunt conductance $G = G_{\text{rad}} + G_{\text{diss}}$ is zero,

because the shunt radiation is fully suppressed with $G_{\text{rad}} = 0$. Such an LWA array has an infinite Bloch impedance $Z_B^+ = \sqrt{R/G}$ and hence an infinite input impedance at broadside that prevents the LWA array to accept and radiate power, even though the theoretical efficiency is 100%. A lossy LWA array according to Figure 3.17(a) has always a finite Bloch impedance, accepts power and radiates with an efficiency of $\eta = \eta_{\text{se}}/2 \leq 50\%$.

All analysis is presented for the infinite case, which might appear, at a first glance, to be far away from practical realizations. In fact, only a small number of LWA lines in the array (around four) is required to severely lower the shunt efficiency in an array. Therefore, despite all theoretical assumptions, the 50% efficiency limitation practically exists in 2D LWA arrays.

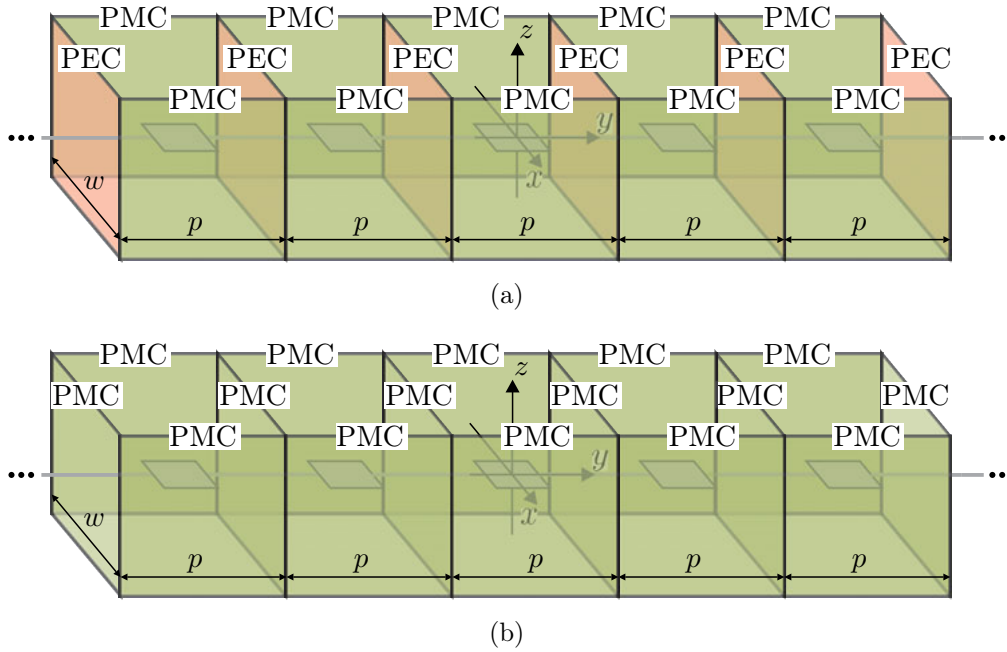


Figure 3.18: Boundary conditions for series and shunt radiation considering the infinite array in Figure 3.17. (a) Series radiation, where the PEC/PMC boundaries only support broadside radiation with electric field polarization in y -direction. (b) Shunt radiation is totally eliminated by the four enclosing PMC boundaries following that $\eta_{\text{sh}} = 0$ and $\eta \leq 50\%$ in an infinite array.

3.6 Case Study LWAs for Model Validation

This section provides two case study LWAs to validate the proposed modeling and resulting radiation efficiency formulas. These antennas are, the SFP LWA [25, 102], which was used for illustration throughout this chapter, and a CRLH LWA [26, 30]. Note that both, the SFP and CRLH structures, could operate as resonant or standing-wave antennas, if they were terminated by an open or a short circuit. However, here they are terminated by a matched load, and therefore they operate in the leaky-wave regime, where they radiate as leaky-wave antennas. The choice of the SFP and CRLH LWAs is somewhat arbitrary and the proposed approach applies to the broad class of LWAs as discussed in Section 2.4. As shown in [34], all LWAs share qualitatively similar properties, although they may exhibit quantitatively different responses in terms of frequency scanning sensitivity and scanning range. Both case study LWAs are designed for a broadside frequency

of 24 GHz. This frequency is convenient to build physically small and electrically long LWA prototypes. The electrical length is important to ensure that nearly all power is leaked out before reaching the termination side.

3.6.1 Series-Fed Patch LWAs

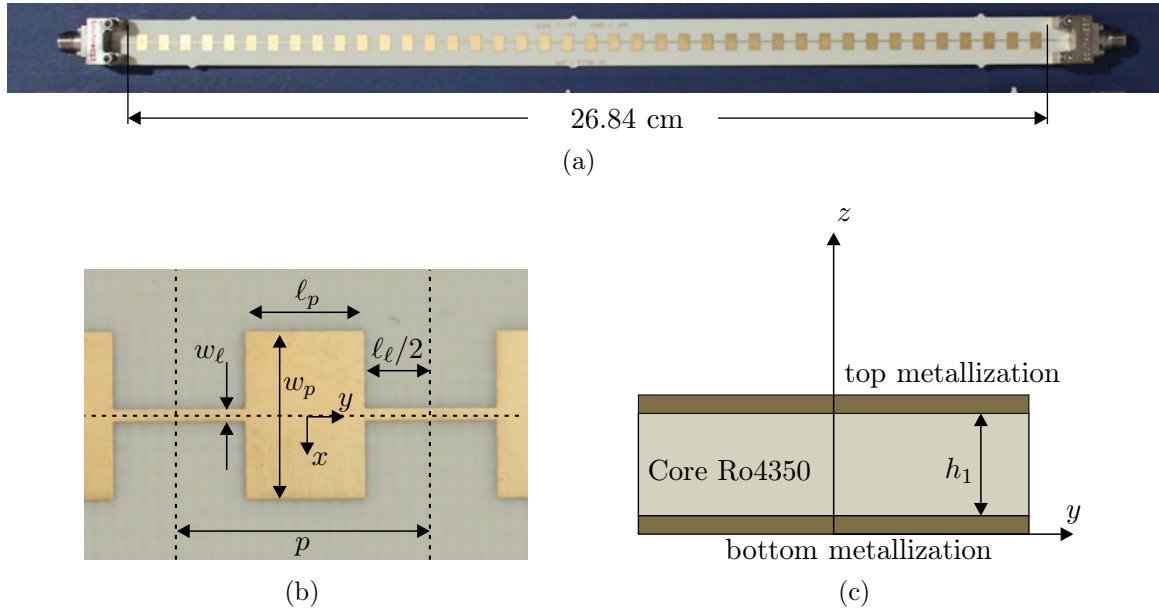


Figure 3.19: SFP LWA with 40 cascaded unit cells. (a) Overall SFP LWA with end launch connectors. (b) Zoomed top view of the SFP unit cell with geometry definitions. The dimensions are $l_p = 3.1$ mm, $w_p = 3.3$ mm, $l_l = 3.6$ mm, $w_l = 0.3$ mm, $p = 6.7$ mm. (c) Stack-up with $h_1 = 500$ μ m.

Figure 3.19 shows the considered SFP LWA, where in Figure 3.19(a) the overall SFP LWA composed of 40 unit cells is shown. The physical length of the aperture is 26.84 cm, which corresponds to an electrical length of approximately $22 \lambda_0$, where λ_0 is the free-space wavelength. The dimensions of the patch element and the transmission line are given in Figure 3.19(b).

The dispersion diagram and the Bloch impedance plot in Figure 3.20 compare the LCRG modeling with the actual frequency behavior. The drivenmode analysis is chosen over the eigenmode analysis here, since the eigenmode analysis evaluates only a single frequency point and does not provide any frequency behavior of the immittance Z_{se} and Y_{sh} . A cascade of 10 unit cells is considered in HFSS to take into account the coupling effects, and the procedure described in Section 3.4.2 is used to find the two-port parameters of the single unit cell. Finally, the frequency-dependent immittances are calculated from (3.2). The solid lines in Figure 3.20 show the actual frequency behavior of the SFP unit cell. The dashed lines show the dispersion and the impedance of the LCRG model, where the immittance Z_{se} and Y_{sh} are linearized according to the procedure described in Section 3.1.2.

Comparing the approximation nature of the LCRG model for the dispersion in Figure 3.20(a) and for the impedance in Figure 3.20(b), one observes a perfect agreement at the broadside frequency of 24 GHz and a reasonably good approximation of around 10%

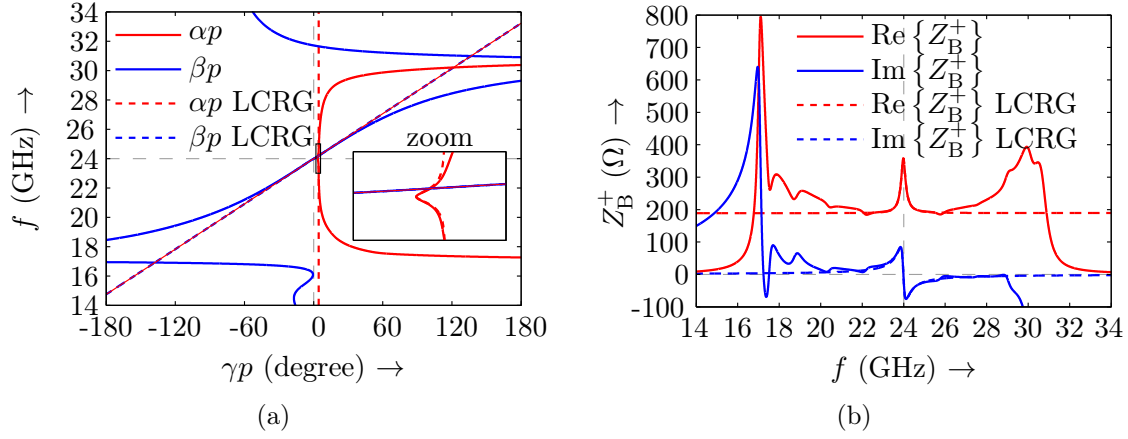


Figure 3.20: Simulated dispersion diagram and Bloch impedance of the SFP LWA showing the approximation capability of the LCRG modeling. The solid lines are directly obtained from simulated two-port data through Equations (3.2), (3.16) and (3.30). The dashed lines correspond to the LCRG model, where a good agreement up to a bandwidth of 8 GHz is observed. (a) Dispersion diagram. (b) Bloch impedance.

deviation up to a frequency bandwidth of 8 GHz, that is centered around broadside. For a larger frequency range than 8 GHz the model is not capturing the behavior of the SFP unit cell. It is obvious that for different LWA type the approximation accuracy of the LCRG model varies. The SFP can be seen as a worst-case example as compared to quasi lumped element LWA implementation (CRLH) radiating in the fundamental β_0 space harmonic. The fact that the structure is electrically large introduced a larger frequency selectivity, which is not captured by the LCRG model.

In Figure 3.21 the S-parameters of the 40 cell LWA are plotted. Figure 3.21(a) shows the measured S-parameters of the prototype in Figure 3.21(a) based on a 50Ω reference impedance, where end launch connectors are employed to access the microstrip transmission line. The SFP LWA has an off-broadside Bloch impedance of around 200Ω and hence a poor matching is observed in Figure 3.21(a), where the S-parameter reference is 50Ω . The transmission parameter $|S_{21}|$ is less than -25 dB so that the remaining power at the termination side of the LWA can practically be neglected. Nevertheless, the parameter

$$|S_{01}|^2 = 1 - |S_{11}|^2 - |S_{21}|^2 \quad (3.91)$$

is defined to account for the reflected power and the power transmitted to the load at the termination side. If $|S_{01}|^2$ is equal to 0 dB, all power is accepted by the LWA and radiated or dissipated. If $|S_{01}|^2$ approaches $-\infty$ dB, all power is either reflected or transmitted without being radiated or dissipated in the LWA. This quantity is required to correct the measured *realized gain* G_{realized} for the reflected and the transmitted powers to finally determine the *antenna gain* [1],

$$G = \frac{G_{\text{realized}}}{|S_{01}|^2}. \quad (3.92)$$

Figure 3.21(b) shows the simulated S-parameter based on a reference impedance of 200Ω , which corresponds to the off-broadside Bloch impedance, as can be confirmed in Figure 3.20(b). The S-parameter reference plane in the simulator is the unit cell interface of the first and last cell. This allows to evaluate the de-embedded S-parameters of the SFP LWA without the effects of the transition and the end launch connectors.

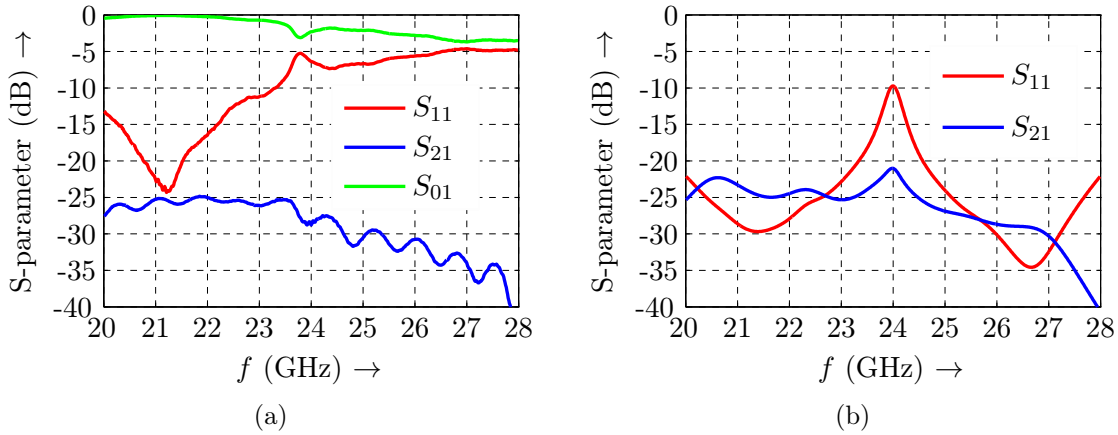


Figure 3.21: Scattering parameters of the SFP LWA with $w_p = 3.3$ mm. (a) Measured S-parameters with end launch connectors [Figure 3.19(a)] based on 50Ω reference impedance. The parameter $|S_{01}|$ shows the power loss due to reflection and transmission according to Equation (3.91). (b) Simulated S-parameters measured at the unit cell interface with reference impedance $Z_{B,\text{off-bs}}^+ \approx 200 \Omega$.

The anechoic chamber at IMST GmbH together the farfield measurement setup is shown in Figure 3.22, where the LWA is mounted on a dielectric-belt-driven-rotator, which is placed on an azimuth positing system. This coordinate system is referred to as *roll-over-azimuth-axes*, which is a common setup used for the farfield characterization of antennas. The system is calibrated with a standard gain horn antenna of well-known gain, so to determine the gain of the antenna under test by comparison.

Figure 3.22(b) shows the LWA under test, which is excited from one side, whereas the other side is terminated with a 50Ω load. The antenna is surrounded by absorbers, which reduces ripples in the radiation patterns particularly at lower gain levels. Generally, such absorbers slightly reduce the efficiency, but they have a negligible effect on the main beam characteristics.

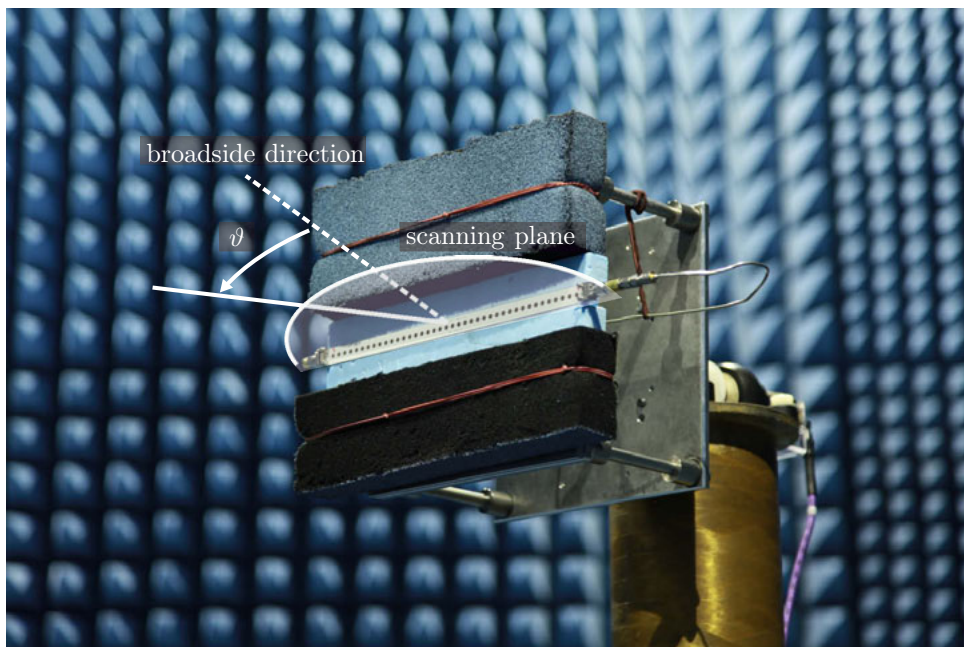
For a frequency range from 22 to 26 GHz the gain patterns are measured and plotted over the azimuth angle ϑ in Figure 3.23(a). As expected, the LWA scans with frequency through the broadside direction, where it radiates exactly broadside ($\vartheta = 0$) at $f = 23.75$ GHz. This frequency deviates from the design frequency 24 GHz, due to fabrication tolerances. A clear broadside degradation is observed in Figure 3.23(a) of approximately 2.5 dB as compared to off-broadside, where the realized gain exhibits a rather constant level for frequencies different than $f = 23.75$ GHz. The *realized gain* is measured including the power losses due to reflection and transmission. The realized gain is therefore corrected by using Equation (3.92), so to determine the *antenna gain* independent of the mismatch and the remaining power in the load at the termination side. Measured and simulated antenna gain are given in Figure 3.23(b) and they show an excellent agreement, also considering the fact that an absolute measurement uncertainty of approximate 0.5 dB exists.

For a quantitative evaluation of the pattern characteristics, Table 3.7 lists the frequency, main beam direction ϑ_{mb} , maximum gain and half power beamwidth (HPBW). The main beam direction ϑ_{mb} is the independent parameter in Table 3.7, showing that a frequency shift of 250 MHz between simulation and measurement for all frequencies exists, which is due to fabrication tolerances, as mentioned before. As consequence, the measured

data is compared to the simulated data with a 250 MHz offset. Two dominate effects can be observed in Table 3.7. The gain and the HPBW are both minimal at broadside, which is supported by the measurement and simulation results. The gain degradation is explained with the broadside efficiency degradation. The HPBW decrease is explained through the minimum of the leakage constant α at broadside, see Figure 3.20, which increases the effective antenna aperture length and therefore lowers the beamwidth. It is worth mentioning that these two effects have an opposite impact on the gain. While the efficiency decrease obviously lowers the gain, the increase in the effective aperture length increases the gain. Eventually, this is the reason why the *radiation efficiency* is preferred to *antenna gain* as figure of merit of LWAs throughout this thesis.



(a)



(b)

Figure 3.22: Anechoic chamber and farfield measurement setup at IMST GmbH. (a) Positioning system with azimuth and roll axis for a full characterization of the antenna under test. (b) Zoomed view of the antenna under test, the SFP LWA, where the antenna gain is measured in azimuth plane (scanning plane).

The simulation of the overall radiation efficiency is a straightforward task, whereas the

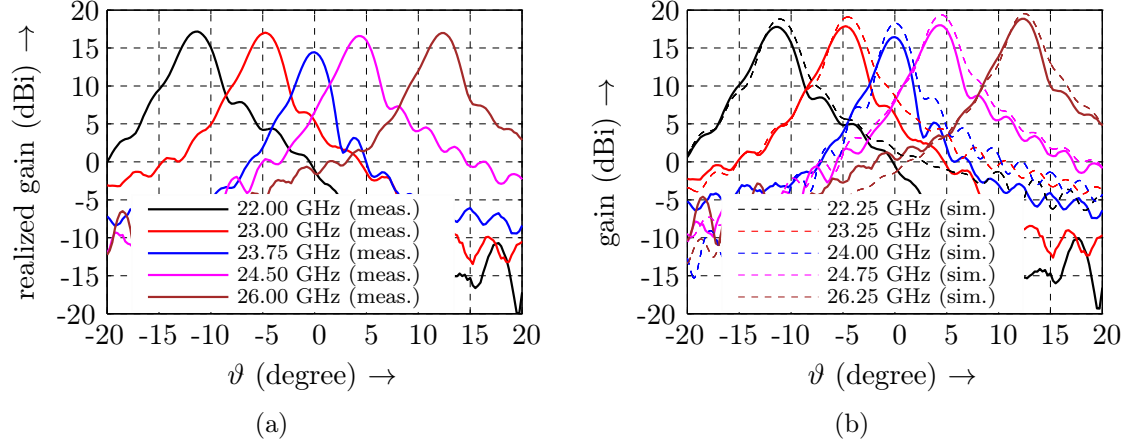


Figure 3.23: Realized gain and antenna gain patterns in the azimuth plane (y - z) for various frequencies. (a) Realized gain (measured) including the mismatch of the SFP LWA to the 50Ω reference impedance. (b) Antenna gain, obtained from measured realized gain corrected by the mismatch and the transmission loss according to Equation (3.92) (solid lines), and simulated antenna gain (dashed lines).

Table 3.7: Comparison of the measured and simulated gain patterns plotted in Figure 3.23(b).

freq. (GHz)		ϑ_{mb} ($^\circ$)		G (dBi)		HPBW ($^\circ$)	
meas.	sim.	meas.	sim.	meas.	sim.	meas.	sim.
22.00	22.25	-11.25	-11.10	17.78	18.81	3.37	3.25
23.00	23.25	-4.75	-4.50	17.87	19.08	3.13	3.13
23.75	24.00	0.00	0.05	16.44	18.26	2.77	2.62
24.50	24.75	4.25	4.50	18.00	19.37	3.06	2.99
26.00	26.25	12.25	12.50	18.85	19.53	3.05	3.02

complete three-dimensional farfield measurement of the LWA under test is extremely time consuming, if the angular steps are sufficiently small to properly resolve the small beamwidth. For an accurate efficiency measurement, an angular increment of approximately 0.2° would have been required, resulting in a measurement time of more than one week. For this reason, it was decided to use a coarser angular resolution of 1° for both, azimuth and roll axis, to measure the LWA, which resulted in a measurement time of one single day. Therefore, the efficiency measurement results need to be carefully interpreted, as they may be inaccurate from the under-sampling. Fullwave simulation mends this deficiency and allows to accurately calculate the radiation efficiencies with a reasonable effort. Moreover, by means of two *independent* fullwave simulation techniques, EMPIRE XPU (FDTD) and HFSS (FEM), it is possible to mutually validate the results and to verify the proposed circuit modeling.

Figure 3.24 compares the measured and simulated radiation efficiencies of the 40-cell SFP LWA of Figure 3.19, where all the plotted curves are corrected for the reflected and transmitted powers [Equation (3.91)]. Both fullwave simulation tools provide direct access to the radiation efficiency, which are internally computed from the integration of the Poynting vector divided by the accepted power. The measured efficiency is obtained from numerical gain integration over the entire sphere.

Figure 3.24(a) shows the results for the single LWA, and Figure 3.24(b) shows the results for the uniform infinite array with PMC walls, as discussed in Section 3.5.2. Generally,

both figures confirm a strong efficiency drop at the broadside frequency of 24 GHz, where the FDTD results from EMPIRE and the FEM results from HFSS are in a good agreement and show a very similar frequency characteristic. The LCRG parameter and the radiation efficiency are extracted using the scheme in Section 3.4.3, and they are listed in Table 3.8. The curve labeled unit cell LCRG model in Figure 3.24, shows the unit cell efficiency [Equation (3.37)] of the circuit model, where the extracted LCRG parameters and the efficiency are listed in Table 3.8. The asymptotic at- and off-broadside efficiencies from Equations (3.41) and (3.44) are also plotted to indicate the fast convergence from the at- to the off-broadside regime.

The efficiency limitation of 50% in the uniformly excited infinite array case is confirmed in Figure 3.24(b), where no measured efficiency is provided, due to the infinite extent of the structure. The measurement of the single LWA in Figure 3.24(a) shows a constant offset, but still follows the trend of the simulations. The reasons for this discrepancy might be the following. A first possible reason is the under-sampling of the measured gain, as previously discussed. Another possible reason might be the metalization and dielectric losses of the substrate material Rogers 4350. At 24 GHz these losses are increased as compared to the ones at 10 GHz, which are provided in the data sheet.

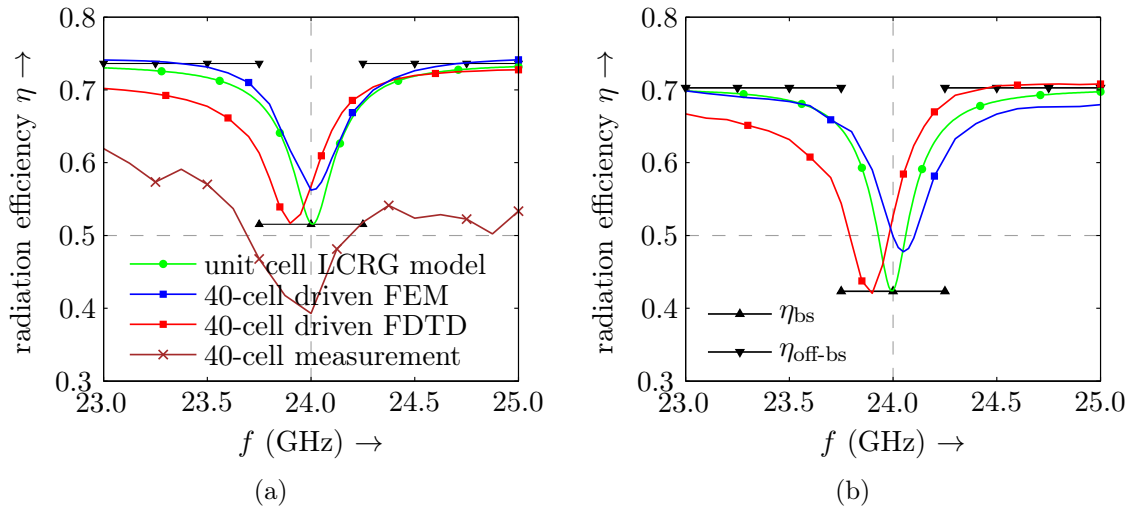


Figure 3.24: Measured and simulated radiation efficiencies of the 40-cell SFP LWA with patch width $w_p = 3.3$ mm. The LCRG model is compared and validated by measurement and by two independent drivenmode simulations (FEM and FDTD). (a) SFP LWA in Figure 3.19. (b) SFP LWA in a uniformly excited array (PMC side walls) according to Figure 3.17, confirming the broadside efficiency limitation of maximal 50%.

In addition, Table 3.8 provides LCRG values and the series and shunt efficiencies for a variation of the patch width w_p . While the series efficiency undergoes only a small increase (77% to 93%), the shunt radiation efficiency strongly increases from 3% to 84% when the patch is varied from 2.3 mm to 5.3 mm. By increasing the patch width, the shunt radiation, which is directed to $\pm x$ -direction, is increased. It is worth mentioning that the shunt radiation contribution does *not* radiate broadside, and it is of orthogonal farfield polarization. Despite the fact that this LWA has an overall broadside efficiency of 88% (column 3), it basically radiates half the power into the “wrong” direction with the “wrong” polarization. Moreover, if it is used in a uniformly excited array, PMC boundaries apply and the shunt radiation is totally suppressed as shown in Table 3.8 under column

4 and 5, where η_{sh} is zero.

The experimental and numerical simulation results in Figure 3.24 and in Table 3.8 verify the proposed LCRG modeling and the derived efficiency formulas based on the SFP case study example. A CRLH LWA as a second example is provided next to further verify the modeling.

Table 3.8: LCRG parameters, quality factor and efficiency results obtained by fullwave eigenmode extraction computed by Equations (3.84) and (3.88). The patch width w_p is varied in three steps showing strong impact on the shunt radiation efficiency η_{sh} . The total suppression of shunt radiation, $\eta_{\text{sh}} = 0$, is confirmed in the infinite array case (PMC), Figure 3.18.

w_p, w_ℓ (mm)	SFP, Figure 3.19					CRLH, Figure 3.25	
	PML			PMC		PML	PMC
	2.3	3.3	5.3	3.3	5.3	0.7	0.7
column no.	1	2	3	4	5	6	7
L_{se} (nH)	4.21	5.58	6.92	5.38	7.72	0.54	0.56
C_{se} (fF)	10.43	7.86	6.35	8.19	5.69	81.28	77.98
R (Ω)	11.32	23.15	53.60	20.18	60.61	2.86	2.43
R_{rad} (Ω)	8.67	19.91	49.79	17.05	56.59	2.54	2.06
R_{die} (Ω)	2.26	2.95	3.49	2.85	3.87	0.28	0.29
R_{con} (Ω)	0.39	0.29	0.32	0.28	0.16	0.05	0.07
C_{sh} (fF)	135.03	128.91	196.17	130.71	212.46	326.55	328.12
L_{sh} (pH)	0.33	0.34	0.22	0.34	0.21	0.14	0.13
G (μS)	106.67	117.06	767.81	99.54	139.51	338.87	277.18
G_{rad} (μS)	3.64	20.01	641.76	0.20	0.10	62.81	0.01
G_{die} (μS)	72.24	68.57	101.12	69.51	108.91	191.55	192.19
G_{con} (μS)	30.78	28.49	24.93	29.84	30.50	84.52	84.98
f_{se} (GHz)	24.01	24.02	24.01	23.99	24.03	23.96	24.00
f_{sh} (GHz)	24.01	24.01	24.02	23.99	24.02	23.96	23.97
Q_{se}	56.11	36.41	19.49	40.17	19.22	28.56	35.00
Q_{sh}	190.97	166.12	38.56	197.98	229.86	145.10	178.31
η_{se}	0.77	0.86	0.93	0.84	0.93	0.89	0.85
η_{sh}	0.03	0.17	0.84	0.00	0.00	0.19	0.00
η_{bs}	0.40	0.52	0.88	0.42	0.47	0.54	0.42
$\eta_{\text{off-bs}}$	0.60	0.74	0.90	0.70	0.86	0.77	0.71

3.6.2 Composite Right/Left-Handed LWAs

Figure 3.25(a) shows the considered CRLH LWA which is composed of 60 unit cells and is approximately $11\lambda_0$ long, where λ_0 is the free-space wavelength. In Figure 3.25(b) a zoomed view of the unit cell with dimensions is provided and Figure 3.25(c) shows the corresponding stack-up. It is a multilayer planar structure including stub inductors and metal-insulator-metal (MIM) series capacitors [103–105]. The period is much smaller than the guided wavelength ($p = \ell_\ell < \lambda_g/4$), as the structure operates in an effective metamaterial frequency range [31]. The unit cell is fully symmetric as shown in Figure 3.25(b) and comprises two identical stubs of length $\ell_s \approx \lambda_g/4$, where λ_g is the guided wavelength of the microstrip line. Both stubs are symmetrically placed with respect to the axis of the structure and each terminated by a shorting via to provide a parallel LC resonator.

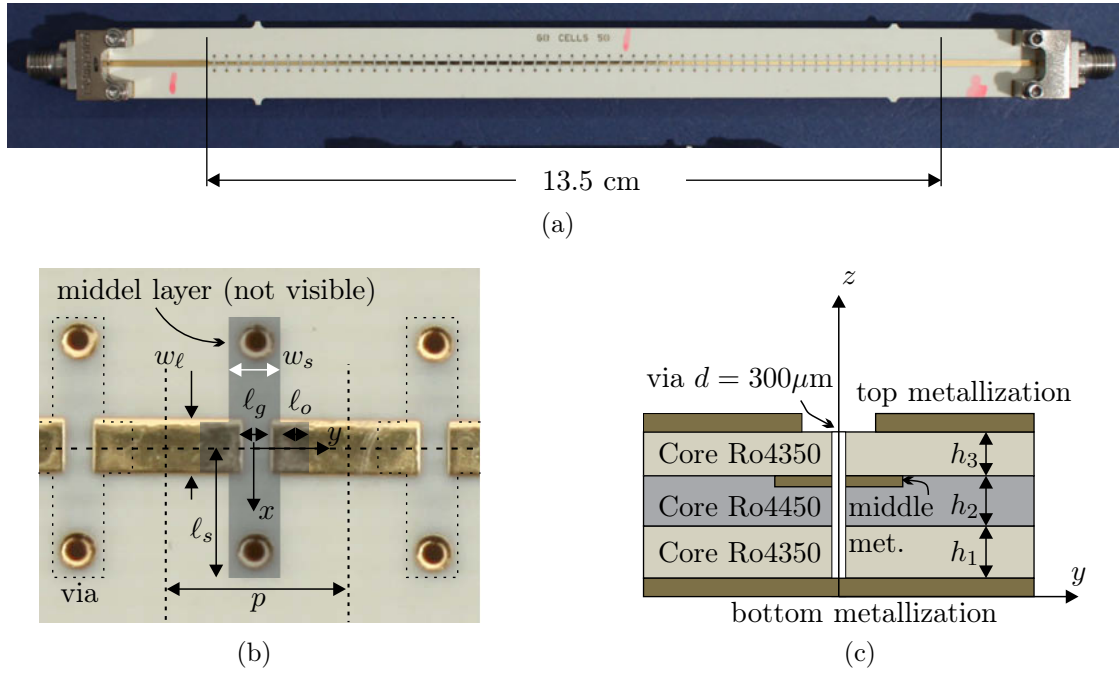


Figure 3.25: CRLH LWA with 60 cascaded unit cells. (a) Overall CRLH LWA with end launch connectors. (b) Zoomed top view of the CRLH unit cell with geometry definitions. (c) Stack-up.

For the CRLH LWA, no parametric study is made and the LCRG values together with the series and shunt efficiencies are listed in Table 3.8 under column 6 and 7. The CRLH LWA is optimized for a broadside frequency of 24 GHz. By properly adjusting the MIM gap by the parameter ℓ_g and the stub length ℓ_s , the series and shunt resonance frequencies are tuned to 24 GHz, respectively. The series efficiency is 89%, whereas the shunt efficiency is 19%, clearly showing that the symmetric CRLH LWA exhibits almost identical characteristics as the SFP with $w_p = 3.3$ mm. In the array case, shown under column 7 in Table 3.8, the shunt efficiency drops to zero as expected. Figure 3.26 shows the measured and simulated radiation efficiencies comparing the LCRG model with efficiencies of the 60-cell LWA. The agreement of the LCRG model is not so good as compared to the SFP example, particularly at off-broadside frequencies. Nevertheless, the broadside degradation at 24 GHz is confirmed in Figure 3.26(a). Furthermore, the 50% efficiency limit for the infinite CRLH array is verified in Figure 3.26(b). The reason for the deviation at off-broadside frequencies might be the small period of the unit cell, which results in a larger scanning sensitivity with frequency [34]. As a result from the larger scanning sensitivity with frequency, the LCRG parameters and the series and shunt efficiencies may also vary with frequency, whereas they are expected to be constant in the modeling. The measured efficiency shows a larger discrepancy with unsatisfactory results when compared to the simulation, which is due to the two reasons already addressed in the SFP case. Nevertheless, the fact that measurement and simulation show the efficiency drop at broadside, is a clear indication that the fully symmetric CRLH prototype suffers from the broadside degradation.

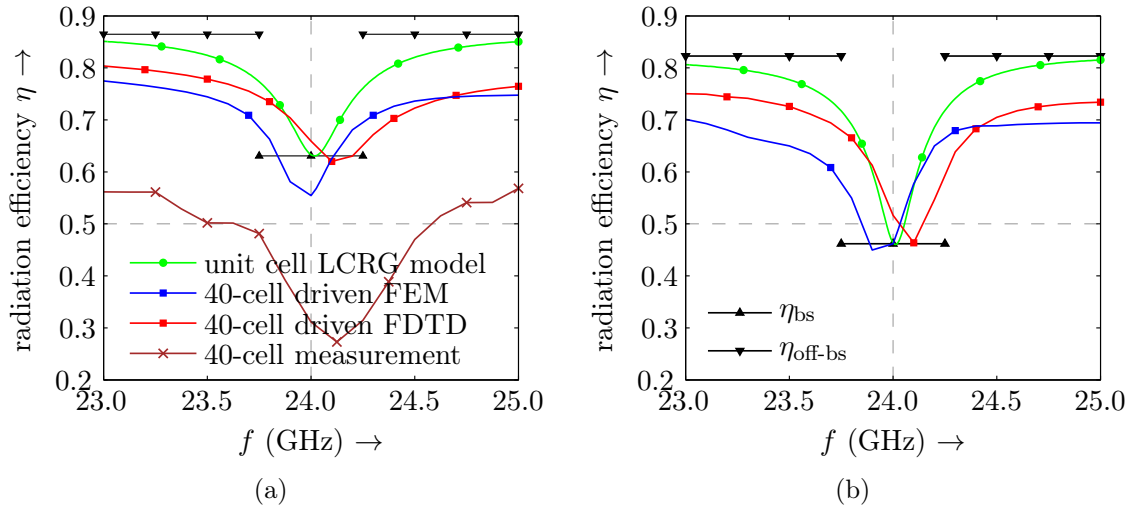


Figure 3.26: Measured and simulated radiation efficiencies for the 60-cell CRLH LWA. The LCRG model is compared and validated by measurement and simulation. (a) CRLH LWA of Figure 3.25. (b) CRLH LWA in a uniformly excited array (PMC side walls) according to Figure 3.17, confirming the broadside efficiency limitation of maximal 50%.

3.7 Summary of Symmetry Properties

Finally, the important features and limitations of fully symmetric LWAs are summarized as follows

- unit cells are classified into four canonical cases:
frequency-balanced/imbalance and quality-factor-balanced/imbalance
- series power and shunt power are always equal at broadside:
 $P_{se} = P_{sh}$ from (3.63)
- broadside efficiency is the arithmetic mean of the series and shunt efficiency:
 $\eta = (\eta_{se} + \eta_{sh})/2$ from (3.41)
- off-broadside efficiency depends on the series and shunt quality factors:
 $\eta_{off-bs} = \frac{\eta_{se}Q_{sh} + \eta_{sh}Q_{se}}{Q_{sh} + Q_{se}}$ from (3.44), allows to realize higher efficiencies
- broadside radiation contribution only from series radiation
- series and shunt radiation are orthogonally polarized
- efficiency limitation of 50% in an infinite array

This chapter is closed by establishing fundamental radiation limitations in *fully symmetric* LWAs. *Transversal asymmetry* is the key to overcome these limitations, which is demonstrated in the next chapter.

Transversally Asymmetric LWAs for Solving the Broadside Problem

This chapter considers the class of *transversally asymmetric* LWAs as illustrated in Figure 4.1. The proposed model of Chapter 3 is extended to take into account this class of unit cell asymmetry. The formulas for the propagation constant, the Bloch impedance and the radiation efficiency are then derived and discussed. It is demonstrated that moderate transversal asymmetry dominantly controls these quantities exactly at the broadside frequency, whereas the off-broadside frequency regime is unaffected. The broadside radiation efficiency is then increased by increasing the degree of asymmetry in the unit cell to equalize the at- and off-broadside radiation efficiencies. Finally, an analytical equalization condition for the optimum asymmetry degree is derived and the broadside problem is fully resolved in several case study LWAs by fulfilling this condition. This chapter is based on the author's journal publication in [61].

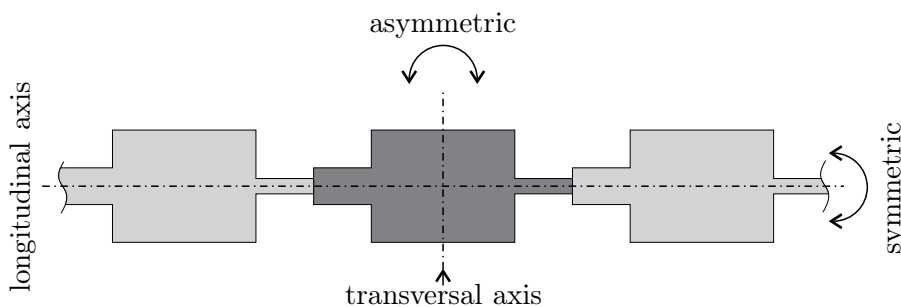


Figure 4.1: Class of *transversally asymmetric* LWAs that is considered in this chapter.

4.1 Two-Port Model for Transversally Asymmetric UCs

This section develops a generic transformer-lattice circuit model for transversally asymmetric LWAs. This model is based on the lattice circuit of Chapter 3, which is extended

by four ideal transformers, all having the same transformation ratio T , to account for transversal asymmetry by this single and simple parameter. For $T = 1$ the model obviously reduces to the lattice circuit and therefore inherently includes the symmetric case. A very beneficial property of the transformer-lattice circuit is that T solely controls the propagation constant, the Bloch impedance and the radiation efficiency around broadside, whereas the off-broadside parameters are unaffected. The fact that a circuit model with such a property exists, is an interesting discovery per se, which generally proves that broadside optimized LWAs can be realized by means of passive and reciprocal components.

4.1.1 Transformer-Lattice Circuit Model

For the derivation of the transformer lattice circuit, the symmetric lattice circuit is first decomposed into the series and shunt immittances and then recombined through four ideal transformers as shown in Figure 4.2. Figure 4.2(a) recalls the lattice circuit unit cell model for symmetric LWA structures from Chapter 3. Applying the bi-section theorem [87, 88],

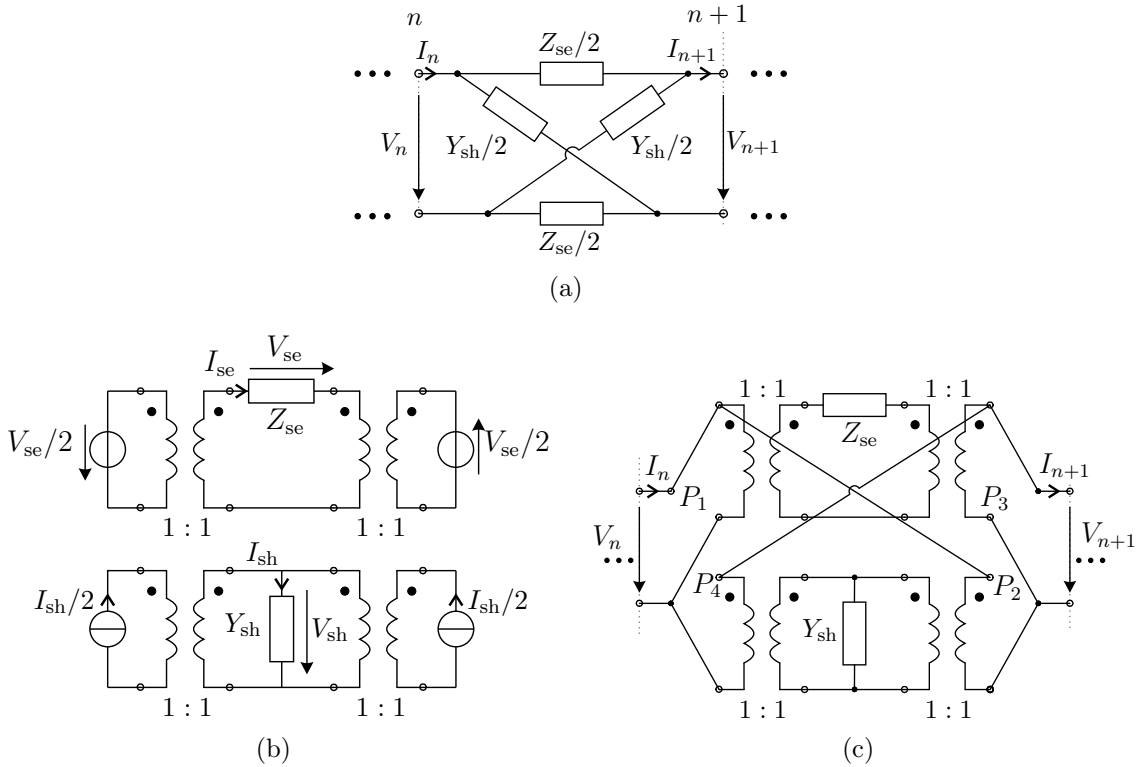


Figure 4.2: Derivation of the equivalent lattice circuit with ideal transformers in preparation for asymmetry modeling. (a) Lattice model from Chapter 3 for symmetric unit cells. (b) Decomposition of the circuit in (a) into odd and even responses and formal introduction of ideal galvanic isolation transformers with transformation ratio 1 : 1. (c) Recombination of the circuits in (b) to form the *transformer-lattice circuit model* that is equivalent to the circuit in (a).

the lattice circuit of Figure 4.2(a) is decomposed into its series and shunt immittances, Z_{se} and Y_{sh} , as already done in Figure 3.3. Now, by adding two ideal *isolation transformers* with transformation ratio 1:1, as shown in Figure 4.2(b), one does not alter the response of the two circuits. The lattice circuit and the transformer-lattice circuit, shown in Figures

4.2(a) and 4.2(c), respectively, differ from each other in the sense that the former has a differential structure (two ports each formed by two terminals excited out of phase) while the latter has a single-ended structure (two ports each formed by one terminal and a common ground). However, they are equivalent in terms of their two-port behavior, such as for instance their transfer matrices, as will be shown next in Section 4.1.2. The transformers are introduced to provide floating potentials, which will be required to avoid a short-circuiting in the forthcoming circuit recombination. Moreover, it prepares for the case of non-unity transformation ratios to model transversally asymmetric structures.

Combining the two circuits in Figure 4.2(b) forms the *transformer-lattice circuit* of Figure 4.2(c), that is equivalent to the lattice of Figure 4.2(a). This can be easily verified by decomposing it again through applying odd and even excitations. It is worth mentioning, that connecting P_1 to P_4 (instead of to P_2) and P_3 to P_2 (instead of to P_4) in Figure 4.2(c) would lead to a non-equivalent circuit, since the shunt path would then short the series element. The circuit topology of the transformer-lattice circuit in Figure 4.2(c) is not unique, in a sense, that other recombination possibilities with the same elements exist¹, providing an equivalent two-port response. Nevertheless, the topology is chosen as in Figure 4.2(c), so that in the forthcoming introduction of non-unity transformation ratios, only the broadside characteristic is affected as explained before. This is a particular feature of this topology, which also leads to simpler formulas.

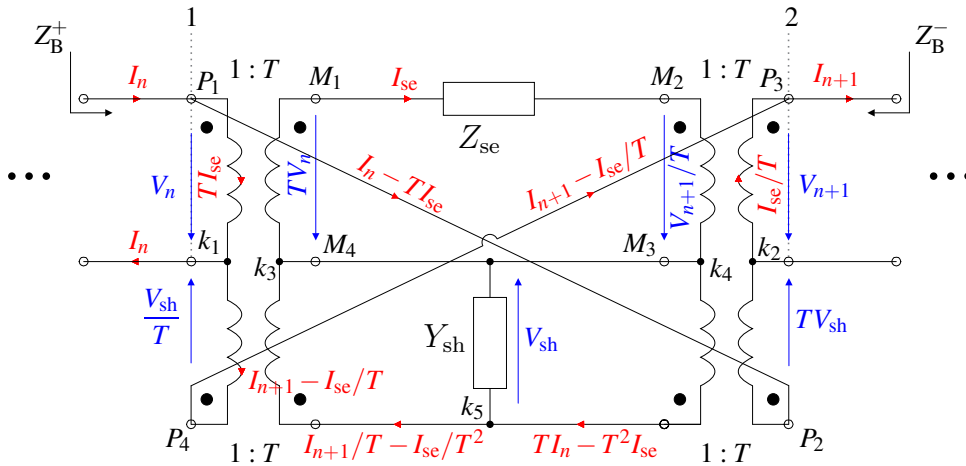


Figure 4.3: Transformer-lattice circuit model for asymmetrical unit cells. This circuit is obtained from Figure 4.2(c) by introducing a transformation ratio T different from unity, where the parameter T accounts for the degree of asymmetry.

Figure 4.3 shows the *transformer-lattice*² model for asymmetric LWAs, where the transformation ratio T is introduced in all four transformers. This model is a generalization of the *equivalent* lattice circuit in Figure 4.2(c), where a transformation ratio T different from unity is introduced to model transversal asymmetry. The transformation ratio represents the degree of structural asymmetry³, with $T = 1$ corresponding to a symmetric structure and $|T| \neq 1$ being proportional to the degree of asymmetry. As is shown later in this chapter, T only affects the broadside characteristics, whereas the off-broadside

¹To provide one simple example of an alternative topology: transformer-transformer-lattice-transformer-transformer.

²Note, that the shunt resonator Y_{sh} including the two transformers is horizontally flipped for topological simplicity as compared to the model in Figure 4.2(c).

³A quarter wavelength transformer is used in [38] to implement transversal asymmetry in the unit cell, which can also be modeled by an ideal transformer.

characteristics are independent of it. Moreover, this model will lead to a closed-form expression for the *optimal transformation ratio*, T_{opt} , equalizing the Bloch impedance and hence the radiation efficiency through broadside.

4.1.2 Two-Port Parameters of the Transformer-Lattice Circuit

The transmission matrix \mathbf{ABCD} , the impedance matrix \mathbf{Z} and admittance matrix \mathbf{Y} for the transformer lattice circuit in Figure 4.3 are derived, following the calculation of the immittances Z_{se} , Y_{sh} and transformation ratio T based on these matrix parameters.

In order to determine the transmission matrix for the circuit in Figure 4.3, one first evaluates the closed voltage loop P_1 - P_2 - P_3 - P_4 - P_1 to obtain

$$V_{\text{sh}} \left(T + \frac{1}{T} \right) = V_n + V_{n+1} = V_n(1 + e^{-\gamma p}), \quad (4.1a)$$

where the second equality is obtained by applying Floquet theorem with γ being the propagation constant and p the unit cell period. From the evaluation of the currents at node k_1 , one also finds

$$I_{\text{se}} \left(T + \frac{1}{T} \right) = I_n + I_{n+1} = I_n(1 + e^{-\gamma p}). \quad (4.1b)$$

The closed voltage loop M_1 - M_2 - M_3 - M_4 - M_1 next provides

$$I_{\text{se}} Z_{\text{se}} = T V_n - \frac{V_{n+1}}{T}. \quad (4.1c)$$

Finally, the current through the shunt element corresponding to $V_{\text{sh}} Y_{\text{sh}}$ is calculated based on the evaluation of node k_5 and reads

$$V_{\text{sh}} Y_{\text{sh}} = T I_n - \frac{I_{n+1}}{T} + I_{\text{se}} \left(\frac{1}{T^2} - T^2 \right) = T I_n - \frac{I_{n+1}}{T} - 2 I_{\text{se}} \tau, \quad (4.1d)$$

where τ is defined as

$$\tau = \frac{1}{2} \left(T^2 - \frac{1}{T^2} \right), \quad (4.2)$$

for later convenience. The transmission matrix of the unit cell is then obtained by eliminating I_{se} and V_{sh} and solving for V_n and I_n in terms of V_{n+1} and I_{n+1} . The result is

$$\begin{aligned} \mathbf{ABCD} &= \begin{pmatrix} A & B \\ C & D \end{pmatrix} \\ &= \frac{1}{\left(T + \frac{1}{T}\right)^2 - Z_{\text{se}} Y_{\text{sh}}} \begin{pmatrix} \frac{1}{T^2} \left(T + \frac{1}{T}\right)^2 + Z_{\text{se}} Y_{\text{sh}} & \left(T + \frac{1}{T}\right)^2 Z_{\text{se}} \\ \left(T + \frac{1}{T}\right)^2 Y_{\text{sh}} & T^2 \left(T + \frac{1}{T}\right)^2 + Z_{\text{se}} Y_{\text{sh}} \end{pmatrix}. \end{aligned} \quad (4.3)$$

For $T = 1$, corresponding to the symmetric case, Equation (4.3) simplifies to

$$\mathbf{ABCD}_{\text{sym}} = \frac{1}{4 - Z_{\text{se}} Y_{\text{sh}}} \begin{pmatrix} 4 + Z_{\text{se}} Y_{\text{sh}} & 4 Z_{\text{se}} \\ 4 Y_{\text{sh}} & 4 + Z_{\text{se}} Y_{\text{sh}} \end{pmatrix}, \quad (4.4)$$

which corresponds, as expected, to the transmission matrix in Equation (3.14) for the symmetric lattice in Figure 3.2.

For $T \neq 1$, the transformation ratio may conveniently be expressed solely in terms of the transmission matrix elements as

$$T = \sqrt{\frac{D+1}{A+1}}. \quad (4.5)$$

Equation (4.5) is obtained by solving A and D in Equation (4.3) for the product $Z_{se}Y_{sh}$, which then is eliminated. Practically, Equation (4.5) allows to directly calculate the transformation ratio from the transmission matrix, and hence via two-port conversions from *any* circuit or fullwave simulation results.

Next, the admittance and impedance matrices are determined and Z_{se} , Y_{sh} and T are calculated based upon them. These results are required later, since they form the basis for the LCRG circuit parameter extraction through fullwave drivenmode analysis as done in Section 3.4.1 for transversally symmetric unit cells.

Using conversion formulas, one first expresses the two-port circuit in Figure 4.3 in terms of its admittance parameters. Converting the transmission matrix in Equation (4.3) to its admittance counterpart [78] yields

$$\mathbf{Y} = \begin{pmatrix} Y_{11} & Y_{12} \\ Y_{21} & Y_{22} \end{pmatrix} = \frac{1}{(T + \frac{1}{T})^2 Z_{se}} \begin{pmatrix} T^2 (T + \frac{1}{T})^2 + Z_{se}Y_{sh} & -(T + \frac{1}{T})^2 + Z_{se}Y_{sh} \\ -(T + \frac{1}{T})^2 + Z_{se}Y_{sh} & \frac{1}{T^2} (T + \frac{1}{T})^2 + Z_{se}Y_{sh} \end{pmatrix}. \quad (4.6)$$

To isolate Z_{se} , one combines the elements of this matrix as

$$Y_{11} + Y_{22} - 2Y_{21} = \frac{(T + \frac{1}{T})^2 (\frac{1}{T^2} + 2 + T^2)}{(T + \frac{1}{T})^2 Z_{se}} = \frac{(T + \frac{1}{T})^2}{Z_{se}}. \quad (4.7)$$

Next, expressing T in Equation (4.5) in terms of the admittance parameters using again two-port conversion formulas, gives

$$T = \sqrt{\frac{Y_{21} - Y_{11}}{Y_{21} - Y_{22}}}. \quad (4.8)$$

Inserting Equation (4.8) into (4.7) provides the intrinsic impedance Z_{se} in terms of admittance parameters as follows

$$Z_{se} = \frac{Y_{11} + Y_{22} - 2Y_{21}}{(Y_{21} - Y_{11})(Y_{21} - Y_{22})}. \quad (4.9)$$

Similarly, the intrinsic shunt resonator Y_{sh} is derived starting with the impedance matrix,

$$\mathbf{Z} = \begin{pmatrix} Z_{11} & Z_{12} \\ Z_{21} & Z_{22} \end{pmatrix} = \frac{1}{(T + \frac{1}{T})^2 Y_{sh}} \begin{pmatrix} \frac{1}{T^2} (T + \frac{1}{T})^2 + Z_{se}Y_{sh} & (T + \frac{1}{T})^2 - Z_{se}Y_{sh} \\ (T + \frac{1}{T})^2 - Z_{se}Y_{sh} & T^2 (T + \frac{1}{T})^2 + Z_{se}Y_{sh} \end{pmatrix}, \quad (4.10)$$

next combining the elements of this matrix as $Z_{11} + Z_{22} + 2Z_{21}$, isolating Y_{sh} , and replacing T by

$$T = \sqrt{\frac{Z_{22} + Z_{21}}{Z_{11} + Z_{21}}}, \quad (4.11)$$

which is again obtained from two-port conversion. Finally, the intrinsic shunt admittance is

$$Y_{\text{sh}} = \frac{Z_{11} + Z_{22} + 2Z_{21}}{(Z_{11} + Z_{21})(Z_{22} + Z_{21})}. \quad (4.12)$$

4.1.3 Propagation Constant

The implicit formula to calculate the complex propagation constant γ in terms of the two-port transmission matrix is taken from Equation (2.27), which reads $\cosh(\gamma p) = \cosh(\alpha + j\beta) = (A + D)/2$, where α is the leakage constant and β the phase constant. Substituting the transmission matrix elements of Equation (4.3) into (2.27) yields the complex propagation constant

$$\gamma = \frac{1}{p} \operatorname{arccosh} \left[\frac{\frac{1}{2} \left(\frac{1}{T^2} + T^2 \right) \left(T + \frac{1}{T} \right)^2 + 2Z_{\text{se}}Y_{\text{sh}}}{\left(T + \frac{1}{T} \right)^2 - Z_{\text{se}}Y_{\text{sh}}} \right], \quad (4.13)$$

for asymmetric unit cells. Following the same approximations as done for the symmetric case in Section 3.1.3, the propagation constant is simplified by means of a Taylor series expanded around broadside, where $|\gamma| \approx 0$ holds. By first squaring Equation (4.13) and then developing the resulting expression in a first order Taylor series with expansion point $Z_{\text{se}}Y_{\text{sh}} = 0$ one writes

$$\begin{aligned} (\gamma p)^2 &\approx (\gamma p)^2|_{Z_{\text{se}}Y_{\text{sh}}=0} + Z_{\text{se}}Y_{\text{sh}} \left[\frac{d}{d(Z_{\text{se}}Y_{\text{sh}})} (\gamma p)^2 \right]_{Z_{\text{se}}Y_{\text{sh}}=0} \\ &= 4 \ln^2(T) + Z_{\text{se}}Y_{\text{sh}} \frac{\ln(T)}{\frac{1}{4} \left(T^2 - \frac{1}{T^2} \right)}. \end{aligned} \quad (4.14)$$

The last equality in Equation (4.14) provides the evaluation of the constant and the linear Taylor coefficient, which are obtained after going through a rather lengthy calculation. By furthermore restricting the range of the transformation ratio⁴ to $0.8 < T < 1.2$, the natural logarithm can be approximated by

$$\ln(T) \approx \frac{1}{4} \left(T^2 - \frac{1}{T^2} \right). \quad (4.15)$$

The approximation quality is illustrated in Figure 4.4. Figure 4.4(a) compares $\ln(T)$, the first-order Taylor approximation of $\ln(T)$, which is $T - 1$, and the proposed approximation in Equation (4.15), which reads $\frac{1}{4} \left(T^2 - \frac{1}{T^2} \right)$, to clearly demonstrate the superior approximation property of the latter one. Figure 4.4(b) compares the complex propagation for the three aforementioned cases, where the transformation is set to $T = 1.2$. The LCRG parameters and the quality factors, $Q_{\text{se}} = 5$ and $Q_{\text{sh}} = 100$, correspond to the frequency-balanced and Q-imbalanced example in the second column of Figure 3.7, so that here only the transformation ratio is changed from 1 to 1.2. All three curves are nearly superimposed, yet the best fit is provided by the approximation in Equation (4.15). The inset in Figure 4.4(b) shows a zoomed view of the leakage constant at broadside and it clearly verifies that the best approximation is achieved by Equation (4.15).

⁴This is a reasonable restriction, since all LWAs investigated within this thesis require only a very moderate asymmetry with $0.9 < T < 1.1$, which is shown and discussed later in this chapter.

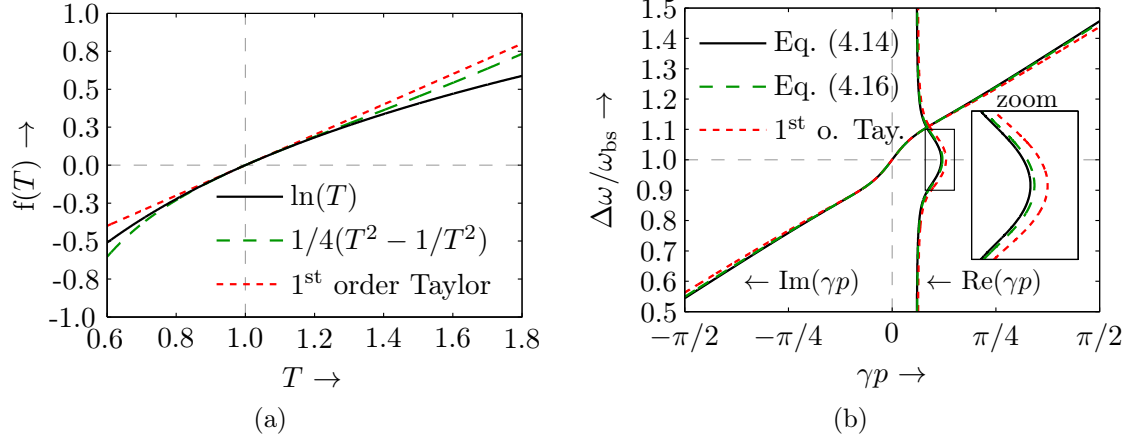


Figure 4.4: Approximation of the dispersion relation in (4.13). (a) Approximation of $\ln(T)$ with $1/4(T^2 - 1/T^2)$ [Equation (4.15)] provides a better fitting in the range $0.8 < T < 1.2$ than the first order Taylor approximation with $T - 1$. (b) Propagation constant for these three approximation cases, demonstrating the superior approximation nature of Equation (4.16).

Substituting Equation (4.15) into (4.14) and, furthermore, by recalling the quantity $\tau = \frac{1}{2}(T^2 - \frac{1}{T^2})$, as this is defined in Equation (4.2), the propagation constant simplifies to

$$\gamma = \frac{1}{p} \sqrt{\frac{1}{4} \left(T^2 - \frac{1}{T^2} \right)^2 + Z_{se} Y_{sh}} = \frac{1}{p} \sqrt{\tau^2 + Z_{se} Y_{sh}}. \quad (4.16)$$

In the symmetric case ($T = 1$), this expression reduces to $\gamma \approx \frac{1}{p} \sqrt{Z_{se} Y_{sh}}$, which is consistent with Equation (3.19) of Chapter 3. Inserting the linearized immittances of Equation (3.8) and (3.13) into (3.19) and evaluating the result at broadside, where $\Delta\omega = 0$, one gets $\alpha_{bs} = \sqrt{RG}/p$ [Equation (3.59b)]. This result clearly shows that *both* series and shunt contributions are required ($R \neq 0$ and $G \neq 0$) in the *transversally symmetric* case, in order to avoid a zero leakage constant, as discussed in [31, 36].

In the asymmetric case ($T \neq 1$), if either R or G is zero, and hence $Z_{se} Y_{sh}$ is zero, Equation (4.16) simplifies to

$$\alpha_{bs} = \frac{1}{p} \frac{1}{2} \left| T^2 - \frac{1}{T^2} \right| = \frac{|\tau|}{p}. \quad (4.17)$$

This is an interesting result revealing that in case of a single non-zero loss element (radiation and dissipation) – either R or G –, the leakage constant at broadside solely depends on the transformation ratio T , and hence on the degree of transversal asymmetry.

4.1.4 Bloch Impedance

The Bloch impedance is derived from (4.1c), which after substituting $Z_B^+ = \frac{V_n}{I_n} = \frac{V_{n+1}}{I_{n+1}}$ reads

$$I_{se} Z_{se} = T I_n \frac{V_n}{I_n} - I_{n+1} \frac{V_{n+1}}{I_{n+1} T} = Z_B \left(T I_n - \frac{I_{n+1}}{T} \right). \quad (4.18)$$

Dividing this relation by Z_B and substituting the result into (4.1d), one obtains

$$V_{\text{sh}}Y_{\text{sh}} = \frac{I_{\text{se}}Z_{\text{se}}}{Z_B} + I_{\text{se}} \left(\frac{1}{T^2} - T^2 \right) = \frac{I_{\text{se}}Z_{\text{se}}}{Z_B} - 2I_{\text{se}}\tau, \quad (4.19)$$

with τ defined in (4.2). To eliminate I_{se} and V_{sh} , first divide (4.1a) by (4.1b) to get

$$\frac{V_{\text{sh}}}{I_{\text{se}}} = \frac{V_n(1 + e^{\gamma p})}{I_n(1 + e^{\gamma p})} = Z_B, \quad (4.20)$$

next divide (4.19) by I_{se} and insert the result into (4.20), which yields

$$Z_B^2 + \frac{2}{Y_{\text{sh}}}Z_B\tau - \frac{Z_{\text{se}}}{Y_{\text{sh}}} = 0. \quad (4.21)$$

The two solutions⁵ and represent the Bloch impedances for the wave traveling in the positive y -direction and in the negative y -direction, respectively,

$$Z_B^{\pm} = \frac{\mp\tau}{Y_{\text{sh}}} + \sqrt{\left(\frac{\tau}{Y_{\text{sh}}}\right)^2 + Z_{\text{B,sym}}^2}, \quad (4.22)$$

where $Z_{\text{B,sym}}^2 = \frac{Z_{\text{se}}}{Y_{\text{sh}}}$ is the *symmetric Bloch impedance* of the corresponding symmetric unit cell ($T = 1$ or $\tau = 0$). Generally, it can be shown that the Bloch impedance in positive and negative y -direction are related as follows

$$Z_B^+ Z_B^- = Z_{\text{B,sym}}^2. \quad (4.23)$$

The Bloch impedance in the broadside regime is obtained by first inserting the linearized immittances in Equation (3.8) and (3.13) into (4.22), and next evaluating the resulting expression for $\Delta\omega \rightarrow 0$ to find the broadside Bloch impedance

$$Z_{\text{B,bs}}^+ = \lim_{\Delta\omega \rightarrow 0} Z_B^+ = \frac{-\tau}{G} + \sqrt{\left(\frac{\tau}{G}\right)^2 + \frac{R}{G}}. \quad (4.24)$$

The Bloch impedance in the off-broadside regime is similarly obtained for $\Delta\omega \rightarrow \infty$, and is given by

$$\begin{aligned} Z_{\text{B,off-bs}}^+ &= \lim_{\Delta\omega \rightarrow \infty} Z_B^+ \\ &= \lim_{\Delta\omega \rightarrow \infty} \frac{-\tau}{G + j2C\Delta\omega} + \sqrt{\left(\frac{\tau}{G + j2C\Delta\omega}\right)^2 + \frac{R + j2L\Delta\omega}{G + j2C\Delta\omega}} = \sqrt{\frac{L}{C}}. \end{aligned} \quad (4.25)$$

At this point it might be important to recall from Section 4.1.1, that the specific transformer lattice topology in Figure 4.3 is selected over other possibilities for T to solely control broadside without affecting the off-broadside regime. This property is now confirmed through Equations (4.24) and (4.25), proving that the Bloch impedance at broadside in Equation (4.24) depends on T , whereas the off-broadside Bloch impedance in Equation (4.25) is totally independent of T .

⁵ Note the reference direction of the Bloch impedance in Figure 4.3, where $Z_B^+ = V_n/I_n$ defines the impedance for wave propagation in the direction of increasing n and $Z_B^- = -V_{n+1}/I_{n+1}$ defines the impedance for wave propagation in the direction of decreasing n .

To gain some further insight into these results, consider, for example, the case $T \neq 1$ ($\tau \neq 0$) with $R \neq 0$ and $G = 0$. Evaluating the limit of the right side for $G \rightarrow 0^+$ in Equation (4.24) yields

$$Z_{B,bs}^+ \Big|_{G=0} = \lim_{G \rightarrow 0^+} Z_{B,bs}^+ = \frac{R}{2\tau} = R \frac{T^2}{T^4 - 1}. \quad (4.26)$$

This relation reveals that a single loss element, here R , is sufficient to provide a finite⁶ Bloch impedance, and that this impedance is controlled by T , the degree of transversal asymmetry of the structure.

4.1.5 Radiation Efficiency

Following the same methodology as for the symmetric unit cell in Section 3.1.5 of Chapter 3, the radiation efficiency is calculated based on the dissipated and radiated powers in the series and shunt elements in Figure 4.3. The four transformers are lossless and power dissipation (radiation and loss) only occurs in the series and shunt element, yielding the identical efficiency formula, $\eta = \frac{P_{se,rad} + P_{sh,rad}}{P_{se} + P_{sh}}$, as for the symmetric case in Equation (3.33). $P_{se,rad}$ and $P_{sh,rad}$ are the series and shunt radiated powers and P_{se} and P_{sh} are the total series and shunt powers, respectively. Writing these powers in terms of voltage and current quantities, as they are defined in Figure 4.3, and inserting them into Equation (3.33) leads to

$$\eta = \frac{P_{se,rad} + P_{sh,rad}}{P_{se} + P_{sh}} = \frac{|I_{se}|^2 R_{rad} + |V_{sh}|^2 G_{rad}}{|I_{se}|^2 R + |V_{sh}|^2 G} = \frac{R_{rad} + |V_{sh}/I_{se}|^2 G_{rad}}{R + |V_{sh}/I_{se}|^2 G}, \quad (4.27)$$

where $P_{se,rad} = \frac{1}{2}|I_{se}|^2 R_{rad}$, $P_{se} = \frac{1}{2}|I_{se}|^2 R$ and $P_{sh} = \frac{1}{2}|V_{sh}|^2 G$, $P_{sh,rad} = \frac{1}{2}|V_{sh}|^2 G_{rad}$. Moreover, by recalling the series and the shunt efficiencies $\eta_{se} = R_{rad}/R$ and $\eta_{sh} = G_{rad}/G$ from Equations (3.5) and (3.11), respectively, and inserting (4.20) into (4.27) yields the radiation efficiency for *transversally asymmetric* LWA,

$$\eta = \frac{\eta_{se}R + \eta_{sh}G|Z_B^+|^2}{R + G|Z_B^+|^2}. \quad (4.28)$$

It is interesting to note that this efficiency formula for an *asymmetric* LWA is formally identical to that for the *symmetric* LWA in Equation (3.37), the information on asymmetry being completely absorbed in the Bloch impedance Z_B^+ .

The efficiency at broadside is obtained by inserting the Bloch impedance (4.24) into (4.28), which results in

$$\eta_{bs} = \frac{\eta_{se}RG + \eta_{sh}|- \tau + \sqrt{\tau^2 + RG}|^2}{RG + |- \tau + \sqrt{\tau^2 + RG}|^2}. \quad (4.29)$$

For the symmetric case ($\tau = 0$), Equation (4.29) reduces to $\eta_{bs} = \frac{\eta_{se} + \eta_{sh}}{2}$, which confirms the fundamental efficiency limit of 50% of Chapter 3 for the case where only one radiation mechanism, either $\eta_{se} = 0$ or $\eta_{sh} = 0$, is present.

⁶In the symmetric case, the broadside Bloch impedance for $G \rightarrow 0$ is infinite, since $Z_{B,sym,bs} = \sqrt{R/G} \rightarrow \infty$.

Off-broadside, the radiation efficiency is obtained by inserting the Bloch impedance (4.25) into (4.28), which yields

$$\eta_{\text{off-bs}} = \frac{\eta_{\text{se}}Q_{\text{sh}} + \eta_{\text{sh}}Q_{\text{se}}}{Q_{\text{sh}} + Q_{\text{se}}}. \quad (4.30)$$

The definition of the series and shunt quality factors, $Q_{\text{se}} = \frac{\omega_{\text{se}}L}{R}$ and $Q_{\text{sh}} = \frac{\omega_{\text{sh}}C}{G}$, from Equations (3.7) and (3.12), respectively, is used to express the final results in Equation (4.30) solely in terms of the resonator efficiencies and the quality factors.

Consistent with the off-broadside Bloch impedance, the off-broadside radiation efficiency in (4.30) is independent of T , which again confirms its insensitivity to transversal asymmetry.

At broadside, the Bloch impedance is a function of the transformation ratio, i.e. $Z_{\text{B,bs}}^+ = Z_{\text{B,bs}}^+(T)$, as seen in (4.24). By controlling the broadside Bloch impedance (assuming constant LCRG parameters), one may optimally combine the series and the shunt efficiencies to achieve equalization, where the broadside efficiency is increased to be equal to the off-broadside efficiency.

4.1.6 Comparison At-/Off-BS of Symmetrical/Asymmetrical UCs

Table 4.1 summaries the formulas for the asymmetric unit cell.

Table 4.1: Summary of the at- and off-broadside formulas for transversally asymmetric unit cells. The broadside regime is strongly affected by asymmetry ($\tau \neq 0$ corresponding to $T \neq 1$) and the off-broadside parameters are identical to the ones for the symmetric case in Table 3.2.

	at-broadside (bs)	off-broadside (off-bs)
αp	$\sqrt{\tau^2 + RG}$	$\frac{1}{2}\omega_{\text{bs}}\sqrt{LC} \left(\frac{1}{Q_{\text{se}}} + \frac{1}{Q_{\text{sh}}} \right) = \frac{1}{2}\sqrt{RG} \frac{Q_{\text{se}} + Q_{\text{sh}}}{\sqrt{Q_{\text{se}}Q_{\text{sh}}}}$
Z_{B}^+	$\frac{-\tau}{G} + \sqrt{\left(\frac{\tau}{G}\right)^2 + \frac{R}{G}}$	$\sqrt{\frac{L}{C}}$
η	$\frac{\eta_{\text{se}}RG + \eta_{\text{sh}} \left -\tau + \sqrt{\tau^2 + RG} \right ^2}{RG + \left -\tau + \sqrt{\tau^2 + RG} \right ^2}$	$\frac{Q_{\text{sh}}\eta_{\text{se}} + Q_{\text{se}}\eta_{\text{sh}}}{Q_{\text{se}} + Q_{\text{sh}}}$

4.2 Optimal Asymmetry Condition for Equalization

4.2.1 Bloch Impedance and Efficiency Equalization

The LCRG parameters and the series and shunt efficiencies are nearly constant within a moderate frequency range around broadside, which is already addressed for the symmetric case considered in Chapter 3. Therefore, the radiation efficiency reflects the frequency

behavior of the Bloch impedance as the main beam of the LWA is steered through broadside. In other words, equalizing the Bloch impedances equalizes the radiation efficiency as well. By equating the Bloch impedance at-broadside and off-broadside,

$$Z_{B,bs}^+ = Z_{B,off-bs}^+, \quad (4.31)$$

one equalizes the radiation efficiency. Upon substituting Equation (4.24) and Equation (4.25) in this relation, and solving for τ , one obtains the optimal degree of asymmetry

$$\tau_{\text{opt}} = \frac{G}{2} \sqrt{\frac{C}{L}} \left(\frac{R}{G} - \frac{L}{C} \right), \quad (4.32a)$$

expressed in terms of the LCRG parameters. The optimal asymmetry may also be conveniently expressed as

$$\tau_{\text{opt}} = \frac{G}{2Z_{B,\text{sym},\text{off-bs}}} (Z_{B,\text{sym},\text{bs}}^2 - Z_{B,\text{sym},\text{off-bs}}^2), \quad (4.32b)$$

where $Z_{B,\text{sym},\text{bs}} = \sqrt{R/G}$ and $Z_{B,\text{sym},\text{off-bs}} = \sqrt{L/C}$ are the broadside and off-broadside Bloch impedances, respectively, of the corresponding symmetric ($\tau = 0$ and $T = 1$) unit cell.

Moreover, τ_{opt} may also be alternatively expressed in terms of the quality factors, $Q_{\text{se}} = \frac{\omega_{\text{se}}L}{R}$ and $Q_{\text{sh}} = \frac{\omega_{\text{sh}}C}{G}$ defined in Equations (3.7) and (3.12), and $\alpha_{\text{sym},\text{bs}}p = \sqrt{RG}$ as

$$\tau_{\text{opt}} = \sqrt{RG} \frac{\frac{C}{G} - \frac{L}{R}}{2\sqrt{\frac{LC}{RG}}} = \alpha_{\text{sym},\text{bs}}p \frac{Q_{\text{sh}} - Q_{\text{se}}}{2\sqrt{Q_{\text{sh}}Q_{\text{se}}}}. \quad (4.32c)$$

The last two equivalent results for τ_{opt} show that *mismatch* between the Bloch impedances of the two frequency regimes [Equation (4.32b)], or *imbalance* between the intrinsic quality factors [Equation (4.32c)], calls for an optimal τ different from zero and hence asymmetry. In a symmetric unit cell that is already Q-balanced, τ_{opt} is zero, which is consistent with the theory for symmetric unit cells presented in Chapter 3.

In the optimal case, the equalized Bloch impedance reads

$$Z_{B,\text{opt}}^+ = Z_{B,bs}^+ = Z_{B,off-bs}^+ = \sqrt{\frac{L}{C}}, \quad (4.33)$$

leading to the radiation efficiency

$$\eta_{\text{opt}} = \eta_{\text{bs}} = \eta_{\text{off-bs}} = \frac{\eta_{\text{se}}Q_{\text{sh}} + \eta_{\text{sh}}Q_{\text{se}}}{Q_{\text{sh}} + Q_{\text{se}}}. \quad (4.34)$$

Finally, the optimum transformation ratio may be determined by solving (4.2) for T , which yields

$$T_{\text{opt}} = \sqrt{\tau_{\text{opt}} + \sqrt{\tau_{\text{opt}}^2 + 1}}. \quad (4.35)$$

Equation (4.35) together with Equation (4.32) form a simple yet powerful result to resolve the broadside problem by equalizing the broadside and off-broadside regime. The fact that this closed-form expression in Equation (4.35) exists, results from the specific transformer-lattice topology in Figure 4.3. There are alternative topologies with ideal transformers, which show qualitatively a similar behavior and T can be adjusted for equalization, yet their analytical description is more complex and a compact closed-form equalization criterion may not be found.

4.2.2 Illustration of Asymmetry Controlling Broadside

An overview comparing the propagation constant, the Bloch impedance and the radiation efficiency is provided in Figure 4.5, where each column represents a different asymmetry degree. The LCRG parameters and the series and shunt efficiencies ($L = 40$ nH, $C = 16$ pF, $\eta_{se} = 0.9$ and $\eta_{sh} = 0.2$) are identical to the ones used in Figure 3.7 illustrating the transversally symmetric case in Chapter 3. Here, the starting point is a *frequency-balanced* and *Q-imbalanced* unit cell representing the most common and relevant case as discussed in Section 3.2. All parameters, except for the transformation ratio T are fixed and T is increased in Figure 4.5 from the left to the right column in four steps, $T = 0.79$, $T = 1$, $T = 1.26$ and $T = 1.8$. In column two the propagation constant, the Bloch impedance and the radiation efficiency for $T = 1$ are plotted, which obviously is identical to the symmetric case ($T = 1$) and hence these plots are the same as in Figure 3.7.

By first evaluating the Bloch impedance [Equation (4.22)], second row in Figure 3.7, one observes a strong impact at the broadside frequency, where with increasing T , the real part of the Bloch impedance strongly decreases. The imaginary part qualitatively follows the real part, yet it has a zero crossing at broadside where the sign changes. The off-broadside impedance is constant and the condition of equalization is met in column three ($T = T_{opt} = 1.26$), where the two regimes are unified and a flat response over frequency is observed. Moreover, the imaginary part of the impedance totally vanishes, resulting in a purely real Bloch impedance. By further increasing asymmetry ($T = 1.8$), the real part of the Bloch impedance at broadside is lower than the off-broadside. The imaginary part of the impedance changes the slope from negative to positive at broadside. Here, it is clearly demonstrated how the transformation ratio and hence the asymmetry is exploited to control the Bloch impedance at broadside over a large range.

Next, evaluating the radiation efficiency [Equation (4.28)], third row in Figure 4.5, one observes an increase of the broadside efficiency, with larger values for T . In the third column, a flat efficiency response is given following from the equalized impedance under the optimal case. Generally, the efficiency plots in Figure 4.5 clearly show that the poor broadside efficiency of a symmetric unit cell is systematically increased with the degree of unit cell asymmetry. This finally resolves the broadside problem in periodic LWAs.

If asymmetry beyond the equalization point is applied, the efficiency at broadside can even be higher than off-broadside as shown in the fourth column of Figure 4.5. A slight increase as compared to the off-broadside values is here observed, where the overall radiation efficiency approaches η_{se} . This effect of *efficiency enhancement* for $T > T_{opt}$ may be explained as follows. The Bloch impedance varies the ratio V_{sh}/I_{se} , which is proportional to the power ratio P_{sh}/P_{se} . By controlling the Bloch impedance at broadside, one can direct the power to the radiation element (series or shunt) that has a higher intrinsic resonator efficiency. Since here $\eta_{se} \gg \eta_{sh}$, one needs to lower the ratio V_{se}/I_{se} and hence lower the Bloch impedance for that purpose. Theoretically, for $Z_B \rightarrow 0$, the overall efficiency approaches $\eta = \eta_{se}$, as easily seen in (4.28). Conversely, increasing the Bloch impedance at broadside to infinity, leads to $\eta = \eta_{sh}$. However, in both of these extreme cases of zero or infinite Bloch impedance, wave propagation is prohibited, indicating that these efficiencies are theoretical and cannot be practically achieved. Yet, these asymptotic cases help to understand and interpret the radiation efficiency of transversally asymmetric LWAs at broadside.

The propagation constant for the four asymmetry degrees is discussed in the following. It is interesting to note that the leakage constant in the first column ($T = 0.89$), shows a flat behavior which might suggest that the structure is equalized. This is in fact true and the unit cell is equalized for wave propagation in negative y -direction (direction of decreasing n). Here, the asymmetry is reversed with $T < 1$, which equalizes the Bloch impedance Z_B^- . Moreover, it is worth mentioning that even though the unit cell is frequency-balanced, a well-defined band gap is formed for $T \neq 1$ in the lossless case, where $R = G = 0$, indicated by the thin black lines in the dispersion diagrams. This is a very important point, revealing the existence of a coupling mechanism between the two intrinsic series and shunt resonators, where the coupling is zero for the symmetric case and proportional to T in case of asymmetry. Therefore, equalization might alternatively be understood, as carefully coupling two resonators to balance their losses.

From a practical point of view, an LWA design that is based *only* on the analysis of the propagation constant, is very difficult, if not impossible. The propagation constant of an asymmetric unit cell does not provide the information on the intrinsic resonator frequencies, and it does not clearly isolate the frequency shifts due to coupling. This can be understood by comparing the dispersion diagram in the third column in Figure 3.7 with the one in the fourth column in Figure 4.5. Both diagrams show nearly the same quantitative behavior, however, their underlying resonance mechanisms are different. One major advantage of the transformer-lattice topology is to provide this isolation feature which *circuit-wise* decouples the series and shunt resonator through the ideal transformer and hence analytically allows their isolation.

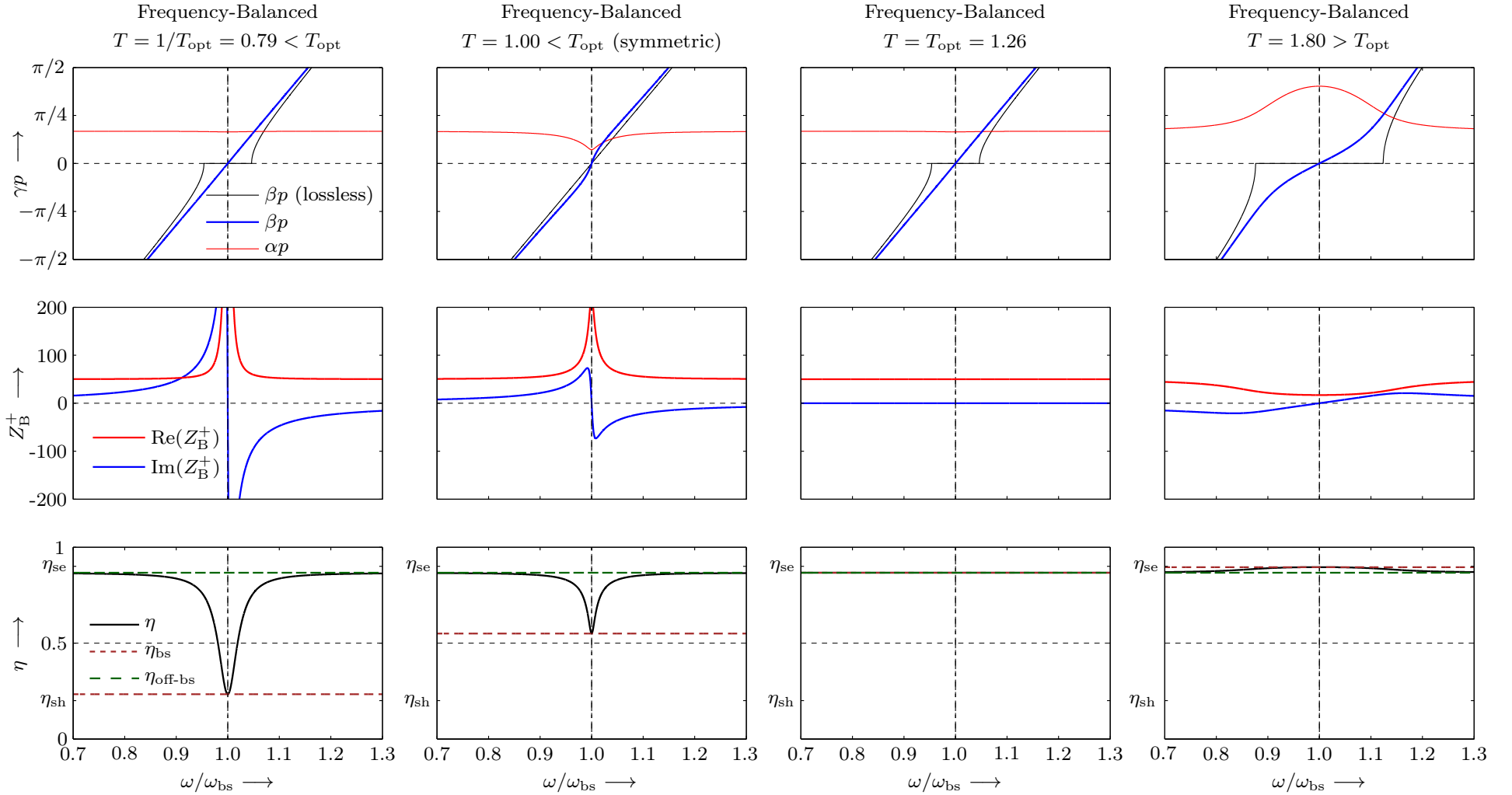


Figure 4.5: Overview asymmetry variation (increasing transformation ratio T from left to right column) in a frequency-balanced unit cell. The series and shunt efficiencies are set to $\eta_{\text{se}} = 0.9$ and $\eta_{\text{sh}} = 0.2$, respectively. The broadside efficiency η_{bs} is controlled by T and can be adjusted between η_{sh} and η_{se} . Column three shows the case of optimum asymmetry $T = T_{\text{opt}}$, where equalization is achieved.

4.3 Complex Frequency Approach and Q-Balancing

This section presents a *complex frequency domain* approach to asymmetric unit cells, which is a generalization of the eigenmode simulation analysis in Section 3.4.3. The need for such an analysis is twofold. First, it allows to derive a fullwave parameter extraction scheme for transversally asymmetric unit cells that is similar to the one in Section 3.4.3. Second, it unifies the analyses of transversally *symmetric* and *asymmetric* LWAs within a single condition, *complex frequency-balancing*, which ultimately results in equalization. The definition of *coupled* quality factors in this chapter, generalizes⁷ the concept of Q-balancing, so that the simultaneous satisfaction of *frequency-balancing* and *Q-balancing* provides equalization also in the transversally asymmetric case.

4.3.1 Complex Propagation Constant versus Complex Frequency

Figure 4.6 illustrates two approaches, which are commonly used for the modeling of periodic structures. The complex propagation constant approach is extensively used in Chapter 3 and it represents the natural operating condition of an LWA exhibiting a spatial field decay when one side is excited and the other is perfectly terminated by the Bloch impedance. The complex frequency analysis approach is first introduced in Section 3.4.3 to extract the LCRG parameter from eigenmode fullwave simulation. This approach does not reflect the natural operation of an LWA, since the complex frequency models a time decay, while having constant amplitude distribution. This is illustrated in Figure 4.7, visualizing the duality of the two techniques, where Figure 4.7(a) sketches the spatial decay and Figure 4.7(b) the time decay, corresponding to the complex propagation constant and complex frequency analysis, respectively. Moreover, the latter approach is commonly used in commercial eigenmode solver, where a phase shift Φ between unit cell boundaries is specified to account for the periodicity.

Figure 4.6 compares the approaches on a two-port basis together with their dispersion diagrams. In Figure 4.6(a) the unit cell network model is given with the input-output voltage and current definitions, related by the complex propagation constant γ . Figure 4.6(c) shows the dispersion diagram, where a given *real* frequency ω_1 leads to the determination of the complex γ . This might be referred to as a horizontal dispersion approach with the frequency as the independent parameter, where $\omega \in \mathbb{R} \rightarrow \gamma \in \mathbb{C}$, as indicated by the arrows in the diagram.

Figure 4.6(b) shows the unit cell, where the input-output voltages and currents are linked through a *real* given phase angle Φ as independent parameter, following that $\Phi \in \mathbb{R} \rightarrow \Omega \in \mathbb{C}$. The dispersion diagram in Figure 4.6(d) implies a vertical approach, since the independent parameter Φ is mapped onto the complex frequency axis.

Generally, the dispersion diagram obtained through these two approaches are not easily transferable among one another. In the special case of a lossless unit cell, where $\text{Re}\{\gamma\} = 0$ and $\text{Im}\{\Omega\} = 0$, it follows $\beta p = \Phi$ and $\omega = \text{Re}\{\Omega\}$, and hence the two dispersion diagrams are identical. Obviously, this condition of a lossless unit cell is not satisfied in an LWA, which generally results in two different sets of dispersion diagrams. In the forthcoming

⁷The generalized quality factors are referred to as *coupled* quality factors and they are only identical to the intrinsic quality factors, Q_{se} and Q_{sh} in case of a transversally symmetric unit cell as is shown later in this section.

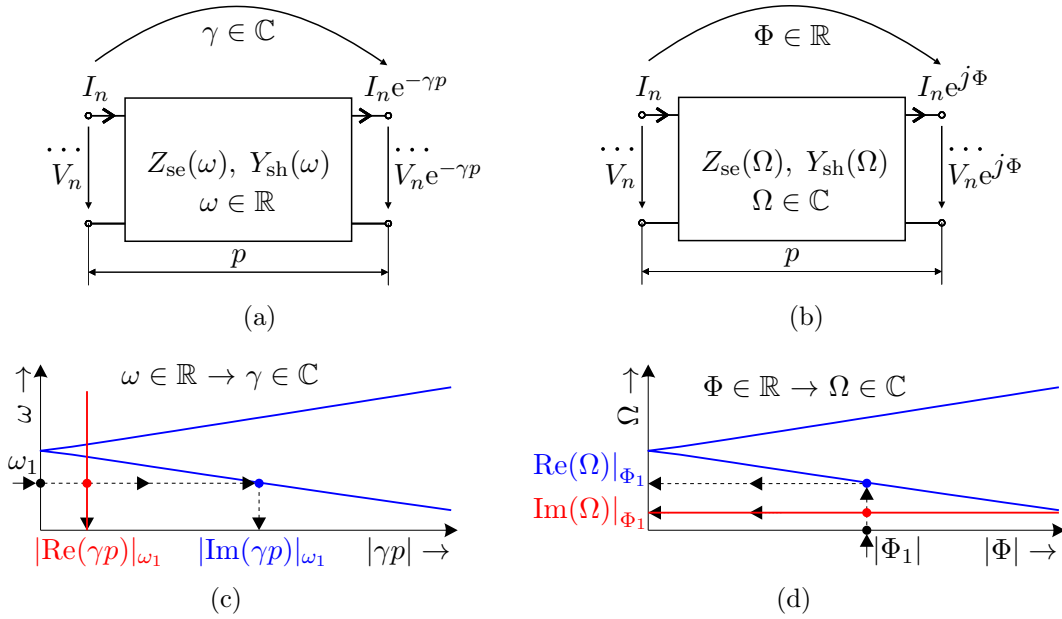


Figure 4.6: Two approaches to dispersion modeling of periodic structures. (a) and (c) Complex propagation constant two-port model and dispersion relation, respectively. A real frequency ω_1 is the argument of the complex γ : $\gamma(\omega_1) \in \mathbb{C}$. (b) and (d) Complex frequency two-port model and dispersion relation, respectively. For a real phase argument Φ_1 the complex frequency Ω is calculated: $\Omega(\Phi_1) \in \mathbb{C}$. For a lossless unit cell these two approaches are identical.

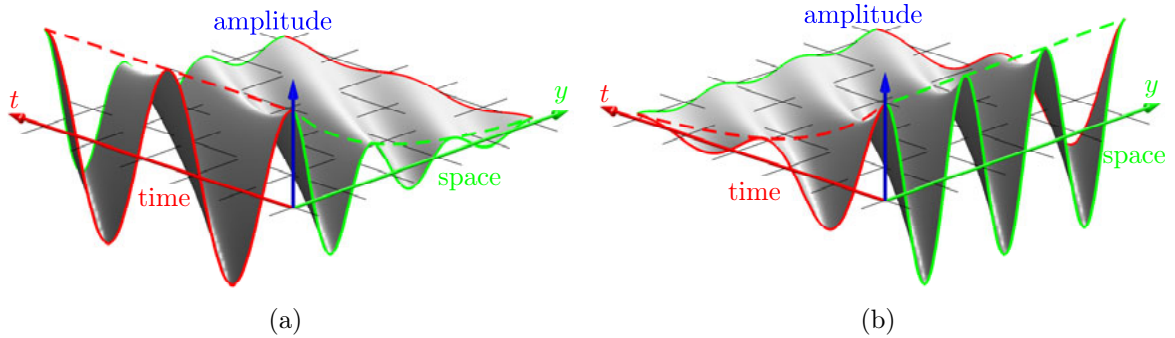


Figure 4.7: Comparison of the spatial and temporal amplitude behavior. (a) Complex propagation constant models a spatial decay. This approach corresponds to the natural driven excitation of the LWA. (b) Complex frequency models a time decay. This is a common approach of commercial fullwave eigenmode solvers employing periodic boundaries.

analysis it is shown that when the equalization condition is fulfilled in an asymmetric unit cell, the two dispersion diagrams have a simple one-to-one correspondence. This fact, strongly supports the analysis and the optimization of unit cells by means of the complex propagation constant, even though this analysis does not inherently represent the operational LWA case as discussed before.

The complex frequency is defined in Equation (3.81) and reads $\Omega = \Omega_{\text{re}} + j\Omega_{\text{im}}$, where the real part accounts for the actual oscillation frequency and the imaginary part for the temporal damping due to radiation and loss. The complex frequency is now expressed as

$$\Omega = \Omega_0 + \Delta\Omega_{\text{re}} + j\Delta\Omega_{\text{im}}, \quad (4.36)$$

where $\Delta\Omega_{\text{re}} \in \mathbb{R}$ is a real deviation from $\Omega_0 \in \mathbb{R}$ and $\Delta\Omega_{\text{im}} \in \mathbb{R}$ is an imaginary contribution potentially accounting for radiation and loss⁸. One may alternatively write Equation (4.36) as

$$\Omega = \Omega_0 + \Delta\Omega, \quad (4.37a)$$

where

$$\Delta\Omega = \Delta\Omega_{\text{re}} + j\Delta\Omega_{\text{im}}. \quad (4.37b)$$

By formally substituting ω with Ω and γp with $j\Phi$ in Equation (4.13), the dispersion relation transforms into

$$\cos(\Phi) = \frac{1}{2} \frac{\left(\frac{1}{T^2} + T^2\right) \left(T + \frac{1}{T}\right)^2 + 2Z_{\text{se}}(\Omega)Y_{\text{sh}}(\Omega)}{\left(T + \frac{1}{T}\right)^2 - Z_{\text{se}}(\Omega)Y_{\text{sh}}(\Omega)}. \quad (4.38)$$

In this relation, given the substitution $\gamma p \rightarrow j\Phi$, Φ represents the phase difference between the terminals of the periodic unit cell as shown in Figure 3.12. Therefore, solving Equation (4.38) under specified values of Φ consists in solving the periodic boundary problem⁹ associate with the original problem described by (4.13).

Equation (4.38) may be solved for the immittance product to yield

$$Z_{\text{se}}(\Omega)Y_{\text{sh}}(\Omega) + K^2 = 0, \quad (4.39)$$

with

$$K^2 = \frac{(T^2 + 1)^2}{2T^4} \frac{T^4 - 2 \cos(\Phi) T^2 + 1}{\cos(\Phi) + 1}, \quad (4.40)$$

being the coupling coefficient, which is defined for later mathematical convenience.

The immittances in terms of the complex frequency are found by formally substituting ω with Ω in (3.8) and (3.13), which yields

$$Z_{\text{se}}(\Delta\Omega) = R + j2L\Delta\Omega = R \left(1 + j2Q_{\text{se}} \frac{\Delta\Omega}{\Omega_0}\right), \quad (4.41a)$$

$$Y_{\text{sh}}(\Delta\Omega) = G + j2C\Delta\Omega = G \left(1 + j2Q_{\text{sh}} \frac{\Delta\Omega}{\Omega_0}\right). \quad (4.41b)$$

Finally, inserting (4.41) into (4.39) produces the following quadratic equation in $\Delta\Omega$:

$$(R + j2L\Delta\Omega)(G + j2C\Delta\Omega) + K^2 = 0, \quad (4.42)$$

⁸Fundamentally, this imaginary contribution will ensure that the forthcoming new dispersion relation will have mathematical solutions for all choices of parameters.

⁹The same substitutions, $\omega \rightarrow \Omega$ and $\gamma p \rightarrow j\Phi$, are inherent to most commercial eigenmode simulators solving periodic boundary problems.

whose two solutions read

$$\Delta\Omega_{1,2} = \frac{1}{2\sqrt{LC}} \left(\pm \sqrt{K^2 + RG - \left(\frac{LG + CR}{2\sqrt{LC}} \right)^2} + j \frac{LG + CR}{2\sqrt{LC}} \right). \quad (4.43)$$

The corresponding *coupled* quality factors are directly obtained from the complex frequencies, using the relationship $\Omega \leftarrow \Omega_{\text{re}} \left(1 + j \frac{1}{2Q} \right)$ [78], and read

$$Q_{1,2} = \frac{\text{Re}(\Omega_{1,2})}{2 \text{Im}(\Omega_{1,2})} = \frac{\Omega_0 + \Delta\Omega_{\text{re}1,2}}{2 \Omega_{\text{im}1,2}}. \quad (4.44)$$

The complex frequencies $\Omega_{1,2} = \Omega_0 + \Delta\Omega_{1,2}$ generally represent *mathematical* solutions of the periodic boundary problem associated with the original electromagnetic (complex propagation constant) problem. It is important to realize that these mathematical modes do *not* necessarily represent the *physical propagation modes* under the LWA's operational condition, as discussed before.

Now, a numerical example is provided comparing the dispersion diagrams obtained through the complex propagation constant and the complex frequency analysis. The following set of parameters is used: $L = 2$ nH, $C = 0.4$ pF, $R = 12.57$ Ω , $G = 0.126$ mS and $\omega_{\text{bs}} = 2\pi \cdot 10$ GHz. The intrinsic quality factors according to Equations (3.7) and (3.12) are $Q_{\text{se}} = \frac{\omega_{\text{bs}}L}{R} = 10$ and $Q_{\text{sh}} = \frac{\omega_{\text{bs}}C}{G} = 200$, respectively. Even though these quantities are fictitious, they represent realistic practical values, adapted from [61, 62].

The leakage constant and the phase constant of the complex propagation constant are calculated with the exact formula in (4.13). Figures 4.8(a), (c) and (e) plot the complex propagation constant $T = 1$ (symmetric case), $T = T_{\text{opt}} = 1.0431$ (optimal transversal asymmetry case) and $T = 1.1$, respectively. It is mostly the broadside frequency region that is affected by transformation ratios and hence asymmetry variations, whereas the off-broadside region is only marginally affected as already pointed out in Section 4.2. Moreover, at broadside, the phase constant only exhibits minor slope (group velocity) variations, whereas the leakage constant at broadside experiences considerable variations. In the optimum case of Figure 4.8(c), the group velocity at broadside (10 GHz) is equal to the group velocity off-broadside (< 9 GHz and > 11 GHz), since the dispersion curve is perfectly linear, whereas this is not the case otherwise.

In Figure 4.8(a) (symmetric case), a dip in the leakage constant at broadside is observed. This dip is due to imbalance $Q_{\text{se}} = 10$ and $Q_{\text{sh}} = 200$ between the series and the shunt losses [34]. In Figure 4.8(c) (optimal asymmetry), the leakage constant is flat across broadside, due to the equalization between the broadside and off-broadside Bloch impedances. This is practically the most interesting case, where asymmetry is exploited for achieving equalized radiation efficiency when the beam scans through broadside. In Figure 4.8(e) ($T > T_{\text{opt}}$), a peak is observed in the leakage constant at broadside, indicating a situation where transversal asymmetry has become excessive.

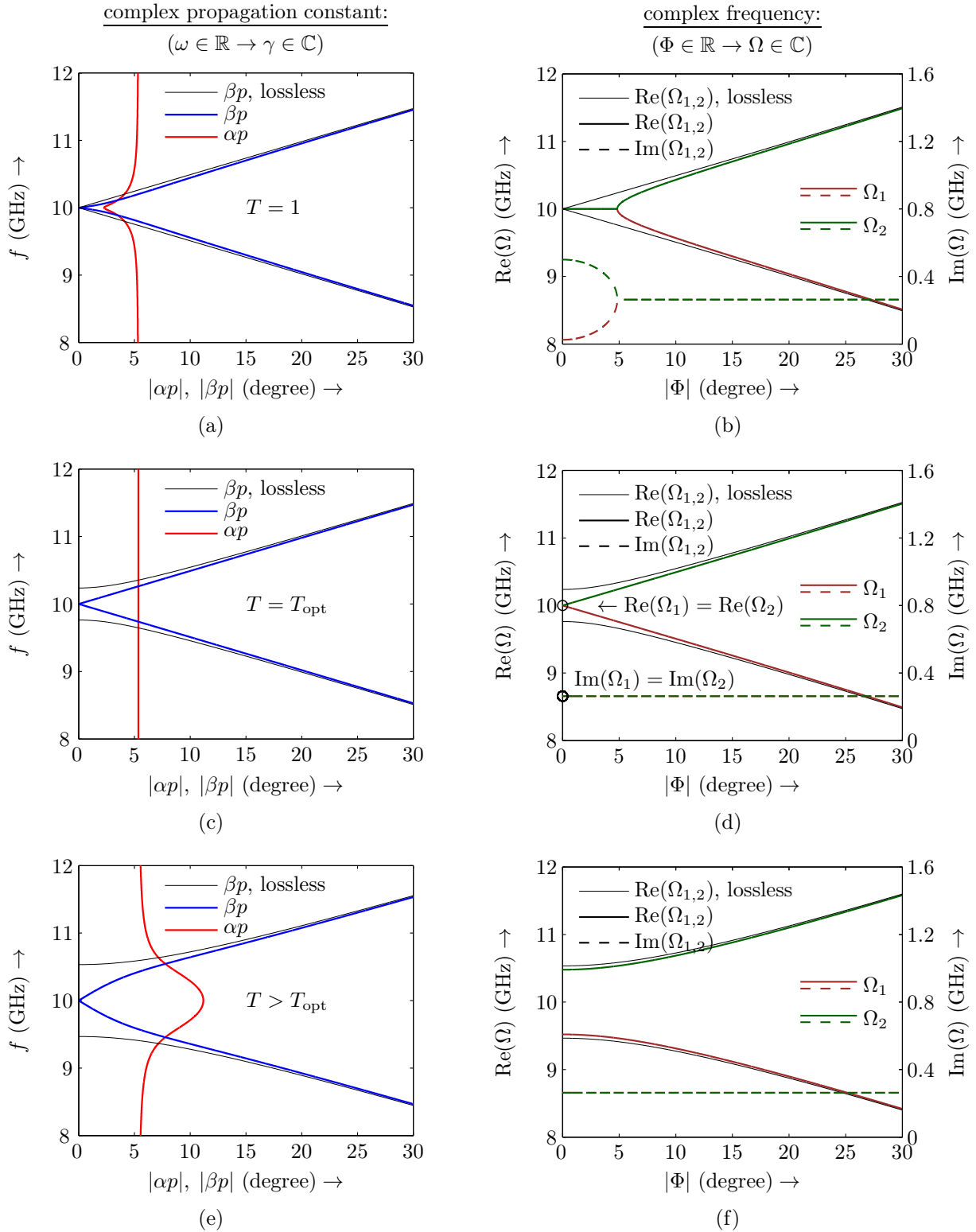


Figure 4.8: Dispersion diagram comparison of the *complex propagation constant* (left) and the *complex frequency* (right) for different transformation ratios. Dispersion from the complex propagation constant for: (a) Symmetric case where $T = 1$. (c) Optimal case, where $T = T_{\text{opt}}$. (e) $T > T_{\text{opt}}$. Dispersion from the complex frequency for: (b) Symmetric case ($T = 1$). (d) Optimal case ($T = T_{\text{opt}}$). (f) $T > T_{\text{opt}}$. (The black solid lines show the dispersion for the lossless case, where $R = G = 0$).

Figures 4.8(b), (d) and (f) show the dispersion diagram obtained by the complex fre-

quency analysis, computed by Equation (4.43) together with Equation (4.40). The same general observation as for the complex propagation constant analysis is made, where T strongly affects the broadside regime and has little effect in the off-broadside regime. Under optimal asymmetry in Figure 4.8(d), it is found that the two complex solutions are identical in their real *and* imaginary parts following that $\Omega_1 = \Omega_2$ holds for the complex frequency, which is analyzed in detail later in Section 4.3.3. Moreover, the comparison of Figures 4.8(c) and (d) show that identical responses are obtained from the complex propagation constant approach and the complex frequency approach. In this case there is a one-to-one correspondence between the two approaches, as already pointed out in [51] for a symmetric cell. In case of *over-coupling* ($T > T_{\text{opt}}$), represented in Figures 4.8(e) and 4.8(f), a stopband occurs for real frequencies, although the resonance frequencies of the intrinsic resonators are balanced with $f_{\text{se}} = f_{\text{sh}}$. The black solid lines in Figure 4.8 show the dispersion for the corresponding *lossless* unit cell ($R = G = 0$).

Figure 4.9 compares the quality factors of the complex propagation constant and the complex frequency analysis. The intrinsic Q s are chosen to be $Q_{\text{se}} = 10$ and $Q_{\text{sh}} = 200$, as aforementioned. The transmission line quality factor of Equation (3.58), $Q = \omega \frac{\partial \beta / \partial \omega}{2\alpha}$ is directly calculated through the propagation constant, whereas the complex frequency quality factors (*coupled* quality factors) are computed by Equation (4.44). The horizontal axes of the two approaches differ, frequency for the propagation constant modeling and phase angle Φ for the complex frequency modeling, which both are the respective independent parameters. A direct quantitative comparison is therefore not possible. Nevertheless, it is observed that the two approaches give very similar quality factors in the off-broadside regime, whereas at broadside the quality factors generally differ. Figure 4.9(a) shows the quality factor for the symmetric case, $T = 1$. The asymptotic at- and off-broadside Q s are derived in Section 3.3 and they read $Q_{\text{bs}} = \frac{\omega}{\omega_{\text{bs}}} \frac{Q_{\text{se}} + Q_{\text{sh}}}{2}$ [Equation (3.60)] and $Q_{\text{off-bs}} = \frac{\omega}{\omega_{\text{bs}}} \frac{2}{1/Q_{\text{se}} + 1/Q_{\text{sh}}}$ [Equation (3.66)]. Substituting the intrinsic Q s, the at- and off-broadside quality factors are $Q_{\text{bs}} = \frac{\omega}{\omega_{\text{bs}}} \cdot 105$ and $Q_{\text{off-bs}} \approx \frac{\omega}{\omega_{\text{bs}}} \cdot 19$, respectively, which is confirmed in Figure 4.9(a). Figure 4.9(b) shows the coupled Q s for the symmetric cell calculated from the complex frequency using Equation (4.44). As expected, the coupled Q s are identical to the intrinsic ones at $\Phi = 0$, which indicates that the two resonators are fully decoupled. Consequently, the coupled quality factors are most general and they obviously include the symmetric case as well.

For the optimal asymmetry case in Figures 4.9(c) and (d), the two approaches agree. Moreover, the two modes obtained from the complex frequency analysis in Figure 4.9(d) exhibit the exactly same Q s with $Q_1 = Q_2$ at $\Phi = 0$, which is a natural consequence from the complex frequency solution $\Omega_1 = \Omega_2$. This clearly demonstrates the unification of Q -balancing, so that this condition is applicable to symmetric and asymmetric unit cells for achieving equalization.

Figures 4.9(e) and (f) illustrate the case where asymmetry is applied beyond the optimal equalization point. The transmission line quality factor in Figure 4.9(e) shows a wide and pronounced dip at broadside. The coupled quality factors in Figure 4.9(f) show a nearly constant behavior over the variation of Φ , yet at $\Phi = 0$ a small gap comes up, which is explained through the splitting of the real frequency $\Omega_{\text{re}1,2}$, whereas Ω_0 and $\Omega_{\text{im}1,2}$ are constant in $Q_{1,2} = \frac{\Omega_0 + \Delta \Omega_{\text{re}1,2}}{2 \Omega_{\text{im}1,2}}$ [Equation (4.44)].

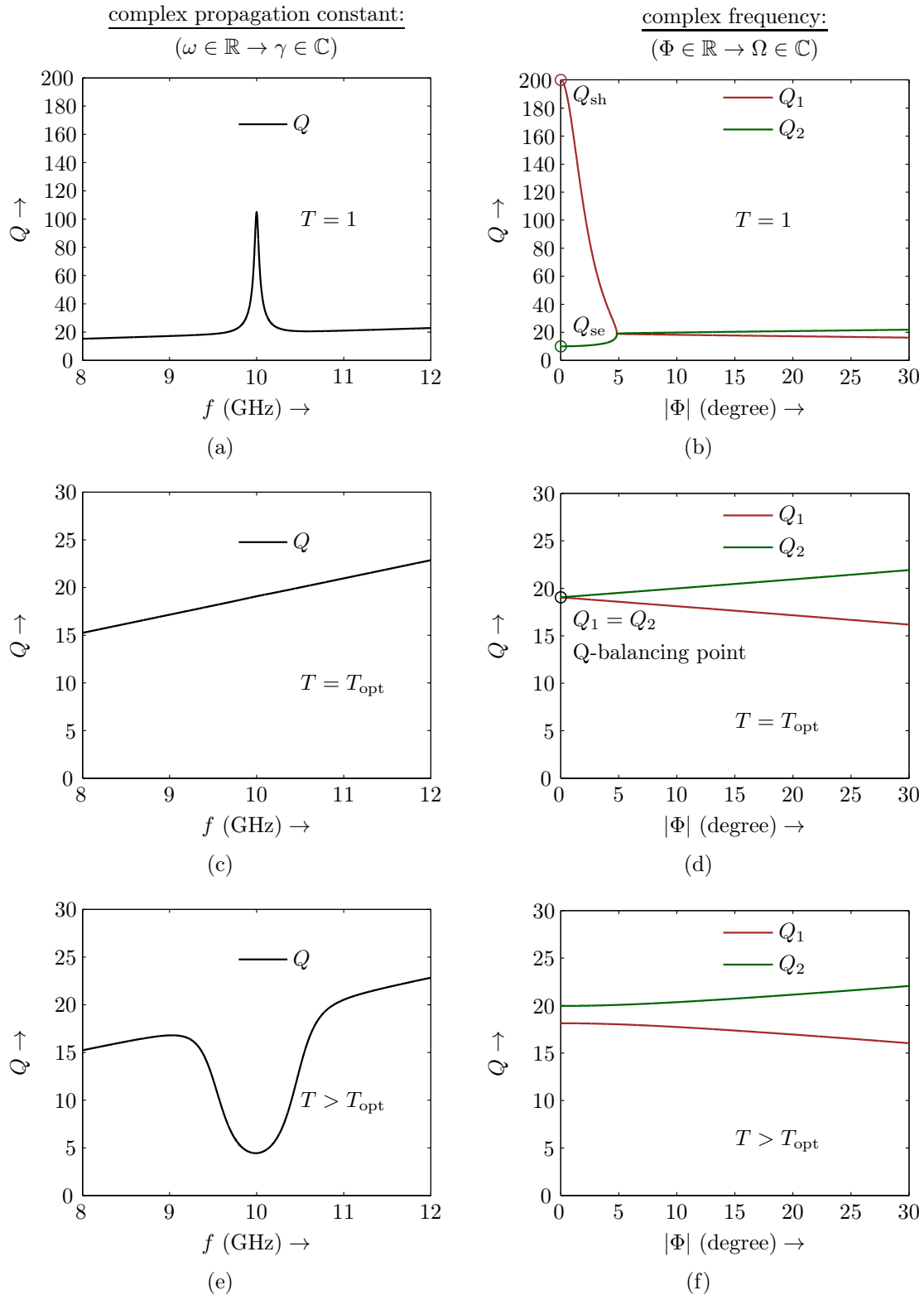


Figure 4.9: Quality factor comparison of the *complex propagation constant* (left) and the *complex frequency* (right) for different transformation ratios. Transmission line quality factor from the complex propagation constant for: (a) Symmetric case where $T = 1$. (c) Optimal case where $T = T_{\text{opt}}$. (e) $T > T_{\text{opt}}$. Coupled quality factors from the complex frequency for: (b) Symmetric case ($T = 1$). (d) Optimal case ($T = T_{\text{opt}}$). (f) $T > T_{\text{opt}}$.

4.3.2 Equality of the Two Analyses under Optimal Asymmetry

In the previous section the equality under optimal asymmetry of the two approaches is qualitatively discussed in Figure 4.8(c) and (d). Here, this link is formally established. Equation (4.40) simplifies to

$$K^2 \approx \frac{1}{4} \left(T^2 - \frac{1}{T^2} \right) + \Phi^2, \quad (4.45)$$

where Equation (4.40) is approximated by a Taylor series around the point $\Phi = 0$ assuming that T_{opt} is close to one. By inserting Equation (4.45) into Equation (4.43) and furthermore assuming the optimal asymmetry condition in (4.32) is fulfilled, one obtains the following solution for the complex frequency

$$\Delta\Omega = \Delta\Omega_{\text{re}} + j\Delta\Omega_{\text{im}} = \frac{1}{2\sqrt{LC}}|\Phi| + j\frac{LG + CR}{4LC}. \quad (4.46)$$

A linear slope over Φ of the real frequency $\Delta\Omega_{\text{re}}$ is observed in Equation (4.46). The imaginary frequency $\Delta\Omega_{\text{im}}$ is constant over Φ . Both of these conditions are confirmed in Figure 4.8(d), where a linear dispersion curve is shown.

Following the similar idea for the complex propagation constant and evaluating it under the optimal case, one simplifies Equation (4.16) to

$$\gamma = \alpha + j\beta = \frac{1}{p} \left(\frac{LG + CR}{2\sqrt{LC}} + j2\Delta\omega\sqrt{LC} \right), \quad (4.47)$$

where again, a linear dispersion along with a constant leakage over frequency is observed, as shown in Figure 4.8(c).

Now, by comparing the phase angle terms and the loss terms in Equations (4.46) and (4.47), it follows for the phase angles

$$\Delta\Omega_{\text{re}} = \frac{|\Phi|}{2\sqrt{LC}} \quad \text{and} \quad \Delta\omega = \frac{\beta p}{2\sqrt{LC}}, \quad (4.48a)$$

and for the loss terms

$$\Delta\Omega_{\text{im}} = \frac{LG + CR}{4LC} \quad \text{and} \quad \frac{\alpha p}{2\sqrt{LC}} = \frac{LG + CR}{4LC}. \quad (4.48b)$$

From Equation (4.48) the simple one-to-one correspondence is derived as

$$\Delta\Omega_{\text{re}} \longleftrightarrow \Delta\omega \quad \text{and} \quad \Delta\Omega_{\text{im}} \longleftrightarrow \frac{\alpha p}{2\sqrt{LC}}, \quad (4.49)$$

where $|\Phi| = \beta p$ is the phase shift across a unit cell unifying the two approaches. Equation (4.49) links the complex propagation constant analysis to the complex frequency analysis and vice versa, revealing a simple and straight forward relationship between them, for unit cells satisfying the optimal asymmetry condition. Only under this condition, the real part of the *complex frequency* is identical to the *real frequency*. Hence, both approaches are suitable to design and optimize LWAs for equalized efficiency through broadside.

4.3.3 Q-Balancing and Mode Degeneration

The Q-balancing condition for the coupled quality factors of the complex frequency analysis is illustrated in Figure 4.9(d). There, it is demonstrated by means of a numerical example that under optimal asymmetry the two coupled quality factors are identical. This section formally proves that optimal asymmetry results in *coupled quality-factor-balancing*. Furthermore, it demonstrated that, if one resonator is lossless and non-radiative with $R = 0$ or $G = 0$, the two coupled modes become degenerate with an identical field distribution under optimal asymmetry.

At broadside one has $\Phi = 0$ and $\cos(\Phi) = 1$, and therefore (4.40) reduces to

$$K^2 = \frac{1}{4} \left(T^2 - \frac{1}{T^2} \right)^2 = \tau^2, \quad (4.50)$$

where the second equality follows from (4.2). It may be important to point out that *no approximation* is made in the derivation of Equation (4.50) and as well for the upcoming derivations in this section, following analytically exact results.

Inserting $K = \tau_{\text{opt}}$ given by Equation (4.32a) into Equation (4.43) suppresses the radicand in (4.43) and reduces the two complex frequencies to the unique frequency

$$\Omega_1 = \Omega_2 = \Omega_0 + \Delta\Omega_{1,2} = \Omega_0 + j \frac{LG + CR}{4LC}. \quad (4.51)$$

This result is identical to the one previously derived in Equation (4.46) when $\Phi = 0$ in (4.46). Nevertheless, the derivation of Equation (4.51) through (4.50) is presented here to emphasize that the complex frequency result and the forthcoming Q-balancing condition are not approximative as aforementioned. Evaluating Equation (4.51) clearly shows that the two complex frequencies are equal. This situation is thus called *complex frequency-balancing* as initially announced and demonstrated in Figure 4.8(d).

The corresponding quality factors, obtained by inserting (4.51) into (4.44), are

$$Q_{\text{bal}} = Q_1 = Q_2 = \frac{\Omega_0}{2(LG + RC)/4LC} = \frac{2}{1/Q_{\text{se}} + 1/Q_{\text{sh}}}, \quad (4.52)$$

where $Q_{\text{se}} = \omega_{\text{bs}}L/R$ and $Q_{\text{sh}} = \omega_{\text{bs}}C/G$ are the intrinsic quality factors under the condition that $\Omega_0 = \omega_{\text{bs}}$. Equation (4.52) confirms the Q-balancing condition for the coupled modes in the optimal asymmetry case as shown in Figure 4.9(d). The transmission line quality factor calculated through the complex propagation constant and the coupled quality factor as given in Equation (4.52) are identical at broadside, which is confirmed in Figures 4.9(c) and 4.9(d).

Now, the field distribution of the two eigenmodes is investigated to show that these modes exhibit the same field distributions. Previously, it is phenomenologically observed that the complex eigenfrequencies are equal and the result should be a modal degeneration.¹⁰

The SFP example is used again to demonstrate and illustrate the analysis. Here, this example is reduced to a strongly simplified one-dimensional transmission line model as

¹⁰Only if one resonator, series or shunt, is lossless and non-radiative with $R = 0$ or $G = 0$. Note that for the *symmetric* and equalized unit cell with $Q_{\text{se}} = Q_{\text{sh}} = Q_1 = Q_2$ and $T = 1$, the modes are obviously not degenerate.

shown in Figure 4.10. This abstraction layer forms an absolute minimum which is chosen for two reasons. First, the fields can be represented by voltages and currents and they just depend on a single coordinate, which makes the evaluation much simpler as compared to three-dimensional field data. Second, the transformation ratio T can be calculated analytically, which allows to set up the perfect optimum.¹¹

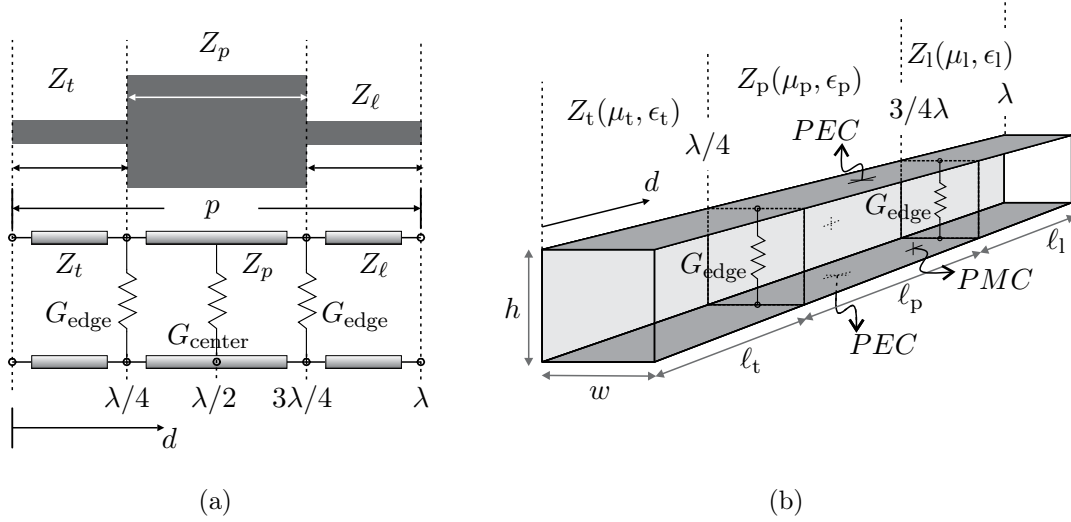


Figure 4.10: SFP model simplification with $G = G_{\text{center}} = 0$ for the illustration of degenerated modes. (a) SFP layout and corresponding simplified ideal transmission line model with radiation conductances for series (G_{edge}) and shunt (G_{center}) radiation. (b) Fullwave eigenmode parallel plate waveguide model with PEC and PMC boundaries corresponding to the ideal transmission line model in (a). At $d = \lambda/4$ and $d = 3\lambda/4$ sheet conductors with G_{edge} are placed. G_{center} is set to zero.

Figure 4.10(a) shows the abstraction of the SFP unit cell by modeling it with three cascaded transmission lines. These three lines have the characteristic impedances Z_t for the transformation line, Z_p for the wide patch element and Z_ℓ for the connecting line. Their lengths are $\lambda/4$, $\lambda/2$ and $\lambda/4$, respectively, where λ is the free-space wavelength at the broadside frequency. The conductances G_{edge} model the patch radiation from the series mode and the conductance G_{center} models the shunt radiation, which obviously follows from the distributions in Figure 3.5.

Figure 4.10(b) shows the corresponding fullwave simulation model, where an ideal parallel plate waveguide is chosen as transmission line type. The boundaries at the top and bottom (dark gray) are PEC walls, whereas the side walls (bright gray) are PMC boundaries so to obtain the homogeneous field distribution of the parallel plate waveguide in the cross section. The edge conductances G_{edge} are implemented by means of sheet resistors providing the required conductance and are located at $d = \lambda/4$ and $d = 3\lambda/4$. The center conductance G_{center} is set to zero for simplicity. The characteristic impedance of the left line Z_t is varied so to apply asymmetry to the unit cell. For convenience, the cross section area of the three sections in Figure 4.10(b) shall be equal and moreover, the overall unit cell length of each subsection ($\lambda/4$, $\lambda/2$ and $\lambda/4$) shall be constant and correspond to the free-space wavelength even if Z_t , i.e. T , is varied. With these constraints, only the

¹¹Technically, the overall field distribution of the one-dimensional transmission line model could also be solved analytically. Yet, the numerical solution from HFSS [96] is preferred for the sake of consistency.

permittivity and the permeability in each line section can be adjusted and they have to be carefully chosen to link the models of Figures 4.10(a) and 4.10(b) under the given constraints.

Table 4.2 lists the parameters and formulas used to set up the fullwave model of Figure 4.10(b). The product of the permittivity and the permeability in each line section is one, so that the guided wavelength $\lambda_g = \frac{\lambda_0}{\sqrt{\epsilon_r \mu_r}}$ in each line section corresponds to the free-space wavelength λ_0 . This might cause some relative material parameters to be less than one, which is commonly not realizable with conventional materials at microwave frequencies. Nevertheless, the purpose of this setup is mainly to illustrate and compare the field distributions rather than providing a physical realizability.

Table 4.2: Parametrization of the fullwave transmission line model in Figure 4.10(b). The frequency f_0 is set to 24 GHz. The permittivity and the permeability are artificially manipulated so that under the variation of Z_t the geometry of the model is not altered.

Name	Value	Unit	Name	Value	Unit	Name	Value	Unit
Z_t	60...100	Ω	μ_t	$\sqrt{\frac{\epsilon_0}{\mu_0} \frac{w}{h}} Z_t$		ϵ_t	$1/\mu_t$	
Z_p	40	Ω	μ_p	$\sqrt{\frac{\epsilon_0}{\mu_0} \frac{w}{h}} Z_p$		ϵ_p	$1/\mu_p$	
Z_1	100	Ω	μ_1	$\sqrt{\frac{\epsilon_0}{\mu_0} \frac{w}{h}} Z_1$		ϵ_1	$1/\mu_1$	
G_{edge}	1/400	Siemens	p	$\ell_t + \ell_p + \ell_1$	m	ℓ_t	$\frac{c_0}{4f_0} = \lambda_0/4$	m
h	0.01	mm	p	c_0/f_0	m	ℓ_p	$\frac{c_0}{2f_0} = \lambda_0/2$	m
w	0.01	mm	p	λ_0	m	ℓ_1	$\frac{c_0}{4f_0} = \lambda_0/4$	m

The transformation ratio is calculated from the overall transmission matrix, which is obtained through cascading the five individual ABCD matrices (transformation line, conductance, patch line, conductance and connecting line in Figure 4.10). It follows for the overall cascade

$$\mathbf{ABCD} = \begin{pmatrix} 0 & jZ_t \\ j/Z_t & 0 \end{pmatrix} \begin{pmatrix} 1 & 0 \\ G_{\text{edge}} & 1 \end{pmatrix} \begin{pmatrix} -1 & 0 \\ 0 & -1 \end{pmatrix} \begin{pmatrix} 1 & 0 \\ G_{\text{edge}} & 1 \end{pmatrix} \begin{pmatrix} 0 & jZ_1 \\ j/Z_1 & 0 \end{pmatrix} \quad (4.53)$$

$$= \begin{pmatrix} Z_t/Z_1 & 2Z_t Z_1 G_{\text{edge}} \\ 0 & Z_1/Z_t \end{pmatrix}. \quad (4.54)$$

Recalling Equation (4.5), $T = \sqrt{\frac{D+1}{A+1}}$, and inserting the matrix parameters from (4.54) into it, results in

$$T = \sqrt{\frac{Z_1}{Z_t}}, \quad (4.55)$$

which is the transformation ratio for the transmission line model in Figure 4.10. Figure 4.11 plots the complex frequency solutions obtained from HFSS [96], where a constant phase shift $\Phi = 0$ is applied across the unit cell and the impedance of the transformation line, Z_t is varied from 100 to 60 Ω . The horizontal top and bottom axis read the degree of asymmetry, where Z_t is provided on the top axis and T on the bottom axis. Both axes are linked by Equation (4.55).

The plot in Figure 4.11 is qualitatively very similar to the one in Figure 4.8(a), where the complex frequency solution are plotted for a *symmetry cell* under the *variation of the phase angle* Φ . Comparing these two figures, it is interesting to observe that increasing the asymmetry in Figure 4.11 has *qualitatively* the same effect as increasing the phase shift in a symmetric unit cell. Both result into the equalization point, where $\Omega_1 = \Omega_2$. With a phase shift different from zero, the *symmetric* cell naturally encounters an *asymmetric* field distribution and hence these two effects are strongly linked. Thus, one might interpret the optimal asymmetry case as an optimal *phase shift* that is transformed to broadside.

The optimal asymmetry for the simplified transmission line model is read from Figure 4.11, where $Z_{T,\text{opt}} = 85.85 \Omega$, corresponding to $T_{\text{opt}} = 1.079$ according to Equation (4.55).

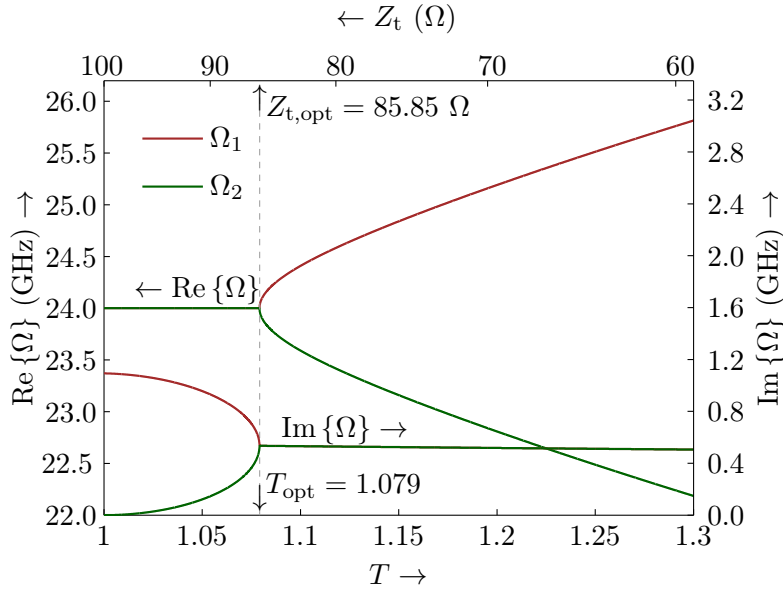


Figure 4.11: Complex frequency versus the transformation ratio T for $\Phi = 0$, simulated with HFSS. The bottom horizontal axis shows T and the top axis the corresponding transmission line impedance Z_t according to (4.55). T_{opt} is 1.079 ($Z_{t,\text{opt}} = 85.85 \Omega$). At this point the two modes become degenerate with $\Omega_1 = \Omega_2$.

The field distribution in terms of normalized voltage across the transmission line model is examined for different asymmetry scenarios. Figure 4.12 shows the voltages calculated with HFSS along the unit cell, where the normalized amplitude is given in the upper plots and the phase is given the plots beneath. Figure 4.12(a) shows the case, where the unit cell is symmetric following two perfect standing wave resonance distributions as indicated by the phase distribution. These two modes are the series and the shunt mode as previously extensively discussed in Chapter 3. By applying only moderate asymmetry, which means less than the optimal case would require, one obtains a field distribution as shown in Figure 4.12(b) for the case where $Z_t = 90 \Omega$, corresponding to $T = 1.054$. Here, the intrinsic series and shunt modes are not present anymore and they start to couple through the boundaries forming new modes, which are referred to as to *mode 1* and *mode 2*. This type of moderate asymmetry is deliberately chosen to demonstrate the *transition* from the ideal perfect series and shunt modes to the coupled modes, where in Figure 4.12(b) a dominate series and shunt characteristic is still present. Moreover, Figure 4.12(b) reveals that mode 1 and mode 2 are turning into traveling waves, which is supported by the linear phase distribution.

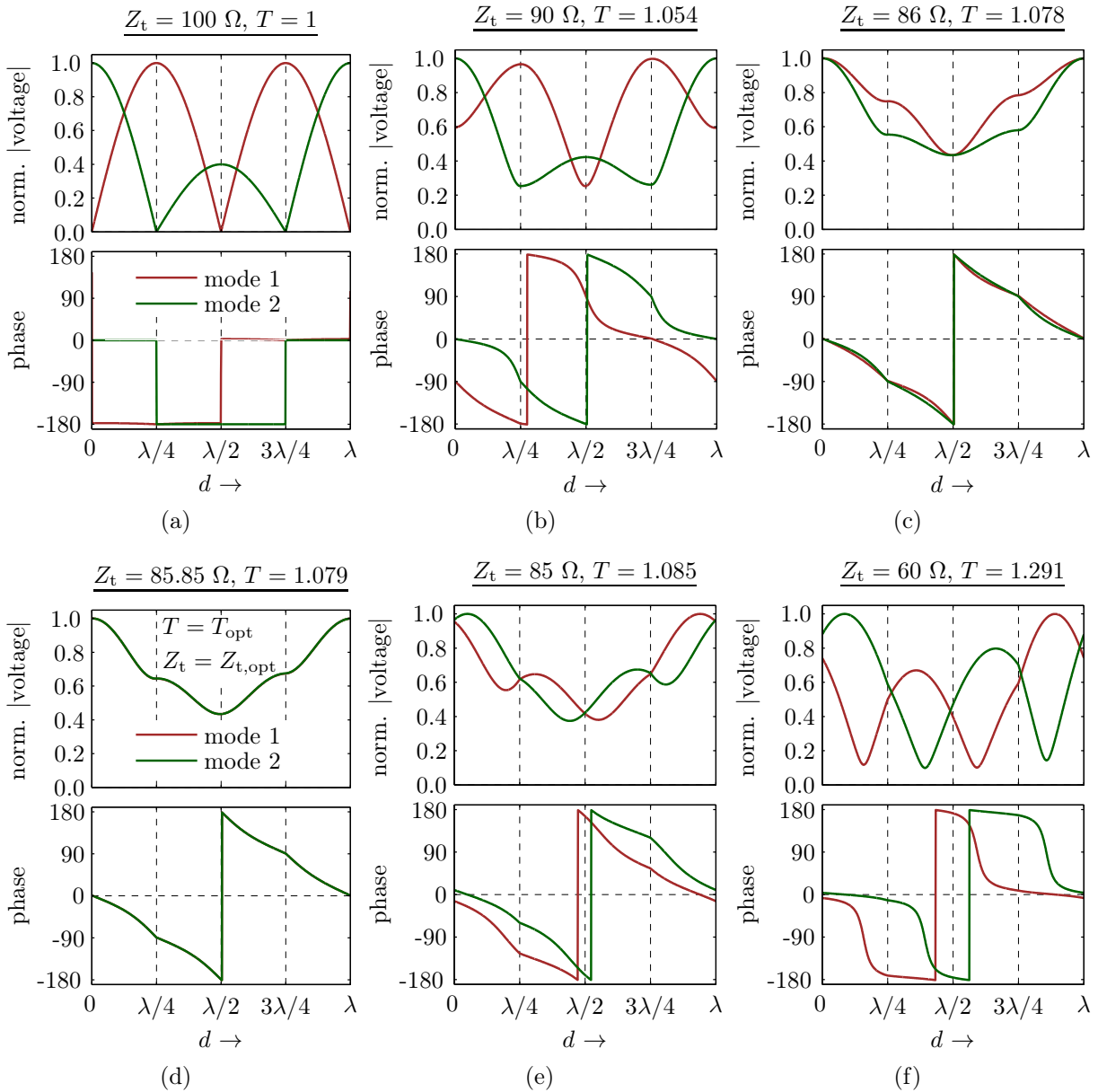


Figure 4.12: Normalized voltage distribution (eigenmodes) along the fullwave unit cell model of Figure 4.10(b). The unit cell asymmetry is varied from (a) to (f) by changing Z_t from 100Ω to 60Ω . The mode degeneration is observed for the optimum case in (d), where the two eigenmodes become degenerate by exhibiting an identical voltage distribution.

Very close to the optimal case, the phase distributions of the two modes are almost overlapping, whereas the amplitude distribution still encounters discrepancies as shown in Figure 4.12(c). Under this scenario, a dominate series and shunt nature in the two modes is no longer present. Finally, Figure 4.12(d) shows the optimal case with a perfect superposition of the voltage amplitude and phase distribution. The phase is almost perfectly linear indicating the traveling nature, so that this mode degeneration point goes along with a perfect traveling wave distribution. If the asymmetry is applied beyond the optimal point, as plotted in Figures 4.12(e) and 4.12(f), one observes a splitting of the two modes and the formation of standing waves. This can be confirmed in Figure 4.12(f), where the phase dominantly alternates between 0° and 180° implying a standing wave.

4.3.4 The “Complex-Frequency-Balancing” Condition – Unification of Frequency and Q-Balancing Conditions

Eventually, one concludes that optimal asymmetry in the structure yields optimal *field* asymmetry, which results in two identical complex frequency solutions. They are identical in their real and imaginary parts, a condition defined as *complex frequency-balancing*. This is a necessary and sufficient condition for equalization, which unifies the two conditions, frequency-balancing *and* Q-balancing within one single condition, namely *complex frequency-balancing*. By defining the coupled quality factor as in Equation (4.44), the Q-Balancing concept is generalized under the frame of complex frequency-balancing, in order to characterize both, symmetric and asymmetric, LWA.

4.4 Fullwave Optimization based on Eigenmode Solutions in the Complex Frequency Domain

This section proposes an optimization scheme, based on the one described in Section 3.4.3, to design LWAs with equalized radiation characteristics through broadside. A major problem that occurs is to tune the unit cell for the Q-balancing point, which is highly sensitive. This sensitivity can also be understood from Figure 4.11, where a small deviation from T_{opt} causes a rapid splitting either for the real or imaginary frequency solution. Moreover, for the *initial* LWA unit cell the intrinsic series and shunt resonators are most likely not frequency-balanced and hence an optimization procedure needs to be devised that is capable of extracting these intrinsic resonance frequencies. In other words, asymmetry and the intrinsic resonance frequencies both affect the complex frequency solution. Unfortunately, the complex frequency solution with periodic boundaries ($\Phi = 0$) does not provide isolation of these two effects due to coupling. An optimization scheme that based on the complex frequency solution of the periodic boundary problem is therefore difficult to devise, if not impossible.

The solution here consists in separating the two coupled modes by using PEC and PMC boundaries instead of periodic boundaries to isolate the series and the shunt modes, respectively. The simplified one-dimensional transmission line model in Figure 4.10 is used again to illustrate the separation of the coupled modes. Figure 4.13 compares the amplitude of the normalized voltage and current distribution under periodic, PEC and PMC boundaries, where $Z_t = 86 \Omega$ ($T = 1.078$), same as in Figure 4.12(c). The upper plots provide the magnitude of the normalized voltages, whereas the lower ones show the magnitude of the normalized currents along the transmission line model of Figure 4.10. Figure 4.13(b) plots the voltage and current distribution under PEC boundaries and clearly shows that the series mode is present, while the shunt mode is totally suppressed. Observing Figure 4.13(c) confirms the isolation of the shunt mode and the suppression of the series mode by the PMC boundary condition corresponding to an open.

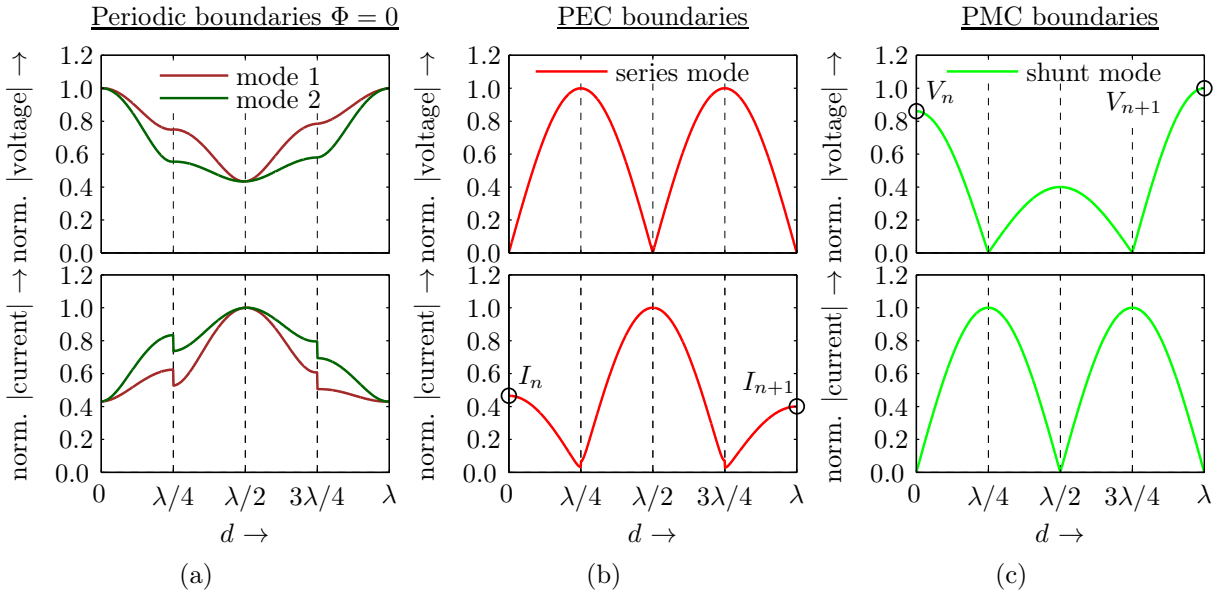


Figure 4.13: Voltage and current distributions (eigenmodes) for the asymmetric case $Z_T = 86 \Omega$ for different imposed boundary conditions located at $d = 0$ and $d = \lambda$. (a) Distributions under periodic boundaries with $\Phi = 0$ corresponding to Figure 4.12(c), where the two non-orthogonal modes couple. (b) Distributions under PEC boundaries for the isolation of the series mode. (c) Distributions under PMC boundaries at for the isolation of the shunt mode.

4.4.1 Isolation of the Series Mode with PEC Boundaries

The PEC boundary condition imposes $V_n = V_{n+1} = 0$, which leads to $V_{sh} = 0$ from Equation (4.1a) and hence isolates Z_{se} , where only the upper part of the transformer lattice circuit in Figure 4.14(b) subsists. This corresponds to a PEC resonant mode, where the series currents I_n and I_{n+1} are computed from the electromagnetic eigenmode as

$$I_n = \oint_{\mathcal{C}_n} \bar{H} \cdot d\bar{l} \quad \text{and} \quad I_{n+1} = \oint_{\mathcal{C}_{n+1}} \bar{H} \cdot d\bar{l}, \quad (4.56)$$

similarly to approach in Section 3.4.3 for the symmetric unit cell. \bar{H} is the magnetic field existing on the PEC boundaries and $\mathcal{C}_n, \mathcal{C}_{n+1}$ are the closed integration contours indicated in Figure 4.14(a). As an initial step towards determining I_{se} and T , one inserts I_{se} from Equation (4.1b) with $V_{sh} = 0$ into Equation (4.1d) to find

$$0 = TI_n - \frac{I_{n+1}}{T} + \frac{I_n + I_{n+1}}{\left(T + \frac{1}{T}\right)} \left(\frac{1}{T^2} - T^2\right), \quad (4.57)$$

and solve this equation for T so to get

$$T = \sqrt{\frac{I_n}{I_{n+1}}}. \quad (4.58)$$

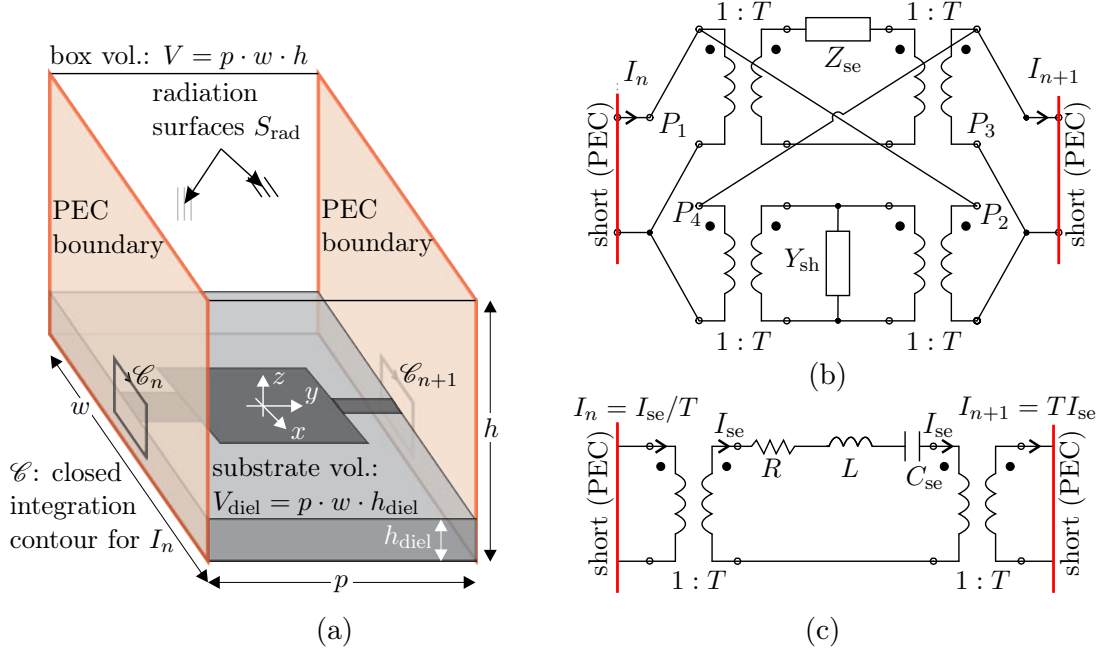


Figure 4.14: PEC boundary condition to isolate the series mode. (a) Fullwave model from Figure 3.14(a), which is adapted to asymmetry by monitoring I_n and I_{n+1} with \mathcal{C}_n and \mathcal{C}_{n+1} , respectively. (b) Overall transformer lattice circuit where the input and output is shorted corresponding to the PEC condition. (c) Resulting circuit where only the series impedance subsists due to the suppression of the shunt resonance with $V_{sh} = 0$.

Upon substituting Equation (4.58) into Equation (4.1b), one finds that the PEC series current, I_{se} , is the *geometric mean* of the eigenmode terminal currents, i.e.

$$I_{se} = \frac{I_n + I_{n+1}}{\left(T + \frac{1}{T}\right)} = \sqrt{I_n I_{n+1}}. \quad (4.59)$$

Recalling the energy and power relations from Equation (3.83),

$$W = W_e + W_m = 2W_m = 2W_e, \quad (4.60a)$$

$$W = 2\frac{1}{4}\mu_0 \int_V \bar{H} \cdot \bar{H}^* dv, \quad (4.60b)$$

$$P_{rad} = \frac{1}{2} \int_{S_{rad}} \text{Re} \{ \bar{E} \times \bar{H}^* \} \cdot d\bar{s}, \quad (4.60c)$$

$$P_{die} = \frac{1}{2} \int_{V_{die}} \bar{E} \cdot \bar{J}^* dv, \quad (4.60d)$$

$$P_{con} = \frac{R_s}{2} \int_{S_{con}} \bar{H}_{tan} \cdot \bar{H}_{tan}^* ds, \quad (4.60e)$$

since they are not restrictive to symmetric unit cells, one obtains the series LCRG parameters as follows

$$\begin{aligned}
 L = L_{se} &= \frac{4W_m}{|I_{se}|^2}, \quad C_{se} = \frac{1}{\omega_{se}^2 L_{se}}, \\
 R_{rad} &= \frac{2P_{rad}}{|I_{se}|^2}, \quad R_{die} = \frac{2P_{die}}{|I_{se}|^2}, \quad R_{con} = \frac{2P_{con}}{|I_{se}|^2}, \\
 R &= R_{rad} + R_{die} + R_{con},
 \end{aligned} \tag{4.61}$$

where

$$\omega_{se} = 2\pi f_{se} = \text{Re}(\Omega_{se}) \tag{4.62}$$

is the series resonance frequency. Equations (4.61) and (4.62) are identical to the symmetric case, so that once the correct T and I_{se} is determined, one can essentially follow the same steps as described in Section 3.4.3. The series radiation efficiency is then given by

$$\eta_{se} = R_{rad}/R \tag{4.63}$$

and the quality factor of the intrinsic series resonance mode reads

$$Q_{se} = \frac{\text{Re}(\Omega_{se})}{2\text{Im}(\Omega_{se})} = \frac{\text{Re}(\Omega_{se})L_{se}}{R}. \tag{4.64}$$

It is important to note that the quality factor computed by Equation (4.64) is the *intrinsic* and not the *coupled* quality factor due to the mode isolation with PEC. Moreover, it is worth mentioning that, for the symmetric case, the PEC boundary condition is a natural consequence from the periodicity with $\Phi = 0$. Here, for the asymmetric case the PEC boundary condition is externally imposed to achieve decoupling by the suppression of the shunt mode.

4.4.2 Isolation of the Shunt Mode with PMC Boundaries

Similarly to the previous case, one now applies PMC boundary condition to isolate and characterize the shunt resonator as shown in Figure 4.15(a). This PMC condition is externally forced and it imposes $I_n = I_{n+1} = 0$. This leads to $I_{se} = 0$ from Equation (4.1b) and hence isolates Y_{sh} , where only the lower part of the transformer lattice circuit model in Figure 4.15(b) subsists.

This corresponds to a PMC resonant mode, where the shunt voltages V_n and V_{n+1} are computed from the electromagnetic eigenmode as

$$V_n = \int_{\mathcal{L}_n} \bar{\mathbf{E}} \cdot d\bar{\mathbf{l}} \quad \text{and} \quad V_{n+1} = \int_{\mathcal{L}_{n+1}} \bar{\mathbf{E}} \cdot d\bar{\mathbf{l}}, \tag{4.65}$$

where $\bar{\mathbf{E}}$ is the electric field existing on the PMC boundaries and \mathcal{L}_n , \mathcal{L}_{n+1} are the integration lines as indicated in Figure 4.15(a).

Inserting $I_{se} = 0$ into Equation (4.1c) yields

$$T = \sqrt{\frac{V_{n+1}}{V_n}}. \tag{4.66}$$

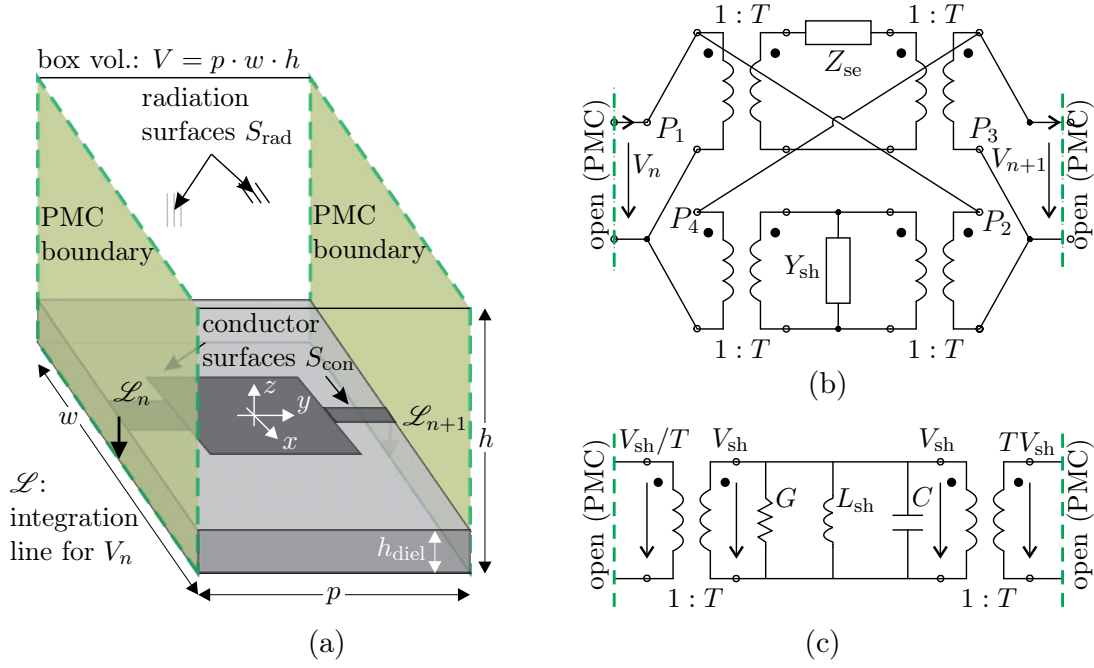


Figure 4.15: PMC boundary condition to isolate the shunt mode. (a) Fullwave model from Figure 3.14(b), which is adapted to asymmetry by monitoring V_n and V_{n+1} with \mathcal{L}_n and \mathcal{L}_{n+1} , respectively. (b) Overall transformer lattice circuit where the input and output is open corresponding to the PMC condition. (c) Resulting circuit where only the shunt admittance subsists due to the suppression of the series resonance with $I_{se} = 0$.

The transformation ratios T obtained from PEC and PMC simulation in Equations (4.58) and (4.66), respectively, are necessarily equal.

Upon substituting (4.66) into (4.1a), one finds the PMC shunt voltage as the geometric average of the eigenmode terminal voltages, i.e.

$$V_{sh} = \frac{V_n + V_{n+1}}{\left(T + \frac{1}{T}\right)} = \sqrt{V_n V_{n+1}}. \quad (4.67)$$

Using the energy and power relations in (4.60), one then determines the shunt parameters as follows

$$\begin{aligned} C = C_{sh} &= \frac{4W_e}{|V_{sh}|^2}, & L_{sh} &= \frac{1}{\omega_{sh}^2 C_{sh}}, \\ G_{rad} &= \frac{2P_{rad}}{|V_{sh}|^2}, & G_{die} &= \frac{2P_{die}}{|V_{sh}|^2}, & G_{con} &= \frac{2P_{con}}{|V_{sh}|^2} \\ G &= G_{rad} + G_{die} + G_{con}, \end{aligned} \quad (4.68)$$

where

$$\omega_{sh} = 2\pi f_{sh} = \text{Re}(\Omega_{sh}) \quad (4.69)$$

is the shunt resonance frequency. The shunt radiation efficiency

$$\eta_{sh} = G_{rad}/G, \quad (4.70)$$

is then obtained by Equation (3.11), and the intrinsic shunt quality factor is given by

$$Q_{sh} = \frac{\text{Re}(\Omega_{sh})}{2\text{Im}(\Omega_{sh})} = \frac{\text{Re}(\Omega_{sh})C_{sh}}{G}. \quad (4.71)$$

4.4.3 Optimization Procedure

An optimization procedure to design equalized LWAs, which is based on the PEC and PMC mode isolation is proposed comprising the following steps:

1. initial start with an transversally symmetric unit cell
2. simulate the unit cell with PEC to extract L, R, T and $\omega_{se} = \text{Re} \{ \Omega_{se} \}$
3. simulate the unit cell with PMC to extract C, G, T and $\omega_{sh} = \text{Re} \{ \Omega_{sh} \}$
4. balance the intrinsic series and shunt resonances by modified the unit cell geometry and repeat steps 2.) and 3.) to minimize the error function $\text{err}(\omega) = |\omega_{se} - \omega_{bs}| + |\omega_{se} - \omega_{bs}|$, which accounts for the frequency-imbalancing
5. if $\text{err}(\omega)$ is sufficiently small, the unit cell is considered frequency-balanced and the optimal transformation ratio T_{opt} [Equations (4.32) and (4.35)] is calculated
6. the degree of asymmetry is gradually increased following a frequency re-tuning in step 4.) to minimize the error function $\text{err}(T) = |T_{\text{opt}} - T|$
7. if both error functions, $\text{err}(\omega)$ and $\text{err}(T)$, are simultaneously less than the specified termination criteria, the unit cell is considered optimal and hence the LWA is equalized

A reasonable termination criterion is empirically found to be $\text{err}(\omega) < \omega_{bs} \cdot 10^{-3}$ for the frequency-balancing. Similarly, for the degree of asymmetry the criterion $\text{err}(T) < T_{\text{opt}} \cdot 10^{-3}$ is a good compromise. These values may be seen as a rule thumb in a sense that different LWA types show different sensitivity behaviors with respect to geometrical variations. Therefore, some unit cells can be optimized in a rather robust way according to the given criteria, whereas other unit cells are too sensitive so that even in the simulator these criteria cannot be met by a reasonable geometry parameter stepping.

It is worth mentioning that for the optimization procedure as discussed before, the simulation with periodic boundary condition with $\Phi = 0$ is not even required. All the relevant information to fully characterize the unit cell is extracted from PEC and PMC simulation. Nevertheless, the simulation with periodic boundaries can be done as a final step to verify the optimization and to confirm the complex frequency-balancing condition.

The actual implementation of this optimization scheme in the simulator HFSS is slightly different from what is outline before. It is, for several reasons, most desirable to have the same spatial discretization (the same FEM mesh) for the three possible boundary scenarios, PEC, PMC and periodic boundaries. Especially, if these different boundary cases are to be compared on a very accurate basis, one has to eliminate simulation inaccuracies caused by different meshes. Obviously, by using the same mesh for the PEC, the PMC and the periodic simulation, one avoids this inaccuracies and obtains highly comparable results. The simulator HFSS provides adaptive meshing, where the mesh is refined until a defined convergence criterion is met. The idea consists in using this adaptive meshing to generate and refine a mesh for the periodic boundaries simulation and then reuse the *same* mesh for the PEC and PMC simulations. This discretization or meshing issue and the resultant simulation sequence, first periodic and then PEC/PMC, is inherent to the

simulator HFSS.¹² Yet, it is considered important to provide the details, since this scheme is extensively used to optimize unit cells in upcoming section.

4.5 Case Study LWAs for Model Validation

This section uses the CRLH LWA of Chapter 3 and introduces asymmetry to the unit cell as a first case study example. In addition, this section presents a novel series-fed coupled patch (SFCP) LWA [49] as a second case study example to validate the theory and to demonstrate the resolution of the broadside degradation.

The two independent extraction methods, eigenmode [Section 4.4] and drivenmode [Section 4.1.2 in combination with Section 3.4.2] are employed, for the determination of the LCRG equivalent circuit parameters and the series/shunt efficiencies. While the eigenmode extraction technique is explicitly described for *asymmetric* unit cells in Section 4.4, the drivenmode extraction for *asymmetric* unit cells is not explicitly outlined so far. Nevertheless, the relevant formulas to extract T , Z_{se} and Y_{sh} from the two-port parameters, obtained from drivenmode simulation, are provided in Section 4.1.2 for asymmetric unit cells. Once these parameters are found, the immittance linearization technique in Section 3.1.2 is applied to find the intrinsic LCRG parameters of the lattice. This extraction can also be combined with the multiple unit cell evaluation in Section 3.4.2, where a cascade of N cells is simulated, in order to better take into account the periodicity. This multiple unit cell method is *not restricted* to the evaluation of only symmetric unit cells.

Finally, this section compares the radiation efficiencies predicted by the LCRG circuit model [Equation (4.28)] with the overall radiation efficiencies of the corresponding LWAs composed of 50 unit cells to experimentally confirm the control over the broadside efficiency.

The following design and simulation parameters are chosen for the two LWAs. The dielectric constant of the substrate is $\epsilon_r = 3.66$ with $\tan \delta = 0.004$ (Rogers 4350). The copper metalization is modeled as an infinitely thin sheet of surface resistivity $R_s = 0.02 \Omega$ per square to take into account the skin effect around the broadside frequency that is set to 10 GHz. For both, extracting the LCRG equivalent circuit parameters and computing the efficiency of the finite length LWAs, the two commercial fullwave electromagnetic simulators, EMPIRE (FDTD) [95] and HFSS (FEM) [96] are employed. The modeling of LWAs by these simulators, using the aforementioned extraction methods, have been extensively validated against measurements in Chapter 3, and one shall therefore rely on them as the benchmark for the validation in this section.

4.5.1 Composite Right/Left-Handed LWA

Figure 4.16 shows the configuration and design parameters of the metal-insulator-metal (MIM) CRLH LWA. An MIM CRLH configuration was first demonstrated in [103] and

¹² The simulation with periodic boundaries requires an *identical* mesh on each boundary at $y = -d/2$ and $y = +d/2$ to realize the field mapping with $\Phi = 0$. The simulation with PEC/PMC boundaries do not have such a constraint and the meshes on the boundaries can be different. Therefore, the PEC/PMC simulations can employ the generated and refined mesh from the periodic boundary simulation. In contrast, the periodic simulation cannot employ the meshes generated with PEC/PMC boundaries, as these meshes do not allow the field mapping with $\Phi = 0$.

later further investigated and refined in [58, 62, 66]. As already discussed in Chapter 3, CRLH LWAs radiate in their fundamental ($\mathbf{n} = 0$) space harmonic. The structure consists of three metalization layers, as shown in Figure 4.16(d). The middle layer provides a plate for the MIM capacitor in its center and two stub lines on the sides, which are shorted to the ground by metalized via holes. The top layer is a microstrip line section with a gap that forms the MIM capacitor together with the middle layer. The capacitor and the line section (series inductance) form a series resonance circuit. Topologically, this unit cell is identical to the CRLH unit cell in Section 3.6.2, except for the *dimensions*, which here corresponds to a design for a 10 GHz broadside frequency and the *asymmetry*. The asymmetry is introduced via an offset, d , with respect to the symmetric layout, as shown in Figure 4.16(c). Table 4.3 lists the extracted LCRG parameters, resonance frequen-

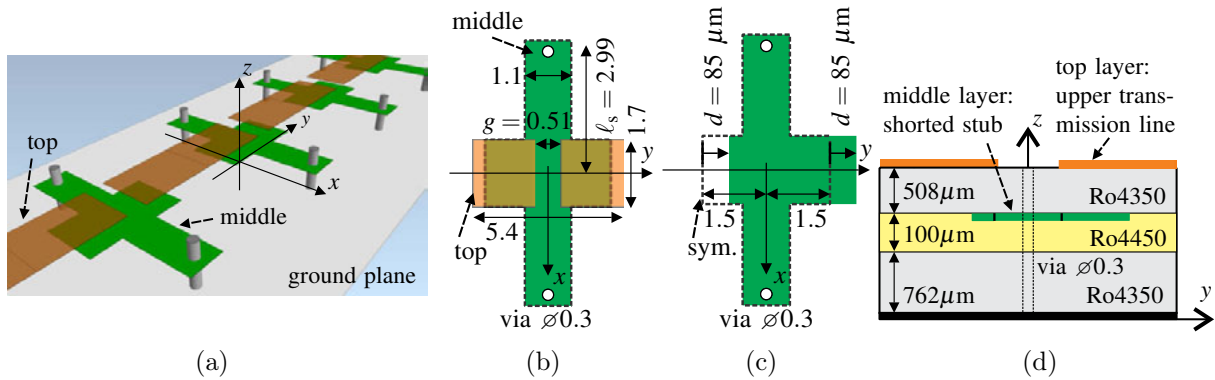


Figure 4.16: Composite right/left-handed (CRLH) LWA. (a) Perspective view. (b) Layout of the symmetric unit cell with top and middle metalization layer. (c) Asymmetry parameter d in the middle layer, where the dashed line indicates the outline of the symmetric unit cell in (a) (top layer is the same as in (a) and is not shown). (d) Stack-up. (All the dimensions are given in mm.)

cies, transformation ratios and radiation efficiencies using the eigenmode and drivenmode methods described in Section 4.4 and Section 3.4.2/4.1.2, respectively. The equivalent circuit models are given in Figures 4.14(c) and 4.15(c).

The CRLH unit cells are designed for the broadside frequency $f_{bs} = f_{se} = f_{sh} = 10$ GHz (rows 7-8, eigenmode: cols. 1-3, drivenmode col. 7-9). The parameter g is varied to tune f_{se} to 10 GHz and the parameter l_s is varied to tune f_{sh} to the same frequency, in order to achieve frequency-balancing using the scheme in Section 4.4.3. The degree of asymmetry takes three successive values: $d = 0$, $d = 85$ and $d = 200$ μm . The variation of d over this range has only a negligible effect on the resonance frequencies f_{se} and f_{sh} , so that a resonance frequency re-tuning is not necessarily required. The asymmetry parameter is defined in a way that the overall metalization area remains constant [Figure 4.16(c)] so that the total MIM capacitance (sum of left and right side) is unchanged. This does not affect the intrinsic series and shunt resonance frequencies for moderate asymmetries, as demonstrated in [48]. From the optimization point of view, this is beneficial, as the frequency-balancing and the optimal asymmetry optimizations can be run independently reducing the computational effort.

Table 4.3: LCRG parameters and efficiencies for CRLH and SFCP unit cells extracted by eigenmode and drivenmode methods as described in Sections 4.4 and 4.1.2, respectively.

d (μm) row\col.	Eq.	LCRG eigenmode parameter extraction						Eq.	LCRG drivenmode parameter extraction						
		CRLH			SFCP				CRLH			SFCP			
		0	85	200	0	300	600		0	85	200	0	300	600	
		1.)	2.)	3.)	4.)	5.)	6.)			7.)	8.)	9.)	10.)	11.)	12.)
1.) L_{se} (nH)	Eq. (4.61)	2.28	2.37	2.40	8.27	8.43	8.63	Eq. (4.9)	1.90	1.91	1.94	7.11	7.17	7.32	
2.) C_{se} (fF)	Eq. (4.61)	110.75	106.92	105.47	30.67	30.05	29.29	Eq. (4.9)	132.65	132.52	131.08	35.66	35.32	34.57	
3.) R (Ω)	Eq. (4.61)	9.16	9.47	9.48	12.89	13.28	13.93	Eq. (4.9)	8.68	8.68	8.74	11.28	11.44	11.86	
4.) C_{sh} (fF)	Eq. (4.68)	895.24	894.68	894.55	847.48	846.36	848.49	Eq. (4.12)	879.56	880.24	889.25	882.85	883.71	887.33	
5.) L_{sh} (pH)	Eq. (4.68)	282.80	283.51	282.72	299.10	299.73	298.36	Eq. (4.12)	288.19	287.33	285.84	287.23	286.29	284.77	
6.) G (μS)	Eq. (4.68)	627.46	624.38	627.45	281.39	283.57	286.37	Eq. (4.12)	643.73	639.98	624.12	289.13	289.38	288.29	
7.) f_{se} (GHz)	Eq. (4.62)	10.01	10.00	10.00	9.99	10.00	10.01	Eq. (3.3)	10.01	10.00	9.99	10.00	10.00	10.00	
8.) f_{sh} (GHz)	Eq. (4.69)	10.00	9.99	10.01	10.00	9.99	10.00	Eq. (3.9)	10.00	10.01	9.98	9.99	10.01	10.01	
9.) Q_{se}	Eq. (4.64)	15.7	15.7	15.9	40.3	39.9	39.0	Eq. (3.7)	13.8	13.8	13.9	39.6	39.4	38.8	
10.) Q_{sh}	Eq. (4.71)	89.7	90.0	89.6	189.2	187.4	186.2	Eq. (3.12)	85.8	86.5	89.4	191.7	192.0	193.6	
11.) η_{se}	Eq. (4.63)	0.83	0.83	0.83	0.80	0.80	0.80	Eq. (3.5)	0.87	0.87	0.87	0.80	0.80	0.80	
12.) η_{sh}	Eq. (4.70)	0.50	0.50	0.50	0.02	0.02	0.02	Eq. (3.11)	0.52	0.52	0.52	0.10	0.10	0.10	
13.) $\text{Re}(\Omega_1)/2\pi$	Eq. (4.37)	10.00	9.93	9.67	9.99	9.98	9.92	-	-	-	-	-	-	-	
14.) $\text{Re}(\Omega_2)/2\pi$	Eq. (4.37)	10.01	10.06	10.31	10.00	10.01	10.10	-	-	-	-	-	-	-	
15.) Q_1	Eq. (4.44)	89.7	27.0	25.4	40.3	80.4	67.5	-	-	-	-	-	-	-	
16.) Q_2	Eq. (4.44)	15.7	26.4	28.0	189.3	55.9	62.9	-	-	-	-	-	-	-	
17.) T	Eq. (4.66)	1.000	1.038	1.092	1.000	1.026	1.054	Eq. (4.5)	1.000	1.039	1.094	1.000	1.023	1.048	
18.) T_{opt}	Eq. (4.35)	1.038	1.039	1.038	1.026	1.027	1.028	Eq. (4.35)	1.040	1.040	1.040	1.025	1.026	1.026	
19.) η_{bs}	Eq. (4.29)	0.66	0.78	0.81	0.41	0.66	0.75	Eq. (4.29)	0.69	0.82	0.86	0.45	0.67	0.75	
20.) $\eta_{\text{off-bs}}$	Eq. (4.30)	0.78	0.78	0.78	0.66	0.66	0.67	Eq. (4.30)	0.82	0.82	0.82	0.68	0.68	0.69	

Table 4.3 shows (rows 11-12, eigenmode: cols. 1-3, drivenmode cols. 7-9) that in this design the series radiation efficiency (eigenmode: $\eta_{se} = 0.83$, drivenmode: $\eta_{se} = 0.87$) is larger than the shunt radiation efficiency (eigenmode: $\eta_{sh} = 0.50$, drivenmode: $\eta_{sh} = 0.52$). The unit cell is longitudinally symmetric and therefore only series radiation is directed towards broadside, whereas shunt radiation is mainly directed to the sides ($\pm x$ -direction) with a radiation null at broadside as discussed in Section 3.5.1; more importantly, the series and shunt efficiencies remain unchanged under variation of d . The same is true for the LCRG parameters (rows 1-6, eigenmode: cols. 1-3, drivenmode cols. 7-9) and the intrinsic quality factors (rows 9-10, eigenmode: cols. 1-3, drivenmode cols. 7-9), which also show only minor variation under the three asymmetry cases.

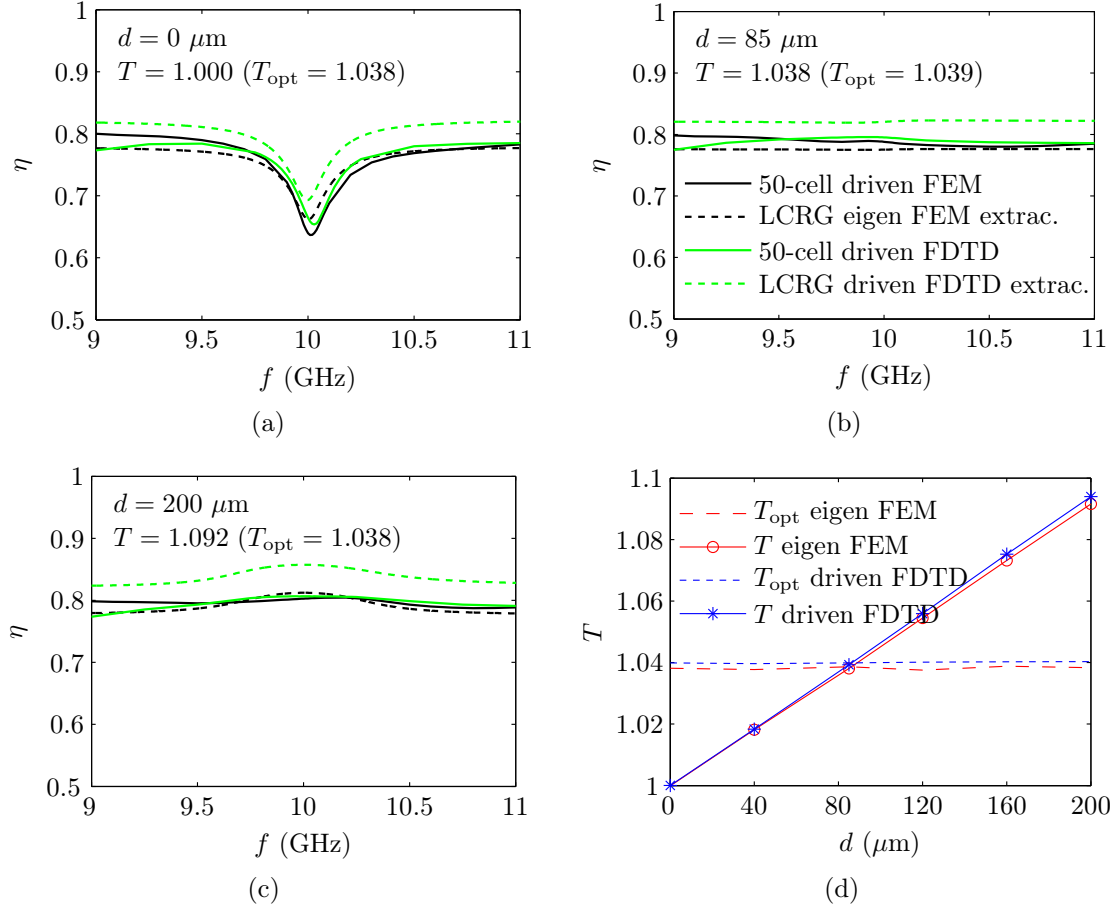


Figure 4.17: Radiation efficiency comparison for 50-cell CRLH LWAs (overall length $\approx 9\lambda_0$, -32 dB power at the terminated end) between fullwave results and LCRG circuit model predictions for different asymmetries. (a) Symmetric case with $d = 0 \mu\text{m}$ ($T = 1$). (b) Optimal asymmetry case with $d = 85 \mu\text{m}$ ($T = T_{opt}$). (c) Excessive asymmetry with $d = 200 \mu\text{m}$ ($T > T_{opt}$). (d) Dependency of T and T_{opt} versus asymmetry (d).

The evaluation of T (row 17, eigenmode: cols. 1-3, drivenmode cols. 7-9) shows that d clearly controls the transformation ratio in the circuit model, where the symmetric cell with $d = 0 \mu\text{m}$ obviously results in $T = 1$. The optimal transformation ratio as calculated by Equation (4.35) is listed in row 18. By comparing T with T_{opt} , one finds that the CRLH unit cell is optimal for $d = 85 \mu\text{m}$, and that the eigenmode and drivenmode extraction techniques for T and T_{opt} are in perfect agreement (rows 17-18, compare eigenmode: cols. 1-3 with drivenmode cols. 7-9).

The overall broadside and off-broadside efficiencies (η_{bs} and $\eta_{\text{off-bs}}$) are calculated based on Equations (4.29) and (4.30) (rows 19-20, eigenmode: cols. 1-3, drivenmode cols. 7-9). Efficiency equalization in the optimal case of the broadside and off-broadside regime is confirmed by eigenmode extraction with $\eta_{\text{bs}} = \eta_{\text{off-bs}} = 0.78$ and by drivenmode extraction with $\eta_{\text{bs}} = \eta_{\text{off-bs}} = 0.82$. In the symmetric case ($d = 0$), one observes a strong degradation of η_{bs} (rows 19-20, eigenmode: col. 1, drivenmode col. 7), whereas for the over-optimal case ($d = 200 \mu\text{m}$) a small increase of η_{bs} as compared to $\eta_{\text{off-bs}}$ is seen.

The LWA simulation model with 50 cascaded unit cells is setup to form a finite-length CRLH LWA for each of the three asymmetry cases. This LWA is excited from one side with the other being terminated by a matched load. The LWA length is approximately $9\lambda_0$, where λ_0 is the free-space wavelength. The power at the terminated end is less than -30 dB and can therefore be neglected in the evaluation of the overall radiation efficiency. The overall efficiency, referred to as the 50-cell LWA efficiency, is calculated by the ratio of the total radiated power over the accepted input power. This 50-cell LWA efficiency is calculated independently by the two fullwave simulators, HFSS (FEM) and EMPIRE (FDTD), and subsequently compared to the circuit model efficiency.

Figures 4.17(a)-(c) compare the simulated radiation efficiencies for the 50-cell CRLH LWAs to the circuit model radiation efficiency [LCRG, η_{se} , η_{sh} and T from Table 4.3 inserted into Equation (4.28)] for the three asymmetry cases. Except for the circuit model efficiency from drivenmode mode extraction, there is a nearly perfect agreement of the overall LWA efficiency with the circuit model efficiency in all three asymmetry cases. The fact that the drivenmode extraction is over-estimating the efficiency as compared to the other results, might be explained by the over-estimation of η_{se} and η_{sh} in the efficiency extraction procedure. The degradation of the broadside efficiency is clearly confirmed in Figure 4.17(a) for the symmetric case and in agreement with the circuit model result. The equalized efficiency under the optimal T condition is plotted in Figure 4.17(b) and confirms the theory. The over-optimal efficiency in Figure 4.17(c) just shows a marginal efficiency improvement, due to the fact that $\eta_{\text{sh}} = 0.5$ is already rather high. This “overshoot” in the efficiency would have been more pronounced if the ratio $\eta_{\text{se}}/\eta_{\text{sh}}$ had been larger. This is the case in the second case study example the SFCP LWA in the forthcoming Section 3.6.2, where $\eta_{\text{sh}} \ll \eta_{\text{se}}$.

Figure 4.17(d) shows T and T_{opt} versus the asymmetry parameter, d , for the eigenmode and drivenmode extraction methods. Intermediate points, at $d = 40, 120, 160 \mu\text{m}$, are also evaluated. An almost linear behavior is observed for T , whereas T_{opt} remains constant, as expected from the aforementioned insensitivity of the LCRG to d . Thus, the optimization criterion $T = T_{\text{opt}}$ is robust and easily achievable by means of simple gradient optimization.

Now, the field distributions of the two eigenmodes are examined for the symmetric ($d = 0 \mu\text{m}$), an intermediate ($d = 40 \mu\text{m}$) and the optimal asymmetry ($d = 85 \mu\text{m}$) steps. Figure 4.18 shows vector plots for the eigenmode surface current density on the middle and the top metalization layers under periodic boundary condition with a phase shift of $\Phi = 0$. The simulation setup here is identical to the one in Section 4.3.3, where the coupled eigenmodes of the idealized transmission line model [Figure 4.10] are investigated. The solid red arrows in Figure 4.18 indicate the dominant vector fields and shall help to interpret the plots. The field strength of the vectors is represented by a colormap from blue to red corresponding to the conventional representation of temperature. It appears in Figures 4.18(a) and (d) that the two modes, series and shunt, are orthogonal to each other.

They are consequently fully decoupled as discussed in Section 4.4. Breaking symmetry, as shown in Figures 4.18(b) and (e), couples the two modes and therefore alters their distributions, although dominance of the series mode in mode 1 [Figure 4.18(c)] and of the shunt mode in mode 2 [Figure 4.18(d)] is still apparent. Further increasing asymmetry leads to the optimal case represented in Figures 4.18(c) and (f). Here, the classification into series (odd) and shunt (even) modes is clearly no longer possible.

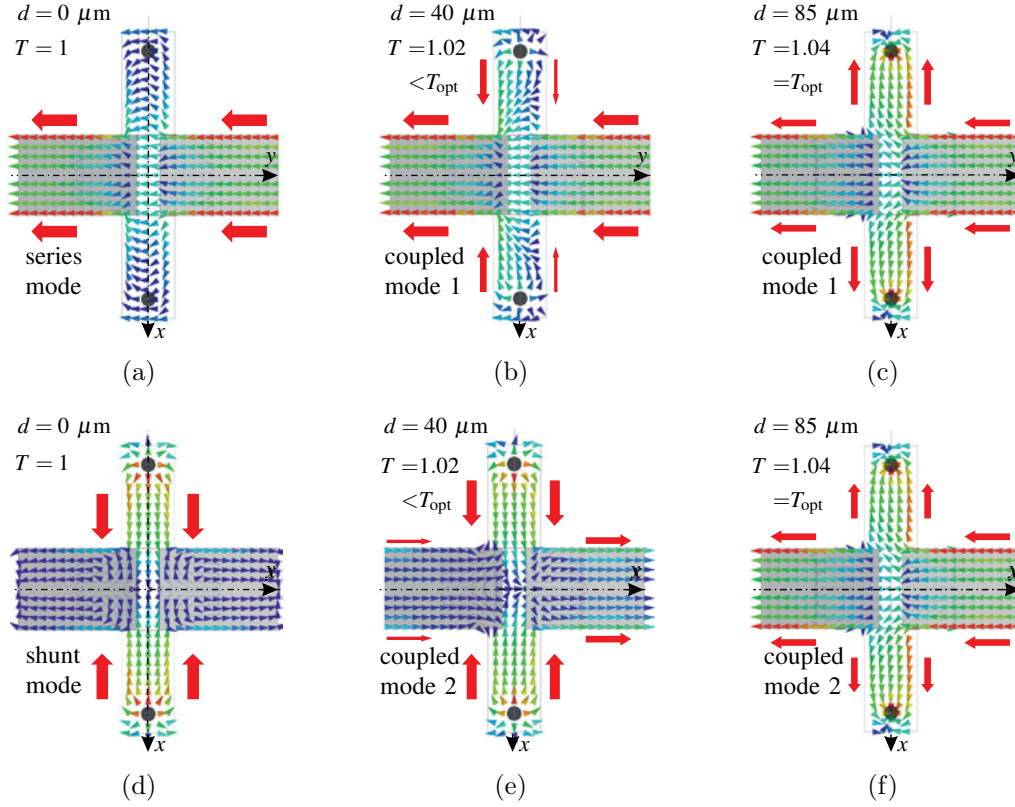


Figure 4.18: Surface current density vector distribution for the two eigenmodes under the periodic boundary condition $\Phi = 0$. Blue and red colors in the vector fields refer to low and high field strengths, respectively. The solid red arrows indicate the dominant fields. (a) and (d) Series and shunt modes, respectively, for the symmetric unit cell. (b) and (e) Weak asymmetry case, where coupling between the two modes is observable. (c) and (f) Optimal asymmetry case.

The following note regarding the nature of the waves for different degrees of transversal asymmetries completes the above eigenmode analysis with periodic boundaries. At $T = 1$, the series and shunt modes are purely *standing waves* (corresponding to the scenario in Figure 4.12(a)), since they represent completely decoupled PEC and PMC cavity modes, respectively, as seen from their field distributions in Figures 4.18(a) and (d). In contrast, at $T = T_{\text{opt}}$, the fully-coupled modes are purely *traveling waves* (corresponding to the scenario in Figure 4.12(d)). These coupled field waveforms are not restricted to PEC (zero terminal voltages) or PMC (zero terminal currents), such that they can simultaneously take on any terminal current or voltage value as long as the phase relation $\Phi = 0$ is satisfied. In the intervals $T \in]1, T_{\text{opt}}[$ and $T \in]T_{\text{opt}}, +\infty[$, the modes are a mixture of standing and traveling waves, with a standing wave ratio that progressively approaches one as $T \rightarrow T_{\text{opt}}$.

4.5.2 A Novel Series-Fed Coupled Patch (SFCP) LWA Design

Figure 4.19 shows the series-fed coupled patch (SFCP) LWA. Here, for the SFCP the $\mathbf{n} = -1$ higher order space harmonic is dominating. The structure has three metalization layers, the patch layer (top), the feed layer (middle) and the ground layer at the bottom. The concept of a feed line gap coupled to an on-top-stacked patch was presented in [69], where a potential application as unit cell of a series-fed patch array was only mentioned and not realized. The actual series-fed patch LWA with gap coupling to the feed line was just recently demonstrated in [49].

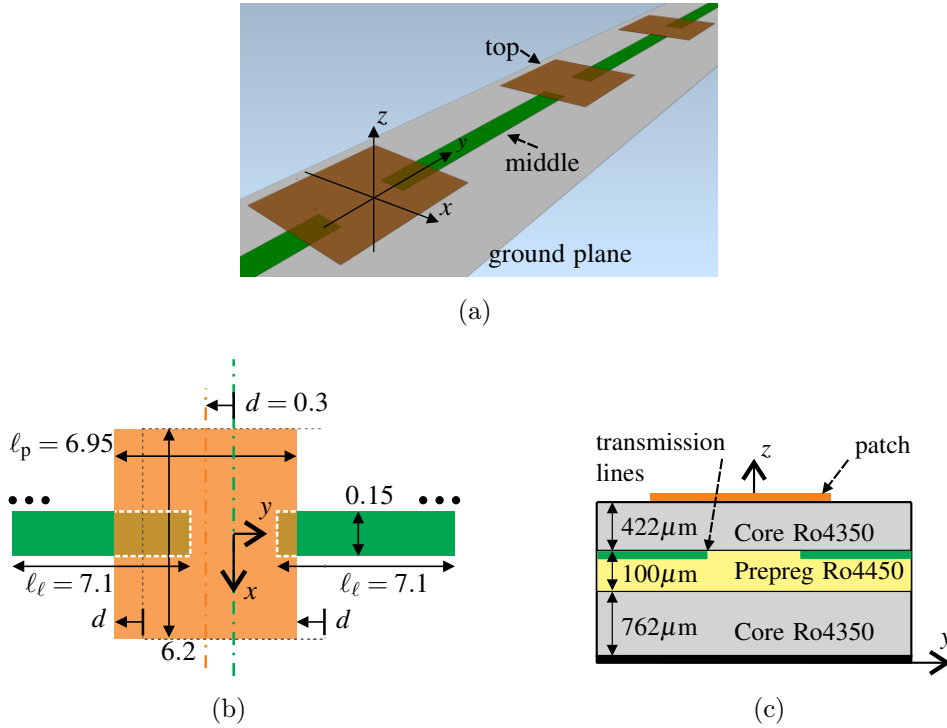


Figure 4.19: Series-fed coupled patch (SFCP) LWA. (a) Perspective view. (b) Metalization layout, where d is the patch offset distance from the unit cell center (green dashed line) for asymmetry. (c) Stack-up. (All the dimensions are given in mm.)

The same two extraction methods as in Section 4.5.1 are employed to populate Table 4.3 for the SFCP LWA. The antenna was designed for the broadside frequency $f_0 = f_{se} = f_{sh} = 10$ GHz (rows 7-8, eigenmode: cols. 4-6, drivenmode cols. 10-12). The two parameters, ℓ_p and ℓ_l , had to be varied to tune the two resonance frequencies to 10 GHz, the former controlling f_{se} and the latter f_{sh} , as shown in [49]. Three values of the degree of asymmetry are considered: $d = 0$, $d = 300$ and $d = 600$ μm . As in the CRLH case, no frequency re-tuning is required over this asymmetry range, which is due to the way the asymmetry is introduced [48].

Examining η_{se} and η_{sh} in Table 4.3 (rows 11-12, eigenmode: cols. 4-6, drivenmode cols. 10-12) indicates that the shunt radiation efficiency (eigenmode: $\eta_{sh} = 0.02$, drivenmode: $\eta_{sh} = 0.10$) is much smaller than the series radiation efficiency (eigenmode: $\eta_{se} = 0.80$, drivenmode: $\eta_{se} = 0.80$), suggesting that the SFCP LWA produces less *side* radiation than its CRLH counterpart. While eigenmode and drivenmode extraction perfectly agree on η_{se} , they show a relatively high discrepancy for η_{sh} , which may be explained by the comparatively much smaller radiated power levels together with the radiation properties of the shunt mode [Section 3.4.2].

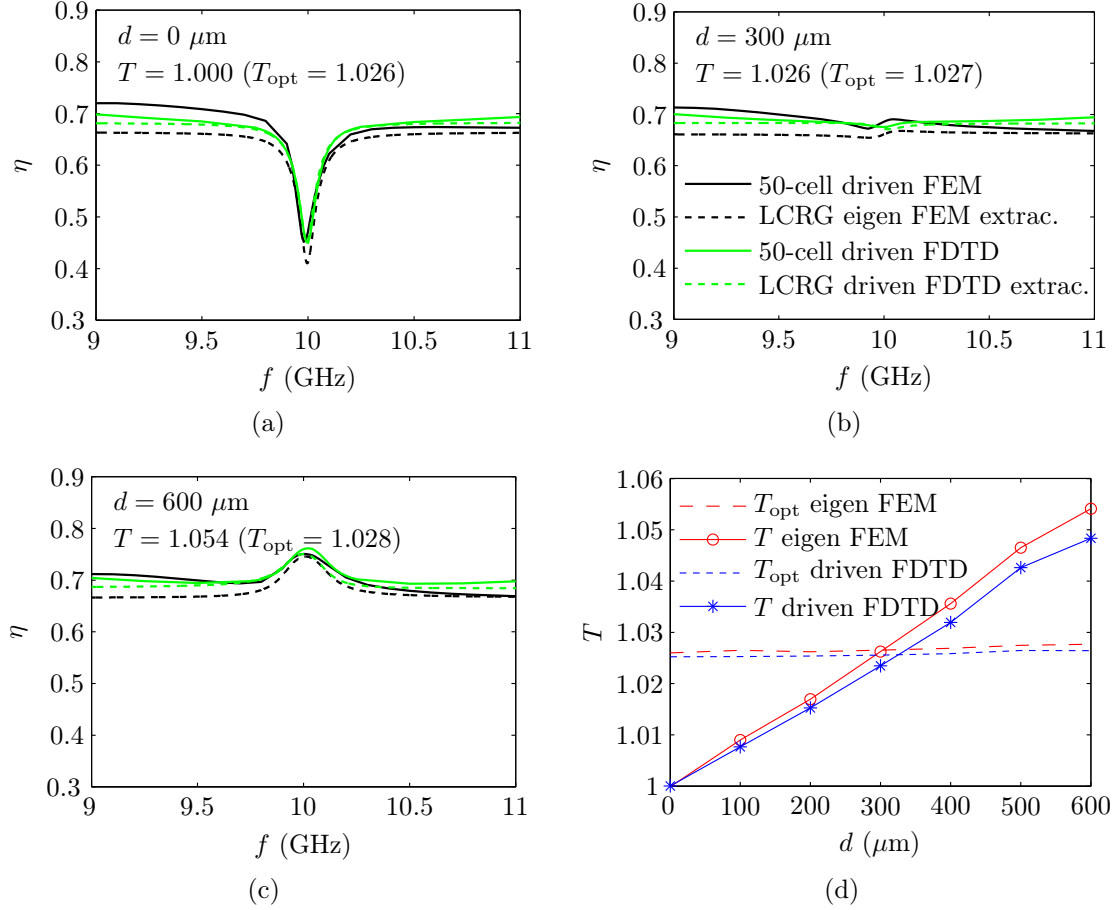


Figure 4.20: Radiation efficiency comparison for 50-cell SFCP LWA (overall length $\approx 29\lambda_0$, -28 dB power at the terminated end) between fullwave results and LCRG circuit model predictions for different asymmetries. (a) Symmetric case with $d = 0 \mu\text{m}$ ($T = 1$). (b) Optimal asymmetry case with $d = 300 \mu\text{m}$ ($T = T_{\text{opt}}$). (c) Excessive asymmetry case with $d = 600 \mu\text{m}$ ($T > T_{\text{opt}}$). (d) Dependency of T and T_{opt} versus asymmetry d .

The evaluation of T (row 17, eigenmode: cols. 4-6, drivenmode cols. 10-12) shows again that T can be controlled by the degree of asymmetry, optimal value being here $d = 300 \mu\text{m}$ (rows 17-18, eigenmode: col. 5, drivenmode col. 11). The agreement between eigenmode and drivenmode results is reasonably good.

Efficiency equalization is achieved here with $\eta_{\text{bs}} = \eta_{\text{off-bs}} = 0.66$ for eigenmode (rows 19-20, col. 5) and $\eta_{\text{bs}} = 0.67 \approx \eta_{\text{off-bs}} = 0.68$ for drivenmode (rows 19-20, col. 11). As in the CRLH case, the symmetric design ($d = 0$) exhibits efficiency degradation at broadside, while the over-coupled¹³ design exhibits a radiation efficiency peak at broadside compared to the equalized case, of 75% instead of 66% for eigenmode (row 19, compare cols. 5 and 6) and 75% instead of 67% (row 19, compare cols. 11 and 12).

Similarly to the CRLH case, a finite length LWA of 50 unit cells is considered here to determine the overall efficiency. The electrical length is around $27\lambda_0$, with a power decay of -28 dB at the terminated end.

¹³ Vector field plots are not shown for these cases, but the same fundamental uncoupled/coupled and standing/traveling-wave principles hold, as for the ideal transmission line model in Figure 4.12.

Figure 4.20(a)-(c) compares the simulated radiation efficiencies of the 50 cell LWAs with the circuit model radiation efficiencies. All curves are in a very good agreement and exhibit the same trends as in the CRLH LWA case, with the broadside efficiency dip in the symmetric design [Figure 4.20(a)], equalization in the optimal asymmetry design [Figure 4.20(b)] and efficiency increase in the over-coupled design [Figure 4.20(c)]. The efficiency peak in Figure 4.20(c) is more pronounced than in the CRLH case, consistently with the fact that $\eta_{sh} \ll \eta_{se}$.

Finally, Figure 4.20(d) shows T versus d being varied in steps of $100 \mu\text{m}$. Despite a small discrepancy between the two extraction methods, T linearly depends on asymmetry, while T_{opt} remains constant.

4.6 Summary of Symmetry Properties

The most important properties and features of asymmetric unit cells to design LWA with efficient broadside radiation are summarized as follows

- the unit cell inherits the longitudinal symmetry properties of Chapter 3 (i.e. shunt radiation is canceled in broadside direction and the radiation is linearly polarized in longitudinal direction)
- the power ratio P_{se}/P_{sh} at the broadside frequency f_{bs} is controlled through transversal asymmetry (in the transversally symmetric case this ratio is *always* equal to one: $P_{se}/P_{sh} = 1$)
- moderate transversal asymmetry does not affect the off-broadside properties
- transversal asymmetry adjusts the broadside efficiency η_{bs} in the range: $\min(\eta_{sh}, \eta_{se}) < \eta_{bs} < \max(\eta_{sh}, \eta_{se})$
- η_{bs} can therefore be larger than η_{off-bs}
- under optimal transversal asymmetry the broadside efficiency is equalized to the off-broadside efficiency: $\eta_{bs} = \eta_{off-bs}$
- under optimal transversal asymmetry, the coupled quality factors are equal $Q_1 = Q_2$ and the unit cell is Q-balanced

Transversal asymmetry is the key to overcome fundamental broadside radiation limitations in periodic LWAs. An optimum asymmetry condition for equalization is analytically derived resulting in *quality-factor-balancing*. Therefore, a consistent theory for achieving equalization in symmetric and asymmetric LWAs is established. The two case study examples, a metamaterial and conventional LWAs, show that the at-broadside efficiency can even exceed the off-broadside efficiency, a behavior which, to the author's best knowledge, has only been reported in the context of this work.

Longitudinally Asymmetric LWAs for Achieving Circular Polarization

This chapter investigates LWA asymmetry with respect to the *longitudinal* axis as illustrated in Figure 5.1. The LWA unit cells considered here are *longitudinally asymmetric* and transversally symmetric. This chapter proves that series and shunt broadside radiation contributions, corresponding to longitudinal and transversal electric farfield components, respectively, are always in phase quadrature, so that these antennas are inherently elliptically polarized. This fact is theoretically proven and validated through measurements by two case study examples, a CRLH LWA and an SFP LWA. Finally, for the case of the SFP LWA, it is demonstrated that the axial ratio is controlled and minimized by the degree of *longitudinal* asymmetry. This chapter is based on the author's journal publication in [58].

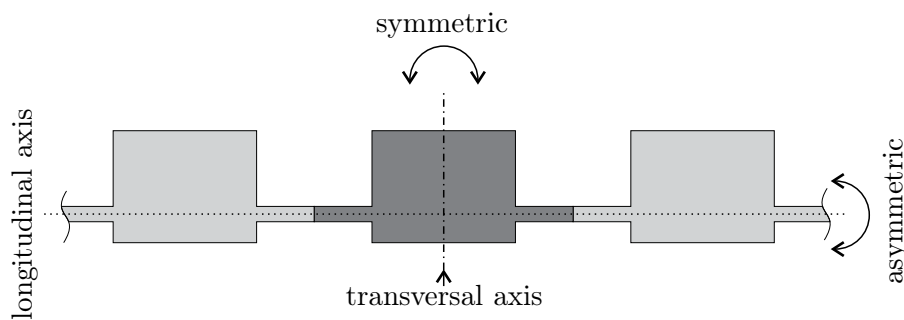


Figure 5.1: Class of *longitudinally asymmetric* LWAs that is considered in this chapter.

5.1 Modeling of Series/Shunt Radiation Contributions

This section defines and systematically derives the series and shunt radiation contributions based on sampled voltages in the LWA unit cell. In the previous Chapter 3, series and shunt radiation contributions of fully symmetric unit cells are *macroscopically* discussed

with the focus on their direction and polarization [Section 3.5.1], without considering the structural details in the unit cell. Here, a *microscopic* modeling is presented, which calculates the broadside farfield radiation components from the actual near field distribution within the unit cell. Using this approach one can then determine the phase difference between the series and shunt farfield components. This is done in preparation for Section 5.2, where the quadrature phase relationship between these two radiation contributions is proven.

5.1.1 Edge Radiation from Equivalent Voltage Sources

Electromagnetic radiation follows from charge acceleration (or deceleration) [106]. In antennas, such acceleration is obtained by curving, bending, terminating, truncating or discontinuing the conductors supporting electric currents [2]. In periodic LWAs, discontinuities are the most common sources of radiation. These discontinuities are most often provided by conductor edges or slots in conductors, which are generally modeled by magnetic current densities in antenna theory [2]. Since edge radiation and slot radiation represent dual mechanisms, by virtue of Babinet principle [2, 106], the focus lies only on edge radiation, without loss of generality. Radiating edges may be for instance sharp contours of metal strips in a microstrip structures [2, 102].

Figure 5.2 represents the unit cell of a periodic LWA with a generic shape including several radiating edges. The overall LWA is formed by repeating this unit cell along the y -direction, and is assumed to be of infinite extent¹. Furthermore, it is assumed throughout this chapter that the unit cell is symmetric with respect to the transversal axis (x -axis) as indicated in Figure 5.2.

The cell includes *vertical edges*, parallel to the transversal axis (x -axis) and supporting the magnetic currents represented in Figure 5.2(a), and *horizontal edges*, parallel to the longitudinal axis (y -axis) and supporting the magnetic currents represented in Figure 5.2(b).

Next, the concept of the equivalent magnetic surface current density [2] is applied, to quantify the amount of radiation from the two edge types (horizontal and vertical). This current reads here

$$\bar{M} = \bar{E} \times \hat{n} \approx E_z \hat{z} \times \hat{n}, \quad (5.1)$$

where \bar{E} is the electric field vector between the edge and the ground conductor, E_z is the field component in the z -direction, and \hat{n} is the vector normal to the surface between the conductor edge and the ground conductor. Assuming that the edge-ground conductor distance, h , is much smaller than the wavelength, $h \ll \lambda/10$, E_z is essentially constant. Therefore, the voltage integral $V = \int \bar{E} \cdot d\bar{l}$ reduces to

$$V \approx -E_z h, \quad (5.2)$$

where the negative sign defines the voltage from the edge to the ground conductor, i.e. along the $-\hat{z}$ direction.

¹The forthcoming results straightforwardly apply to practical, finite-size LWAs provided that these LWAs are either electrically sufficiently long or they are terminated by a matched load, in order to avoid reflections from the termination side.

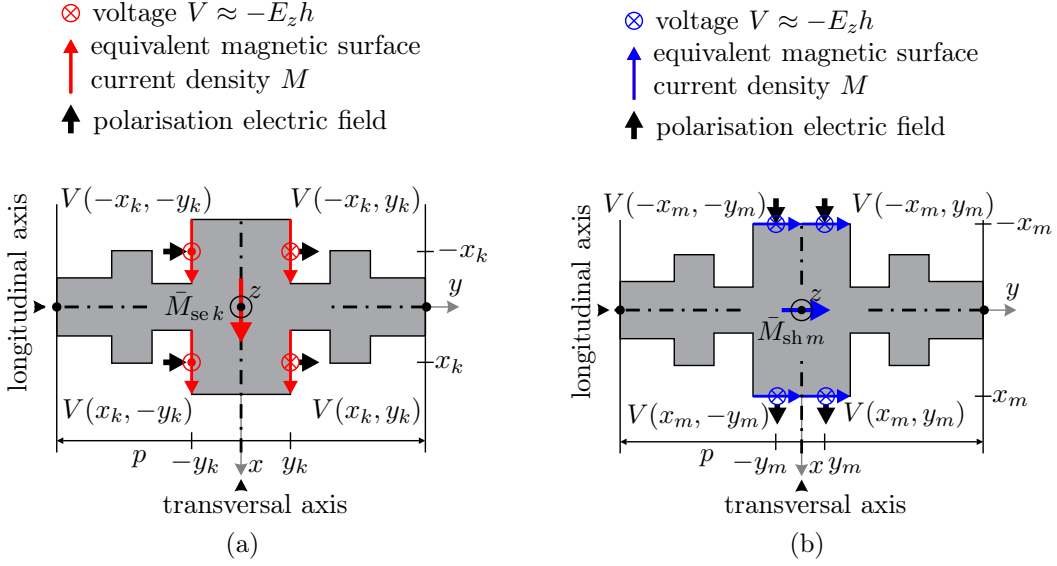


Figure 5.2: Arbitrary layout of a fully symmetric unit cell with symmetric voltage sampling points V at the radiating edges. For an observer placed at *broadside* in the farfield (z -direction), the voltage *difference* in the y and x directions is proportional to the series and shunt radiation field contributions, respectively. (a) The series radiation contributions (indexed k) from the vertical edges, polarized in the y -direction, are non-zero due to phase variation of the traveling wave in this direction. (b) The shunt radiation contributions (indexed m) from the horizontal edges, polarized in the x -direction, are zero due to symmetry.

5.1.1.1 Series Radiation

According to Figure 5.2(a), the *series radiation magnetic surface current density* reads

$$\bar{M}_{\text{se } k} = \bar{M}(-x_k, -y_k) + \bar{M}(-x_k, y_k) + \bar{M}(x_k, -y_k) + \bar{M}(x_k, y_k), \quad (5.3)$$

where the index k refers to a sample representing any point of the vertical edges². The quantity $\bar{M}_{\text{se } k}$ measures the series radiation toward broadside and may be interpreted as a *magnetic dipole moment* located at the *center* (coordinate origin) of the unit cell with the corresponding electric farfield being polarized in the y -direction. If one evaluates the *series radiation magnetic surface current density* in Equation (5.3) using Equations (5.1) and (5.2) together with the proper orientation of the normal vector at the series edges, $\hat{n} = \pm\hat{y}$, one may write

$$\begin{aligned} \bar{M}_{\text{se } k} \cdot \hat{x} &= \frac{1}{h} [-V(-x_k, -y_k) + V(-x_k, y_k) \\ &\quad -V(x_k, -y_k) + V(x_k, y_k)] = \frac{1}{h} V_{\text{se } k}, \end{aligned} \quad (5.4)$$

where the final result of $\bar{M}_{\text{se } k}$ is projected onto the x -direction. The last equality in Equation (5.4) defines the *series radiation equivalent voltage source*, $V_{\text{se } k}$, which accounts for the series radiation contribution (amplitude and phase) as

$$\begin{aligned} V_{\text{se } k} &= -V(-x_k, -y_k) + V(-x_k, y_k) \\ &\quad -V(x_k, -y_k) + V(x_k, y_k), \end{aligned} \quad (5.5)$$

²In Figure 5.2(a), the series voltages are indicated only at the edges of the center patch for simplicity. The vertical edges of the two side patches must naturally also be taken into account, as is seen in Figure 5.4.

revealing that the difference of the edge voltages in the y -direction contributes to series broadside radiation, which is polarized in longitudinal direction (y -direction).

5.1.1.2 Shunt Radiation

According to Figure 5.2(b), the *shunt radiation magnetic surface current density* reads

$$\bar{M}_{\text{sh } m} = \bar{M}(-x_m, -y_m) + \bar{M}(-x_m, y_m) + \bar{M}(x_m, -y_m) + \bar{M}(x_m, y_m), \quad (5.6)$$

where the index m refers to a sample representing any point of the horizontal edges. Similarly to the previous case, Equation (5.1) and Equation (5.2) are used together with the normal vector \hat{n} oriented in $\pm\hat{x}$ direction at the horizontal edges to find the *shunt radiation magnetic surface current density* projected on the y -direction

$$\begin{aligned} \bar{M}_{\text{sh } m} \cdot \hat{y} &= \frac{1}{h} [-V(-x_m, -y_m) - V(-x_m, y_m) \\ &\quad + V(x_m, -y_m) + V(x_m, y_m)] = \frac{1}{h} V_{\text{sh } m}. \end{aligned} \quad (5.7)$$

The last equality in Equation (5.7) defines the *shunt radiation equivalent voltage source*, $V_{\text{sh } m}$, as

$$\begin{aligned} V_{\text{sh } m} &= -V(-x_m, -y_m) - V(-x_m, y_m) \\ &\quad + V(x_m, -y_m) + V(x_m, y_m), \end{aligned} \quad (5.8)$$

showing that the edge voltage difference in the y -direction contributes to shunt broadside radiation, which is polarized in transversal direction (x -direction).

5.1.2 Fully Symmetric Unit Cell

Before the longitudinally asymmetric unit cell is examined, the fully symmetric unit cell, presented in Chapter 3, is analyzed first. This is done, in order to verify the series and shunt radiation properties derived in Section 3.5.1. The fully symmetric unit cell, exhibiting symmetry with respect to both axes, its longitudinal and transversal axes, is shown in Figure 2.6(a). It is assumed, as in the previous chapters that the LWA is excited by a TEM field, a quasi-TEM field or by any other field, whose transverse distribution is fully symmetric with respect to the longitudinal axis. Under this assumption, a longitudinally symmetric *field* distribution, and hence a symmetric distribution of the *voltage*, follows from longitudinal symmetry of the *structure*. The longitudinal symmetry in the voltage is expressed as

$$V(x_k, y_k) = V(-x_k, y_k) \quad \text{and} \quad V(x_k, -y_k) = V(-x_k, -y_k), \quad (5.9)$$

where the longitudinal axis is the symmetry axis. Inserting Equation (5.9) into Equation (5.5) yields the equivalent series voltage

$$V_{\text{se } k} = 2[-V(x_k, -y_k) + V(x_k, y_k)] \neq 0, \quad (5.10)$$

which is generally nonzero since the wave propagation in the y -direction implies a phase difference between the two voltages $V(x_k, -y_k)$ and $V(x_k, y_k)$. Thus, the fully symmetric

unit cell provides series radiation, and this radiation contribution is polarized in the longitudinal direction, namely the y -direction, which is in perfect agreement with polarization found in Section 3.5.1.

Inserting now Equation (5.9) into Equation (5.8), the equivalent shunt voltage is found to be

$$V_{sh\ m} = 0, \quad (5.11)$$

which reveals that no shunt radiation contribution exists, due to cancellation between the bottom edge and top edge transversally polarized fields in x -direction.

In conclusion, the results of Section 3.5.1 are confirmed by the edge radiation modeling, where an LWA composed of fully symmetric unit cells radiates broadside only from its series contributions and is *linearly polarized* in its longitudinal direction.

5.1.3 Asymmetric Unit Cell with Respect to the Longitudinal Axis

Consider now the case of a unit cell that is asymmetric with respect to the longitudinal axis while being still symmetric with respect to the transversal axis, as shown in Figure 5.3. The asymmetry may be represented by *complex* asymmetry factors, $\alpha_{se\ k}$ and $\alpha_{sh\ m}$, for the series and shunt voltages, respectively. This asymmetry factor links the field components through a multiplication and the factor is one if the structure is symmetric.

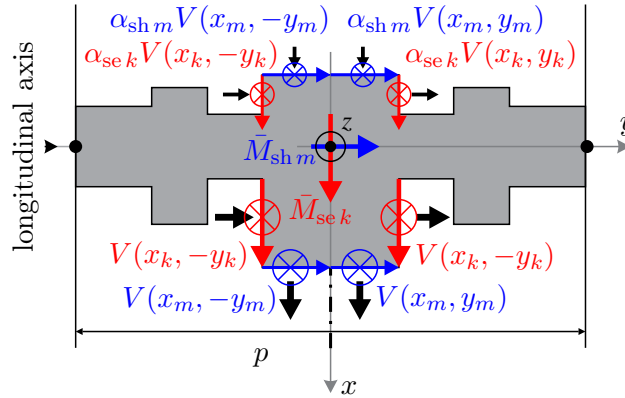


Figure 5.3: Asymmetric unit cell with respect to the longitudinal axis. The series contribution, $V_{se\ k}$, is the *difference* of the voltages with index k according to Equation (5.13). The shunt contribution, $V_{sh\ m}$, is the *sum* of the voltages with index m . The shunt radiation is *not* canceled and therefore contributes to the farfield in the broadside direction.

Substituting

$$V(-x_k, -y_k) = \alpha_{se\ k} V(x_k, -y_k) \quad (5.12a)$$

and

$$V(-x_k, y_k) = \alpha_{se\ k} V(x_k, y_k) \quad (5.12b)$$

into Equation (5.5), the *series radiation equivalent voltage source* reads

$$\begin{aligned} V_{se\ k} &= -V(x_k, -y_k)[1 + \alpha_{se\ k}] + V(x_k, y_k)[1 + \alpha_{se\ k}] \\ &= -V_k^- + V_k^+, \end{aligned} \quad (5.13)$$

where the last equality introduces the compact notation $V_k^- = V(x_k, -y_k)[1 + \alpha_{se k}]$ and $V_k^+ = V(x_k, y_k)[1 + \alpha_{se k}]$, the \pm superscripts referring to y -positive/negative coordinates. The *voltage difference* of the symmetrically placed (with respect to the transversal axis) voltage samples contribute to series radiation.

Similarly, substituting

$$V(-x_m, -y_m) = \alpha_{sh m} V(x_m, -y_m) \quad (5.14a)$$

and

$$V(-x_m, y_m) = \alpha_{sh m} V(x_m, y_m) \quad (5.14b)$$

into Equation (5.8), the *shunt radiation equivalent voltage source* reads

$$\begin{aligned} V_{sh m} &= V(x_m, -y_m)[1 - \alpha_{sh m}] \\ &\quad + V(x_m, y_m)[1 - \alpha_{sh m}] = V_m^- + V_m^+ \end{aligned} \quad (5.15)$$

where $V_m^- = V(x_m, -y_m)[1 - \alpha_{sh m}]$ and $V_m^+ = V(x_m, y_m)[1 - \alpha_{sh m}]$. Here, the *voltage sum* contributes to shunt radiation due to asymmetry ($\alpha_{sh m} \neq 1$).

Note the simplicity of the final results of this section: series radiation is represented by a simple voltage difference [last equality in Equation (5.13)], while shunt radiation is represented by a simple voltage sum [last equality in Equation (5.15)]. These voltage difference and sum correspond to the odd and even decomposition of Section 3.1.2.4.

5.2 Quadrature Phase Relation in Periodic LWA

Based on the simple odd/even difference/sum formalism established in Section 5.1.3, this section proves that the series and shunt radiation contributions, $V_{se k}$ and $V_{sh m}$, are in quadrature phase for arbitrary k and m .

Figure 5.4 shows an LWA unit cell that is asymmetric with respect to the longitudinal axis with the index k accounting for the vertical edges and the index m accounting for the horizontal edges. For visualization simplicity, Figure 5.4 represents the case³ $\alpha_{se k} = 0$ and $\alpha_{se m} = 0$.

The phase reference is set to 0° at the unit cell input terminals n , which are located at $y = -p/2$. By introducing Φ , as the phase shift due to wave propagation across the unit cell, the phase at the unit cell output terminals $n + 1$, located at $y = +p/2$, is Φ . The phase on the transversal axis, at the *center* of the unit cell (at $y = 0$), is then

$$\Phi_{sym} = \Phi/2. \quad (5.16)$$

The transversal axis is thus the *phase-symmetry axis* of the unit cell. Here, it is assumed that the unit cell is

1. topologically symmetric with respect to the transversal axis,

³The quadrature phase relationship is independent of the $\alpha_{se k}$ and $\alpha_{sh m}$ coefficients, whose importance is discussed later in this section.

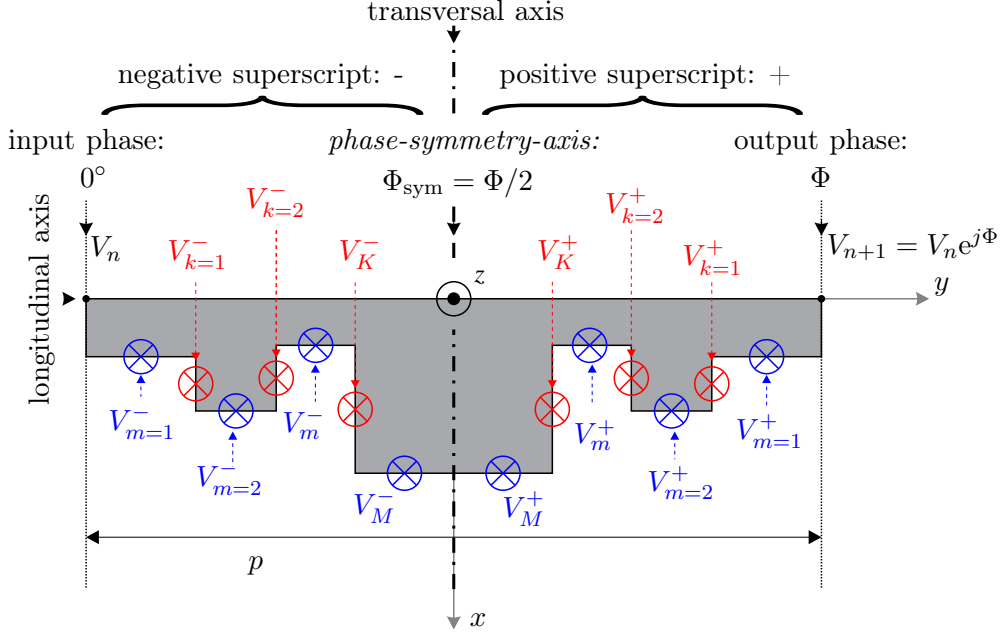


Figure 5.4: Series and shunt voltage sampling at the vertical and horizontal edges with indices k and m , respectively. In general, a phase shift Φ exists between the input/output voltages, V_n and V_{n+1} , respectively. The phase along at $y = 0$, which defines the transversal axis, is therefore $\Phi_{\text{sym}} = \Phi/2$ and represents the *phase-symmetry axis* of the unit cell.

2. lossless⁴ and
3. that the LWA operates in the passband⁵.

The complex vertical (series) and horizontal (shunt) edge voltages at the points k and m , respectively, may be written as

$$V_k^\pm = |V_k^\pm| e^{j\Phi_k^\pm} \quad \text{and} \quad V_m^\pm = |V_m^\pm| e^{j\Phi_m^\pm}. \quad (5.17)$$

By symmetry about the phase-symmetry axis, one may write

$$V_k^+ = |V_k^+| e^{j(\Phi_{\text{sym}} + \Delta\Phi_k)} \quad \text{and} \quad V_k^- = |V_k^-| e^{j(\Phi_{\text{sym}} - \Delta\Phi_k)}, \quad (5.18a)$$

where

$$\Delta\Phi_k = (\Phi_k^+ - \Phi_k^-)/2 \quad (5.18b)$$

is the phase difference between Φ_{sym} and $\angle V_k^\pm$.

Similarly, the shunt voltages follow with

$$V_m^+ = |V_m^+| e^{j(\Phi_{\text{sym}} + \Delta\Phi_m)} \quad \text{and} \quad V_m^- = |V_m^-| e^{j(\Phi_{\text{sym}} - \Delta\Phi_m)}, \quad (5.19a)$$

where

$$\Delta\Phi_m = (\Phi_m^+ - \Phi_m^-)/2 \quad (5.19b)$$

⁴Typically, $\alpha/k_0 = \alpha\lambda_0/(2\pi) \sim 10^{-2}$, where α is the leakage factor, k_0 is the free-space wavenumber and λ_0 is the free-space wavelength, with $p \lesssim \lambda_0$, so that $\alpha p \lesssim \alpha\lambda_0 \sim 2\pi \cdot 10^{-2}$. Then the power lost across the unit cell due to leakage is $P_{\text{u.c.}}^{\text{leakage}} = |20 \log_{10} e^{-\alpha p}| < 0.5$ dB ($e^{-\alpha p} > 0.94$), while the corresponding power due to dissipation is usually much smaller than this quantity at microwaves.

⁵For operation in the passband the phase angle Φ across the unit cell is a *real* quantity, as opposed to an operation in the stop-band of the LWA, where Φ would be purely *imaginary*.

is the phase difference between Φ_{sym} and $\angle V_m^\pm$.

Inserting Equation (5.18a) into Equation (5.13) yields

$$V_{\text{se}k} = |V_k^+| e^{j(\Phi_{\text{sym}} + \Delta\Phi_k)} - |V_k^-| e^{j(\Phi_{\text{sym}} - \Delta\Phi_k)} \quad (5.20)$$

for the series radiation equivalent voltage source, while inserting Equation (5.19a) into Equation (5.15) yields

$$V_{\text{sh}m} = |V_m^+| e^{j(\Phi_{\text{sym}} + \Delta\Phi_m)} + |V_m^-| e^{j(\Phi_{\text{sym}} - \Delta\Phi_m)} \quad (5.21)$$

for the shunt radiation equivalent voltage source.

Now, it is recalled that the structure is lossless, having neither radiation loss nor dissipation loss. Although this assumption goes against the physical nature of an LWA, it serves as a reasonable approximation for the purpose of the forthcoming argument because the amount of leakage and dissipation across a periodic LWA unit cell is very small, which is generally supported by the results of the previous Chapters 3 and 4. Under this assumption, the voltages that are symmetrically placed to either side of the symmetry axis do not undergo an amplitude decay so to obtain

$$|V_k^+| = |V_k^-| = |V_k| \quad \text{and} \quad |V_m^+| = |V_m^-| = |V_m|. \quad (5.22)$$

Under these conditions, Equation (5.20) and Equation (5.21) reduce, via Euler's formula, to the expressions

$$V_{\text{se}k} = 2j|V_k| \sin(\Delta\Phi_k) e^{j\Phi_{\text{sym}}}, \quad (5.23)$$

$$V_{\text{sh}m} = 2|V_m| \cos(\Delta\Phi_m) e^{j\Phi_{\text{sym}}}, \quad (5.24)$$

whose ratio,

$$\frac{V_{\text{se}k}}{V_{\text{sh}m}} = j \frac{|V_k| \sin(\Delta\Phi_k)}{|V_m| \cos(\Delta\Phi_m)}, \quad (5.25)$$

proves the quadrature phase relationship between the series and shunt radiation contributions. This holds for unit cells that are symmetric with respect to their transversal axis and asymmetric with respect to their longitudinal axis.

$V_{\text{se}k}$ and $V_{\text{sh}m}$ are generally non-zero. In the particular case of a CRLH LWA, it might a priori seem that $V_{\text{se}k}$ in Equation (5.20) vanishes because at broadside the input/output phase shift is zero, $\Phi = 0$, so that $\Phi_{\text{sym}} = 0$ according to Equation (5.16). On the other hand $\Delta\Phi_k$ and $\Delta\Phi_m$ are non-zero due to the voltage variations occurring *within* the unit cell [107]. So, Equation (5.25) is clearly determined and provides the axial ratio of the polarization.

Figure 5.5 provides a graphical representation of this phase quadrature proof. Figure 5.5(a) plots the vector $V_{\text{se}k}$ as the *difference* of the vectors V_k^+ and V_k^- , according to (5.20) with (5.18), while Figure 5.5(b) plots the vector $V_{\text{sh}m}$ as the *sum* of the vectors V_m^+ and V_m^- , according to (5.21) with (5.18). In both of these graphs, the symmetries about the phase-symmetry axis between the input and output voltages and between the negative and positive point voltages is clearly apparent, and the proof follows from the perpendicularity between the complex numbers $V_{\text{se}k}$ and $V_{\text{sh}m}$,

$$V_{\text{se}k} = \xi_{km} V_{\text{sh}m} e^{j\pi/2} = j\xi V_{\text{sh}m}, \quad (5.26a)$$

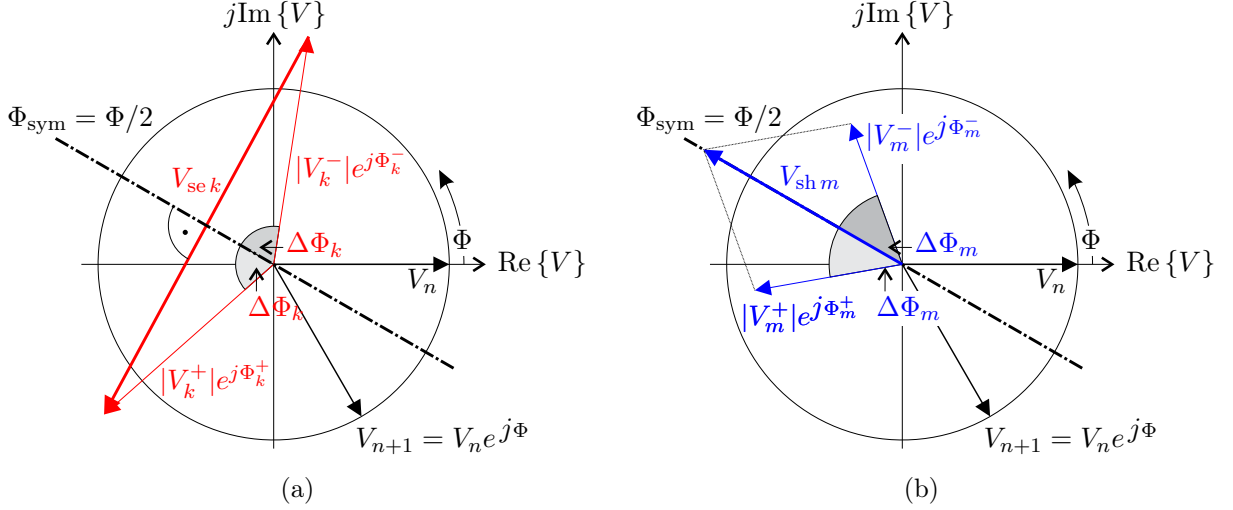


Figure 5.5: Graphical proof of the quadrature phase relationship between $V_{se k}$ and $V_{sh m}$ in the complex voltage plane. Both graphs include the voltages at the input and at the output of the unit cell, V_n and V_{n+1} , respectively, and the phase-symmetry axis (dashed line). The vectors $V_{se k}$ and $V_{sh m}$, obtained by the difference and sum of the corresponding series or shunt sample vectors according to Equation (5.20) and Equation (5.21), respectively, and fulfilling the condition Equation (5.22), are perpendicular to each other, and thus in phase quadrature. (a) $V_{se k}$. (b) $V_{sh m}$.

or

$$\frac{V_{se k}}{V_{sh m}} = j\xi_{km}, \quad (5.26b)$$

which provides the same quadrature phase relationship as (5.25), with the real proportionality factor

$$\xi_{km} = \frac{|V_k| \sin(\Delta\Phi_k)}{|V_m| \cos(\Delta\Phi_m)}. \quad (5.27)$$

Since it is demonstrated for *arbitrary* voltage sample points (k and n), phase quadrature naturally extends to the *integral sum* of all the edge voltages associated with radiation. Therefore, the phase quadrature proof provided above applies to the *entire* LWA structure, and reveals that an LWA whose unit cell is asymmetric with respect to its longitudinal axis necessarily exhibits elliptical polarization radiation, or *circular polarization radiation* with broadside axial ratio obtained from (5.27) along with (5.13) and (5.15) as

$$\xi = \frac{\sum_k |V_k(\alpha_{se k})| \sin(\Delta\Phi_k)}{\sum_m |V_m(\alpha_{sh m})| \cos(\Delta\Phi_m)}. \quad (5.28)$$

It is therefore expected that the axial ratio of the LWA can be controlled by tuning the amount of asymmetry with respect to the longitudinal axis, as done in [108] for the case of a *uniform* LWA. This is demonstrated in Section 5.4.

5.2.1 Simplified Illustration using the SFP LWA

Figure 5.6 illustrates the phase quadrature relationship between the series and shunt radiation fields in an SFP LWA. For simplicity an ideal sinusoidal voltage distribution

is assumed, corresponding to a traveling wave along an ideal homogeneous transmission line. Figure 5.6(a) shows this idealized voltage distribution along the LWA at a time instance t_1 , where a maximum voltage at the vertical patch edges is present and the LWA produces series radiation. At a later time instance t_2 , corresponding to a 90° phase lag, the voltage maximum excites the horizontal edge, whereas the voltage at vertical edges is zero. This distribution is clearly producing shunt radiation, which can also be confirmed in Figure 3.5, where the series and shunt resonance modes for the SFP are illustrated.

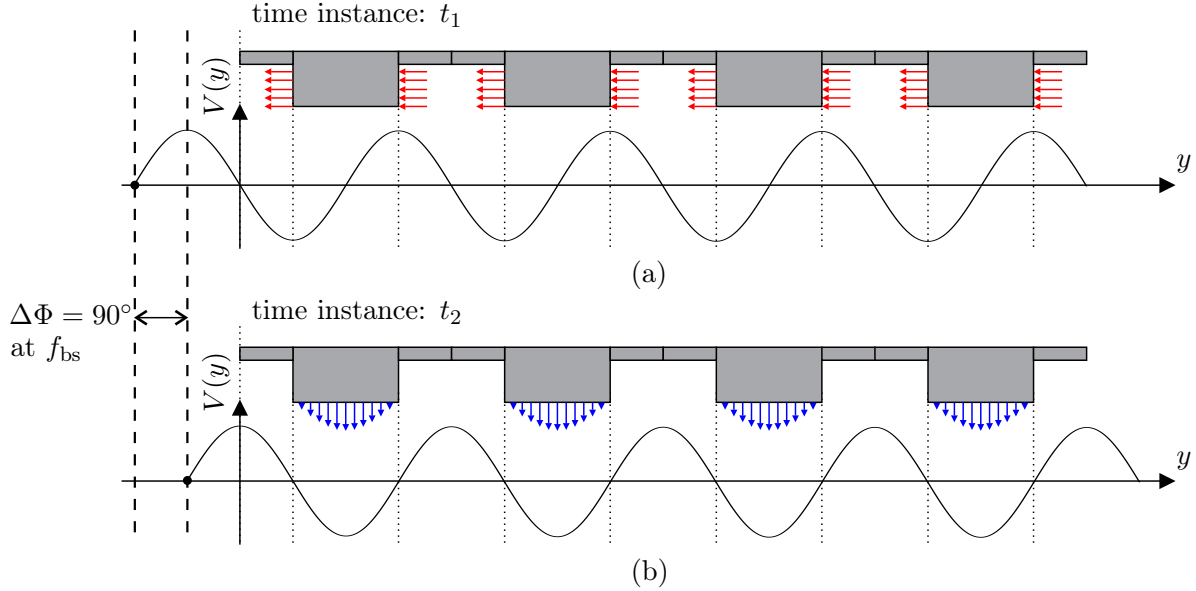


Figure 5.6: Simplified illustration of the phase quadrature relationship between the series and shunt radiation fields in an SFP LWA. An ideal sinusoidal wave is traveling in positive y -direction and alternately exciting the series and the shunt radiation modes. (a) At a time instance t_1 series farfield radiation is realized. (b) At a time instance t_2 , corresponding to a 90° phase lag, the LWA radiates in its shunt mode.

The electric field in Figure 5.6(a) is oriented in y -direction and the electric field in Figure 5.6(b) is oriented in x -direction. Thus, they are spatially orthogonal and their superposition in the farfield results in circular polarization, if the farfield amplitudes are equal. For the broadside radiation direction one can control the amplitude of the shunt radiation by the degree of longitudinal asymmetry, which may intuitively follow from the fact that in the fully symmetric unit cell of Chapter 3 the shunt radiation is canceled due to symmetry. A more detailed investigation of this is provided later in Section 5.4, where the axial ratio of the SFP LWA is optimized.

5.3 CRLH and SFP Case Study LWAs

This Section reuses the CRLH and the SFP case study examples of Chapter 3 and modifies them by introducing longitudinal asymmetry to their unit cells. First, the quadrature phase relationship is verified by comparing voltage samples of an ideal circuit model with corresponding samples obtained from fullwave simulation. Then, simulated and measured farfield pattern and axial ratio results are presented.

Table 5.1: Layout dimensions (μm) for the CRLH unit cell in Figure 5.7(a) and the SFP unit cell in Figure 5.7(b)

CRLH		SFP	
l_1	2250	l_1	3200
w_1	700	l_p	3425
l_g	350	w_1	300
l_o	450	w_p	1800
w_s	470	d	750
l_s	1875		

5.3.1 CRLH and SFP LWA Structures

Figures 5.7(a) and 5.7(b) show the unit cell geometries and layer stack-up for the CRLH and SFP LWAs, respectively. These unit cells are derived from their symmetric counterparts in Chapter 3. The CRLH unit cell in Figure 5.7(a) is modified in way that the double sided stub [Figure 3.25] is changed to a single sided one. Moreover the via ground connection is removed with the effect that the stub length must be increased by about a quarter wavelength to have the same shunt resonance frequency as before [36, 62]. This increase has a positive effect on the shunt radiation in a sense that the shunt efficiency also increases. The SFP unit cell is made asymmetric by shifting the feed line out off the longitudinal symmetry axis as shown in Figure 5.7(b). The corresponding geometry data for both unit cells is provided in Table 5.1.

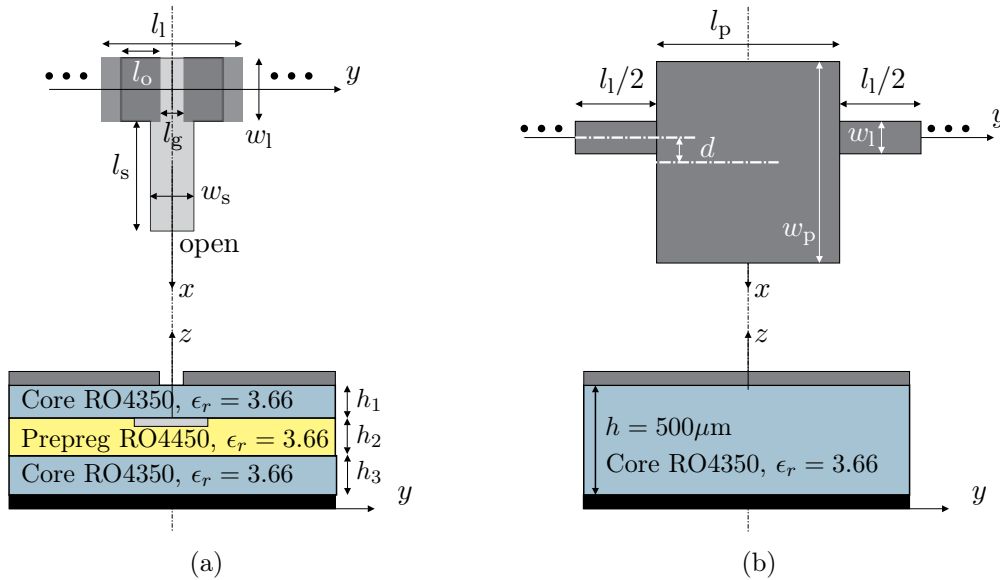


Figure 5.7: Examples of periodic LWAs with a longitudinally asymmetric unit cell. Shown are the layout (top) and layer stack-up (bottom). (a) Unit cell of a CRLH LWA with metal insulator metal (MIM) capacitor ($h_1 = 170 \mu\text{m}$, $h_2 = 100 \mu\text{m}$, $h_3 = 250 \mu\text{m}$). (b) Unit cell of a series-fed patch (SFP) LWA.

Both LWAs are optimized for a broadside frequency of $f_{bs} = 24 \text{ GHz}$ by realizing the frequency-balancing condition $f_{se} = f_{sh} = f_{bs}$ [Section 3.2], where the same optimization procedure as in Chapters 3 and 4 is used. In the CRLH LWA, l_g is used to tune f_{se} and

l_s is used to tune f_{sh} . In the SFP, one has to tune l_l and l_p simultaneously, since each of them affects both resonance frequencies, f_{sh} and f_{se} , [34]. The resonators are formed by quasi-lumped elements ($p \ll \lambda$) in the CRLH LWA, whereas in the SFP LWA the resonators are formed by distributed (transmission-line) resonators with an overall length of $p \approx \lambda$ across the unit cell, as discussed in the previous chapters.

5.3.2 Circuit Modeling

Figures 5.8(a) and 5.8(b) show the *specific* equivalent circuit models for the CRLH LWA and the SFP LWA, respectively. The lattice circuit model of Chapter 3 is a black box representation that models the two-port response without detailed knowledge of the interior. This is referred to as macroscopic modeling. Here, the interior is essential, since one wants to sample voltages in the circuit, so that a microscopic modeling is required, leading to the *specific* equivalent circuit models in Figures 5.8(a) and 5.8(b).

The CRLH LWA circuit model comprises the following circuit elements: the series inductance of the small transmission-line section L_R , the gap capacitance C_g , the capacitance to the middle metalization layer C_{MIM} , the ground capacitance C_{gnd} , and the transmission line of impedance Z_s and length l_s for the open ended stub line. For completeness, the series and shunt radiation conductances are also shown in the gap and at the end of the stub line, respectively.

The SFP LWA is modeled by three transmission-line sections, with different impedance, of 1) quarter wavelength, 2) half wavelength, 3) quarter wavelength at the broadside frequency, which is taken from Section 4.3.3, Figure 4.10. The quarter-wavelength lines have the impedance Z_l and the half-wavelength patch has the impedance Z_p . Series radiation is modeled by the conductance G_{edge} located at the vertical patch edge and the shunt conductance G_{center} located at the center of the horizontal patch edge.

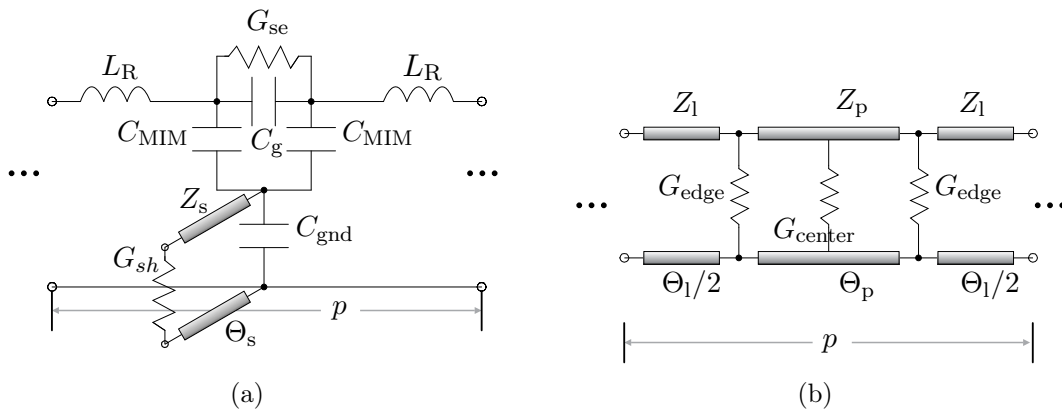


Figure 5.8: Specific equivalent circuit models of the unit cells in Figure 5.7. (a) CRLH LWA. (b) SFP LWA, where the equivalent circuit model is recalled from Figure 4.10(a).

Table 5.2 provides the extracted circuit parameters, obtained through a curve fitting procedure from fullwave simulated scattering parameters using a circuit simulator. The conductances, modeling radiation, are set to zero to represent a lossless circuit model under the same conditions as the theoretical proof in Section 5.2.

Table 5.2: Element parameters for the equivalent circuit of the CRLH unit cell in Figure 5.8(a) and the SFP unit cell in Figure 5.8(b)

CRLH		SFP	
L_R	0.44 nH	Z_l	90 Ω
C_g	0.02 pF	Z_p	35 Ω
C_{MIM}	0.06 pF	Θ_l	180°
C_{gnd}	0.43 pF	Θ_p	180°
Z_s	40.5 Ω		
Θ_s	110.82°		

5.3.3 Experimental Validation of the Quadrature Phase

The numerical results from circuit and fullwave simulations are now provided to illustrate the established quadrature phase relationship proven in Section 5.2.

Figure 5.9(a) and (b) show the fullwave models in EMPIRE XPU with the voltage probing positions. The voltages are obtained from electric field integration in z -direction. A sufficient number of $n = 100$ unit cells are cascaded and the voltages are sampled at the center cell ($n = 50$), in order to avoid reflection and truncation effects associated with the finiteness of the structure.

Figure 5.9(c) and (d) show the corresponding circuit models. A truly infinite periodic environment is emulated by terminating the unit cell with the exact, *a priori* calculated, Bloch impedance, Z_B^+ , coinciding with the input impedance for an infinite structure. This is done through a two-step procedure: first, the Bloch impedance is calculated as $Z_B^+ = \sqrt{Z_{se}/Y_{sh}}$ [Equations (3.30)] with the immittance parameters and the transmission matrix parameters defined in Chapter 3; next, a second simulation is launched, sampling the voltages, with the unit cell driven by a voltage source and terminated with Z_B^+ . The circuit modeling is essentially lossless and therefore does not account for radiation. This is in order to follow the assumption used in the proof of Section 5.2.

The voltage ratio, V_{sek}/V_{shm} , as given by (5.25), is plotted in Figure 5.10, which compares circuit and fullwave simulation results. Figure 5.10(a) plots the voltage ratio (amplitude and phase) for the CRLH LWA. A perfect broadband phase quadrature is clearly confirmed by the circuit simulation result. The CRLH structure, whose transition frequency is at 24 GHz, has its LH low-pass *stop-band* [26] around 22 GHz. Below this frequency, the amplitude and phase evaluation is naturally meaningless. The fullwave results are consistent with the circuit ones, and support the phase quadrature within a 10% variation. The ratio of the amplitude varies from 0 at the lower stopband to about 3 at 30 GHz, which affects the axial ratio over frequency.

Figure 5.10(b) shows the voltage ratio amplitude and phase for the SFP LWA. The circuit simulation reveals an ideal quadrature phase relationship from 16 GHz to 30 GHz, covering a huge bandwidth of 14 GHz. Across this bandwidth, the phase variation is only 20% in the fullwave model, which corresponds to an axial ratio limit for circular polarization. The amplitude, which is the second quantity of interest for obtaining a small axial ratio, is almost constant in the range between 18 GHz and 28 GHz, hence promising a rather frequency-independent axial ratio.

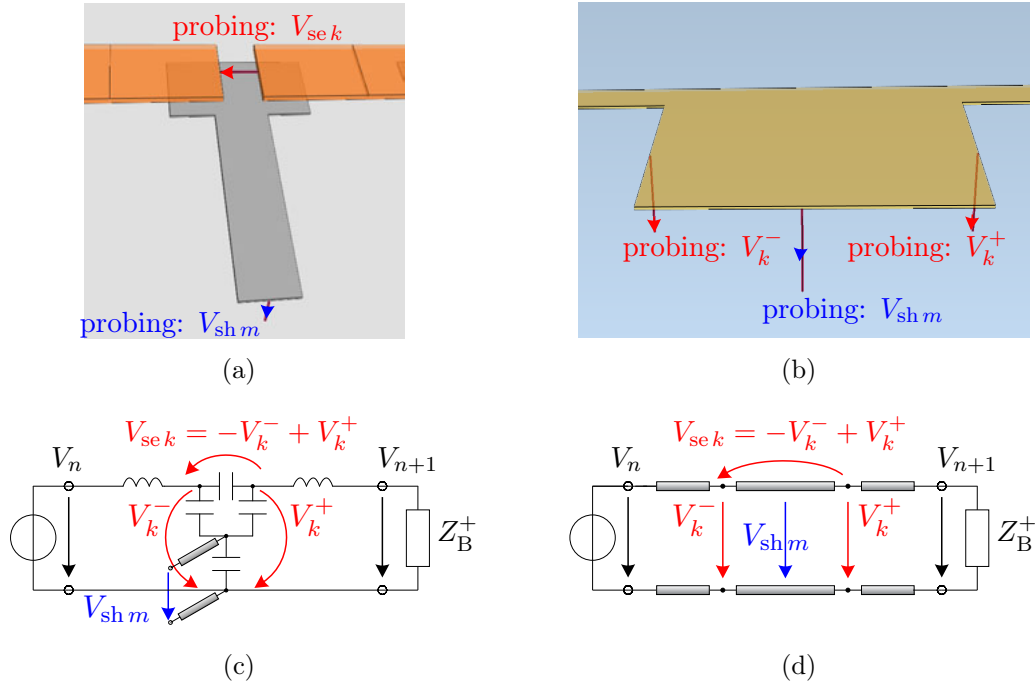


Figure 5.9: Voltage probing across the unit cell in a periodic structure (infinite repetition of the unit cell). (a) and (b) show the electromagnetic models with voltage probes for the CRLH and the SFP unit cell, respectively. A quasi-periodic environment is emulated by including a large number of unit cells so minimize reflections (< -40 dB) from the end. (c) and (d) show the *lossless* circuit models with voltage probes for the CRLH and the SFP unit cell, respectively. A perfectly periodic environment is emulated by terminating the unit cell with the exact, *a priori* calculated, Bloch impedance Z_B^+ .

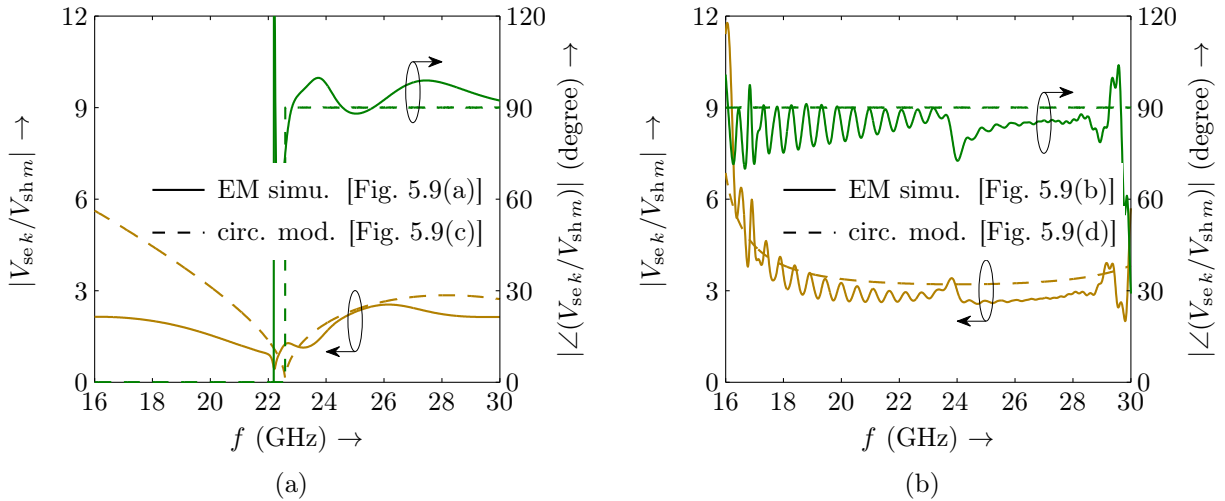


Figure 5.10: Voltage ratio V_{sek}/V_{shm} amplitude and phase obtained from circuit (dashed lines) and fullwave simulations (solid lines). A broadband phase difference of 90° between V_{sek} and V_{shm} is observed in an infinite periodic configuration for both LWAs. (a) CRLH unit cell. The amplitude and phase evaluation below approximately 22 GHz (lower stop-band) is not meaningful. (b) SFP unit cell having a broadband quadrature phase relationship of 14 GHz.

The phase discrepancies, between the electromagnetic simulation and the theoretical results in Figures 5.10, are due to radiation loss, air coupling between unit cells and to the existence of a small band gap in the SFP case in Figure 5.10(b). Such effects are not taken into account in the idealized lossless circuit models. Reflections from the end of the finite LWA are minimized by using a large number of cascaded cells, in order to ensure that these phase discrepancies are *not* attributed to reflections from the LWA termination side.

In Summary, Figure 5.10 verify the broadband nature of the quadrature phase relationship required as a first condition for circular polarization. The second condition - equal field amplitudes - is not exactly represented by sampled voltages, since accurate determination of the radiated farfield requires integration over all radiating edges.

Therefore, the amplitudes in Figure 5.10 are *relative* quantities in terms of the radiated fields, which only indicate the expected frequency variation of the axial ratio.

5.3.4 Measurement of Circularly Polarized LWA Prototypes

Figures 5.11(a) and 5.11(b) show the fabricated prototypes for the CRLH and SFP LWAs, respectively. The CRLH LWA is composed of 15 unit cells and is electrically relatively small, featuring a length of $L \approx 2.8 \lambda$ without the feeding-line sections. The SFP LWA is electrically much larger, with $L \approx 22 \lambda$ compared to the CRLH LWA. The reason for the different electrical lengths is simply that these antennas were fabricated in different contexts. The length difference does not represent any limitation to the forthcoming experimental validation, since the polarization does not depend on the length of the LWA.

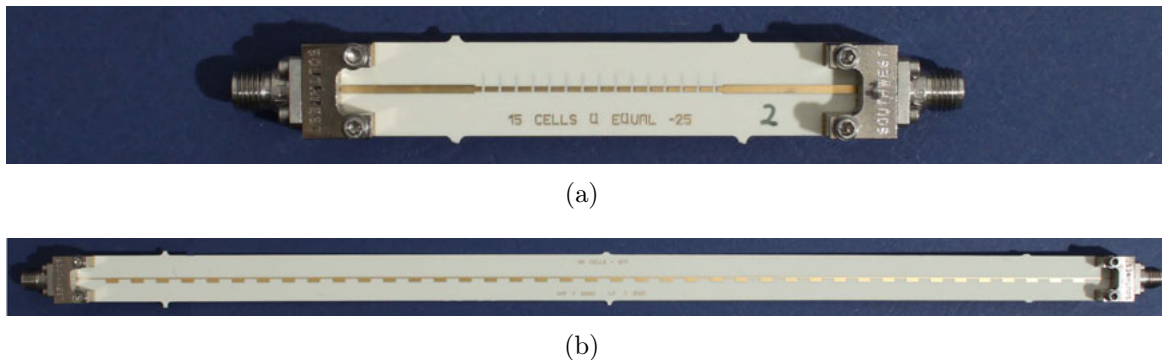


Figure 5.11: Fabricated LWA prototypes with end-feed connectors. (a) CRLH LWA with 15 unit cells (electrical length $\approx 2.8 \lambda$). (b) SFP LWA with 40 unit cells (electrical length appr. $\approx 22 \lambda$).

The Bloch impedance of the CRLH LWA is in the order of 50Ω , and hence does not require an additional matching section at the LWA excitation side. The SFP LWA, on the other hand, requires a quarter-wavelength transformer at its input to match the Bloch impedance of $\approx 170 \Omega$ to 50Ω . The LWAs are excited from one side while the other side is terminated with a matched load. An enlarged view of the prototypes is provided in Figure 5.12. The dashed lines in Figure 5.12(a) indicate the middle metalization layer beneath the top metalization.

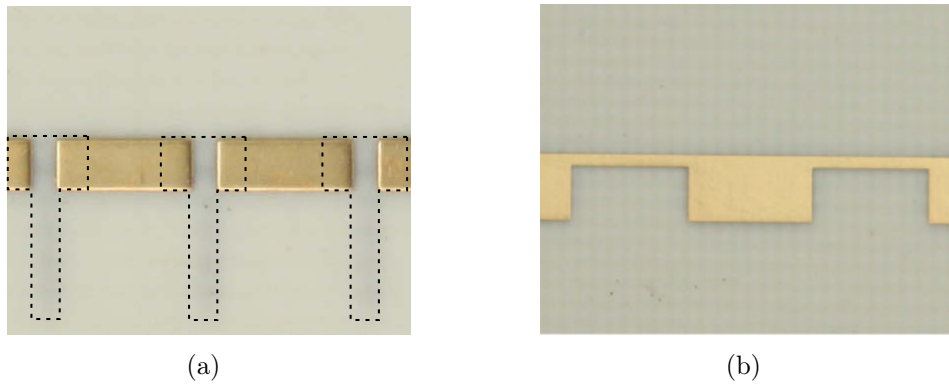


Figure 5.12: Enlarged views of the fabricated LWAs showing the unit cell details. (a) CRLH LWA. (b) SFP LWA.

The LWAs are characterized by a cylindrical nearfield measurement in the anechoic chamber at IMST GmbH, shown in Figure 5.13. The electric field is sampled on a cylindrical surface (excluding the circular top and bottom faces, where radiation is negligible) using an open-ended waveguide probe. The vertical and horizontal fields are measured, so as to fully characterize the LWA in their nearfield zone. Finally, the nearfield data is transformed to the farfield using the commercial antenna measurement software package MiDAS (from ORBIT/FR, Inc) in order to provide the antenna gain and polarization.

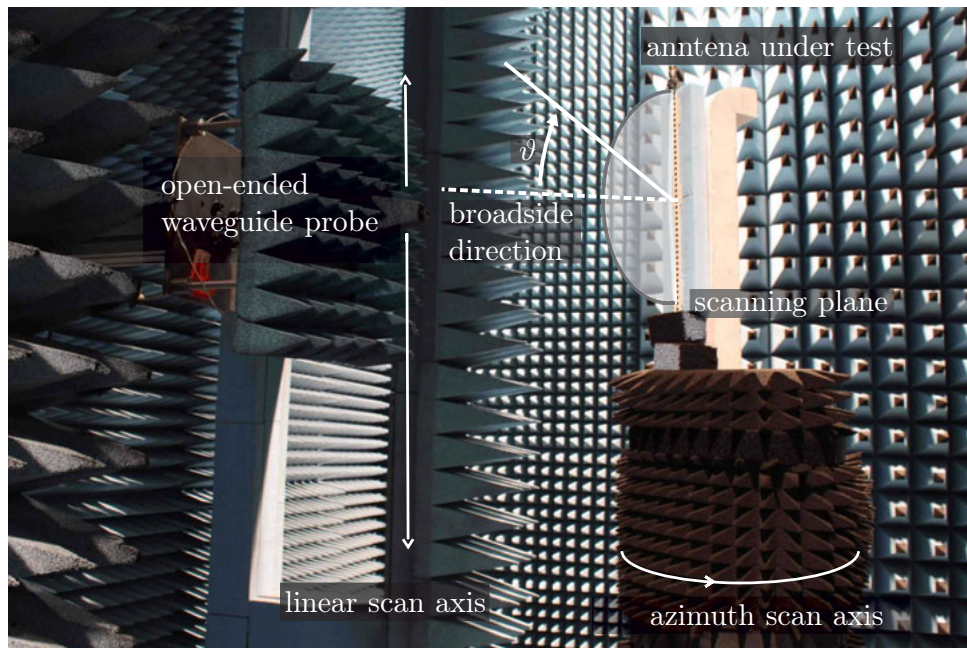


Figure 5.13: Cylindrical nearfield measurement setup in the anechoic chamber at IMST GmbH. The measured nearfield data are transformed to the farfield and the RHCP/LHCP gain components are evaluated using the commercial measurement software MiDAS.

Figure 5.14 shows the simulated and measured co- and cross-polarization gains at 23, 24 and 25 GHz. Both LWAs are right-hand circular polarized (RHCP) with the left-hand circular polarization (LHCP) being the cross-polarization. In general, an excellent agreement between the simulated and measured co- and cross-polarization is observed. The cross-polarization agreement is not so good as the co-polarization agreement, which

is due the fact that the cross-polarization is more sensitive to fabrication, alignment and measurement errors.

Figure 5.14(a) shows that the CRLH LWA exhibits a relatively large half-power beamwidth, as an expected consequence of its small electrical length. On the other hand the LWA scanning sensitivity with frequency is relatively high, due to the small period p of the unit cell [34]. This LWA has a moderate circular polarization response, with a cross polarization rejection varying from about 23 dB at 23 GHz up to 10 dB at 25 GHz, as shown in Figure 5.15(a). The agreement between simulation and measurement is reasonably good in the main beam direction. Comparison of the axial ratio in Figure 5.15(a) with the voltage-based amplitudes in Figure 5.10(a) shows the same trend of increase with frequency for the CRLH case.

Unfortunately, only the backward radiation region, at 23 GHz, exhibits a good axial ratio, of less than 3 dB. However, no optimization is carried out, and this result experimentally demonstrates the circular (or elliptical) polarization response of the longitudinally asymmetric CRLH LWA.

Figure 5.14(b) shows that the SFP LWA exhibits a smaller half-power beamwidth, as a result of its electrically much larger size. The scanning sensitivity with frequency of this LWA is much smaller than that of the SFP, due to its larger period p . This LWA has an excellent circular polarization response at broadside, with a cross polarization rejection of more than 20 dB. For the backward and forward radiation zones, the cross polarization rejection is less, ranging from 18 to 13 dB. The corresponding axial ratio is plotted in Figure 5.15(b), consistently with the cross polarization rejection in Figure 5.14(b). Comparison of the axial ratio in Figure 5.15(b) with the voltage based amplitudes in Figure 5.10(b) shows the same frequency insensitivity for the SFP case. Finally, the circular polarization characteristics of the SFP LWA are experimentally demonstrated.

The theoretical analysis in Section 5.1 is restricted to *only* the broadside direction (z -direction). However, as it is shown in this section, the circular polarization feature is maintained also for off-broadside radiation directions within a scanning range in the order of $[-20^\circ, +20^\circ]$ around broadside. This is investigated by inspecting the fundamental relation (5.25). In terms of phase, Equation (5.25) is inherently broadband, since the phase is always $\pi/2$ irrespectively to frequency. Therefore, a quadrature phase relationship exists for broadside and off-broadside angles. In contrast, in terms of amplitude, Equation (5.25) clearly depends on frequency via k, m . However, when the radiating array structure is electrically relatively large, as is the case in LWAs, the radiation characteristics are essentially determined by the array factor, while the element factor plays a minor role [109]. The element factor can therefore only have a minor effect on the radiation property of the LWA, since the frequency sensitivity of the unit cell magnitude in Equation (5.25) is an element factor quantity. Hence, despite its frequency dependence, Equation (5.25) is a broadband relationship and thus extends to off-broadside radiation angles.

5.4 Axial Ratio Optimization

This section presents a parametric study showing that, as predicted in Section 5.2, the axial ratio of longitudinally asymmetric LWAs can be minimized by adjusting the degree of asymmetry in the structure. This study is presented only for the case of the SFP LWA, whose asymmetry does not affect the resonance frequencies. In the CRLH LWA, the stub

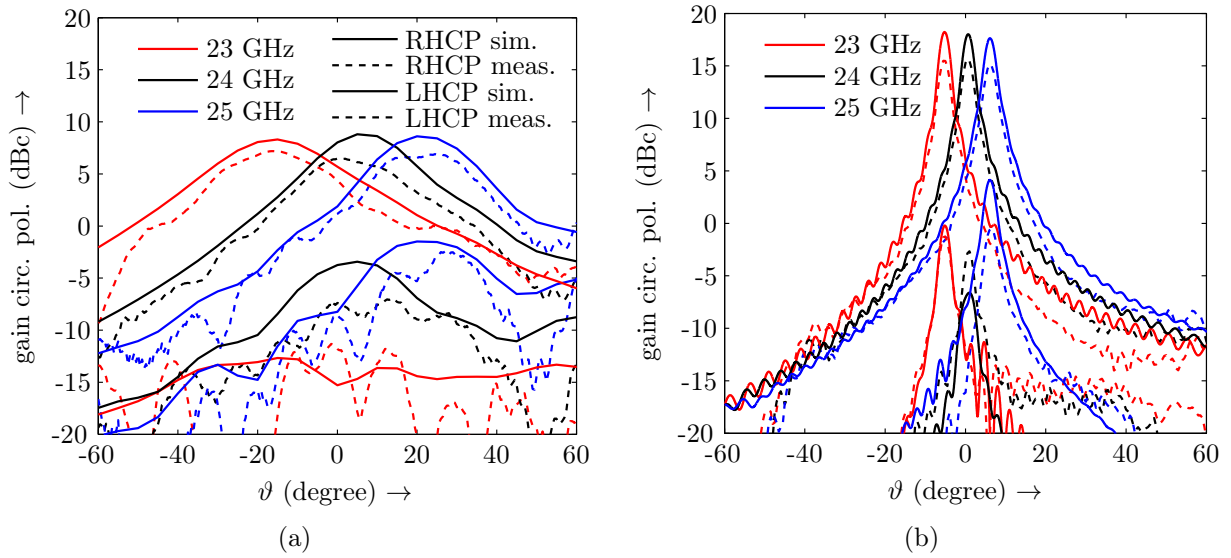


Figure 5.14: Measured and simulated radiation patterns in the scanning plane. Circular polarization is confirmed by comparing RHCP (co-pol.) gain and LHCP gain (cross-polarization) for three frequencies 23 GHz, 24 GHz and 25 GHz. (a) CRLH LWA. (b) SFP LWA.

length controls the shunt resonance frequency and can therefore not straightforwardly be exploited as an independent asymmetry parameter.

The degree of asymmetry is proportional to the parameter d , shown in Figure 5.7(b), which represents an offset between the longitudinal axis of the feed line and the center of the patch. For each d value, the line length (l_1) and the patch length (l_p) are optimized to achieve broadside radiation at $f_{bs} = f_{se} = f_{sh} = 24$ GHz from equalized series and shunt resonances.

Figure 5.16(a) plots the SFP LWA axial ratio in the scanning plane for different values of d versus the elevation angle for three frequencies, 23, 24 and 25 GHz, corresponding to the beam pointing angles -6° , 0° , and $+6^\circ$, respectively. The elevation angular range is divided in three sectors: -15° to -4° for backward radiation (23 GHz), -3° to $+3^\circ$ for broadside radiation (24 GHz) and $+4^\circ$ to $+15^\circ$ for forward radiation (25 GHz) to evaluate the axial ratios of the main beams. The half-power beamwidth in each sector is indicated by the shaded rectangular zones. It clearly appears that the axial ratio decreases with increasing d up to $d = 450$ μm . Figure 5.16(b) provides the axial ratio over a smaller scale for better visualization of the results around $d = 500$ μm . The best trade-off, with an axial ratio of less than 0.8 dB in the backward, broadside and forward regions, is found at $d = 500$ μm . If d is further increased as done in Figure 5.16(c), one observes in the backward and forward regimes that the trend is reversed, the axial ratio increasing with further increasing asymmetry.

Figures 5.16(b) and 5.16(c) show, for asymmetries providing *near optimum* axial ratios, that the axial ratio at broadside is 1) relatively low and close to 0 dB and 2) relatively insensitive to asymmetry variation, whereas in the backward and forward regimes it strongly depends on asymmetry variation. The low axial ratio at broadside and the sensitivity difference of the axial ratio between the broadside and off-broadside regimes is next explained. This is done by investigating the series and shunt powers, P_{se} and P_{sh} , using the theoretical framework established in Section. 3.3.

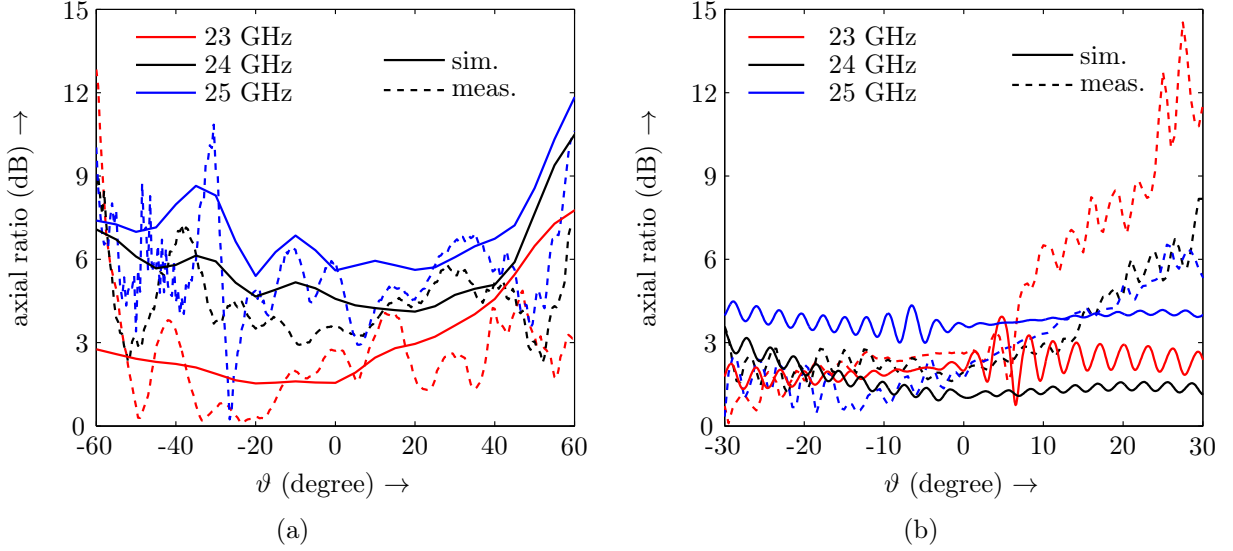


Figure 5.15: Axial ratio (dB) in the scanning plane. (a) CRLH LWA. (b) SFP LWA.

In the forthcoming developments the dissipation loss is neglected, which is a reasonable assumption in typical cases where radiation leakage is significantly larger than dissipation. This is equivalent to assuming that the total series and shunt powers are equal to the radiated series and shunt powers following that $\eta_{se} = \eta_{sh} = 1$. In addition, the degree of asymmetry is now restricted to axial asymmetries which provide *near optimum* axial ratios. Radiation at broadside results from the sum of the two equivalent and orthogonal magnetic dipoles representing respectively the series and shunt radiation contributions, as indicated in Figure 5.3. Although rotationally offset by 90° in their common plane (xy -plane), these dipoles, given their identical toroidal patterns, exhibit relatively similar radiation patterns around broadside. Assuming that these patterns are identical, which is a reasonable approximation in a small solid angle around broadside, including small backward and forward angles, the axial ratio can be simply expressed in terms of the series and shunt powers⁶. Under these three conditions (no dissipation, near-broadside radiation and *near-optimum* axial ratios), the axial ratio is approximated by

$$AR \approx \sqrt{\frac{P_{se,rad}}{P_{sh,rad}}} = \sqrt{\frac{P_{se}}{P_{sh}}}. \quad (5.29)$$

5.4.0.1 Broadside

At the broadside frequency f_{bs} , and under the frequency-balanced condition ($\omega_{se} = \omega_{sh} = \omega_{bs}$), the total series and shunt powers (radiation + dissipation) are always *equal*.⁷ Recalling Equation (3.63) from Chapter 3,

$$P_{se} = P_{sh} = \frac{1}{2}P, \quad (5.30)$$

⁶In the case of a fully symmetric structure, there is a null in the shunt pattern [Figure 3.5] at broadside, leading to linear longitudinal polarization. So, this argument naturally relates only to the case of asymmetric structures, in particular *near optimum* axial ratio structures.

⁷This is true for both longitudinally symmetric and longitudinally asymmetric LWAs, as long as they are symmetric with respect to the transversal axis, so that the theory of Chapter 3 can be applied.

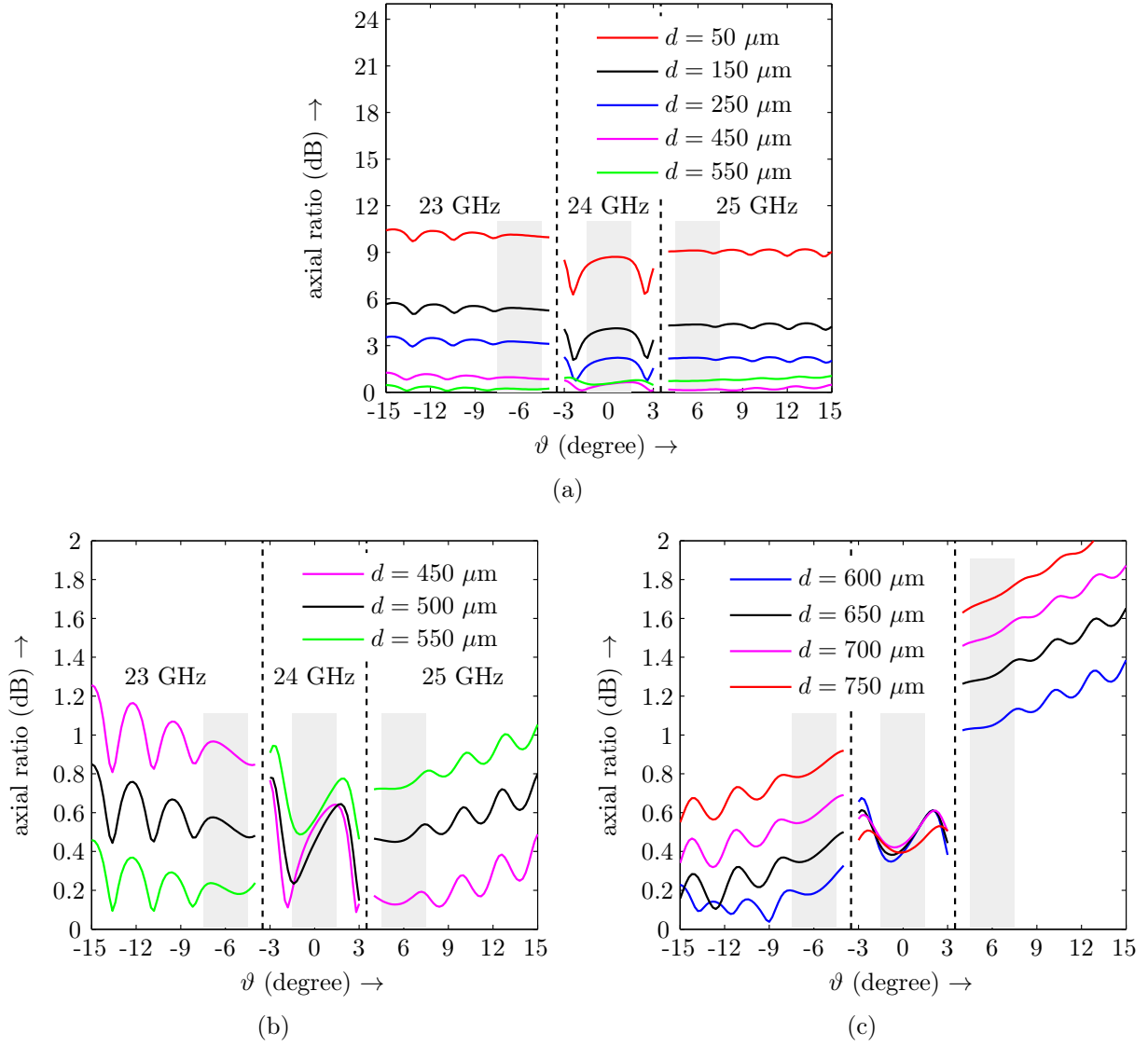


Figure 5.16: Simulated axial ratio (dB) in the scanning plane using EMPIRE XPU. The degree of asymmetry with respect to the longitudinal axis is parameterized by d . The shaded areas indicate the half-power beamwidth. (a) Coarse variation from $d = 50 \mu\text{m}$ to $d = 550 \mu\text{m}$. (b) Fine variation with $\pm 50 \mu\text{m}$ around the optimum axial ratio of $d = 500 \mu\text{m}$. (c) Fine variation with $\pm 50 \mu\text{m}$ from $d = 550 \mu\text{m}$ to $d = 750 \mu\text{m}$, which represents the maximum asymmetry, see prototype in Figure 5.12(b).

and inserting it into (5.29), approximates the at-broadside axial ratio by

$$AR_{\text{bs}} \approx 1. \quad (5.31)$$

This result shows that, under the aforementioned conditions, the axial ratio is equal to one (0 dB) at the broadside frequency, resulting in perfect circular polarization. Moreover, since the axial ratio in Equation (5.31) is a constant, the axial ratio is obviously invariant under asymmetry variation for near-optimum values.

5.4.0.2 Off-Broadside

For off-broadside frequencies, the series and shunt powers are generally *different*, whereas here, the time-average stored energies are *equal*. Recalling Equation (3.69) from Chapter 3,

$$W_{se} = W_{sh} = \frac{1}{2}W, \quad (5.32)$$

confirms that off-broadside series and shunt energies are equal. Furthermore, recalling the quality factor in Equation (3.58)

$$Q = \omega \frac{\text{energy per unit length}}{\text{power loss per unit length}} = \omega \frac{W}{P}, \quad (5.33)$$

the series and shunt powers are related to their respective quality factors by

$$P_{se} = \omega \frac{W_{se}}{Q_{se}} \quad \text{and} \quad P_{sh} = \omega \frac{W_{sh}}{Q_{sh}}. \quad (5.34)$$

Inserting Equation (5.34) into (5.29), and using the energy relation $W_{se} = W_{sh}$ [Equation (5.32)], approximates the off-broadside axial ratio by

$$AR_{\text{off-bs}} \approx \sqrt{\frac{Q_{sh}}{Q_{se}}}. \quad (5.35)$$

This result shows that the axial ratio is generally not equal to one and that it varies according to the ratio of the series and shunt quality factors for near-optimum values. Moreover, Equation (5.35) reveals that, although the off-broadside axial ratio is generally different from one, it is exactly one in the particular case of Q-balancing ($Q_{se} = Q_{sh}$) [Equation (3.48)], which is thus also the condition for minimum axial ratio off-broadside. From a practical viewpoint, this last point is very convenient, since it indicates that optimum circular polarization is inherently associated with optimum broadside radiation.

Since the axial ratio in (5.35) depends on the two quality factors, one needs to investigate the dependence of the quality factors on asymmetry to better understand the corresponding axial ratio behavior. The series and shunt quality factors of the SFP LWA are plotted in Figure 5.17 versus the asymmetry parameter d as defined in Figure 5.7(b). These quality factors are obtained using the drivenmode extraction technique described in Section 3.4.2.

Figure 5.17 shows that Q_{sh} strongly depends on asymmetry, whereas Q_{se} is essentially insensitive to asymmetry. Q_{sh} is maximum for the fully symmetric configuration ($d = 0$), where shunt radiation is canceled at broadside, and strongly decreases when asymmetry is introduced and increased, according to Equation (5.34), due to the progressive reduction of radiation cancellation associated with increased shunt radiation power. The asymmetry invariant behavior of Q_{se} is due to the absence of structural variation along the longitudinal axis⁸. The Q-balancing condition is approximately met at $d \approx 550 \mu\text{m}$.

The axial ratio behavior in Figure 5.16 may now be understood by evaluating Equation (5.31) at broadside, and Equation (5.35) together with the Q-factors in Figure 5.17 off-broadside.

⁸The parameter d does not change the overall length of the series radiating edges, which remains constant: $w_p - w_l = 1500 \mu\text{m}$.

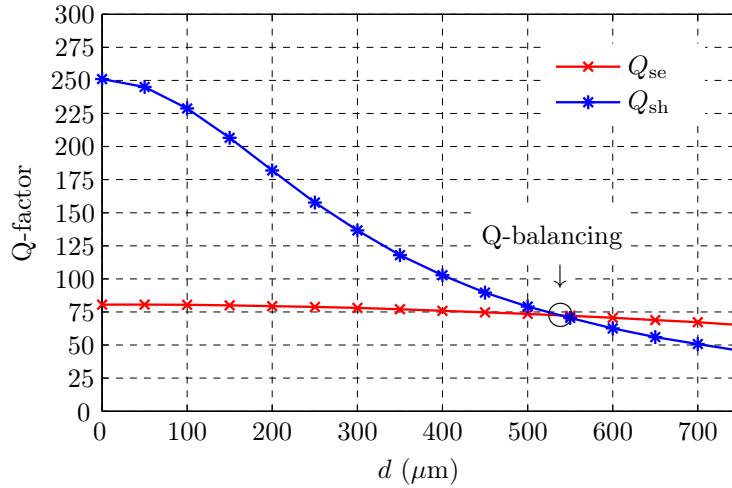


Figure 5.17: Simulated series and shunt quality factors of the unit cell versus the patch offset d (degree of longitudinal asymmetry). Q-balancing is achieved at $d \approx 550 \mu\text{m}$.

In Figure 5.16(a) the axial ratio at broadside does *not* behave according to (5.31), where a constant and low axial ratio, independent of asymmetry, is expected. The reason is that the shunt radiation pattern is strongly affected by the asymmetry in near-symmetric structures. Indeed, the shunt radiation pattern has a null at broadside for the fully symmetric configuration [Figures 3.5 and 3.16] and its pattern is thus totally different from the series radiation pattern, which exhibits a maximum at broadside. Here, the aforementioned assumption of identical patterns is thus violated, and hence the behavior of the axial ratio is not captured by Equation (5.31). On the other hand, the axial ratio in the off-broadside regime qualitatively behaves according to Equation (5.35), i.e. it decreases as Q_{sh} decreases.

Figures 5.16(b) and (c) show the axial ratio in the near-optimum asymmetry range. Here, the radiation characteristics of the series and shunt contributions are not strongly affected by the asymmetry variation, due to the similarity of the corresponding radiation pattern. At broadside, the axial ratio is relatively low and insensitive to asymmetry variations, in agreement with Equation (5.31). Off-broadside, the exact behavior predicted by (5.35) is observed, with Q_{se} being constant and Q_{sh} decreasing with increasing d . First, the axial ratio is decreased to its minimum [Figure 5.16(b)] and next it increases with further increasing asymmetry [Figure 5.16(c)]. While the optimum axial ratio is observed in Figure 5.16(b) at around $d = 500 \mu\text{m}$, Q-balancing is found in Figure 5.17 at around $d \approx 550 \mu\text{m}$. Given the approximations in (5.35) (no dissipation loss and identical series and shunt patterns), this is considered an excellent agreement. If the asymmetry is further increased, beyond the Q-Balancing condition ($d > 550 \mu\text{m}$), the shunt radiation power starts to dominate the series radiation power, following (5.29), which increases the off-broadside axial ratio.

5.5 Summary of Symmetry Properties

Longitudinally asymmetric and transversally symmetric LWAs exhibit the following characteristics:

- they naturally inherit the transverse symmetry properties from Chapter 3 (i.e. all properties of the symmetric lattice circuit of Figure 3.2)
- series radiation is longitudinally polarized in broadside direction
- shunt radiation is transversally polarized in broadside direction
- a broadband quadrature phase relationships exists between these components
- shunt broadside radiation is controlled by the degree longitudinal asymmetry, and is totally eliminated under longitudinal symmetry
- circular polarization is achieved under the Q-balancing condition
- polarization is robust against frequency scans through broadside and a low axial ratio is maintained in a broad frequency range

In this chapter, a broadband quadrature phase relationship between series and shunt radiation contributions in *longitudinal asymmetric* LWAs is derived. It is demonstrated that the degree of longitudinal asymmetry, together with the quadrature phase relationship, can be optimally exploited for the design of circularly polarized LWAs.

Summary, Conclusion and Outlook

In this chapter, the main research results are summarized and the broadside radiation properties of each LWA symmetry class are reviewed. Finally, a conclusion and an outlook on future works is presented.

6.1 Summary and Conclusion

The present dissertation has systematically analyzed the broadside degradation problem and resolved it by means of asymmetry in the LWA geometry. Two fundamental conditions, *frequency-balancing* and *quality-factor-balancing*, have been established to characterize LWAs around broadside. The term *open-stopband*, which is most often used in the literature when referring to the strong variations of the complex propagation constant, is not clearly defined and hence does not provide a quantitative measure of this degradation, whereas *frequency-balancing* and *quality-factor-balancing* does provide such measure. The simultaneous satisfaction of both conditions results in frequency independent impedance, gain and efficiency, as the LWA scans through the critical broadside direction.

The proposed model, together with the evaluation of the electromagnetic field on the unit cell boundaries, has revealed a fundamental broadside radiation efficiency limitation in *fully symmetric* LWAs. They suffer from an efficiency limitation at broadside, since only the series mechanism is radiating broadside, whereas the shunt mechanism is dissipative and has a radiation null in broadside direction. An inevitable *equal* power split exists between the series and the shunt mechanisms at the broadside frequency. If only one mechanism is radiating with the other only being dissipative, half the power is lost and hence the radiation efficiency limitation of 50% persists. Without this understanding and considering the fact that humans have a natural preference for symmetry, LWAs have most often been designed of fully symmetric unit cells in the past and are thus strongly limited in their broadside performance.

Breaking the symmetry with respect to the *transversal* axis overcomes the broadside limitation. By properly tuning the degree of *transversal asymmetry* in the unit cell,

quality-factor-balancing has been achieved, and the broadside impedance, gain and efficiency have been equalized to their corresponding off-broadside values. Specifically, the broadside efficiency has been increased by controlling the power ratio between the series and the shunt resonators through transversal asymmetry, where the power level in the radiating series resonator has been increased and the power level in the dissipative shunt resonator has been decreased. Moreover, it has been proven that the broadside efficiency can even exceed the off-broadside level, a behavior which, to the author's best knowledge, had not been reported in the context of LWAs until now.

Breaking the symmetry with respect to the *longitudinal axis* results in broadside radiation from the shunt mechanism, which is polarized in the transversal direction. The existence of a *quadrature phase* relationship between the series and the shunt farfield radiation contributions, polarized in longitudinal and transversal direction, respectively, has been discovered. It has been demonstrated for an SFP LWA that quality-factor-balancing can be achieved by properly adjusting the degree of *longitudinal asymmetry*, which eventually equalizes the amplitudes of the two orthogonal farfield contributions. The equalized farfield amplitudes together with the quadrature phase relationship, lead to circularly polarized broadside radiation. Little attention has been paid to the polarization characteristics and controllability in the literature. This thesis contributes to mend this deficiency and may stimulate the design of new LWA types with efficient circular polarization.

The *double asymmetry* case (transversally and longitudinally asymmetric) has not been considered in this dissertation. Generally, the properties and features of the two asymmetry classes can be combined in a way that more degrees of freedom are available to design LWAs with specific impedance, radiation and polarization characteristics. That detailed analysis and discussion is beyond the scope of this thesis, as there are no further fundamental *research* results expected from the pure combination of the two asymmetry classes. Nevertheless, from an *application* viewpoint, the double asymmetry class still offers an innovative concept for polarization switching between longitudinal and transversal polarization, as demonstrated in [65].

Based on the fundamental results of this dissertation, the author concludes that *asymmetry* is the key to solve the broadside problem in periodic LWAs. Metamaterial LWAs, and here specifically CRLH LWAs, do *not* exhibit extraordinary broadside radiation properties over conventional LWAs, which has been a common misconception widely spread in the literature. If asymmetry is properly considered and the LWAs are compared on an equal footing, both types show identical broadside properties and both suffer from the same efficiency limitations. Nevertheless, the CRLH transmission line theory has strongly stimulated this research yielding a universal LWA modeling approach, which allows to consider conventional LWAs from a different perspective.

6.2 Outlook

The outlook on future work is separated into two parts. The first part discusses open points that are directly related to the proposed modeling or even limit the proposed modeling. These points have a practical impact on the design of periodic LWAs and series-fed array antennas. The second part reviews current technology trends and explores how they may benefit from the research results of this dissertation.

The application of this theory to hollow metallic waveguide LWAs or SIW LWAs is to be investigated as an extension of this work. Particularly, the introduction of resonant radiating slots in such waveguide LWAs may limit the proposed modeling approach.

The existing exponential power decay profile along the periodic LWA structure leads to a fixed radiation pattern characteristic with a certain sidelobe level and beamwidth. By applying a geometrical taper, where each *unit cell*¹ element is of different geometry, the power profile along the periodic LWA structure is controlled and hence a desired pattern characteristic is obtained. For a moderate geometrical taper, it is expected that the field distribution is very similar to the true periodic case and that the theory and symmetry considerations of this thesis provide a good design guide. For a strong geometrical taper, which in many applications is not required, the modeling has to be revised.

As opposed to LWAs, series-fed array antennas can have an arbitrary termination condition at their termination side. Therefore, series-fed array antennas form a more general class and they are widely used in low cost RF-modules, where relatively high gain is required. Particularly, the termination with an open- or short-circuit condition produces a standing wave, as opposed to a traveling or leaky wave in the periodic LWA that is terminated with a matched load. The investigation of the transition between leaky wave operation and standing wave operation, which depends on the *termination condition* and on the *electrical length* of a series-fed array antenna, directly opens a future work topic of theoretical and practical relevance.

Terahertz technology is an emerging trend, in which the *terahertz* frequency band for various applications [110] is exploited. The frequency band from 300 GHz to 3 THz is commonly referred to as the terahertz band, and it lies between the microwave band and infrared frequencies, offering a huge absolute bandwidth. In the past, technological barriers have prevented the use of this bandwidth. The advent of nano-technology, together with new semiconductor alloys and advanced foundry processes, has made this frequency band accessible for applications. The applications include, among others, body scanners at airports, cancer detection, spectroscopy of chemicals, short range sensing and short range ultra-high data rate communication systems.

In particular, at higher terahertz frequencies, where the wavelengths are in the sub-millimeter regime, bondwire interconnects are critical, since they may introduce a severe mismatch and their reproducibility is poor. Here, on-chip antennas [111] provide a possibility to avoid these interconnects and also to overcome the 50 Ohm barrier that conventionally exists for connecting RF-blocks. The trend to on-chip antennas is therefore strongly driven by the evolving terahertz technology.

Series-feed concepts are beneficial to realize electrically large (though physically very small) antennas especially on a chip, since they do not require a complex feed network and yet provide a relatively high gain. The fundamental knowledge on LWA symmetry properties, provided in this dissertation, may help to design efficient LWAs for the on-chip environment. Furthermore, LWAs with advanced functionalities, for example, polarization and pattern switching between series and shunt radiation patterns can be thought of, if the active control circuitry is on the chip together with the antenna.

Finally, the beam scanning feature of LWAs may be optimally exploited at terahertz frequencies, where a complex phase shifting network is difficult to realize but a large bandwidth is available. A recent publication in the “nature” journal [112] has reported a

¹In the strict sense, this is not a *unit cell* anymore.

periodic LWA based on photonic crystals scanning the beam with frequency in a band centered around 10 THz, which confirms the originality of cutting-edge research on periodic LWAs.

List of Figures

1.1	Examples of different periodic LWA types. (a) and (b) rectangular waveguide LWAs. (c) Substrate integrated waveguide LWA. (d) to (f) Planar microstrip LWAs.	2
1.2	Illustration of a typical operation of an LWA, where the radiation main beam scans with frequency from the backward quadrant through broadside to the forward quadrant. The shaded half circle indicates the scanning plane.	4
1.3	Qualitative illustration of the broadside radiation problem, where a strong variation in the parameters are observed generally at broadside. (a) Phase constant and leakage constant. (b) Magnitude of the input impedance. (c) Gain patterns showing a beam scan with frequency in the scanning plane. The broadside radiation is degraded compared to the radiation in the backward and forward directions.	6
2.1	SFP LWA as an example for a general periodic structure. The unit cell period is p and the wave propagates along the y -axis.	12
2.2	Dispersion diagram as a graphical representation of the complex propagation constant. Periodic structures generally show passband (white regions) and stopband (grey shaded regions) behaviors over frequency. The spatial harmonics are separated by multiple of $2\pi/p$. The blue solid lines represent the case of power propagation in <i>positive</i> y -direction. The green dashed line represent the case of power propagation in <i>negative</i> y -direction.	14
2.3	Dispersion diagram for an SFP LWA as shown in Figure 2.1 (non-shielded periodic structure). Beam scanning is achieved with the $\mathbf{n} = -1$ space harmonic, which is of fast-wave nature and therefore lies in the radiation regime. The light line with $k_0 = \pm\omega/c_0$ divides the dispersion diagram into the radiation regime and the guided wave regime.	16
2.4	Simplified illustration of full range scanning with a single main beam. The dispersion relation of a homogeneous (non-periodic) transmission line structure without stopbands is shown. The case of an effective permittivity of $\epsilon_{r,\text{eff}} = 9$ is plotted, following that $\omega_{\text{bf},-2} = \omega_{\text{ef},-1}$	18

2.5	Equivalent two-port network representation of LWAs. (a) SFP LWA example formed by a cascade of an infinite number of unit cells. (b) Infinite cascade of equivalent two-port networks represented by the transmission matrix ($ABCD$ -matrix).	20
2.6	Definition of LWA symmetry classes. (a) Fully symmetric unit cell. (b) Transversally asymmetric unit cell. (c) Longitudinally asymmetric unit cell. (d) Transversally and longitudinally asymmetric unit cell.	24
3.1	Class of <i>fully symmetric</i> LWAs that is considered in this chapter.	25
3.2	Lattice circuit model for the unit cell of fully symmetric periodic LWAs.	27
3.3	Equivalent circuits under odd/even excitation. (a) Odd excitation, where the series element Z_{se} is isolated. (b) Even excitation, where the shunt element Y_{sh} is isolated.	27
3.4	Immittances, Z_{se} and Y_{sh} , and linearization procedure using the SFP example. (a) Linearization of the reactance $\text{Im}\{Z_{se}\}$ at the resonance frequency ω_{se} . (b) Linearization of the susceptance $\text{Im}\{Y_{sh}\}$ at the resonance frequency ω_{sh} .	28
3.5	Series-fed patch example under odd and even excitation: Directivity patterns (vector sum of both far-field polarizations) for the SFP example. (a) Odd excitation generating series radiation, where the patch is operated in the conventional $\lambda/2$ -patch mode and radiates broadside. (b) Even excitation generating shunt radiation, where the radiation null in broadside direction is confirmed and the main radiation is directed to the $\pm x$ - and $\pm y$ -directions. (c) Qualitative sketch of the electric field in the x - y -plane and simplified voltage/current distributions ⁴ along the patch under odd excitation. (d) Simplified distributions ⁴ under even excitation.	31
3.6	Equivalent lattice circuit with the definition of the inner series current and shunt voltage quantities.	34
3.7	Overview <i>frequency-balancing</i> and <i>Q-balancing</i> conditions. The series and shunt efficiencies are chosen to be $\eta_{se} = 0.9$ and $\eta_{sh} = 0.2$, respectively. The broadside radiation efficiency is $\eta_{bs} = (\eta_{se} + \eta_{sh})/2$ in all four cases. (The thin solid black lines in the dispersion diagrams show the corresponding <i>lossless</i> cases, with $R = G = 0$, to clearly indicate that only in a <i>lossless</i> periodic structure a well-defined stopband is delimited by ω_{se} and ω_{sh} .)	42
3.8	Single unit cell simulation model. The two-port parameters are obtained from a drivenmode simulation and the immittance Z_{se} , Y_{sh} and the LCRG parameters are calculated using the procedure described in Sections 3.1.1 and 3.1.2, respectively.	51
3.9	Multiple unit cell simulation model to consider the effect of mutual coupling. The overall transmission matrix \mathbf{ABCD}^N of the cascade of N unit cells is obtained from driven mode simulation. The two-port data, following the immittances and the LCRG parameters, for the de-embedded unit cell are calculated by taking the N^{th} -root of \mathbf{ABCD}^N to find \mathbf{ABCD} .	54
3.10	Extracted LCRG parameters from a cascade of N unit cells. The N^{th} -root is taken of the overall transmission matrix, $\mathbf{ABCD}_{N\text{-cells}}$, to obtain the transmission matrix of the unit cell, \mathbf{ABCD} and to extract the LCRG parameters. (a) Series reactance slope L . (b) Shunt susceptance slope C . (c) Series resistance R . (d) Shunt conductance G .	55

3.11 Resonator efficiencies, η_{se} and η_{sh} , comparing the two efficiency extraction methods: gain integration and loss discrimination. (a) Series efficiency with little deviation in the two methods and a good convergence for the loss discrimination method. (b) Shunt efficiency showing a larger discrepancy as in (a) and some non-physical behavior ($\eta_{sh} < 0$) for $N < 7$	56
3.12 Simulation model with periodic boundaries to model the infinite cascade by accurately taking into account all mutual coupling effects. The eigenmode simulation with phase shift $\Phi = 0$ across the cell boundaries in propagation direction (y -axis) results in two modes, the series and the shunt resonance mode.	57
3.13 Illustration of the electric field components taking into account the structural and the vectorial field symmetry of the odd and even mode. (a) Odd mode with an anti-symmetric field distribution. (b) Even mode with a symmetric field distribution.	58
3.14 Eigenmode simulation setup for the unit cell parameter extraction using stored energy and power. (a) Simulation setup with PEC boundaries to extract the series mode parameters. (b) Setup with PMC boundaries to extract the shunt mode parameters. (c) and (d) Equivalent lattice under short circuit and open circuit condition, respectively, where the linear reactance and susceptance slopes are approximated by a LC resonator. . .	60
3.15 Infinite cascade of unit cells with excitation sources for the evaluation of series and shunt radiation. Artificial introduction of spacing Δd , which in the limit, $\Delta d \rightarrow 0$, forms the LWA with period p . All unit cells are uniformly excited with zero phase progression (broadside condition $\beta = 0$). (a) Odd excitation (series radiation) of the array, where the electric field on the planes between two cells (red faces) exhibits the condition of a PEC wall. (b) Even excitation (shunt radiation) of the array, where the magnetic field on the planes between two cells (green faces) exhibits the condition of a PMC wall.	64
3.16 Normalized gain patterns over the angle ϑ in the x - z plane (transverse to the propagation direction) for the SFP example. (a) Series radiation with maximum at broadside, cancellation in the $\pm x$ -direction and electric field polarization in φ -direction (y -direction). (b) Shunt radiation with radiation null at broadside, radiation in the $\pm x$ -direction and electric field polarization in ϑ -direction.	64
3.17 Array configuration in transverse direction of uniformly excited LWAs with spacing w . (a) Infinite model in transverse direction. (b) Equivalent single LWA simulation model with PMC side walls.	65
3.18 Boundary conditions for series and shunt radiation considering the infinite array in Figure 3.17. (a) Series radiation, where the PEC/PMC boundaries only support broadside radiation with electric field polarization in y -direction. (b) Shunt radiation is totally eliminated by the four enclosing PMC boundaries following that $\eta_{sh} = 0$ and $\eta \leq 50\%$ in an infinite array. .	66
3.19 SFP LWA with 40 cascaded unit cells. (a) Overall SFP LWA with end launch connectors. (b) Zoomed top view of the SFP unit cell with geometry definitions. The dimension are $\ell_p = 3.1$ mm, $w_p = 3.3$ mm, $\ell_\ell = 3.6$ mm, $w_\ell = 0.3$ mm, $p = 6.7$ mm. (c) Stack-up with $h_1 = 500$ μ m.	67

3.20	Simulated dispersion diagram and Bloch impedance of the SFP LWA showing the approximation capability of the LCRG modeling. The solid lines are directly obtained from simulated two-port data through Equations (3.2), (3.16) and (3.30). The dashed lines correspond to the LCRG model, where a good agreement up to a bandwidth of 8 GHz is observed. (a) Dispersion diagram. (b) Bloch impedance.	68
3.21	Scattering parameters of the SFP LWA with $w_p = 3.3$ mm. (a) Measured S-parameters with end launch connectors [Figure 3.19(a)] based on 50Ω reference impedance. The parameter $ S_{01} $ shows the power loss due to reflection and transmission according to Equation (3.91). (b) Simulated S-parameters measured at the unit cell interface with reference impedance $Z_{B,off-bs}^+ \approx 200 \Omega$	69
3.22	Anechoic chamber and farfield measurement setup at IMST GmbH. (a) Positioning system with azimuth and roll axis for a full characterization of the antenna under test. (b) Zoomed view of the antenna under test, the SFP LWA, where the antenna gain is measured in azimuth plane (scanning plane).	70
3.23	<i>Realized gain</i> and <i>antenna gain</i> patterns in the azimuth plane (y - z) for various frequencies. (a) Realized gain (measured) including the mismatch of the SFP LWA to the 50Ω reference impedance. (b) Antenna gain, obtained from measured realized gain corrected by the mismatch and the transmission loss according to Equation (3.92) (solid lines), and simulated antenna gain (dashed lines).	71
3.24	Measured and simulated radiation efficiencies of the 40-cell SFP LWA with patch width $w_p = 3.3$ mm. The LCRG model is compared and validated by measurement and by two independent drivenmode simulations (FEM and FDTD). (a) SFP LWA in Figure 3.19. (b) SFP LWA in a uniformly excited array (PMC side walls) according to Figure 3.17, confirming the broadside efficiency limitation of maximal 50%.	72
3.25	CRLH LWA with 60 cascaded unit cells. (a) Overall CRLH LWA with end launch connectors. (b) Zoomed top view of the CRLH unit cell with geometry definitions. (c) Stack-up.	74
3.26	Measured and simulated radiation efficiencies for the 60-cell CRLH LWA. The LCRG model is compared and validated by measurement and simulation. (a) CRLH LWA of Figure 3.25. (b) CRLH LWA in a uniformly excited array (PMC side walls) according to Figure 3.17, confirming the broadside efficiency limitation of maximal 50%.	75
4.1	Class of <i>transversally asymmetric</i> LWAs that is considered in this chapter.	77
4.2	Derivation of the equivalent lattice circuit with ideal transformers in preparation for asymmetry modeling. (a) Lattice model from Chapter 3 for symmetric unit cells. (b) Decomposition of the circuit in (a) into odd and even responses and formal introduction of ideal galvanic isolation transformers with transformation ratio 1 : 1. (c) Recombination of the circuits in (b) to form the <i>transformer-lattice circuit model</i> that is equivalent to the circuit in (a).	78

4.3	Transformer-lattice circuit model for asymmetrical unit cells. This circuit is obtained from Figure 4.2(c) by introducing a transformation ratio T different from unity, where the parameter T accounts for the degree of asymmetry.	79
4.4	Approximation of the dispersion relation in (4.13). (a) Approximation of $\ln(T)$ with $1/4(T^2 - 1/T^2)$ [Equation (4.15)] provides a better fitting in the range $0.8 < T < 1.2$ than the first order Taylor approximation with $T - 1$. (b) Propagation constant for these three approximation cases, demonstrating the superior approximation nature of Equation (4.16).	83
4.5	Overview asymmetry variation (increasing transformation ratio T from left to right column) in a frequency-balanced unit cell. The series and shunt efficiencies are set to $\eta_{se} = 0.9$ and $\eta_{sh} = 0.2$, respectively. The broadside efficiency η_{bs} is controlled by T and can be adjusted between η_{sh} and η_{se} . Column three shows the case of optimum asymmetry $T = T_{opt}$, where equalization is achieved.	90
4.6	Two approaches to dispersion modeling of periodic structures. (a) and (c) Complex propagation constant two-port model and dispersion relation, respectively. A real frequency ω_1 is the argument of the complex γ : $\gamma(\omega_1) \in \mathbb{C}$. (b) and (d) Complex frequency two-port model and dispersion relation, respectively. For a real phase argument Φ_1 the complex frequency Ω is calculated: $\Omega(\Phi_1) \in \mathbb{C}$. For a lossless unit cell these two approaches are identical.	92
4.7	Comparison of the spatial and temporal amplitude behavior. (a) Complex propagation constant models a spatial decay. This approach corresponds to the natural driven excitation of the LWA. (b) Complex frequency models a time decay. This is a common approach of commercial fullwave eigenmode solvers employing periodic boundaries.	92
4.8	Dispersion diagram comparison of the <i>complex propagation constant</i> (left) and the <i>complex frequency</i> (right) for different transformation ratios. Dispersion from the complex propagation constant for: (a) Symmetric case where $T = 1$. (c) Optimal case, where $T = T_{opt}$. (e) $T > T_{opt}$. Dispersion from the complex frequency for: (b) Symmetric case ($T = 1$). (d) Optimal case ($T = T_{opt}$). (f) $T > T_{opt}$. (The black solid lines show the dispersion for the lossless case, where $R = G = 0$).	95
4.9	Quality factor comparison of the <i>complex propagation constant</i> (left) and the <i>complex frequency</i> (right) for different transformation ratios. Transmission line quality factor from the complex propagation constant for: (a) Symmetric case where $T = 1$. (c) Optimal case where $T = T_{opt}$. (e) $T > T_{opt}$. Coupled quality factors from the complex frequency for: (b) Symmetric case ($T = 1$). (d) Optimal case ($T = T_{opt}$). (f) $T > T_{opt}$	97
4.10	SFP model simplification with $G = G_{center} = 0$ for the illustration of degenerated modes. (a) SFP layout and corresponding simplified ideal transmission line model with radiation conductances for series (G_{edge}) and shunt (G_{center}) radiation. (b) Fullwave eigenmode parallel plate waveguide model with PEC and PMC boundaries corresponding to the ideal transmission line model in (a). At $d = \lambda/4$ and $d = 3\lambda/4$ sheet conductors with G_{edge} are placed. G_{center} is set to zero.	100

4.11	Complex frequency versus the transformation ratio T for $\Phi = 0$, simulated with HFSS. The bottom horizontal axis shows T and the top axis the corresponding transmission line impedance Z_t according to (4.55). T_{opt} is 1.079 ($Z_{t,\text{opt}} = 85.85 \Omega$). At this point the two modes become degenerate with $\Omega_1 = \Omega_2$	102
4.12	Normalized voltage distribution (eigenmodes) along the fullwave unit cell model of Figure 4.10(b). The unit cell asymmetry is varied from (a) to (f) by changing Z_t from 100 Ω to 60 Ω . The mode degeneration is observed for the optimum case in (d), where the two eigenmodes become degenerate by exhibiting an identical voltage distribution.	103
4.13	Voltage and current distributions (eigenmodes) for the asymmetric case $Z_T = 86 \Omega$ for different imposed boundary conditions located at $d = 0$ and $d = \lambda$. (a) Distributions under periodic boundaries with $\Phi = 0$ corresponding to Figure 4.12(c), where the two non-orthogonal modes couple. (b) Distributions under PEC boundaries for the isolation of the series mode. (c) Distributions under PMC boundaries at for the isolation of the shunt mode.	105
4.14	PEC boundary condition to isolate the series mode. (a) Fullwave model from Figure 3.14(a), which is adapted to asymmetry by monitoring I_n and I_{n+1} with \mathcal{C}_n and \mathcal{C}_{n+1} , respectively. (b) Overall transformer lattice circuit where the input and output is shorted corresponding to the PEC condition. (c) Resulting circuit where only the series impedance subsists due to the suppression of the shunt resonance with $V_{\text{sh}} = 0$	106
4.15	PMC boundary condition to isolate the shunt mode. (a) Fullwave model from Figure 3.14(b), which is adapted to asymmetry by monitoring V_n and V_{n+1} with \mathcal{L}_n and \mathcal{L}_{n+1} , respectively. (b) Overall transformer lattice circuit where the input and output is open corresponding to the PMC condition. (c) Resulting circuit where only the shunt admittance subsists due to the suppression of the series resonance with $I_{\text{se}} = 0$	108
4.16	Composite right/left-handed (CRLH) LWA. (a) Perspective view. (b) Layout of the symmetric unit cell with top and middle metalization layer. (c) Asymmetry parameter d in the middle layer, where the dashed line indicates the outline of the symmetric unit cell in (a) (top layer is the same as in (a) and is not shown). (d) Stack-up. (All the dimensions are given in mm.)	111
4.17	Radiation efficiency comparison for 50-cell CRLH LWAs (overall length $\approx 9\lambda_0$, -32 dB power at the terminated end) between fullwave results and LCRG circuit model predictions for different asymmetries. (a) Symmetric case with $d = 0 \mu\text{m}$ ($T = 0$). (b) Optimal asymmetry case with $d = 85 \mu\text{m}$ ($T = T_{\text{opt}}$). (c) Excessive asymmetry with $d = 200 \mu\text{m}$ ($T > T_{\text{opt}}$). (d) Dependency of T and T_{opt} versus asymmetry (d).	113
4.18	Surface current density vector distribution for the two eigenmodes under the periodic boundary condition $\Phi = 0$. Blue and red colors in the vector fields refer to low and high field strengths, respectively. The solid red arrows indicate the dominant fields. (a) and (d) Series and shunt modes, respectively, for the symmetric unit cell. (b) and (e) Weak asymmetry case, where coupling between the two modes is observable. (c) and (f) Optimal asymmetry case.	115

4.19	Series-fed coupled patch (SFCP) LWA. (a) Perspective view. (b) Metalization layout, where d is the patch offset distance from the unit cell center (green dashed line) for asymmetry. (c) Stack-up. (All the dimensions are given in mm.)	116
4.20	Radiation efficiency comparison for 50-cell SFCP LWA (overall length $\approx 29\lambda_0$, -28 dB power at the terminated end) between fullwave results and LCRG circuit model predictions for different asymmetries. (a) Symmetric case with $d = 0 \mu\text{m}$ ($T = 1$). (b) Optimal asymmetry case with $d = 300 \mu\text{m}$ ($T = T_{\text{opt}}$). (c) Excessive asymmetry case with $d = 600 \mu\text{m}$ ($T > T_{\text{opt}}$). (d) Dependency of T and T_{opt} versus asymmetry d	117
5.1	Class of <i>longitudinally asymmetric</i> LWAs that is considered in this chapter.	119
5.2	Arbitrary layout of a fully symmetric unit cell with symmetric voltage sampling points V at the radiating edges. For an observer placed at <i>broadside</i> in the farfield (z -direction), the voltage <i>difference</i> in the y and x directions is proportional to the series and shunt radiation field contributions, respectively. (a) The series radiation contributions (indexed k) from the vertical edges, polarized in the y -direction, are non-zero due to phase variation of the traveling wave in this direction. (b) The shunt radiation contributions (indexed m) from the horizontal edges, polarized in the x -direction, are zero due to symmetry.	121
5.3	Asymmetric unit cell with respect to the longitudinal axis. The series contribution, $V_{\text{se}k}$, is the <i>difference</i> of the voltages with index k according to Equation (5.13). The shunt contribution, $V_{\text{sh}m}$, is the <i>sum</i> of the voltages with index m . The shunt radiation is <i>not</i> canceled and therefore contributes to the farfield in the broadside direction.	123
5.4	Series and shunt voltage sampling at the vertical and horizontal edges with indices k and m , respectively. In general, a phase shift Φ exists between the input/output voltages, V_n and V_{n+1} , respectively. The phase along at $y = 0$, which defines the transversal axis, is therefore $\Phi_{\text{sym}} = \Phi/2$ and represents the <i>phase-symmetry axis</i> of the unit cell.	125
5.5	Graphical proof of the quadrature phase relationship between $V_{\text{se}k}$ and $V_{\text{sh}m}$ in the complex voltage plane. Both graphs include the voltages at the input and at the output of the unit cell, V_n and V_{n+1} , respectively, and the phase-symmetry axis (dashed line). The vectors $V_{\text{se}k}$ and $V_{\text{sh}m}$, obtained by the difference and sum of the corresponding series or shunt sample vectors according to Equation (5.20) and Equation (5.21), respectively, and fulfilling the condition Equation (5.22), are perpendicular to each other, and thus in phase quadrature. (a) $V_{\text{se}k}$. (b) $V_{\text{sh}m}$	127
5.6	Simplified illustration of the phase quadrature relationship between the series and shunt radiation fields in an SFP LWA. An ideal sinusoidal wave is traveling in positive y -direction and alternately exciting the series and the shunt radiation modes. (a) At a time instance t_1 series farfield radiation is realized. (b) At a time instance t_2 , corresponding to a 90° phase lag, the LWA radiates in its shunt mode.	128
5.7	Examples of periodic LWAs with a longitudinally asymmetric unit cell. Shown are the layout (top) and layer stack-up (bottom). (a) Unit cell of a CRLH LWA with metal insulator metal (MIM) capacitor ($h_1 = 170 \mu\text{m}$, $h_2 = 100 \mu\text{m}$, $h_3 = 250 \mu\text{m}$). (b) Unit cell of a series-fed patch (SFP) LWA.	129

5.8	Specific equivalent circuit models of the unit cells in Figure 5.7. (a) CRLH LWA. (b) SFP LWA, where the equivalent circuit model is recalled from Figure 4.10(a).	130
5.9	Voltage probing across the unit cell in a periodic structure (infinite repetition of the unit cell). (a) and (b) show the electromagnetic models with voltage probes for the CRLH and the SFP unit cell, respectively. A quasi-periodic environment is emulated by including a large number of unit cells so minimize reflections (< -40 dB) from the end. (c) and (d) show the <i>lossless</i> circuit models with voltage probes for the CRLH and the SFP unit cell, respectively. A perfectly periodic environment is emulated by terminating the unit cell with the exact, <i>a priori</i> calculated, Bloch impedance Z_B^+ .	132
5.10	Voltage ratio $V_{sek}/V_{sh m}$ amplitude and phase obtained from circuit (dashed lines) and fullwave simulations (solid lines). A broadband phase difference of 90° between V_{sek} and $V_{sh m}$ is observed in an infinite periodic configuration for both LWAs. (a) CRLH unit cell. The amplitude and phase evaluation below approximately 22 GHz (lower stop-band) is not meaningful. (b) SFP unit cell having a broadband quadrature phase relationship of 14 GHz.	132
5.11	Fabricated LWA prototypes with end-feed connectors. (a) CRLH LWA with 15 unit cells (electrical length $\approx 2.8 \lambda$). (b) SFP LWA with 40 unit cells (electrical length appr. $\approx 22 \lambda$).	133
5.12	Enlarged views of the fabricated LWAs showing the unit cell details. (a) CRLH LWA. (b) SFP LWA.	134
5.13	Cylindrical nearfield measurement setup in the anechoic chamber at IMST GmbH. The measured nearfield data are transformed to the farfield and the RHCP/LHCP gain components are evaluated using the commercial measurement software MiDAS.	134
5.14	Measured and simulated radiation patterns in the scanning plane. Circular polarization is confirmed by comparing RHCP (co-pol.) gain and LHCP gain (cross-polarization) for three frequencies 23 GHz, 24 GHz and 25 GHz. (a) CRLH LWA. (b) SFP LWA.	136
5.15	Axial ratio (dB) in the scanning plane. (a) CRLH LWA. (b) SFP LWA.	137
5.16	Simulated axial ratio (dB) in the scanning plane using EMPIRE XPU. The degree of asymmetry with respect to the longitudinal axis is parameterized by d . The shaded areas indicate the half-power beamwidth. (a) Coarse variation from $d = 50 \mu\text{m}$ to $d = 550 \mu\text{m}$. (b) Fine variation with $\pm 50 \mu\text{m}$ around the optimum axial ratio of $d = 500 \mu\text{m}$. (c) Fine variation with $\pm 50 \mu\text{m}$ from $d = 550 \mu\text{m}$ to $d = 750 \mu\text{m}$, which represents the maximum asymmetry, see prototype in Figure 5.12(b).	138
5.17	Simulated series and shunt quality factors of the unit cell versus the patch offset d (degree of longitudinal asymmetry). Q-balancing is achieved at $d \approx 550 \mu\text{m}$.	140

List of Tables

3.1 Summary of lattice circuit model parameters for transversally symmetric unit cells	30
3.2 Summary of the asymptotic at- and off-broadside formulas of this section including the asymptotic radiation efficiency results from Sections 3.3.2 and 3.1.7.	50
3.3 LCRG parameters and resonance frequencies extracted from a single SFP unit cell. The results of two commercial fullwave simulators, EMPIRE XPU and HFSS, are compared. (The value $G < 0$ is obviously non-physical, which is carefully addressed in the text.)	52
3.4 Series and shunt efficiencies obtained from the loss discrimination method using EMPIRE XPU and HFSS. (The values $\eta_{\text{sh}} < 0$ and $\eta_{\text{sh}} > 1$ are non-physical, which is carefully addressed in the text.)	53
3.5 Evaluation of the electric and magnetic fields on the cell boundaries located at $y = \pm p/2$ for the anti-symmetric mode and the symmetric mode.	58
3.6 Evaluation of the field components in Table 3.5 under the periodic boundary condition in (3.80) with $\Phi = 0$. The x - and z -field components are tangential in the boundary plane, whereas the y -field component is normal, so that the conditions simply translate to PEC and PMC boundaries for the odd and even mode, respectively.	59
3.7 Comparison of the measured and simulated gain patterns plotted in Figure 3.23(b).	71
3.8 LCRG parameters, quality factor and efficiency results obtained by fullwave eigenmode extraction computed by Equations (3.84) and (3.88). The patch width w_p is varied in three steps showing strong impact on the shunt radiation efficiency η_{sh} . The total suppression of shunt radiation, $\eta_{\text{sh}} = 0$, is confirmed in the infinite array case (PMC), Figure 3.18.	73
4.1 Summary of the at- and off-broadside formulas for transversally asymmetric unit cells. The broadside regime is strongly affected by asymmetry ($\tau \neq 0$ corresponding to $T \neq 1$) and the off-broadside parameters are identical to the ones for the symmetric case in Table 3.2.	86

4.2	Parametrization of the fullwave transmission line model in Figure 4.10(b). The frequency f_0 is set to 24 GHz. The permittivity and the permeability are artificially manipulated so that under the variation of Z_t the geometry of the model is not altered.	101
4.3	LCRG parameters and efficiencies for CRLH and SFCP unit cells extracted by eigenmode and drivenmode methods as described in Sections 4.4 and 4.1.2, respectively.	112
5.1	Layout dimensions (μm) for the CRLH unit cell in Figure 5.7(a) and the SFP unit cell in Figure 5.7(b)	129
5.2	Element parameters for the equivalent circuit of the CRLH unit cell in Figure 5.8(a) and the SFP unit cell in Figure 5.8(b)	131

List of Acronyms and Symbols

Symbols may be reused, if the context allows a clear distinction. Complex quantities are not specifically denoted as such. Phasors quantities, for example, voltage V and current I , are based on peak amplitudes. Throughout this thesis, where phasors are used or are implied, the time convention $e^{j\omega t}$ applies.

Acronyms

- 1D** One-Dimensional
- 2D** Two-Dimensional
- 3D** Three-Dimensional
- 5G** 5th Generation Mobile Networks
- BF** Backfire
- BS** Broadside
- CRLH** Composite Right/Left-Handed
- EF** Endfire
- FDTD** Finite Difference Time Domain
- FEM** Finite Element Method
- HFSS** High Frequency Structure Simulator
- HPBW** Half Power Beamwidth
- IEEE** Institute of Electrical and Electronics Engineers
- LHCP** Left Hand Circular Polarization
- LWA** Leaky-Wave Antenna
- MB** Main Beam

MIM	Metal Insulator Metal
PEC	Perfect Electric Conductor
PMC	Perfect Magnetic Conductor
PML	Perfectly Match Layer
RF	Radio Frequency
RHCP	Right Hand Circular Polarization
SFCP	Series-Fed Coupled Patch
SFP	Series-Fed Patch
SIW	Substrate Integrated Waveguide
SNR	Signal to Noise Ratio
TE	Transverse Electric
TEM	Transverse Electromagnetic
UC	Unit Cells

Styles

$\mathbf{ABCD}, \mathbf{Z}$	matrix quantity
\vec{E}, \vec{H}	vector quantity
n	space harmonic index
\mathcal{C}	closed line integration contour
\mathcal{L}	line integration path
\hat{x}, \hat{n}	unit vector

Latin Symbols

A	matrix element of the transmission matrix
AR	axial ratio
$AR_{\text{bs}}, AR_{\text{off-bs}}$	at-broadside axial ratio, off-broadside axial ratio
\mathbf{ABCD}	transmission matrix of unit cell
$\mathbf{ABCD}_{N\text{-cells}}$	transmission matrix of N cascade unit cells
$\mathbf{ABCD}_{\text{sym}}$	transmission matrix transversally symmetric unit cells
B	matrix element of the transmission matrix
C	shunt slope parameter
C	matrix element of the transmission matrix
$C_g, C_{\text{gnd}}, C_{\text{MIM}}$	gap capacitance, and ground capacitance, and MIM capacitance
$C_{\text{se}}, C_{\text{sh}}$	series capacitance, and shunt capacitance

C'	per-unit-length capacitance of a TL
\mathcal{C}_n	closed line integration contour at the n^{th} terminal
D	matrix element of the transmission matrix
d	distance
d	transversal asymmetry offset distance
d	longitudinal asymmetry offset distance
$d\bar{l}$	infinitesimal line element oriented along the line
ds	infinitesimal surface element
$d\bar{s}$	infinitesimal surface element oriented in normal direction
dv	infinitesimal volume element
\bar{E}	electric field vector
\bar{E}_n	electric field vector of the n^{th} space harmonic
E_x, E_y, E_z	electric field components in $x, y,$ and z direction
\bar{F}	periodic vector field
f	frequency
f_0	harmonic mean frequency
$f_{\text{bs}}, f_{\text{bal}}$	broadside frequency, and balanced frequency
$f_{\text{se}}, f_{\text{sh}}$	series resonance frequency, and shunt resonance frequency
G	shunt conductance
G	antenna gain
G_{realized}	realized gain
G'	per-unit-length conductance
G_{diss}	shunt dissipation conductance
$G_{\text{lossy}}, G_{\text{lossless}}$	shunt conductance with, and without loss consideration
G_{rad}	shunt radiation conductance
$G_{\text{die}}, G_{\text{con}}$	shunt dielectric, and conductor dissipation conductance
$G_{\text{center}}, G_{\text{edge}}$	center conductance, and edge conductance
g	LWA dimension
\bar{H}	magnetic field vector
\bar{H}_{tan}	tangential magnetic field
H_x, H_y, H_z	magnetic field components in x, y or z direction
h	unit cell height
h	TL height
h_1, h_2, h_3	LWA substrate heights
$I_{\text{se}}, I_{\text{sh}}$	series current, and shunt current
I_n, I_{n+1}	current at the n^{th} , and $n^{\text{th}} + 1$ unit cell terminal
K	coupling coefficient
k	integer sampling point for vertical edge voltages
k_0	free-space phase constant
k_1, k_2, k_3, k_4	current nodes
L	series slope parameter

L_R	inductance
L'	per-unit-length inductance of a TL
L_{se}, L_{sh}	series inductance, and shunt inductance
\mathcal{L}_n	line integration path at the n^{th} terminal
l_p, l_1, l_g, l_o, l_s	LWA dimensions
\bar{M}	magnetic current density
M_1, M_2, M_3, M_4	voltage loop points
$\bar{M}_{se,k}$	magnetic current density located a sampling point k
\mathbf{M}	modal matrix
m	integer number
m	integer sampling point for horizontal edge voltages
N	number of cascaded unit cells
n	integer number for unit cell terminal pair
\hat{n}	unit vector in normal direction
\mathbf{n}	space harmonic index
P	power
P_1, P_2, P_3, P_4	voltage loop points
P_{se}, P_{sh}	series power, and shunt power
$P_{se,rad}, P_{sh,rad}$	series radiated power, and shunt radiated power
P_{rad}, P_{diss}	radiated power, and dissipated power
P_{die}, P_{con}	dissipated power in in the dielectric, and in the conductor
p	unit cell length (period)
Q	quality factor
Q_1, Q_2	coupled quality factor of mode 1, and mode 2
Q_{loss1}, Q_{loss2}	quality factor loss mechanism 1, and loss mechanism 2
Q_{bal}	balanced quality factor
Q_{se}, Q_{sh}	series quality factor, and shunt quality factor
Q_{bs}, Q_{off-bs}	at-broadside quality factor, and off-broadside quality factor
R	series resistance
R_{die}, R_{con}	series dielectric, and conductor dissipation resistance
R_{diss}	series dissipation resistance
R_i	inner port resistance
$R_{lossy}, R_{lossless}$	series resistance with, and without loss consideration
R_{rad}	series radiation resistance
R_s	surface resistance
R'	per-unit-length resistance of a TL
S_{ij}	i, j element of the scattering matrix
S_{rad}, S_{con}	radiation surface, and conductor surface
\mathbf{S}	scattering matrix
T, T_{opt}	transformation ratio, and optimum transformation ratio
t_1, t_2	time instance 1, and time instance 2

V	voltage
V	volume unit cell
V_{diel}	substrate volume
V_k^+, V_k^-	series radiation equivalent voltage source
V_m^+, V_m^-	shunt radiation equivalent voltage source
V_n, V_{n+1}	voltage at the n^{th} , and $n^{\text{th}} + 1$ UC terminal
$V_{\text{se}}, V_{\text{sh}}$	series voltage, and shunt voltage
$V_{\text{se}k}, V_{\text{sh}m}$	series, and shunt radiation equivalent voltage source
v_g	group velocity
v_p	phase velocity
W	stored energy
W_e, W_m	stored energy in the electric field, and magnetic field
$W_{\text{se}}, W_{\text{sh}}$	series stored energy, and shunt stored energy
w	width unit cell
w	width of TL
w_p, w_l, w_s	LWA dimensions
x	Cartesian coordinates
\hat{x}	unit vector in x -direction
x_k, x_m	x -coordinate voltage sampling point horizontal, and vertical edges
y	Cartesian coordinate
\hat{y}	unit vector in y -direction
y_0	arbitrary y -location within the unit cell
y_k, y_m	y -coordinate voltage sampling point horizontal, and vertical edges
Y_{ij}	i, j element of the admittance matrix
Y_{sh}	shunt admittance
Y	admittance matrix
Z_0	characteristic transmission line impedance
Z_B	Bloch impedance
Z_B^+, Z_B^-	Bloch impedance in increasing n , and decreasing n direction
$Z_{\text{B,bs}}^+, Z_{\text{B,off-bs}}^+$	at-broadside Bloch impedance, and off-broadside Bloch impedance
$Z_{\text{B,sym}}$	Bloch impedance transversally symmetric unit cell
Z_{ij}	i, j element of the impedance matrix
Z_{se}	series impedance
Z_t, Z_p, Z_l, Z_s	characteristic TL impedances
Z	impedance matrix
z	Cartesian coordinate
\hat{z}	unit vector in z -direction

Greek Symbols

α	leakage constant
----------	------------------

$\alpha_{bs}, \alpha_{off-bs}$	at-broadside leakage constant, and off-broadside leakage constant
$\alpha_{sek}, \alpha_{sh m}$	complex asymmetry factors
β	phase constant
β_0	phase constant of the fundamental space harmonic ($n = 0$)
$\beta_{bs}, \beta_{off-bs}$	at-broadside phase constant, and off-broadside phase constant
γ	propagation constant
$\gamma_{bs}, \gamma_{off-bs}$	at-broadside, and off-broadside propagation constant
Δd	infinitesimal distance
$\Delta\Phi_k, \Delta\Phi_m$	phase difference series, and phase difference shunt
$\Delta\omega$	angular frequency deviation
$\Delta\Omega$	complex angular frequency deviation
$\Delta\Omega_1, \Delta\Omega_2$	complex frequency deviation of mode 1, and mode 2
$\Delta\Omega_{re}, \Delta\Omega_{im}$	real part, and imaginary part complex frequency deviation
$\epsilon_\ell, \epsilon_p, \epsilon_t$	permittivities
ϵ_r	relative permittivity
η	antenna radiation efficiency
η_{bs}, η_{off-bs}	at-broadside, and off-broadside radiation efficiency
η_{bw}, η_{fw}	backward, and forward radiation radiation efficiency
η_{se}, η_{sh}	series radiation efficiency, and shunt radiation efficiency
$\theta_1, \theta_p, \theta_s$	electrical TL lengths
ϑ	spherical coordinate
ϑ_{mb}	main beam angle
λ	wavelength
λ_0	free space wavelength
$\lambda_{1,2}$	eigenvalues
λ_g	guided transmission line wavelength
μ_ℓ, μ_p, μ_t	permeabilities in the TL model
ξ_{km}	proportionality factor
τ, τ_{opt}	coupling factor, and optimum coupling factor
Φ	phase angle for complex frequency
Φ_1	real phase angle (vertical axis)
Φ_k^+, Φ_k^-	phase angles series radiation contributions
Φ_m^+, Φ_m^-	phase angles shunt radiation contributions
Φ_{sym}	phase symmetry angle
φ	spherical coordinate
Ω	complex angular frequency
Ω_0	real mean frequency of the complex angular frequency
Ω_{re}, Ω_{im}	real part, and imaginary part complex angular frequency
ω	angular frequency
ω_0	harmonic mean angular frequency
ω_1	real frequency point (horizontal axis)

$\omega_{\text{bs}}, \omega_{\text{bal}}$	at-broadside angular frequency, and balanced angular frequency
$\omega_{\text{se}}, \omega_{\text{sh}}$	series, and shunt resonance angular frequency

Mathematical and Physical Constants

c_0	$2.998 \cdot 10^8$ m/s	speed of light in vacuum
e	2.718...	Euler's constant
ε_0	8.854 As/Vm	vacuum permittivity
μ_0	$4\pi \cdot 10^{-7}$ Vs/Am	vacuum permeability
π	3.14159...	Pi
j	$j^2 = -1$	imaginary unit

Mathematical Functions and Operators

$\int_{\mathcal{L}} [\cdot] d\vec{l}$	line integral
$\oint_{\mathcal{C}} [\cdot] d\vec{l}$	closed contour integral
$\int_S [\cdot] ds$	surface integral
$\int_V [\cdot] dv$	volume integral
$\frac{d}{d\omega} [\cdot]$	frequency derivative
$\text{Re} \{ \cdot \}$	real part
$\text{Im} \{ \cdot \}$	imaginary part
$[\cdot]^*$	complex conjugate
$\cosh [\cdot]$	cosine hyperbolic
$\text{arccosh} [\cdot]$	inverse cosine hyperbolic
$\arcsin [\cdot]$	inverse sine
$\ln [\cdot]$	natural logarithm
$\text{diag} [\cdot]$	diagonal matrix with elements of $[\cdot]$ in the principal diagonal
$[\cdot]^{-1}$	inverse matrix
$\lim_{\Delta\omega \rightarrow 0} [\cdot]$	limit
$\lim_{G \rightarrow 0^+} [\cdot]$	one-sided limit with G decreasing
$\text{err} [\cdot]$	error function

Bibliography

- [1] “145-2013 - IEEE standard for definitions of terms for antennas,” *IEEE Std 145-2013*, pp. 1–32, April 2013.
- [2] C. A. Balanis, *Antenna Theory: Analysis and Design*, 3rd ed. Wiley-Interscience, 2005.
- [3] J. Andrews, S. Buzzi, W. Choi, S. Hanly, A. Lozano, A. Soong, and J. Zhang, “What will 5g be?” *Selected Areas in Communications, IEEE Journal on*, vol. 32, no. 6, pp. 1065–1082, June 2014.
- [4] C.-X. Wang, F. Haider, X. Gao, X.-H. You, Y. Yang, D. Yuan, H. Aggoune, H. Haas, S. Fletcher, and E. Hepsaydir, “Cellular architecture and key technologies for 5g wireless communication networks,” *Communications Magazine, IEEE*, vol. 52, no. 2, pp. 122–130, February 2014.
- [5] P. Pirinen, “A brief overview of 5g research activities,” in *5G for Ubiquitous Connectivity (5GU), 2014 1st International Conference on*, Nov 2014, pp. 17–22.
- [6] W. Hong, K.-H. Baek, Y. Lee, Y. Kim, and S.-T. Ko, “Study and prototyping of practically large-scale mmwave antenna systems for 5g cellular devices,” *Communications Magazine, IEEE*, vol. 52, no. 9, pp. 63–69, September 2014.
- [7] K. Solbach and R. Schneider, “Antenna technology for millimeter wave automotive sensors,” in *Microwave Conference, 1999. 29th European*, vol. 1, Oct 1999, pp. 139–142.
- [8] J. Schoebel and P. Herrero, “Planar antenna technology for mm-wave automotive radar, sensing, and communications,” *Intech, Radar Technology*, 2010.
- [9] M. Jalilvand, C. Vasanelli, J. Kowalewski, and T. Zwick, “Implementation of antenna array systems for medical imaging,” in *Microwave Conference (GeMIC), 2014 German*, March 2014, pp. 1–4.
- [10] C. Rappaport and F. Morgenthaler, “Localized hyperthermia with electromagnetic arrays and the leaky-wave troughguide applicator,” *Microwave Theory and Techniques, IEEE Transactions on*, vol. 34, no. 5, pp. 636–643, May 1986.

- [11] R. Fetter, P. Gadsby, and J. Kabachinski, "Microwave hyperthermia probe," Jun. 27 1989, uS Patent 4,841,988.
- [12] D. M. Pozar, *Microwave and RF Design of Wireless Systems*. Wiley, 2000.
- [13] S. Haykin and M. Moher, *Communication Systems*. Wiley, 2009.
- [14] T. S. Rappaport, *Wireless Communications: Principles and Practice (2nd Edition)*. Prentice Hall, 2002.
- [15] M. Skolnik, *Introduction to Radar Systems*. McGraw-Hill Education, 2002.
- [16] R. C. Hansen, *Phased Array Antennas*. Wiley-Interscience, 2009.
- [17] A. K. Bhattacharyya, *Phased Array Antennas : Floquet Analysis, Synthesis, BFNs and Active Array Systems*. Wiley-Interscience, 2006.
- [18] J. N. Hines and J. R. Upson, "A wide aperture tapered-depth scanning antenna," *Ohio State Univ. Res. Found., Tech. Rep. 667-7*, Dec 1957.
- [19] A. Hessel, *Antenna Theory, Part II*, R. E. Collin and R. F. Zucker, Eds. New York: McGraw-Hill, 1969, chap. 19.
- [20] J. Volakis, *Antenna Engineering Handbook*, 4th ed. McGraw-Hill Professional, June 7 2007.
- [21] D. R. Jackson, C. Caloz, and T. Itoh, "Leaky-wave antennas," *Proc. IEEE*, vol. 100, no. 7, pp. 2194–2206, 2012.
- [22] J. Liu, D. Jackson, and Y. Long, "Substrate integrated waveguide (siw) leaky-wave antenna with transverse slots," *Antennas and Propagation, IEEE Transactions on*, vol. 60, no. 1, pp. 20–29, Jan 2012.
- [23] T. Metzler, "Microstrip series arrays," *IEEE Trans. Antennas Propag.*, vol. 29, no. 1, pp. 174–178, 1981.
- [24] J. James and P. Hall, "Microstrip antennas and arrays. part 2: New array-design technique," *Microwaves, Optics and Acoustics, IEE Journal on*, vol. 1, no. 5, pp. 175–181, September 1977.
- [25] J. James, P. Hall, and C. Wood, *Microstrip Antenna Theory and Design (Electromagnetic Waves)*. Institution Of Engineering And Technology, 1981.
- [26] C. Caloz and T. Itoh, *Electromagnetic Metamaterials: Transmission Line Theory and Microwave Applications*. Wiley-IEEE Press, 2005.
- [27] L. Liu, C. Caloz, and T. Itoh, "Dominant mode (DM) leaky-wave antenna with backfire-to-endfire scanning capability," *Electron. Lett.*, vol. 38, no. 23, pp. 1414–1416, November 2002.
- [28] D. R. Jackson and A. A. Oliner, *Modern Antenna Handbook*, C. A. Balanis, Ed. Ed. Wiley-Interscience, 2008.
- [29] S. Sengupta, D. Jackson, and S. Long, "Examination of radiation from 2d periodic leaky-wave antennas," in *Radio Science Meeting (Joint with AP-S Symposium), 2014 USNC-URSI*, July 2014, pp. 76–76.
- [30] C. Caloz, T. Itoh, and A. Rennings, "CRLH metamaterial leaky-wave and resonant antennas," *IEEE Antennas Propag. Mag.*, vol. 50, no. 5, pp. 25–39, Oct. 2008.

-
- [31] C. Caloz, D. R. Jackson, and T. Itoh, *Frontiers in Antennas*, F. Gross, Ed. New York: McGraw-Hill, 2010.
- [32] A. Sutinjo, M. Okoniewski, and R. Johnston, "Radiation from fast and slow traveling waves," *IEEE Antennas Propag. Mag.*, vol. 50, no. 4, pp. 175–181, 2008.
- [33] N. Yang, C. Caloz, and K. Wu, "Full-space scanning periodic phase-reversal leaky-wave antenna," *IEEE Trans. Microw. Theory Tech.*, vol. 58, no. 10, pp. 2619–2632, Oct. 2010.
- [34] S. Otto, A. Rennings, K. Solbach, and C. Caloz, "Transmission line modeling and asymptotic formulas for periodic leaky-wave antennas scanning through broadside," *IEEE Trans. Antennas Propag.*, vol. 59, no. 10, October 2011.
- [35] M. Guglielmi and D. R. Jackson, "Broadside radiation from periodic leaky-wave antennas," *IEEE Trans. Antennas Propag.*, vol. 41, no. 1, pp. 31–37, 1993.
- [36] S. Paulotto, P. Baccarelli, F. Frezza, and D. R. Jackson, "Full-wave modal dispersion analysis and broadside optimization for a class of microstrip CRLH leaky-wave antennas," *IEEE Trans. Microw. Theory Tech.*, vol. 56, no. 12, pp. 2826–2837, December 2008.
- [37] J. S. Gomez-Diaz, D. Cañete Rebenaque, and A. Alvarez-Melcon, "A simple CRLH LWA circuit condition for constant radiation rate," *IEEE Antennas Wireless Propag. Lett.*, vol. 10, pp. 29–32, 2011.
- [38] S. Paulotto, P. Baccarelli, F. Frezza, and D. R. Jackson, "A novel technique for open-stopband suppression in 1-D periodic printed leaky-wave antennas," *Antennas and Propagation, IEEE Transactions on*, vol. 57, no. 7, pp. 1894–1906, July 2009.
- [39] J. Williams, P. Baccarelli, S. Paulotto, and D. Jackson, "1-D comblines leaky-wave antenna with the open-stopband suppressed: Design considerations and comparisons with measurements," *IEEE Trans. Antennas Propag.*, vol. 61, no. 9, pp. 4484–4492, 2013.
- [40] J. Gomez-Diaz, A. Alvarez-Melcon, and J. Perruisseau-Carrier, "Analysis of the radiation characteristics of CRLH LWAs around broadside," in *Antennas and Propagation (EUCAP), 2012 6th European Conference on*, 2012, pp. 2876–2880.
- [41] P. Crepeau and P. McIsaac, "Consequences of symmetry in periodic structures," *Proc. IEEE*, vol. 52, no. 1, pp. 33–43, 1964.
- [42] A. Hessel, M. H. Chen, R. C. M. Li, and A. A. Oliner, "Propagation in periodically loaded waveguides with higher symmetries," *Proc. IEEE*, vol. 61, no. 2, pp. 183–195, 1973.
- [43] A. Lai, T. Itoh, and C. Caloz, "Composite right/left-handed transmission line metamaterials," *Microwave Magazine, IEEE*, vol. 5, no. 3, pp. 34–50, Sept 2004.
- [44] A. Bartlett, *The theory of electrical artificial lines and filters*. Wiley, 1930.
- [45] O. J. Zobel, "Phase-shifting network," Feb. 17 1931, uS Patent 1,792,523.
- [46] M. Zedler, U. Siart, and P. Russer, "Circuit theory unifying description for metamaterials," in *2008 URSI General Assembly*, August 2008.

- [47] F. Bongard, J. Perruisseau-Carrier, and J. R. Mosig, "Enhanced CRLH transmission line performances using a lattice network unit cell," *IEEE Microw. Wireless Compon. Lett.*, vol. 19, no. 7, pp. 431–433, July 2009.
- [48] S. Otto and C. Caloz, "Solving the broadside radiation issue in periodic leaky-wave antennas," in *IEEE 4th Asia-Pacific Conference on Antennas and Propagation (APCAP)*, 2015, (Invited Paper).
- [49] A. Al-Bassam, S. Otto, Z. Chen, A. Rennings, and K. Solbach, "A capacitively-coupled series-fed patch leaky-wave antenna and optimization concepts for efficient broadside radiation," in *the 7th German Microwave Conference (GeMiC)*, March 2012, pp. 1–4.
- [50] S. Otto, K. Solbach, and C. Caloz, "Recent advances in the modeling of periodic leaky-wave antennas scanning through broadside," in *Proc. 6th European Conf. Antennas and Propagation (EUCAP)*, 2012, pp. 263–264.
- [51] S. Otto, A. Rennings, K. Solbach, and C. Caloz, "Complex frequency versus complex propagation constant modeling and Q-balancing in periodic structures," in *Microwave Symposium Digest (MTT), 2012 IEEE MTT-S International*, June 2012, pp. 1–3.
- [52] S. Otto, A. Rennings, O. Litschke, and K. Solbach, "A dual-frequency series-fed patch array antenna," in *3rd European Conference on Antennas and Propagation*, Berlin, Germany, 3 2009.
- [53] S. Otto, A. Rennings, T. Liebig, C. Caloz, and K. Solbach, "An energy-based circuit parameter extraction method for CRLH leaky-wave antennas," in *4rd European Conference on Antennas and Propagation*, Barcelona, Spain, April 2010.
- [54] S. Otto, A. Rennings, C. Caloz, P. Waldow, and T. Itoh, "Composite right/left-handed λ -resonator ring antenna for dual-frequency operation," in *Proc. IEEE Antennas and Propagation Society International Symposium*, July 2005, pp. 684–687.
- [55] S. Otto, A. Rennings, C. Caloz, and P. Waldow, "Dual mode zeroth order ring resonator with tuning capability and selective mode excitation," in *Proc. European Microwave Conference*, vol. 1, 4–6 Oct. 2005, p. 3pp.
- [56] S. Otto, O. Litschke, J. Leiß, and K. Solbach, "A unit cell based low side lobe level design for series-fed array," in *Proc. Asia-Pacific Microwave Conference (APMC), Hong Kong, Dec. 2008, CD-ROM*, 2008.
- [57] S. Otto, S. Held, A. Rennings, and K. Solbach, "Array and multiport antenna farfield simulation using EMPIRE, MATLAB and ADS," in *Microwave Conference, 2009. EuMC 2009. European*, Sept 2009, pp. 1547–1550.
- [58] S. Otto, Z. Chen, A. Al-Bassam, A. Rennings, K. Solbach, and C. Caloz, "Circular polarization of periodic leaky-wave antennas with axial asymmetry: Theoretical proof and experimental demonstration," *IEEE Trans. Antennas Propag.*, vol. 62, no. 4, pp. 1817–1829, Apr. 2014.
- [59] S. Otto, C. Caloz, and T. Itoh, "A dual-frequency composite right/left-handed half-wavelength resonator antenna," in *in Proc. Asia-Pacific Microwave Conference (APMC), New Dehli, India, Dec. 2004, CD-ROM.*, 2004.

- [60] S. Otto and C. Caloz, "Importance of transversal and longitudinal symmetry/asymmetry in the fundamental properties of periodic leaky-wave antennas," in *Proc. IEEE Antennas and Propagation Society International Symposium*, 2013, (Invited Paper).
- [61] S. Otto, A. Al-Bassam, A. Rennings, K. Solbach, and C. Caloz, "Transversal asymmetry in periodic leaky-wave antennas for bloch impedance and radiation efficiency equalization through broadside," *IEEE Trans. Antennas Propag.*, vol. 62, no. 4, pp. 1817–1829, Apr. 2014.
- [62] —, "Radiation efficiency of longitudinally symmetric and asymmetric periodic leaky-wave antennas," *Antennas and Wireless Propagation Letters, IEEE*, vol. 11, pp. 612–615, 2012.
- [63] S. Otto, A. Al-Bassam, Z. Chen, A. Rennings, K. Solbach, and C. Caloz, "Q-balancing in periodic leaky-wave antennas to mitigate broadside radiation issues," in *the 7th German Microwave Conference (GeMiC)*, March 2012, pp. 1–4.
- [64] C. Caloz and S. Otto, "Tour on recent developments and discoveries of crucial practical importance in leaky-wave antennas," in *Proc. European Microwave Conference, Nuremberg*, 2013, (Invited Paper).
- [65] A. Al-Bassam, S. Otto, and C. Caloz, "Role of symmetries in periodic leaky wave antennas, with emphasis on the double asymmetry case," in *Proc. 9th European Conf. Antennas and Propagation (EUCAP)*, April 2015.
- [66] T. Liebig, A. Rennings, S. Otto, C. Caloz, and D. Erni, "Comparison Between CRLH Zeroth-Order Antenna and Series-Fed Microstrip Patch Array Antenna," in *3rd European Conference on Antennas and Propagation*, Berlin, Germany, 3 2009.
- [67] B. Jones, F. Chow, and A. Seeto, "The synthesis of shaped patterns with series-fed microstrip patch arrays," *IEEE Trans. Antennas Propag.*, vol. 30, no. 6, pp. 1206–1212, Nov 1982.
- [68] K.-L. Wu, M. Spenuk, J. Litva, and D.-G. Fang, "Theoretical and experimental study of feed network effects on the radiation pattern of series-fed microstrip antenna arrays," *IEE Proceedings H Microwaves, Antennas and Propagation*, vol. 138, no. 3, pp. 238–242, Jun 1991.
- [69] M.-H. Chung and S. Nam, "Analysis of a rectangular patch antenna coupled by microstrip feedline gap discontinuity," in *Antennas and Propagation Society International Symposium, 1993. AP-S. Digest*, June 1993, pp. 1236–1239 vol.3.
- [70] D. Pozar and D. Schaubert, "Comparison of three series fed microstrip array geometries," in *Proc. AP-S Antennas and Propagation Society International Symposium Digest*, 1993, pp. 728–731 vol.2.
- [71] E. Okon and C. Turner, "A wide-band microstrip series array at mm-wave," in *Proc. High Frequency Postgraduate Student Colloquium*, 1999, pp. 88–92.
- [72] J. Freese, R. Jakoby, H.-L. Blocher, and J. Wenger, "Synthesis of microstrip series-fed patch arrays for 77 ghz-sensor applications," in *Proc. Asia-Pacific Microwave Conference*, 2000, pp. 29–33.
- [73] D. Babas and J. Sahalos, "Synthesis method of series-fed microstrip antenna arrays," *Electronics Letters*, vol. 43, no. 2, pp. 78–80, January 18 2007.

- [74] C. Niu, J. She, and Z. Feng, "Design and simulation of linear series-fed low-sidelobe microstrip antenna array," in *Proc. Asia-Pacific Microwave Conference APMC 2007*, 11–14 Dec. 2007, pp. 1–4.
- [75] G. Floquet, "Sur les équations différentielles linéaires à coefficients périodiques," *Annales École Normale Supérieure*, vol. 12, pp. 47–88, 1883.
- [76] R. E. Collin, *Field theory of guided waves*. IEEE Press, 1991.
- [77] K. Zhang and D. Li, *Electromagnetic Theory for Microwaves and Optoelectronics*. Springer, 2007.
- [78] D. M. Pozar, *Microwave Engineering*, 4th ed. Wiley, 2011.
- [79] R. E. Collin, *Foundations for Microwave Engineering*. Wiley-IEEE Press, December 2000.
- [80] M. Guglielmi and G. Boccalone, "A novel theory for dielectric-inset waveguide leaky-wave antennas," *Antennas and Propagation, IEEE Transactions on*, vol. 39, no. 4, pp. 497–504, Apr 1991.
- [81] P. Baccarelli, S. Paulotto, and D. Jackson, "A π -matching network to eliminate the open-stopband in 1-d periodic leaky-wave antennas," in *Antennas and Propagation Society International Symposium (APSURSI), 2012 IEEE*, 2012, pp. 1–2.
- [82] J. Williams, S. Paulotto, P. Baccarelli, and D. Jackson, "Design of a 1-d comblined leaky-wave antenna with the open-stopband suppressed," in *Electromagnetics in Advanced Applications (ICEAA), 2010 International Conference on*, 2010, pp. 83–86.
- [83] N. Yang, C. Caloz, and K. Wu, "Fixed-beam frequency-tunable phase-reversal coplanar stripline antenna array," *IEEE Trans. Antennas Propag.*, vol. 57, no. 3, pp. 671–681, March 2009.
- [84] —, "Wideband phase-reversal antenna using a novel bandwidth enhancement technique," *IEEE Trans. Antennas Propag.*, vol. 58, no. 9, pp. 2823–2830, September 2010.
- [85] —, "Full-space scanning periodic phase-reversal leaky-wave antenna," *IEEE Trans. Microw. Theory Tech.*, vol. 58, no. 10, p. 1, October 2010.
- [86] G. Matthaei, *Microwave filters, impedance-matching networks, and coupling structures*. Dedham, MA: Artech House Books, 1980.
- [87] A. Bartlett, "An extension of a property of artificial lines," *Communication from the Research Staff of the General Electric Co., Wembley*, pp. 902–907, 1927.
- [88] T. Iyer, *Circuit Theory*. Tata McGraw Hill Publishing Company, 1985.
- [89] J.-S. G. Hong and M. J. Lancaster, *Microstrip Filters for RF/Microwave Applications*. Wiley-Interscience, 2002.
- [90] C. Caloz and H. Nguyen, "Novel broadband conventional- and dual-composite right/left-handed (C/D-CRLH) metamaterials: properties, implementation and double-band coupler application," *Applied Physics A*, vol. 87, no. 2, pp. 309–316, 2007.

-
- [91] T. Tamir, *Antenna Theory, Part II*, R. E. Collin and R. F. Zucker, Eds. New York: McGraw-Hill, 1969, chap. 20.
- [92] O. Heaviside, “Electromagnetic induction and its propagation,” *The Electrician*, vol. August 7, pp. pp. 230–231, 1887.
- [93] T. Kokkinos, C. Sarris, and G. Eleftheriades, “Periodic FDTD analysis of leaky-wave structures and applications to the analysis of negative-refractive-index leaky-wave antennas,” *IEEE Trans. Microw. Theory Tech.*, vol. 54, no. 4, pp. 1619–1630, 2006.
- [94] P. Baccarelli, C. Di Nallo, S. Paulotto, and D. R. Jackson, “A full-wave numerical approach for modal analysis of 1-D periodic microstrip structures,” *IEEE Trans. Microw. Theory Tech.*, vol. 54, no. 4, pp. 1350–1362, Jun. 2006.
- [95] *EMPIRE XPU Manual*, IMST GmbH, December 2014. [Online]. Available: www.empire.de
- [96] *HFSSTM Online Help*, ANSYS, Inc., November 2013. [Online]. Available: www.ansys.com
- [97] N. Jamaly and A. Derneryd, “Efficiency characterisation of multi-port antennas,” *Electronics Letters*, vol. 48, no. 4, pp. 196–198, February 2012.
- [98] T. Liebig, S. Held, A. Rennings, and D. Erni, “Accurate parameter extraction of lossy composite right/left-handed (CRLH) transmission lines for planar antenna applications,” in *METAMATERIALS 2009*, Karlsruhe, Germany, September 2010, pp. 456–458.
- [99] T. Liebig, A. Rennings, S. Held, and D. Erni, “Accurate parameter extraction of lossy composite right/left-handed (crlh) transmission lines for planar antenna applications,” in *Fourth International Congress on Advanced Electromagnetic Materials in Microwaves and Optics*, 2010, pp. 13–16.
- [100] G. Valerio, S. Paulotto, P. Baccarelli, P. Burghignoli, and A. Galli, “Accurate bloch analysis of 1-D periodic lines through the simulation of truncated structures,” *Antennas and Propagation, IEEE Transactions on*, vol. 59, no. 6, pp. 2188–2195, June 2011.
- [101] *Fields Calculator Cookbook, HFSSTM 15.0*, ANSYS, Inc., June 2012. [Online]. Available: www.ansys.com
- [102] J. R. James and P. S. Hall, *Handbook of Microstrip Antennas*, 2nd ed., ser. IEE Electromagnetic Waves Series, 28. INSPEC, June 1988.
- [103] M. Kang, C. Caloz, and T. Itoh, “Miniaturized MIM CRLH transmission line structure and application to backfire-to-endfire leaky-wave antenna,” in *Proc. IEEE Antennas and Propagation Society Int. Symp.*, vol. 1, 2004, pp. 827–830.
- [104] A. Rennings, T. Liebig, C. Caloz, and P. Waldow, “MIM CRLH series mode zeroth order resonant antenna (ZORA) implemented in LTCC technology,” in *Proc. Asia-Pacific Microwave Conf. APMC 2007*, 2007, pp. 1–4.
- [105] T. Liebig, A. Rennings, S. Otto, C. Caloz, and D. Erni, “Comparison between CRLH zeroth-order antenna and series-fed microstrip patch array antenna,” in *Proc. 3rd European Conference on Antennas and Propagation EuCAP 2009*, 2009, pp. 529–532.

- [106] J. D. Jackson, *Classical Electrodynamics*, third, Ed. Wiley, 1999.
- [107] M. Zedler and G. Eleftheriades, “Spatial harmonics and homogenization of negative-refractive-index transmission-line structures,” *IEEE Trans. Microw. Theory Tech.*, vol. 58, no. 6, pp. 1521–1531, 2010.
- [108] J. Gomez-Tornero, G. Goussetis, and A. Alvarez-Melcon, “Simple control of the polarisation in uniform hybrid waveguide-planar leaky-wave antennas,” *IET Microwaves, Antennas & Propagation*, vol. 1, no. 4, pp. 911–917, 2007.
- [109] C. Caloz and T. Itoh, “Array factor approach of leaky-wave antennas and application to 1-d/2-d composite right/left-handed (CRLH) structures,” *IEEE Microw. Wireless Compon. Lett.*, vol. 14, no. 6, pp. 274–276, 2004.
- [110] M. Tonouchi, “Cutting-edge terahertz technology,” *Nature Photonics*, vol. 1, no. 2, pp. 97–105, Feb. 2007.
- [111] H. Cheema and A. Shamim, “The last barrier: on-chip antennas,” *Microwave Magazine, IEEE*, vol. 14, no. 1, pp. 79–91, Jan 2013.
- [112] M. Memarian and G. V. Eleftheriades, “Dirac leaky-wave antennas for continuous beam scanning from photonic crystals,” *Nature Communications*, vol. 6, 2015.